Modelling Human-Driver Behaviour Using a Biofidelic Approach

Miguel Martínez García

School of Engineering
University of Lincoln

This dissertation is submitted for the degree of
Doctor of Philosophy

College of Science December 2018

En memoria de mi padre …

Declaration

I hereby declare that except where specific reference is made to the work of others, the contents of this dissertation are original and have not been submitted in whole or in part for consideration for any other degree or qualification in this, or any other university. This dissertation is my own work and contains nothing which is the outcome of work done in collaboration with others, except as specified in the text and Acknowledgements.

Miguel Martínez García
December 2018

Preface

This dissertation results from a PhD research program conducted from September 2014 to August 2018, and is concerned with characterising human driver behaviour, in particular human steering in the control of ground vehicles. The research program was funded internally by the University of Lincoln. The supervisor was Prof. Timothy Gordon, and the co-supervisor Dr. Argyrios Zolotas. For this research, experiments were conducted with human subjects, which were approved by the College of Science Research Ethics Committee of the University of Lincoln with UID COSREC491.

Acknowledgements

To pursue a Ph.D. involves learning numerous things on a daily basis over the span of several years. And as any longstanding venture, it would be almost unattainable without conversation and cooperation with other peers. I would like to acknowledge Prof. Timothy Gordon for taking me as a student, introducing me to a scientific domain which I knew nothing about and being supportive whenever I showed up in his office with bizarre research schemes.

At the same time, I want to thank Mr. Tim Smith, for devoting many hours of his time to the manufacture of a steering system prototype – virtually made from raw materials. Without his help and engineering expertise, I would not have been able to conduct the driving simulation experiments included in this dissertation. Regarding this, also many thanks to Prof. Chris Bingham for providing a torque sensor, and for being always helpful and encouraging to all the researchers at the College of Science.

Other people that work, or have worked, at the University of Lincoln and deserve special mention are: Dr. Yu Zhang – thanks to her I was involved in other research projects during these four years, including an industrial collaboration with Dynex Semiconductor Ltd. and a small participation in Siemens condition monitoring program; and Dr. Michal Weiszer – who made good suggestions regarding optimisation algorithms, and always displayed a stoic approach to work that was inspiring to others.

Likewise I want to thank other members of staff at the University of Lincoln that have done in the past, or still do, very important supporting jobs. With respect to this, a very special thank you to Denise Bateman. Besides being an excellent professional, and a very understanding person, she helped me during a critical time. Additionally, many thanks to Alistair Soons and Jen Smith for always being so supportive in multiple ways.

Certainly, the endeavour achieved during this research program depends on the efforts of the past too; it is over these years that I truly understood what it is meant by *alma mater*. Hence I would like to give my thanks to a very unique place, the *Facultad de Matemáticas y Estadística* (FME) from the *Universidad Politécnica de Cataluña* (UPC) in Spain. From their particular style of teaching, based on self-reliance and analytical thinking, I have inherited most of my skills. I really wish that the FME never forgets its magical, old-school principles. Staff members from the FME that deserve special mention are Prof. Jaume Franch Bullich, who introduced me to fractional calculus, Prof. Tere Martínez-Seara, who directed my M.Sc. dissertation – along with Prof. Pau Martín – and her passion and energy towards mathematics was always contagious to everyone, Prof. Jaume Soler, who heightened my liking for numerical methods, Prof. Rafael Ramírez, who is always so kind and accessible to students with questions and Prof. Joan de Solà-Morales, who has a peculiar way to make mathematics something more understandable. Neither I forget José Manuel Mora from the *Instituto Jaume Balmes* in Barcelona; it is thanks to him that I experienced science as something enjoyable for the first time.

Lastly, and at a personal level, there are a few exceptional people who accompanied me during this adventure. Foremost, a huge thanks to Eve for all her immense support and for the many things I have learned from her. To recall a single episode, exploring the mountains of Mount Lu in China with her is one of the highlights of my entire life. Then, I express my utmost gratitude to my friends Michal Weiszer and Chi Tsang. All the friendship accompanied with interesting informal chat, at what once was our usual pub, will never be forgotten.

Life is a learning experience, that step by step conforms our personal evolution. Thus the fact that I learned so much from all of you, has made you a part of my soul.

Abstract

This dissertation is concerned with the subject of modelling human steering control of ground vehicles. Special care has been taken with respect to designing a model that is *biofidelic*, i.e., a model that operates according to the *principles of human control*.

With this aim, first classical human control theory has been revisited, both from a literature review and an experimental perspective; data have been recorded from test subjects in compensatory and pursuit tracking tasks. The tracking experiments are the first ever to be performed with fractional order plants, which are plants suitable to represent system memory. From the data, an extension of the Crossover model by McRuer's is designed, to include the control of such category of plants. The proposed model is referred to as the *Fractional Crossover Model*. This is followed by a study on modelling memory in human-machine systems from a classical control theory viewpoint. These results broaden the existing array of manual control modelling techniques and can be employed in a modular manner, combined with current models.

More significantly – and still with respect to the domain of generic human control and human-machine systems – a new approach for modelling the human-operator is proposed. This approach consists in treating the problem from a statistical viewpoint. With this methodology a novel human control model based on multiplicative dynamics is presented. The model, which was inspired on actual results in neuroscience, is validated with the tracking data obtained from test subjects and by comparing it to classical models in the literature. Hence the model is useful to analyse human performance or to reproduce human control in simulation, field tests or in the video game industry.

With respect to steering control modelling, which is the main topic of this dissertation, additional experiments with test subjects were conducted in a simple vehicle simulator – with hardware and software specifically developed during this research program to test multiple hypotheses. The data were analysed with the intent of identifying which optical variables drivers employ while controlling a vehicle on public roads; it is seen that the splay angles – which are the projections of the road lines on the retina – are likely candidates for lane keeping at low speeds. This brings on a novel human-centred driver model first proposed

here. This model includes multiplicative human control over the splay angles, and far-point error perception for lane keeping at higher speeds.

The human-centred model has its domain of applicability in the intelligent transportation industry, in particular for the development of shared control systems and advanced driver-assistance systems for semi-autonomous ground vehicles. Additionally, the model can be employed in field testing of ground vehicles – for example, in vehicle durability tests.

Furthermore, the topic of alternative steering devices for driving autonomous and semi-autonomous vehicles is investigated. This leads to another of the contributions in this dissertation. Here it is proposed that for such vehicles, and for the control of systems with a *shared control* perspective, an *isometric steering wheel* can be advantageous under certain schemes – tight rein or loose rein modes according to the H-metaphor. This is supported by additional data collected in the driving simulation experiments. Resulting from this, fractional order transfer functions are employed to increment steering stability and control accuracy with the isometric device. This prototypical steering system is applicable for the control of ground vehicles with the so-called *by-wire* controls, which are already incorporated in some commercially available vehicles.

Table of contents

List of figures

List of tables

Nomenclature

Acronyms / Abbreviations

ACT-R Adaptive Control of Thought – Rational

ADAS Advanced Driver-assistance Systems

AI Artificial Intelligence

AGI Artificial General Intelligence

A1 Primary Auditory Cortex

BIBO Bounded Input Bounded Output

B2V Brain-to-vehicle – Connectivity

CDF Cumulative Distribution Function

cg Centre of gravity

CLT Central Limit Theorem

CNS Central Nervous System

CNYR Critical Normalised Yaw-rate

CO Crossover – model

CSV Comma-separated Values

DSE Driving Simulation Experiments – dataset

FIR Finite Impulse Response

fNIR Functional Near-Infrared – spectroscopy

FPGA Field Programmable Gate Array

FODE Fractional Order Differential Equation

FOE Focus of Expansion

GLUT OpenGL Utility Toolkit

HOCL Hybrid Open-closed Loop

HTE Human-in-the-loop Tracking Experiments – dataset

ID Index of Difficulty – Fitts' Law

IIR Infinite Impulse Response

IP Index of Performance – Fitts' Law

ISW Isometric Steering Wheel

LGN Lateral Geniculate Nucleus

LoHA Level of Haptic Authority

LTM Long Term Memory

MGN Medial Geniculate Nucleus

MHC Multiplicative Human Control

MSE Mean Squared Error

MST Medial Superior Temporal – visual area

MT Medial Temporal – visual area

NDD Naturalistic Driving Data – dataset

ODE Ordinary Differential Equation

OpenGL Open Graphics Library

PCA Principal Component Analysis

PDF Probability Density Function

PI Proportional-integral – transfer function

PSD Power Spectral Density

RMSE Root-mean-squared Error

SAE Society of Automotive Engineers

SBW Steer-by-wire

SG Salvucci & Gray – model

STM Short Term Memory

SW Steering Wheel

TF Transfer Function

TTLC Time to Lane Crossing

VPN Ventral Posterior Nucleus

VPU Vision Processing Unit

VSTM Visual Short Term Memory

V1 Visual Area 1 (Primary Visual Cortex)

V2V Vehicle-to-vehicle – Connectivity

V2X Vehicle-to-infrastructure – Connectivity

YRE Yaw-rate Error

Mathematical Symbols

s Laplace variable

i Imaginary unit

$\mathbb{N}$ Natural numbers

$\mathbb{Z}$ Integer numbers

$\mathbb{R}$ Real numbers

$\mathbb{C}$ Complex numbers

$\lceil \cdot \rceil$ Ceiling function

$\mathcal{I}$ Identity operator

$\Gamma(\cdot)$ Gamma function

$\mathcal{L}\{\cdot\}$ Laplace transform

$L^n\{\cdot\}$ Back-shift operator over n steps

Other Symbols

$C_{\alpha f}$ Cornering stiffness at the front axle

$C_{\alpha r}$ Cornering stiffness at the rear axle

$e(t)$ Tracking error

$h(t), \mathcal{H}(s)$ Human-operator response and frequency response on a tracking task

$h_l(t), \mathcal{H}_L(s)$ Linear equivalent system of the human-operator response

$H_\alpha^d(z)$ IIR discrete model

$H_\alpha^c(s)$ IIR continuous model

I Yaw moment of inertia

l Wheelbase ($l = l_f + l_r$)

l_f Distance from centre of gravity to front axle

l_r Distance from centre of gravity to rear axle

$m(t)$ Machine response

M Mass of the vehicle

$m_{R,L}$ Right and Left Boundary Margin

$r(t)$ Forcing function

$\mathcal{R}(s)$ Nonlinear part or *remnant* of the human-operator frequency response

r_s Steering ratio

T_p Preview time

U Vehicle speed

$y(t)$ Lateral offset of a vehicle

$Y_h(s)$ Human-operator transfer function

$Y_p^{\alpha}(s)$ Controlled plants – HTE

α Fractional coefficient for the plant – CO model

$\beta(t)$ Body slip angle

γ Fractionality of the plant ($\gamma = \alpha - 1$) – CO model

$\delta(t)$ Steering angle at the steering wheel

$\delta_f(t)$ Steering angle at the front wheels

η Steering rate

$\theta_{n,f}$ Angle from the heading of the vehicle to a near/far point at the centre of the lane

λ Fractional coefficient in the FCO model

μ Fractionality of the linear vehicle model

τ Effective time delay

τ_C CNS processing delay

τ_H Human delay without muscle latency

τ_N Neuromuscular lag

τ_P Perception delay

χ CNYR

$\psi(t)$ Heading of the vehicle – global reference frame

$\psi_c(t)$ Heading-relative bearing with respect to road path direction

$\dot{\psi}_{\text{crit}}^{\text{R,L}}$ Right and left critical yaw rate

ω_c Crossover frequency

Chapter 1

Introduction

1.1 Outlook and Scope

During the last years, news broadcasting of science and technology trends has placed a special interest in the possibility of driverless cars pervading the public roads. In spite of the eager news coverage, fully autonomous vehicles may not be materialised in the short term – or not materialised at all. There are a number of technical challenges towards full vehicle automation which presently do not have a clear solution. Conceivably, the most hindering obstacles are amidst the domain of Artificial Intelligence (AI). With the current state of the art in machine learning procedures, it is unthinkable that an intelligent system, able to respond appropriately to every potential situation one may encounter while driving a car, may be developed.

AI design towards full vehicle automation is closer to the realm of Artificial General Intelligence (AGI) than to machine learning. In reality, developing AGI systems is out of reach at this time, and this may be so for a very long time. If AGI systems were to be developed, driverless cars would not necessarily be a specially noticeable technology, among an immense exhibition of stunning technological advances; industrial science in pharmaceutics or lethal autonomous weapons could have a larger impact in society. A recent survey of experts in machine learning and technology yielded an estimate of $30-50$ years for AGI systems to take place [Teg17], although some questioned the feasibility of the idea itself.

In view of this, what is the relevance of intelligent systems research applied to vehicle control? Although conventional cars will not attain full automation anytime soon, multiple offshoots of associated developments will potentially result. An obvious one is the occurrence of autonomous transportation systems within restricted environments; since the problem of AGI is not tractable, driverless cars in simplified environments can be implemented. This

may be accomplished through changes in infrastructure, for instance by building up *eLanes* in which only vehicles in autonomous control mode can circulate [TWM+09]. Vehicles in eLanes would behave in a similar way as vehicles running on rails. Hence eLanes could provide a restricted scenario, in which pedestrians and human driven cars do not exist; and upon the vehicle exiting the eLane, the human would take back vehicle control. Another interesting prospect is that of *shared control* systems, where the control of the machine is shared between the human and the intelligent system simultaneously.

The concept of shared control has been in the literature for quite some time, yet nowadays it is earning momentum. Within the classical literature, the paper by Birmingham and Taylor on human-machine systems [BT54] is an illustrative case; it is affirmed that because of the high adaptability that humans exhibit, they should never be removed from the control loop. Instead, the paper suggests, system design needs to be aimed towards *unburdening* the human-operator. Thus it is introduced the idea of using transfer functions between the control device and the machine, with the intent of facilitating the control of a plant.

The notion of shared control was highlighted through an alternative strategy in a later publication. In [Lic60], it was proposed that the human can be temporarily removed from the control loop, but needs to be ready to 'handle the very-low-probability situations', for which the autonomous system was not designed for. Hence, this shared control scheme is equivalent to what is known today as *conditional automation*, and defined as level 3 automation by the Society of Automotive Engineers (SAE).

A considerable part of the endeavour in this dissertation is directed towards developing tools for achieving both shared-control schemes: simultaneous control facilitation and conditional automation. Inasmuch as these ideas have been hovering in the literature for decades, why is the research related to these concepts relevant nowadays? Several technological advances aid to answer this question.

One of them is the so-called *by-wire* control, which substitutes the mechanical connection from the steering system to the vehicle wheels with an electronic system; in 2014 the first commercially available car with a *steer-by-wire* (SBW) system was released – the Nissan Infinity Q50. Thus designing transfer functions, between the human and the car, to *unburden* the human-operator has attained practicability. Furthermore, SBW systems allow for the integral replacement of conventional steering systems with new synthetic mappings – this matter will be explored in Chapter 5.

Additionally, modern machine learning techniques – such as deep learning – have made practical the embodiment of efficient computer vision systems for vehicle guidance. This huge development of potential, from the algorithmic perspective, has progressed hand in hand with the available computational capacity of low-power devices, such as *field programmable*

gate arrays (FPGA), and *vision processing units* (VPU); all this hardware is particularly appropriate for executing complex algorithms in real time on battery powered systems – to date, these algorithms were run on power-hungry CPUs and GPUs.

Furthermore, although in many regards some principles of operation of humans, while controlling machines or otherwise, can still be considered a *black box*, increasing understanding in neuroscience is opening up new possibilities in biofidelic human modelling. This is a continuing trend; for example, it is only recently that prototypes of portable Functional Near-Infrared (fNIR) Spectroscopy devices have been made available; these devices will allow for on-line functional neuroimaging on test subjects while driving vehicles.

1.2 Research Objectives

In order to implement shared control and conditionally autonomous systems in ground vehicles, a better understanding of the characteristics of human control is needed. Semi-autonomous systems should be uncomplicated to use and intuitive to the driver. Accordingly, one of our fundamental aims is to construct a driver model for controlling the lateral dynamics of ground vehicles, that reproduces faithfully the principles of human control – a biofidelic human steering control model. Conditionally automated systems entail transitions in control between the human and the machine [MJ09], and these should occur in a seamless manner. Thus the control behaviour of the autonomous system must be consistent with that of the human. The same comportment is expected of steering control models that act as an aid in shared control systems.

To achieve this, the possibility of introducing operators with memory, for human control modelling, was set as a research target. Traditional control models do not explicitly include memory effects in their design, but we know that complex systems behaviour is usually characterised by hysteresis and viscoelastic properties.

Another relevant question tackled in this dissertation is the role of the steering wheel in semi-autonomous vehicles. The lateral dynamics of cars have been commonly controlled with a steering wheel since their inception. Since the control of ground vehicles may possibly be shared between the human and the machine in the future, is a conventional steering wheel the best solution for this kind of driving scheme? An elucidating analogy is that of horse-drawn vehicles such as horsecars or stagecoaches, which essentially are shared control systems, where the control is shared between the human and the horse [FCA+17]; although the human is in charge of the decisions at the tactical and strategic levels [GL15], the horse has a certain autonomy at the control level. Would it make sense to control a horsecar with a

conventional steering wheel? Or, for all one knows, would it make more sense to control a semi-autonomous vehicle with some sort of reins?

Autonomous and semi-autonomous cars cannot be regarded as regular cars. And as the transportation industry has transformed itself into an enterprise with new rules and goals, some classical solutions need to be revisited with an open mind.

1.3 Dissertation Structure and Contribution

This dissertation is organised as follows:

- **Chapter 2** includes literature review on underlying neuroscience aspects of visual acquisition (Sec. 2.1), human performance laws (Sec. 2.2), and human-machine systems (Sec. 2.3). The purpose of this chapter is not to provide an exhaustive survey of these fields, as their associated literature is increasingly vast, but to give an overview of some of the qualities found in humans that are relevant towards human control modelling. Each of the subsequent chapters includes additional literature review specific to their content. Accordingly, in Chapter 2, only generic methodologies are reviewed, such as quasi-linear models, Fitts' law and a summary of human constraints relative to control tasks (Sec. 2.4) – response time and bandwidth limitations to name a few.

- **Chapter 3** serves a double purpose. On the one hand, classical human control methodologies are explored, in particular McRuer's Crossover (CO) model and finite impulse response (FIR) filters. On the other hand, the chapter includes the first ever analysis of humans controlling fractional order plants, i.e., plants with memory properties – which can be represented in the framework of fractional calculus and fractional differential equations. From this analysis, an extended version of the CO model to include such plants is proposed here: the Fractional Crossover (FCO) model. Additionally, the topic of modelling memory in the human operator is further investigated with the FIR approach; and through this methodology, intrinsic procedural memory patterns in the human-operator are characterised.

  Some of the research in this chapter has already become published material:

  - The FCO model was first presented at the 2016 IEEE Systems, Man, and Cybernetics (SMC) conference in Budapest, Hungary [MGG16].
  - Memory in human-machine systems was further studied in a publication in the IEEE Access journal [MGGS17], which expanded the results of the conference paper.

  - Another journal paper, related to FIR human control modelling, is currently under review.

  Chapter 3 has two related appendixes:

  - Appendix A comprises an introduction to fractional calculus theory, and the correlated computational methodologies used to integrate fractional order plants. The main body of the chapter also includes an abbreviated introduction to fractional calculus, that although does not cover all the used theoretical knowledge, should suffice to follow the contents of the chapter. Therefore, reading the appendix is optional.
  - In Appendix B.1 a detailed account of the human-in-the-loop tracking experiments (HTE), in which data from test subjects controlling fractional order plants were collected, is offered.

- **Chapter 4** is specifically dedicated to steering control modelling. Through signal processing of naturalistic driving data (NDD), characteristic steering pulses – in which driver's steering signals can be decomposed – are identified. From this, a hybrid open-closed loop control law is designed (Sec. 4.2). This work is an extension of the study by Professor Timothy Gordon in [GS14].

  Further, in Section 4.3 a novel form of human control modelling is developed, that consists in identifying the properties of the human-operator from a statistical perspective. This leads to the formulation of a new human control model based on multiplicative dynamics. It is termed the *Multiplicative Human Control (MHC) model*.

  In Section 4.4, data from experiments with test subjects interacting with an OpenGL 3D simulation is studied. These experiments were designed to contrast different hypotheses regarding visual acquisition in driving tasks. From the knowledge extracted from Sec. 4.2-4.4, in Sec. 4.5 a new human-centred driver model is proposed. The model employs a hybrid control strategy (from Sec. 4.2), biofidelic multiplicative dynamics (Sec. 4.3) and bio-inspired visual acquisition (from Sec. 4.4); and it is one of the main contributions to this research item.

  For this chapter also, some of the research has already been published:

  - The analysis of the NDD and the pulse control model was published in the IEEE Transactions on Industrial Informatics journal [MGZG16].
  - The MHC model was first presented at the 2017 IEEE SMC conference in Banff, Canada [MGG17].

  - The extension of the MHC model to a human-centred steering control model has been accepted for the 2018 IEEE SMC conference (Miyazaki, Japan), where it will be presented shortly with the title *A New Model of Human Steering using Far-point Error Perception and Multiplicative Control* [MGG18].

  Chapter 4 has five related appendixes:

  - In Appendix B.2 information about the NDD – utilised in Sec. 4.2 – is provided, while in Appendix B.3 the specifics of the Driving Simulation Experiments (DSE) are explained; the DSE involved the implementation of a simulation platform with C code and OpenGL graphics. The data employed in Chapter 5 are also from the DSE.
  - In Appendix C, a bootstrap method to establish the goodness of fit to a probability distribution is depicted. This method was used to construct the MHC model.
  - Appendix D covers the stability analysis of the MHC model for the control of second order plants.
  - In Appendix E the relation between optical variables related to lane keeping – *the splay error* – and the lateral offset of the vehicle is computed. This result is part of the justification of the visual variables used in the Human-centred Driver model.
  - The modelling approach in Chapter 4 is validated by comparing the model output with a standard driving performance measure, the *steering entropy*. Appendix F illustrates the algorithm to compute this measure.

- **Chapter 5** deals with the topic of alternative control devices for steering control in semi-autonomous ground vehicles. Here, a new design of steering control device is proposed; it consists of controlling a vehicle by torque instead of through the steering wheel angle. The prototype was evaluated with ten test subjects, as part of the DSE. It is shown that such control devices can be advantageous for the control of shared controlled plants and for regain of control situations in SBW vehicles.

- In **Chapter 6** conclusions are drawn and future work is suggested.

Chapter 2

Characteristics of the Human Operator

Human control is the study of the human operator in control tasks. The aims of human control include the design of models that reproduce human behaviour and the characterisation of their performance [JF03]. Because to study driving is to study human control, several results, theories and approaches regarding human control of dynamical systems are reviewed in this chapter. In the general case, humans may be controlling any machine – physical or numerically simulated *in silico* – or in the most simple case they may be controlling their own limbs. Through the years, multiple techniques from control theory have been applied and incorporated to the human performance and human-machine systems literature. In the same manner, many of these techniques have been assimilated by human driver modellers, as it will be seen in the next chapters.

The intent of this chapter is to summarise some background theories employed during the research presented in this dissertation, and not to perform a complete survey of neuroscience and human-performance modelling applied to human control. The introductory section on each subsequent chapter will add specific background knowledge regarding the contents included in the chapter.

2.1 Physiological Aspects of Human Control

2.1.1 Anatomy of the Visual Pathway

Generally, the most important stimuli in a control task – including driving a vehicle – are visually acquired. Commonly it is proposed that 90% of the driving manoeuvres are a response to visual perception only [Mac03]. Hence, here follows a description of some aspects of neuroscience research, regarding visual acquisition, that are relevant to human motor control.

Vision starts with photoreceptor cells, which are a class of neurons located in the retina – the layer in the back of the eye responsible for perceiving light. There are mainly two types of photoreceptors: rods and cones. Rods are concentrated at the outer edges of the retina and convey peripheral vision. Cones are concentrated in a region at the centre of the retina, the *fovea centralis*, and sense colour perception, high resolution vision and motion detection [CI02]. The fovea only covers about 2° of the visual field, which in the human spans approximately over 160° for each eye.

Because of the relatively small size of the fovea, human eyes constantly sample the surroundings by aiming the fovea at different locations, resulting in a different visual field at each stop. Each transition between two eye orientations is called *a saccade*, and each saccade is sustained during a *fixation* period. Typically there are approximately three saccades and fixations per second, although this number is highly variable – it ranges from 70 ms to 660 ms per saccade [CMN83]. Saccades are very brief, thus most of the time the eye is fixating – on average $200 - 300$ ms. As the retina is a two-dimensional surface, vision is a projection process from a three-dimensional space to a two-dimensional space. From the retina, the visual information departs through retinal ganglion cells into the optic nerve towards the brain[1].

The axons that integrate the optic nerve, cross each other in the *optic chiasma*, an X-shaped nerve junction. After the optic chiasma, the nerve fibres of each optic nerve integrate a different pair of nerve fibres known as *the optic tracts*. In the optic chiasma, only about half of the fibres belonging to the optic nerves are crossed over. This occurs in such a way that, the visual information acquired in the right half of each retina is relayed to the right hemisphere of the brain through the right optic tract. Similarly, the input at the left half of each retina gets relayed to the brain's left hemisphere [HW77]. So about half of the nerve fibres of the optic nerves are crossed to the opposite hemisphere[2]. Subsequently, the optic tracts connect to the brain through the *thalamus*.

The thalamus is a brain structure located near the centre of the brain's hemispheres which relays sensory acquired information to the brain. It is conformed by multiple nuclei specialised in different modes of sensory input. Studies in the macaque monkey brain show that about one million retinal ganglion cell axons reach the lateral geniculate nucleus (LGN), the part of the thalamus that relays the visual pathway [HW77]. The auditory counterpart of the LGN in the thalamus is the medial geniculate nucleus (MGN), while the ventral posterior

[1] Some retinal ganglion cells also exhibit photoreceptive properties, but often are not explicitly categorised as photoreceptors. In addition, photoreceptors are linked to retinal ganglion cells through another class of neurons, the bipolar cells [CI02].

[2] Because of the right and left visual fields are projected in the left and right side of the retina respectively, the right hemisphere of the brain receives information from the left visual field and vice versa.

nucleus (VPN) relays somato-sensory perceptual information. From the LGN, the visual information is relayed through another group of axons to the Visual Area 1 (V1), also known as primary visual cortex or striate cortex. Essentially, the visual field is 'mapped' onto the primary visual cortex where it is linked to other cortical areas, some also responsible for visual perception, through feed-forward and feedback connections. V1 is located in the most posterior part of the brain, and it is organised with a columnar structure.

2.1.2 Columnar Structure of the Cortex

The principle of cortical organisation was discovered by Vernon Mountcastle in 1955 [Mou57] while studying the cat's cortex, and it was later confirmed by Hubel and Wiesel in the primate brain [HW68]. This principle states that cells in the neocortex are arranged in the vertical direction, due to the radial development in the fetus brain. The neocortex develops from its fetal stage to the outside, as neuron cells migrate radially over a scaffold made of glial cells. Thus neurons that share the same receptive properties are packed together in neural groups that have received the name of *cortical columns*. These columns are perpendicular to the surface of the cortex – the *pial surface* – and what characterises them is that their properties seem to be relatively constant by perpendicular penetration [Mou97]. For the primary visual cortex, these receptive properties are mainly of one of two types [HW68]:

1. Neurons in the visual cortex are organised in alternating ocular dominance columns. In each of these columns, the cells seem to respond predominantly to one eye only. Each of these columns has a cross section of about $400\,\mu$m (0.4 mm).

2. More interestingly, neurons are also organised in columns that show different orientation specificity. That is, neurons in a column respond to movement occurring in a certain orientation (light segments oriented or moving at a given fixed angle). The orientation columns have an approximate cross section of $50\,\mu$m (0.05 mm), roughly two times the width of a cortical neuron. However, the columns are not perfectly defined discrete units as they do not posses clear boundaries; orientation specificity seems to vary gradually [HA05]. Each orientation column represents an angle range of approximately 10°.

These two systems of columns are independent of each other. Normally, there is alternation of columns regarding the eye specificity. So two contiguous ocular dominance columns receive input from both eyes and span a cortical cross section of about 0.8 mm. Two contiguous ocular columns with different eye specificity conform what is called a *hypercolumn*. In general, this term is used for a group of columns that cover all the range of a receptive mode.

Thus in the same way, a cross section of 0.9 mm will span a range of 180° over the visual field, and constitutes an orientation hypercolumn. Thus either type of hypercolumn extends across a cortical surface of around 1 mm^2. In this area there are about 10^5 cells from a total of over 10^{10} cells in the human's neocortex, and approximately 10^{11} in the human brain. The same cortical organisation structure has been found in the motor and auditory cortex for its corresponding receptive field [Mou97]; different sound frequencies are mapped to different columns in the primary auditory cortex (A1).

Although columnar organisation seems to be an essential structure in the neocortex architecture, to date no particular brain function has been pinned to columns or hypercolumns [HA05]; there is not a known visual capacity that requires such alternating organisation. Even more curious is the fact that not all the animal species appear to have ocular dominance columns, for example the mouse, the rabbit and the sheep don't have them. Regarding the human brain, a recent study has shown that the cortical organisation of the brain also applies to humans [YHU08].

The most relevant conclusion of the cortical structure of the cortex, thinking in biofidelic modelling of the human operator, is that the human brain seems to be specially well coordinated to accommodate angular orientation information. Nevertheless, other areas belonging to the visual cortex are responsible for direction and motion perception; The Medial Temporal (MT) visual area – or V5 – has direction sensitive neurons and feeds information to the Medial Superior Temporal (MST) visual area, which processes optical flow information [WS00]. Additionally, recent literature shows that direction and motion can be detected at the retina itself. Although photoreceptors are not sensitive to direction or motion, some retinal ganglion cells respond to visual stimuli relative to motion in specific directions. This is achieved by the particular wiring of retinal cells delaying some connections with respect to others to achieve temporal filtering properties [KGZ+14].

The concept of cortical organisation connects to the *single algorithm hypothesis*, which is next discussed.

2.1.3 Single Algorithm Hypothesis

Related to the principle of cortical organisation is the hypothesis that all the neocortex processes information by a single algorithm. According to Mountcastle, the cortical columns are the units of computation through which the neocortex processes sensory information – via a common computational scheme [Mou78]. As the neocortex is built up by replicating the same type of structure, some researchers hypothesise that the different parts of the cortex handle perceptual information in a similar way [Haw07], and that the difference from one area to another is in adaptation to a particular type of input.

Several *cross-modal* experiments conducted by neuroscience investigators support this view. In one experiment, three-eyed frogs were created by implanting a third eye into the forebrain of embryonic frogs [CPL78]. After development, the frogs presented ocular dominance columns for the implanted eye too. Similarly, in a later experiment [MF89], the retinal axons of neonatal hamsters were wired to their VPN. Neural recordings of the same hamsters in adulthood showed that somato-sensory cortical columns were able to process visual information in a similar way as in the visual cortex, including orientation preference. Thus the neocortex seems to work as an unsupervised learning algorithm, and the different areas of the cortex transform their inputs in at least a very similar manner. In an analogous experiment [VMPS00], the auditory cortex of neonatal ferrets was rewired through the MGN to receive retinal axons. When the ferrets reached a mature age, their MGN and auditory cortex were responsive to visual input – again, including orientation specificity.

There is also literature available where the specific workings of the presumed cortical algorithm are hypothesised, although there is no consensus about it. The different hypotheses range from biologically inspired machine learning techniques to probabilistic inference algorithms [Haw07, DCS12].

2.2 Human Performance Laws

In the human performance modelling and man-machine systems literature, generally it is regarded that 'Men are noisy, narrow-band devices' [Lic60], and as such it is often difficult to determine laws about their principles of operation. Nevertheless, there are a number of human performance laws which are accurate on average; that is, they faithfully reproduce average human behaviour when aggregating response recordings from different human subjects or across many trials, and are only approximate for a particular instance of human operator response. Some of these are summarised in this section.

2.2.1 Fitts' Law

One prominent example in the human performance repertory is Fitts' law [Fit54]. This law gives an estimate of the time needed to complete a reaching task according to the distance to a target and the target size.

The mathematical relation that describes the law was first assessed with several reaching behaviour experiments. One of them consisted in transferring disks with a hole of varying size at their centre. The hole was intended to let the disk slide onto a pole situated at a chosen distance – in a similar fashion as in the Tower of Hanoi game.

Fitts' law translates concepts belonging to information theory to characterise human reaching behaviour. To define the law, first an index of difficulty (*ID*) is specified. This index reflects the difficulty in reaching a target of size S (and radius $R = S/2$) located at a distance D from the hand of the human operator:

$$ID = \log_2\left(\frac{2D}{S}\right) = \log_2\left(\frac{D}{R}\right). \tag{2.1}$$

Next, an index of performance is introduced (*IP*), which depends on how much time (T) the human operator needs to complete a reaching task of a given difficulty: $IP = ID/T$. Additionally, a fixed quantity N_t induced by the human neuromuscular response is added to the final equation:

$$T = N_t + \frac{1}{IP}\log_2\left(\frac{D}{R}\right). \tag{2.2}$$

As the law was first proposed through an analogy to information theory [Fit54], *ID* was expressed in bits and *IP* in bits per second. Thus the quantity *IP* serves as a human throughput, and was in the range $7.76 - 11.82\,bits/s$ for the reported experiments[3].

Although Fitts' law gives a very robust result, because it has been tested in multiple experiments, it only applies to reaching behaviour – target acquisition and pointing tasks. For instance, saccadic eye movements do not follow this logarithmic relationship [AMK89], as the duration and the speed of a saccade does not seem to depend on the size of the fixated object.

2.2.2 Hick's Law

A close relative to Fitts' law is Hick's law [CMN83], which determines the approximated time to select among N_c possible choices – for example, the number of keys that can be pressed on a keyboard:

$$T = I_C \log_2(N_c + 1). \tag{2.3}$$

Here I_C^{-1} also represents the human throughput in bits per second, typically around $6.6\,bits/s$ in this context. Conversely to Fitts' law, eye target acquisition is well described by Hick's law, as it has been shown recently [KTIM17].

[3] Another version of Fitts' law, introduced in [Mac89], relates more closely to the notion of information transfer. This version includes a unity constant inside the logarithm to mimic Shannon-Hartley theorem: $T = N_t + \frac{1}{IP}\log_2\left(\frac{D}{R} + 1\right)$. In Shannon-Hartley theorem, D represents the power of a signal and R the power of the noise in a channel.

2.2.3 Power Law of Practice

The power law of practice represents how the time to complete a task decreases with experience. This law was first observed in [Sno26], where experiments were conducted in which test subjects had to trace a predetermined path of complicated geometry – a star-shaped path including several indentations – with a stylus. The law can be written as:

$$T_N = T_0 N^{-\alpha} \tag{2.4}$$

where T_N is the time needed to complete a task that has been repeated previously N times, and α is an empirical constant depending on the type of task being performed.

Peculiarly, the power law of practice has been observed to occur during very long periods, such as cigar rolling during a time span of seven years [Cro59], in which a total of $10,000,000$ cigars were rolled by several individuals using the same rolling machine – but with significant variation on the raw materials.

2.2.4 Weber's and Fechner's Laws

Weber's and Fechner's laws are relevant to visual perception [Gre97] as well as to *steering feel* [NGD07] – that is, the haptic feel of a steering wheel in a driving task. These laws are originated within the framework of *psychophysics* to describe how subjects perceive differences in the intensity of stimuli.

Weber's law is used to characterise the *difference threshold* of a stimulus, i.e. the smallest difference in stimulus magnitude that humans can perceive. The law states that the difference threshold (δS) is proportional to the stimulus magnitude (S):

$$\frac{\delta S}{S} = C_W \tag{2.5}$$

with a proportionality constant C_W, which is dependent on the stimulus type. For steering wheel control, values have been reported of $C_W \approx 0.14$ for steering wheel angle sensing and $C_W \approx 0.15$ for steering wheel force sensing [NGD07].

Regarding visual perception, it has been recognised that the retinal cells of cats, even when in total darkness, transmit a small amount of neural signals through the optic nerve. The magnitude of this *residual firing* increases with age, and it is believed to happen to humans too [Gre97]. Although photoreceptors become excited by the input of a single photon, they only transmit a signal through the optic nerve when they receive several photons over a certain integration period; if around five photons are received over a period of 0.1 s, a neural signal is transmitted down the optic nerve. This trait is partly responsible for the increased

reaction time while driving in low light conditions. It also means that a constant must be added to (2.5) to account for the residual firing (K_W) – noise produced in the retina – which results in another version of Weber's law:

$$\frac{\delta S}{S} + K_W = C_W. \tag{2.6}$$

Another very relevant conclusion is derived from this description: retinal neurons are so sensitive to light that virtually there are no thresholds in visual perception, which Craik suggested as one of the possible causes of the discrete corrections of the human operator (Section 2.3.3). Even so, the CNS sets up a varying threshold to ensure that the retinal activity is commenced by a visual signal and not by neural noise. This threshold varies according to the level of attention – the lower the threshold, the more attentive is the human, but at the same time there is a higher chance of regarding neural noise as a visually perceived phenomenon.

Weber's law can be also expressed by stating that the minimum difference in perception (δP) is proportional to $\delta S/S$:

$$\delta P = K_F \frac{\delta S}{S}. \tag{2.7}$$

And this equation can be rewritten as an ordinary differential equation (ODE),

$$\frac{dP(S)}{dS} = \frac{K_F}{S}, \tag{2.8}$$

which upon integration yields

$$P(S) = K_F \log S + C_F, \tag{2.9}$$

with empirical constants K_F and C_F. Expression (2.9) is known as *Fechner's law*, and it relates change in stimulus with change in perception. This relation has also been confirmed experimentally – for example in the *Limulus*, a logarithm relationship between light intensity and firing rate has been observed.

2.2.5 Stevens' Power Law

There is an alternative law that relates stimulus intensity with perceptual feel; in Steven' law, this relation is expressed as a power law:

$$P(S) = K_S S^{\sigma} \tag{2.10}$$

with empirical constants K_S and σ. Regarding the use of this law for isometric muscle contraction, in [SC70] it is reported an exponent of $\sigma = 1.7$. A comparable value is reported in [NGD07] with respect to the perceived force applied to a steering wheel ($\sigma = 1.39$). And in this same paper, $\sigma = 0.93$ was obtained in experiments with real subjects relating steering angle perception – by visually observing the steering wheel.

2.3 Human-machine Systems

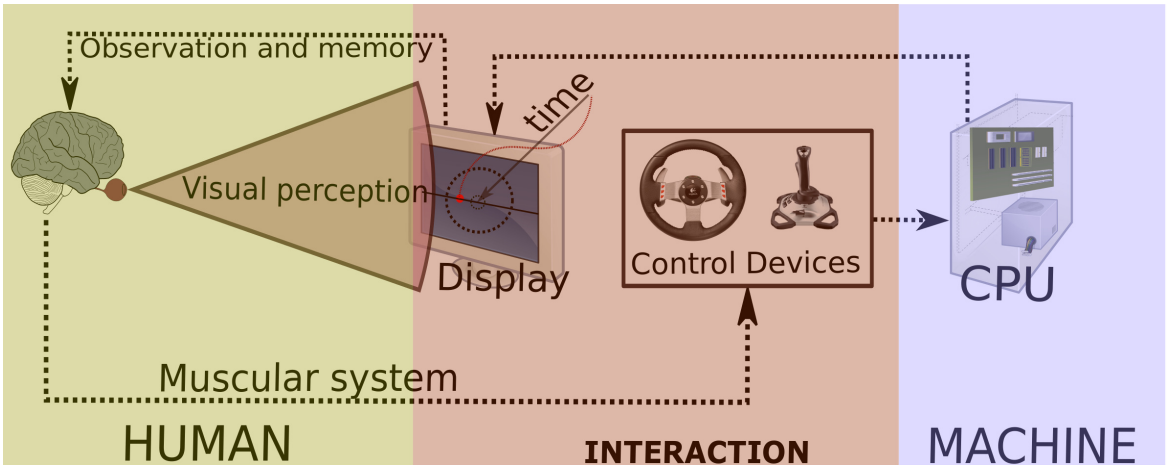

Fig. 2.1 Conceptual diagram of a human-machine system experimental setup. The human operator interacts with a simulated plant by means of a control device – a joystick or a steering wheel for example – and reacts to the present and past observations of a visually perceived input. *Parts of this image are available under a creative commons license CC BY 2.5.*

The human operator can be regarded as an information processing system which responds to perceptual information to achieve an aim [CMN83]. The field of human-machine systems engineering is a special case of human control, where the human operator is assumed to act as a servomechanism using sensory feedback. This research trend can be said to have been started since the 1940s, with the classical experiments conducted by Tustin [Tus47]. Nevertheless, the main aim of human-machine systems engineering, which is achieving effective human-machine integration, was appreciated much before that [MK74].

A part of human-machine systems research is advanced by experiments in which humans have to track a target through a control device (Fig 2.1). The target itself obeys preset dynamical behaviour driven by a forcing function, which conventionally is a sum of sinusoids of different frequencies and randomised phases; i.e. a *pseudo-random* forcing function. The target position is typically presented to the subject through a display. The display shows one

or two moving elements, according to the control mode utilised – *compensatory* or *pursuit* mode.

2.3.1 Compensatory and Pursuit Modes

Within the experimental conditions in human-machine systems research, traditionally two different control modes are studied: compensatory mode and pursuit mode [PDF67]. The main difference between both modes is in the number of moving elements presented in the display. In compensatory mode, there is only one moving element in addition to one fixed reference point. The error $e(t)$ is represented in the display as the Euclidean distance between the moving and the fixed elements. The task of the human operator is to minimise $e(t)$ by manipulating a control device, which allows them to generate an input to the plant. The error is the difference between a quasi-random forcing function $r(t)$ and the plant output $m(t)$ (Fig. 2.2a). Hence, in compensatory mode only the relative error is seen by the human, who does not have direct access to the plant output. The position of the moving object results as the joint effect of the forcing function, the human response and the plant acting in closed-loop.

In pursuit mode two moving elements are presented in the display – there is a moving reference marker instead of a fixed one. The reference point now moves according to the forcing function $r(t)$, and does not depend on the human manipulative control actions. The other moving element, controlled by the human, displays the plant output $m(t)$. In this case neither one of the moving elements directly represents $e(t)$, but the error is perceived also in this mode as the Euclidean distance between the two moving elements (Fig. 2.2b).

Although in real applications the distinction between both modes may not be so clear, a parallelism with ground vehicle driving can be considered. Vehicle driving on a straight path, in the presence of a lateral perturbation, can be interpreted as a compensatory task – while following a curved road path as a pursuit task. Nevertheless, both modes are very different to vehicle driving on curved roads; in a tracking task, unlike in vehicle driving, there is not preview information involved; humans in a compensatory or pursuit tracking task are mostly responding to a pseudo-random perturbation. Thus it seems more correct to assume that both modes are more similar to lane keeping – where random wind and pavement effects modify the trajectory of the vehicle – than to curved road tracking.

2.3.2 Quasi-linear Models

Tustin experiments consisted of humans tracking moving targets with a tank turret, electrically controlled through a spring-centred handle [Tus47]. By observing the test subject's responses,

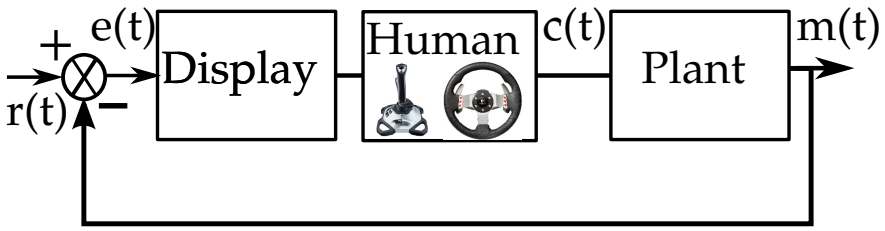

(a) Compensatory mode

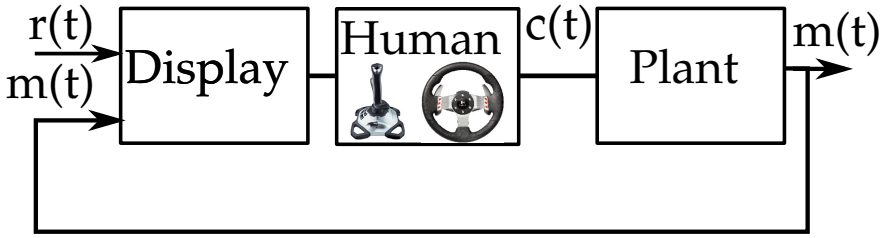

(b) Pursuit mode

Fig. 2.2 Human-machine control loop for the typical experimental setup in both control modes: compensatory and pursuit.

Tustin concluded that the main part of the human operator dynamics can be described as a linear actuator. He was also the first researcher to use the word *remnant* – here denoted as $\mathcal{R}(s)$ – to refer to the difference between the frequency response of the human operator ($\mathcal{H}(s)$) and its corresponding linear model dynamics – the *linear equivalent system* $\mathcal{H}_L(s)$. The superposition of the linear equivalent system with the noisy remnant conforms the theory of *quasi-linear* models:

$$\mathcal{H}(s) = \mathcal{H}_L(s) + \mathcal{R}(s). \tag{2.11}$$

To assume that a veridical model of the human can be described only by means of $\mathcal{H}_L(s)$ is clearly an over-simplification, since the CNS is a complex network of paths, some wired in a feed-forward manner while others in a feedback manner, resulting in a highly non-linear system. Nevertheless, tracking experiments performed with real subjects [Roi62], suggest that $\mathcal{H}_L(s)$ can account for around 90% of the power of the signal $\mathcal{H}(s)$ when low frequency forcing functions are employed.

The most instrumental quasi-linear model, and perhaps also the most noticeable human control model, is the *Crossover* (CO) model [MJ67]. Since it was introduced by McRuer, the CO model has been continuously used in human performance and control research, one example being its application to vehicle steering control [MWJ+75, Gor09, Mac03]. The CO model describes the combined action of a human operator and a controlled plant within a restricted range of frequencies. The model was deduced by recording responses of human subjects to visually presented stimuli in single-loop tracking tasks [MJ67]. In McRuer's

experiments, human test subjects had to control a moving element in a display by means of a control stick held between thumb and forefinger. The position of the moving element represented an error $e(t)$, which was induced by a pseudo-random forcing function as in the description above (Fig. 2.2). The test subjects were requested to minimise the error by moving the controlled element towards a reference point in the centre of the display. The control actions that the human performs over the moving element – with known dynamics given by a chosen transfer function – place the human as a serial element inside the control loop (Fig. 2.2).

It was observed that the manipulative control actions of the human operator are different for different controlled plants, but the combined human-machine behaviour is approximately regular. Thus the CO model exhibits a behavioural invariant of the human in its effort to adapt to the plant, offering a consistent human-machine behaviour depiction. What characterises the human controller is its dexterity in differing contexts. The model is expressed as a product of transfer functions for the combined human-machine system and is characterised by just two parameters: the *crossover frequency* ω_c and a time constant τ, which represent the combined control gain and the *effective time delay* respectively. The effective time delay aggregates the neuromuscular lag and the accumulated transport delays in the response – it is the total human delay needed for responding (see Section 2.4.1). The open-loop transfer function for the forward path in the CO model is

$$Y_h(s)\,Y_p(s) = \frac{\omega_c e^{-\tau s}}{s}, \tag{2.12}$$

where the transfer function $Y_h(s)$ represents the human operator and $Y_p(s)$ the plant. As already mentioned, ω_c is both the crossover frequency and the system gain. The amplitude and phase responses for the model are (Figure 2.3):

$$\mathbf{A}(\omega_f) = 20(\log\omega_c - \log\omega_f) \quad \text{dB}. \tag{2.13}$$

$$\Phi(\omega_f) = -\pi/2 - \tau\omega_f \quad \text{rad}. \tag{2.14}$$

Typically, the frequency spectrum of $e(t)$ presents a peak in ω_c.

One important aspect of the model is that it accurately represents human behaviour only in the vicinity of ω_c. But this is sufficient to ensure closed-loop stability and transient performance, via the gain and phase margins, i.e., via the open-loop responses in the vicinity of the crossover frequency.

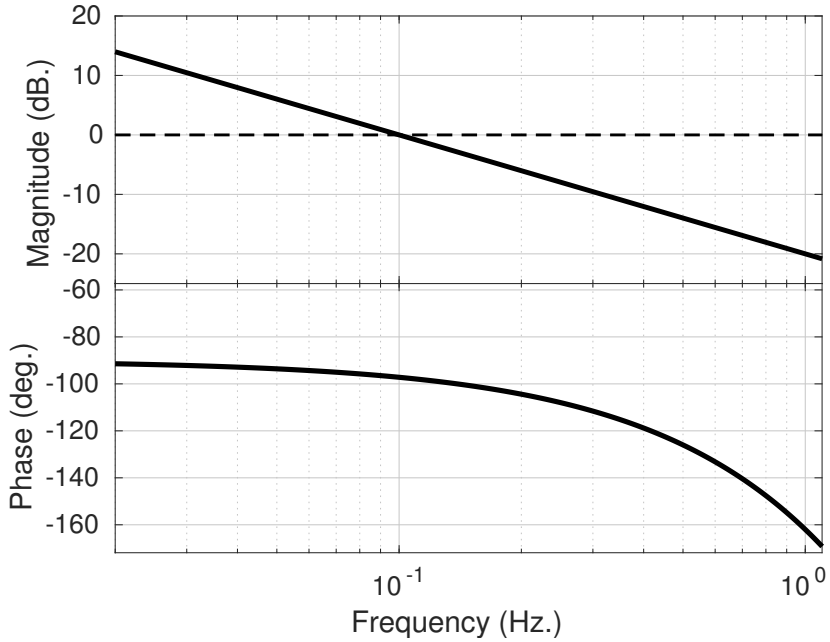

Fig. 2.3 Frequency response of the CO model for $\omega_c = 0.1\,\text{Hz}$ and $\tau = 0.2$.

2.3.3 The Human Operator as a Discrete Servomechanism

Another aspect that has been studied, when considering the human operator as a controller, is the discrete nature of the human response in tracking tasks. In [Cra47] it was first hypothesised that humans behave as *ballistic servomechanisms*, performing intermittent corrections when trying to regulate or control a system. In the same publication it is also mentioned that *counteracting processes* make the human response resemble that of a continuous actuator, suggesting that the operator introduces a smoothing effect into its own response. This is specially true for trained operators.

Craik also stated that the intermittence in human's response is not caused by the jerky saccadic movements of the human eye [Cra48]. In a tracking task, the human eye can fixate a moving target maintaining the gaze continuously over it. Further, it is known that sensory information continuously flows through the optic nerve. Craik suggested as potential reasons, for human control to be discrete in nature, the existence of a refractory period in the response and perceptual thresholds.

More recent research supporting Craik's hypothesis can be found in [MWS93]. In this paper, classical compensatory and pursuit tracking experiments (Section 2.3.1), with a joystick as a control device, were conducted. Intriguingly, it was observed that when the subjects were deprived of visual feedback temporarily, they produced responses much

smoother than when the visual feedback was available. Thus intermittence in the response seems to be an indicatory sign of human control employing feedback perception.

An alternative explanation for the discrete quality of the human response was given in [HBDS97]; it was suggested that the intermittence is a consequence of humans responding only after an error variable surpasses a certain threshold. In this case the error variable was considered to be a sliding variable – a linear combination of the instantaneous tracking error and its first derivative. In this reference it is denied that a refractory period may be the cause of the intermittence, as the human manipulative corrections don't occur with a constant frequency at all times. Thus, according to this publication, the intermittence is a consequence of neurological dead-zones. Nevertheless, it is known that human eye can discriminate between lines separated only by 1 min of arc in the visual field. So these dead-zones are not produced by a limitation in visual acuity.

Although there is not a clear consensus about what causes the apparent intermittence in human's control responses, it seems reasonable to accept that the human operator can be regarded as a discrete servomechanism.

2.3.4 The Internal Model Hypothesis and the Dynamical Systems Perspective

Contrarily to the idea suggested by Wiener [W$^+$48] that motor control, and essentially any other biological process, can be executed as a pure feedback guidance, the *internal model hypothesis* asserts that the human CNS contains internal models of the controlled plant [Hol82]. This includes the particular case where the models represent our own joints and muscles, so that adequate torques can be computed in advance to perform feed-forward control – or to assist in making the feedback control more effective by increasing its stability. Internal models are supposed to be learned and refined by experience.

The proponents of this hypothesis usually argue that quick arm movements can't be explained through feedback control. Thus the brain must learn inverse dynamics, at least for our own anatomy, to execute such rapid motions. Indirect evidence is provided by the fact that, specific patterns of neural activity have been found in the cerebellum while the hand is gripping an object [Kaw99]. Thus it has been proposed that internal models are contained in the cerebellum.

Still, the evidence supporting the internal model hypothesis is not clear. An opposing framework, known as the *dynamical systems perspective*, is held by other researchers. The dynamical systems perspective considers that motor actions are self-organised non-linear outcomes of the human neuromuscular system. This framework borrows ideas belonging to

complex systems and dynamical systems theory such as self-organisation and trajectories around stable fixed points. According to this concept, skill is the result of *dynamic exploratory activity* and not the reproduction of *static representations* [New91]. Supporting the theory is the evidence that the internal model approach cannot explain how models are learned from scratch, or why motor learning can last for extremely long periods (see Section 2.2 for some comments on the power law of practice). Other proposed reasons that make internal model principle unlikely are the following [OF03]:

1. Small differences between an internal model and the actual controlled dynamics can give rise to instability in the system. However, a combination of feed-forward and feedback control could in principle compensate for these differences.

2. The forces produced by the neuromuscular system are very dependent on its position; it is not clear how an internal model will account for every possible position of the human body – or every state of a controlled plant – in order to calculate the needed torques for every motor action.

3. A predetermined arm trajectory can be generated with different combinations of torques in the arm muscles. Humans are able to adjust these torques to increase the stability of the human-machine system [BOF$^+$01]. Thus an internal model is not enough to calculate an arm trajectory among several redundant combinations of muscle activity.

4. Very simple nonlinear models can present a rich dynamical behaviour. Nonlinear systems can control a wide range of dynamics by parameter adaptation without the need of an internal model.

A variant of the dynamical systems perspective is the *equilibrium-point control theory* [Fel86], which states that during motor control the arm is commanded to follow a series of points to reach its intended final position. These points are stable equilibria and, by adjusting the viscoelasticity of the arm through co-contraction of antagonist muscles, the arm is able to follow a path without the need of an internal model.

In [Kaw99] it is also mentioned the interesting possibility that humans do have a few generic and competing internal models. By neural weight adaptation, these different models would superpose their predictions to produce an outcome. This notion brings the idea of internal models closer to the dynamical systems approach.

If the existence of internal models for humans motor dynamics is not clear, even less clear is their existence for external plants, such as ground vehicles. Manual control studies show that subjects adapt to changes in plant dynamics – such as plant gain variation – very quickly ($1-2\,\mathrm{s}$) [Mac03]. One interesting question is: assuming that humans have internal

models, could they adapt and control uncommon dynamics not found in everyday life with brief transient periods too?

Still, some theories of human control assume the existence of internal models. One can somewhat interpret the CO model as an internal model representation. From (2.12), assuming the knowledge of a model for the plant is given ($Y_p(s)$), the response of the human is characterised by:

$$Y_h(s) = \frac{\omega_c e^{-\tau s}}{sY_p(s)}. \tag{2.15}$$

Thus the plant model determines the human response. Nonetheless, this is only true in a vicinity of ω_c. A more clear scheme that assumes the existence of internal models is the optimal control approach for modelling the human.

2.3.5 Optimal Control Models

As the human CNS, and that of all animals, is the result of evolution and adaptation, it can be argued that optimality is a general principle in human control. In addition, from the point of view of engineering, optimal control provides an effective design methodology. In [Roi62] human performance in closed-loop tracking tasks was contrasted with the performance of a linear optimal controller. By comparing the human quadratic error to that of the optimal controller, it was concluded that the human operator displays a near optimal performance. However, only very simple plants were tested in these experiments.

A more well known application of the optimality principle is the model designed by Baron and Kleinman [BK69]. This model adds a Kalman filter to the optimal controller to emulate the predictive capabilities of humans. The predictor component from the filter contains a model of the internal dynamics of the plant too, thus the whole approach is assembled from engineering concepts that may not have any real affinity to the CNS comportment. Baron and Kleinman also concluded that human behaviour is close to that of an optimal controller. In the literature there can also be found applications of the optimality principle to steering control; for example, in [Mac81] it is proposed an optimal controller that minimises the accumulated predicted lateral deviation.

Even so, the presupposition that humans have an internal representation of the controlled dynamics contradicts the fact that humans adapt very quickly to changes in the given dynamics in a very natural manner. In addition, the dynamical systems perspective (Section 2.3.4) underlines that control is an emergent property, resulting from the complex interaction between the CNS and the musculo-skeletal system.

Another disadvantage of the optimal control method is that it only reproduces skilled performance [Tod04]. In reality there is not a clear quantitative definition of what performance means. Humans may be optimising different things at different instants. For example, drivers may be maximising information acquisition at times – by reducing the speed in order to observe the driving scenario more carefully – or they may be minimising time, steering effort, risk or discomfort – and potentially, any combination of these. Further, as the cost function must include physiological constraints, usually the approach becomes over-complicated with a large number of parameters.

2.4 Physiological Constraints of the Human Operator

The human operator has a number of limitations concerning reaction time, range of frequencies they can respond to and visual acuity among others. These must be considered when modelling the human, and are summarised in this section, which concludes the chapter. At the end of the section, these values are organised in Table. 2.2, along with other relevant physiological constants, some were already discussed in this chapter.

2.4.1 Human Response Delay

The most critical human constraint is their response delay or *effective time delay* τ (Section 2.3.2). Usually it is reported that the human response delay is approximately 200 ms, but this is only true for simple tasks such as pressing a key after a triggering stimulus [Cra48]. More precise estimates are 113-328 ms for single choice response and 133-528 ms for multiple choice – 2 to 4 choices – response [War67].

Part of the human delay is produced by their neuromuscular lag τ_N. The neuromuscular lag includes neural transmission delays to the limbs – 10-20 ms – and the time to produce a motor response or *muscle latency* – 30-70 ms. Besides the neuromuscular lag we have to add photochemical transduction delays in the retina τ_P – lasting approximately 38-120 ms – and central processing delays τ_C, which typically last for 50-100 ms depending on the complexity of the decision making task needed before responding [War67, CMN83, SG04] (Table 2.1).

Thus, the effective time delay can be approximated by the relation:

$$\tau = \tau_P + M_C \tau_C + \tau_N, \tag{2.16}$$

where the parameter M_C reflects the fact that the time to decide a response depends on the complexity of the task, number of possible choices, and if the CNS processing needs to

access memories [CMN83]. M_C can be approximated from the logarithmic relation in Hick's law (Eq. 2.3):

$$M_C = \log_2 (N_C + 1) \tag{2.17}$$

for a given number of choices N_C. So for example, when considering a real steering task where one can only steer to the right or to the left ($N_C = 2$) then $\tau \approx 157 - 270\,\text{ms}$. But in a steering task, besides the steering direction its magnitude has to be decided, and short-term memories are also involved. This means that probably it is more correct to choose $N_C > 2$. On the other hand, depending on the modelling approach, a human control model may already reflect muscle latency τ_N. In that case it is more convenient to consider the human response delay without adding up τ_N:

$$\tau_H = \tau_P + M_C \tau_C. \tag{2.18}$$

2.4.2 Other Physiological Constraints

Other relevant parameters with respect to human control and performance modelling are the following:

Frequency of Response

The maximum frequency that humans are able to track and control depends on several factors. One of them is the predictability in the forcing function acting on the controlled plant. An approximate estimate for the frequency limit is 1 Hz for pseudo-random forcing functions. When the forcing function is a simple sinusoidal input – or a signal with a very narrow band – the controllable frequency range extends to 5 Hz [Pew07]. In [War67] it is reported a limit in the range 0.75-1.5 Hz for compensatory and pursuit tasks without preview information. Although in most cases humans rarely surpass the 0.5 Hz threshold [BT54].

With reference to the CO model (Equation 2.12), the typical crossover frequency is reported to be in the range 3-5 rad/s (0.5-0.8 Hz) [MJ67, Mac03]. But this value depends on

τ_P	τ_C	τ_N
Perception delays	CNS processing delays	Neuromuscular lag
38-120 ms	50 ms – single choice –	40-90 ms

Table 2.1 Constraints on response time caused by different physiological aspects: neural transmission rate, information processing delays and muscle contraction.

several factors too, such as the level of skill of the operator – ω_c increases with practice [McR80].

Human Induced Noise

An approximated figure for the level of observational noise (Section 2.2) in tracking tasks is $\approx 3\%$ of the power of the signal [KBL71]. Nevertheless, we have seen that humans adapt their detection threshold to reduce the effect of the noise (Sec. 2.2.4). In the same reference it is also reported that motor noise accounts for $\approx 1\%$ of the power of the response signal.

Visual Acuity

The human eye possesses a surprisingly high acuity. The eye is able to differentiate between lines 1 minute of an arc apart [Cra48]. Even so, these high levels of precision are not used commonly when performing a task such as driving. This value refers to fixed stationary objects, a highly attentive state of mind, and during short periods of time.

Causal Connection and Visual Retention

As the time between a visual stimulus reaches the retina and humans actually see it – neural transmission delays – is $\tau_P \approx 100$ ms, dots changing position in a display are perceived as a moving dot at around 10 frames/s [CMN83]. Comparable magnitudes for τ_p have been reported in other sources: from 38 ms in [War67] to 120 ms in [Bur80]. Thus the estimates for τ_P are relevant in establishing appropriate frame rates for displays in control tasks. Although highly trained operators can perform control using a display with a frame rate of 2 frames/s, less than 10 frames/s may produce stress in humans [CT07]. Additionally, the performance level starts to decrease in some cases with rates less than 30 frames/s. In any case control displays with a refresh rate of less than 15 frames/s are not recommended.

The estimated values for τ_P are consistent with another physical constraint constant, the decay time of a visually acquired image, which is in the range 90-1000 ms (typically 200 ms). This has been measured in experiments where human subjects are shown an array of characters during 50 ms, and after that are asked to retrieve from their short term memory the character in a particular position of the array [AC61].

Symbol	Physiological Constant	Value	References
		Empirical laws parameters	
IP	Throughput – Fitts' law	7.76-11.82 $^{bits}/_{s}$	[Fit54] [CMN83]
I_C^{-1}	Throughput – Hick's law	6.6 $^{bits}/_{s}$	[CMN83]
C_W	Weber's law constant	0.14 – steering wheel angle 0.15 – steering wheel force	[NGD07]
σ	Steven's power law exponent	1.7 – isometric muscle contraction 0.93 – steering wheel angle 1.39 – steering wheel force	[SC70] [NGD07]
		Physiological parameters	
	Saccade + fixation period	70-660 ms, typically 230 ms	[Cra48] [CMN83] [JF03]
	Saccade period	30-50 ms	[Cra48]
ω_c	Crossover frequency	0.3-1.2 Hz – typically 0.64 Hz for driving	[Cra47] [MJ67] [Mac03] [MGG16]
τ_P	Perception delay	38-120 ms	[War67] [CMN83] [Bur80] [Gre97]
τ_C	CNS processing delay	50-100 ms – depending on task complexity	[War67] [CMN83] [SG04]
τ_N	Neuromuscular lag	40-90 ms	[War67] [MJ67]
τ	Human overall delay (effective time delay)	107-528 ms – 180 ms in ideal conditions	[Cra47] [War67] [MJ67] [CMN83] [MGG16] [Mac03]
	Delay in identification of an image	150 ms	[TFM96]
	Decay time of acquired image	90-1000 ms – typically 200 ms	[AC61] [CMN83]
	Human observational noise	$\approx 3\%$	[KBL71]
	Human motor noise	$\approx 1\%$	[KBL71]
	Maximum trackable frequencies by humans	5 Hz – predictable input 0.75-1.25 Hz – unpredictable input	[War67] [BT54] [Pew07]
	Recommended frame rate	15-30 Hz	[CT07]
	Threshold in detection of angular misalignments	1 sec of arc – lab	[Cra48]
TH_Θ	Threshold in detection of misalignments in splay lines	1 deg	[WH$^+$88]

Table 2.2 Summary table of physiological constraints in human control

Chapter 3

Modelling Memory in Human-machine Systems

3.1 Effects of Memory in Human Control

The execution of learned motor skills involves a series of coordinated actions by the muscular system. These actions are generally a response to perceived stimuli and are carried out automatically. Traditionally in the literature on human-machine systems, humans are assumed to respond to objective variables resulting from the controlled machine, which might be translational or angular displacements, ratios of such variables and their future predictions [JF03, Lap14], or visual field information derived from the *focus of expansion generated by the motion of a vehicle* [GM76]. Until now, little attention has been given to the question of how these variables are processed by the visual system and the brain prior to the generation of a response action. Further, there has been little research into the manner in which *memories* of these inputs are used in human control.

It is widely known that the response of a system modelled by ordinary differential equations (ODE) – or equivalently, in the linear case, modelled by transfer functions – to any given input is determined by a single initial condition vector. For instance, in a mechanical system, these are usually the generalised position and velocity variables that describe the available degrees of freedom. On the contrary, it seems natural that human tracking behaviour, and biological systems in general, elicit a response based on a series of past observations [Mag06].

Thus a mathematical approach that explicitly includes memory processes is motivated. In this chapter two different approaches to model the memory aspects of human-control are considered: fractional differential operators and finite impulse response filters.

3.2 Classification of Human Memory

Human memory can be classified according to the following scheme [Wil15]:

- **Short term memory:** *Short term memory* (STM), also referred to as *working memory*, retains information for up to 30 s. One example is the perceptual information used during the completion of a manual task – such as typing on a keyboard. The hippocampus, which is the area of the brain usually associated to memory, is not involved in the acquisition or retrieval of STMs. When the perception mode corresponds to visual acquisition, STM is termed *visual short term memory* (VSTM).

  One particular case of VSTM is visual retention with respect to the saccadic motions of the eye. The human eyes move actively and selectively to sample the surroundings, performing on average three saccades per second, so that the fovea can sample high resolution inputs from the most relevant parts of the visual scene (Sec. 2.1.1). However, even if vision consists of a chain of discrete actions, we perceive the environment as a unified continuous image. It has been verified that VSTMs are retained during saccadic periods resulting in what is known as *transaccadic memory*. During each saccadic period visual perception is temporarily halted and humans are basically blind [Mat74], but changes in natural scenes during saccadic periods are detected after the saccade [HRL08]; humans are able to maintain object correspondence between saccades. Additionally, in [CI02] it is suggested that visual motion detection would be impossible without some sort of prefiltering of the perceived optical variables.

- **Long term memory:** *Long term memory* (LTM) is held for more than 30 s and can be further categorised into *implicit memories* and *explicit memories*.

  1. *Implicit memories:* These are unconscious memories. The hippocampus does not participate in the neural processes corresponding to implicit memories. One particular case of implicit memory is that of *procedural memories*, which are the memories that hold learned motor skills [Squ04]. Procedural memories are learned by repetition of a particular task, hence this is the type of memory represented by the power law of practice (Sec. 2.2.3). Examples of actions performed through procedural memories are: writing a character and language articulation, which can be executed in a feed-forward (open-loop) manner [Kaw99] – the time needed to write a character is independent on the size of the character [Fre14] – or driving a vehicle and executing a compensatory or pursuit control task, which require of feedback control, although may also include open-loop components [Don78, GS14].

2. *Explicit memories:* These are coordinated by the hippocampus and correspond to what is generally understood as *remembering*. The main characteristic of explicit memories is that they are declarative, that is, they can be verbally expressed. They are further subdivided into two types: autobiographical memories – which record experiences – and semantic memories – which record facts. Explicit memories are not involved in motor control, but they are relevant at a strategic level in driving – for example while deciding the destination or the chosen route [GL15].

Learned patterns of motor control, which are stored in the cerebellum, are in the form of implicit memories. And visual memories are processed through an implicit procedural memory pattern in order to elicit a control response to visually acquired inputs[1].

Another provenance of memory effects in human control includes the effects produced by the human understood as a dynamical system. For example, the musculoskeletal system is composed of viscoelastic polymers with memory properties [TVPM13]. Additionally, oculomotor neurons have memory attributes too [Ana94]. This type of memory, which is produced by the dynamical properties of a system, and not by the explicit storage of information, in the following will be referred to as *system memory*.

3.3 The Fractional Calculus Approach

With the purpose of modelling memory in the human-operator, the method of fractional calculus is considered in this section, based on the property that fractional derivatives add memory processes to a dynamical system.

The following exposition is a brief introduction to fractional calculus. The subsequent comments are sufficient to understand how fractional calculus has been used in this research for modelling memory in human-machine systems, albeit omitting several technicalities. A more formal exposition to fractional calculus – consisting of further mathematical details – is enclosed in Appendix A, which includes the methods utilised in this dissertation to integrate fractional differential equations and to analyse the stability of fractional order systems.

3.3.1 Introduction to Fractional Calculus in the Frequency Domain

In the fractional calculus approach, the traditional notions of integral and derivative are extended to define non-integer powers of the integral and differential operators – which are

[1]The literature sometimes employs the term *visual memories* to refer to short and long term visually acquired memories. Here by visual memories we refer to VSTM only.

jointly referred to as the *differintegral operator*. For an integer number n of nested integrals, the classical integral operator over a function f is defined as:

$$ {}_hD_t^{-n} f(t) := \int_h^t dt_1 \int_h^{t_1} dt_2 \int_h^{t_2} dt_3 \dots \int_h^{t_{n-1}} f(\xi)\, d\xi. \tag{3.1} $$

For simplicity, in the following the lower limit of integration h will be considered to be zero – ${}_0D_t^{-n} f(t)$.

Similarly, for consecutive derivatives the differential operator is defined as:

$$ D^n f(t) := \frac{d}{dt}\frac{d}{dt}\dots\frac{d}{dt} f(t) = \frac{d^n}{dt^n} f(t). \tag{3.2} $$

We want to construct an operator in which we can replace $n \in \mathbb{N}$ by an arbitrary real number $\nu \in \mathbb{R}$. Usually this is done by defining first a fractional integral operator – ${}_0D_t^{\nu} f(t)$ for $\nu < 0$. And then, for fractional differentiation one needs only to combine fractional integration with classical differentiation[2]. That is, for $\nu > 0$

$$ {}_0D_t^{\nu} f(t) = D^{\lceil \nu \rceil} \{ {}_0D_t^{\nu - \lceil \nu \rceil} f(t) \}, \tag{3.3} $$

where $\lceil \cdot \rceil$ denotes the ceiling function. As fractional differentiation is defined through fractional integration, the integration limits must be specified for differentiation too. Still, we have not defined fractional integration yet.

The difficulty in trying to explain fractional calculus in an intuitive manner is the lack of a suitable geometrical interpretation. Unlike classical derivatives, which have a very intuitive explanation, geometrical arguments in the time domain for fractional operators yield only abstract concepts. Thus for example, in [PDSM07] fractional integrals are explained as a projection on the $y-z$ plane of a classical integral in a higher dimensional space. Although this is an interesting result from a mathematical perspective, it does not make the concept more interpretable for modelling system memory. However, here a simple interpretation in the frequency domain is offered. This interpretation leads in an alternative manner to one of the standard definitions of fractional operator.

It is well known that the Laplace transform of the nested integrals functional (3.1) is $\mathcal{L}\{D^{-n} f(t)\} = {}^{F(s)}/_{s^n}$ when $\mathcal{L}\{f(t)\} = F(s)$. Further, whenever the initial conditions of f are zero, then $\mathcal{L}\{D^n f(t)\} = s^n F(s)$. Hence for $\nu \in \mathbb{Z}$, and assuming the initial conditions to be zero, we have

$$ \mathcal{L}\{D^{\nu} f(t)\} = s^{\nu} F(s) \text{ for } \nu \in \mathbb{Z}. \tag{3.4} $$

[2]There is an alternative way to define fractional operators in which the derivative is applied first followed by a fractional integral [Die10].

In the frequency domain this means that, when varying $\nu \in \mathbb{Z}$, discrete transitions in the slope of the corresponding transfer function occur; the slope of the magnitude in the frequency response is always a multiple of 20 dB/decade, while the phase response is a multiple of $\pi/2$ rad (Figure 3.1). Thus a generalisation of (3.4) can be produced by letting $\nu \in \mathbb{R}$.

Bearing this in mind another property of the Laplace transform is considered. It is known that [Pod98],

$$\mathcal{L}\{t^{-\nu-1}/\Gamma(-\nu)\} = s^{\nu} \tag{3.5}$$

for $\nu \in \mathbb{R}^-$, where Γ represents the Gamma function, a generalisation of the factorial operator for non-integer values [3]. Now, by using the Convolution Theorem of the Laplace transform on Equation (3.5), it can be readily shown

$${}_0D_t^{\nu} f(t) = \mathcal{L}^{-1}\{s^{\nu}F(s)\} = \mathcal{L}^{-1}\{s^{\nu}\} * \mathcal{L}^{-1}\{F(s)\} = \frac{1}{\Gamma(-\nu)} \int_0^t (t-\xi)^{-\nu-1} f(\xi)\, d\xi. \tag{3.6}$$

Equation 3.6 coincides with the Riemann-Liouville definition of the fractional integral operator (Appendix A). One important comment is that the Gamma function is not defined for negative integers – neither for zero. Nevertheless, by combining (3.3) and (3.6), the differintegral fractional operator can be defined $\forall \nu \in \mathbb{R}$ as follows:

$$\begin{cases} {}_0D_t^{\nu} f(t) = \frac{1}{\Gamma(-\nu)} \int_0^t (t-\xi)^{-\nu-1} f(\xi)\, d\xi & \text{for } \nu < 0 \\ {}_0D_t^{\nu} f(t) = \mathcal{I}\{f(t)\} & \text{for } \nu = 0 \\ {}_0D_t^{\nu} f(t) = D^{\lceil \nu \rceil}\{{}_0D_t^{\nu - \lceil \nu \rceil} f(t)\} & \text{for } \nu > 0 \end{cases}$$

where $\mathcal{I}$ is the identity operator.

Hence the geometrical interpretation is that, as ν is decreased lower frequencies have more effect on the response, while higher frequencies are less important. So by decreasing ν the memory in the system is gradually increased, as the system responds more to long term information than to instant variations (Figure 3.2). For integer order differintegration this was already known, as more integration means more memory. The difference now is that this effect can be controlled in small increments, and that in the fractional calculus approach differentiation has memory too; it is no longer a local operator.

[3] It satisfies $\Gamma(z) = (z-1)\Gamma(z-1) \quad \forall z \in \mathbb{C} \setminus \{\mathbb{Z}^- \cup \{0\}\}$ (See Appendix A).

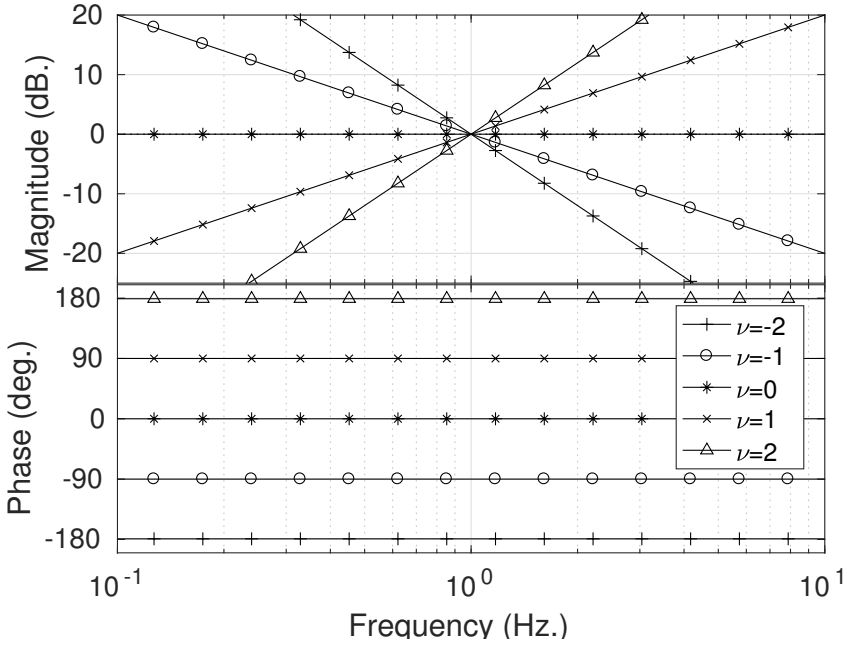

Fig. 3.1 Frequency response of (3.4) by varying ν within $\mathbb{Z}$. The slope of the magnitude response is $\nu \cdot 20$ dB/decade while the phase response is $\nu \cdot \pi/2$ rad with $\nu \in \mathbb{Z}$.

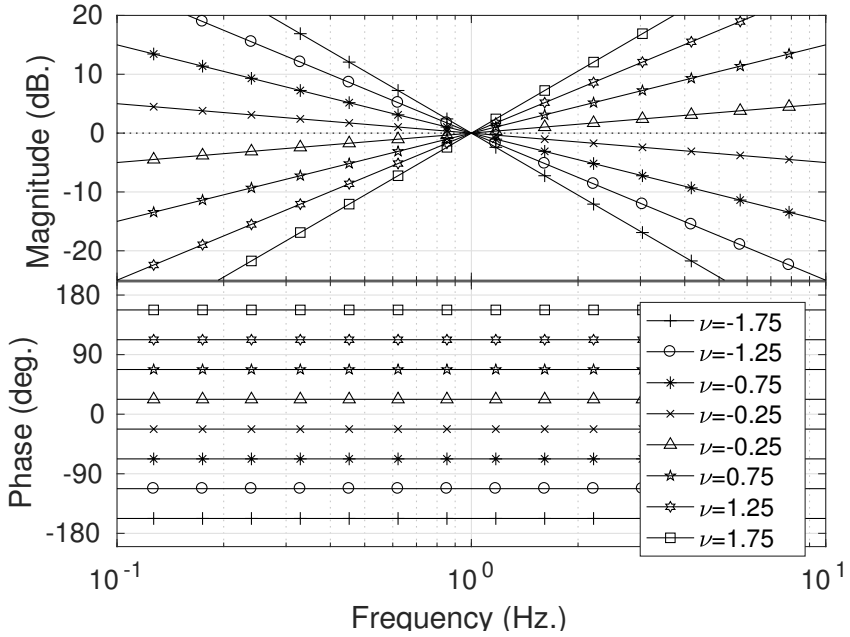

Fig. 3.2 Frequency response of (3.4) by varying ν within $\mathbb{R}$. The slope of the magnitude response is $\nu \cdot 20$ dB/decade while the phase response is $\nu \cdot \pi/2$ rad with $\nu \in \mathbb{R}$.

3.4 Extended Crossover Model for Human-control of Fractional Order Plants

Besides fractional operators, there are other ways in which a dynamical system can represent memory processes. The states of a system are memory variables themselves, as well as transport delays. Memory can also be held in a dynamical system in a cumulative manner, such as a mean of previous states, an integrator, a Bayesian model or a Kalman filter. This last approach has been considered in human control to design optimal control models [BK69]. Additionally, cognition models such as the ACT-R framework (Section 4.1) integrate memory as a list of symbols[4]. However, fractional operators model memory in a more natural form: they consider a memory history of every past state which decays through time[5]. Hence, fractional calculus presents a *temporal footprint* suitable to characterise system memory. Besides, as fractional calculus is included within the framework of differential equations, it is a very practical way to incorporate memory into already existing dynamical models. In addition, a fractional operator characterises its memory properties with only one parameter.

Further motivation for considering this method is that fractional operators introduce wider power law behaviour into the frequency spectrum of a system (Fig. 3.2); for example it is known that pink noise occurs naturally in biological systems [SVS01]. In Section 3.5 the human-operator memory will also be studied through classical control, and this other approach will be compared to the one of fractional calculus.

To test out the relevance of the memory effects of fractional-order dynamics in human-machine systems, experiments were conducted on human tracking behaviour for plants which have the dynamic characteristics of fractional-order systems. The experiments in which the data were collected involved using a steering wheel and a joystick to control such plants, which had additional challenge; thus they generalise the classical experiments found in the literature. Additionally, these tests were performed in compensatory and pursuit control modes (Sec. 2.3.1) and are referred to as *human-in-the-loop tracking experiments* (HTE). Further details are found in Appendix B.1. Briefly, the naïve test subjects had to control plants of the form:

$$Y_p^{\alpha}(s) = \frac{1}{s^{\alpha}(Ts+1)}, \tag{3.7}$$

with parameters $\alpha = 0.5, 0.75, 1, 1.25, 1.5$ (and $T = 0.1$) by means of a control device – a joystick or a steering wheel – and a display. Figure 3.3 shows the impulse response of (3.7)

[4]The ACT-R model has been applied to model the human driver [CG07].

[5]The weights in Definition (A.3.1) satisfy the property that recent states of the system are more relevant than older events (Fig. A.2).

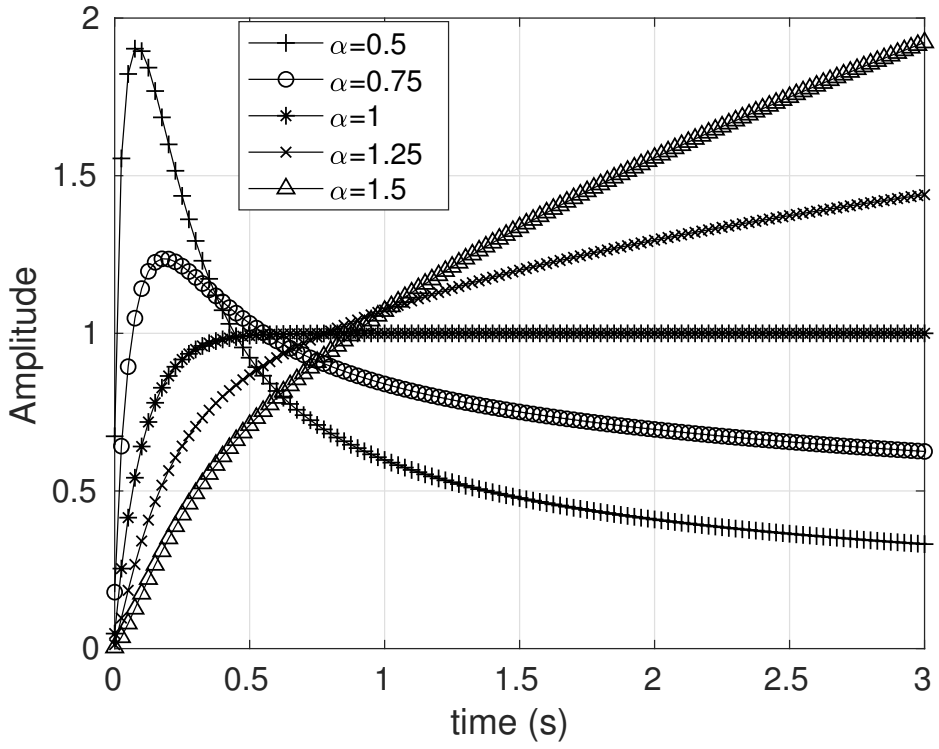

Fig. 3.3 Impulse response of the plants (3.7) for their particular fractional order α.

for different values of α, while in Figure 3.4 an example of the recorded signals in the HTE is presented.

3.4.1 HTE dataset fitting to the classical CO model

Firstly, the question of whether the human operator is able to interact and control skillfully fractional-order plants is examined. To study this possibility, The CO model (2.12) is fitted to the recorded control movements in the HTE dataset corresponding to non-fractional ($\alpha = 1$) and fractional-order plants ($\alpha \neq 1$).

In order to fit the CO model to the frequency response estimates of the human control actions, the delay parameter τ was approximated first. For this purpose, the error signal $e(t)$ is shifted by consecutive time units, and the cross-correlation between $e(t)$ and the human response signal $c(t)$ is calculated. The number of shifting units that yields a maximum cross-correlation approximates the average time delay τ of a recorded signal (See Table 3.1 and Fig. 3.5). To compute the crossover frequency ω_c, the estimated frequency response is fitted through linear regression. The intersection with 0 dB yields ω_c (Fig. 3.6). In addition, the slope of the regression line is compared to that of the CO model.

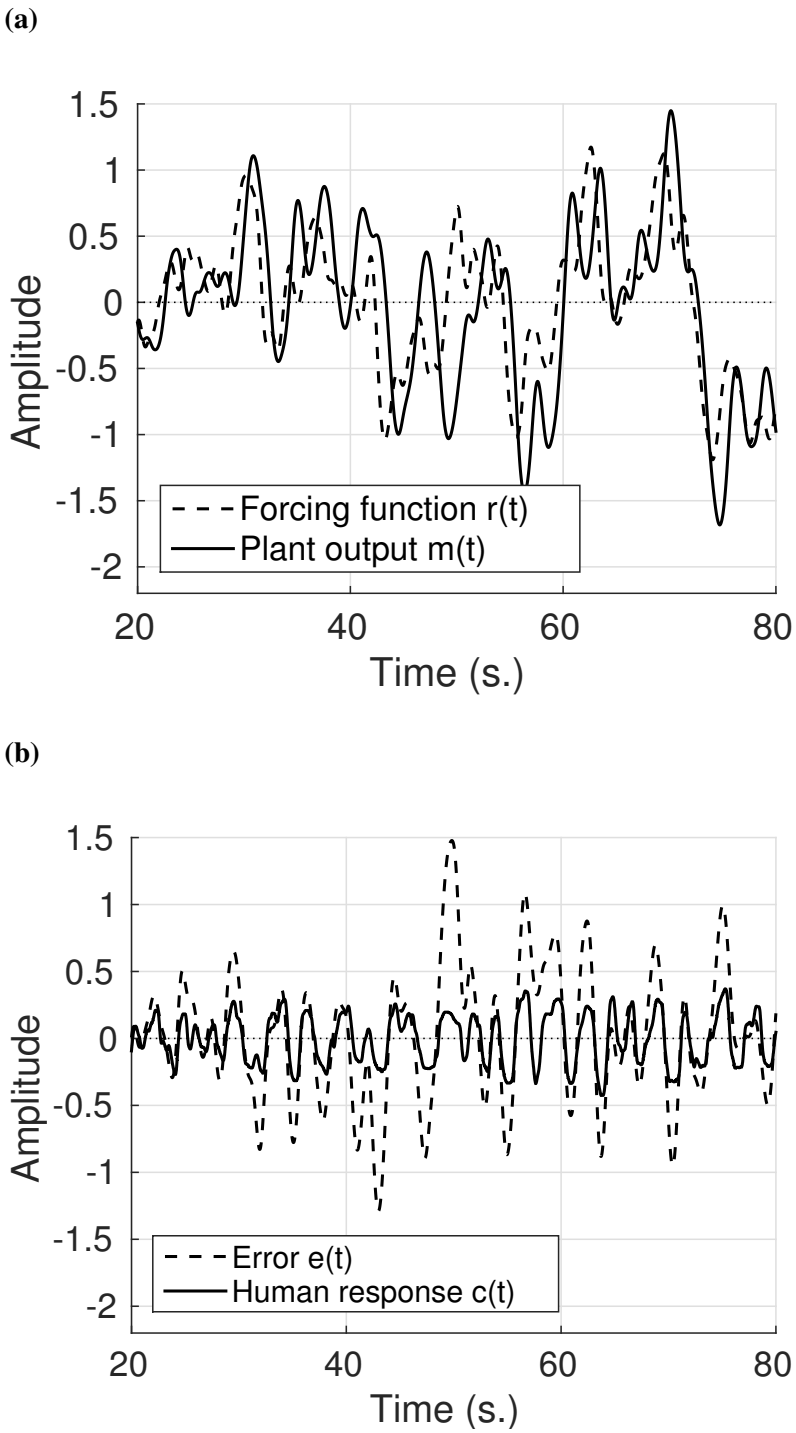

Fig. 3.4 Recorded signals from Subject 3 corresponding to the test with steering wheel, display in pursuit mode and $\alpha = 1.5$. (a) The output of the plant follows the forcing function after a delay determined by the subject's effective time delay and the plant response. (b) Human response to the visually perceived error after an average effective time delay of 0.31 s for this test.

Subject	Delay (s.) Joystick	MSE Joystick	Delay (s.) S. wheel	MSE S. wheel
S1	0.342	0.168	0.438	0.183
S2	0.314	0.094	0.537	0.295
S3	0.202	0.072	0.284	0.088
S4	0.308	0.133	0.472	0.353
S5	0.266	0.138	0.347	0.161
S6	0.443	0.291	0.644	0.291
S7	0.461	0.220	0.504	0.255
S8	0.281	0.106	0.366	0.143
S9	0.179	0.155	0.335	0.125
S10	0.353	0.177	0.404	0.155
Mean	0.315	0.155	0.433	0.205

Table 3.1 Effective time delay and mean squared error (MSE) between the error signal and the human response signal for each subject. The results are tabulated for each control device.

The invariance property of the classical CO implies that a slope of -20 dB per decade occurs in the magnitude of the response. From the slopes of the fitted regression lines it is observed that the invariance property does not hold when using fractional order plants. The slope varies according to the fractional order of the plant (Fig 3.7). Furthermore, the phase response does not match that of the classical CO model.

An initial examination (Fig. 3.7) of a representative set of test data exhibits that the slope and phase conditions (2.13), (2.14) are no longer satisfied. Indeed, by analysing the particular cases the following pattern is observed:

- For $\alpha = 1$ the classical CO model is consistently verified as described in the literature [MJ67] (Fig. 3.7b).

- For $\alpha < 1$ the slope of the frequency response magnitude is greater than the $-20\,{}^{dB}/_{\text{decade}}$ predicted by the CO model. Besides, there is an additional positive constant shift in phase (Fig. 3.7a).

- For $\alpha > 1$ the slope of the frequency response magnitude is less than the predicted $-20\,{}^{dB}/_{\text{decade}}$. In this case there is an additional negative constant shift in phase (Fig. 3.7c).

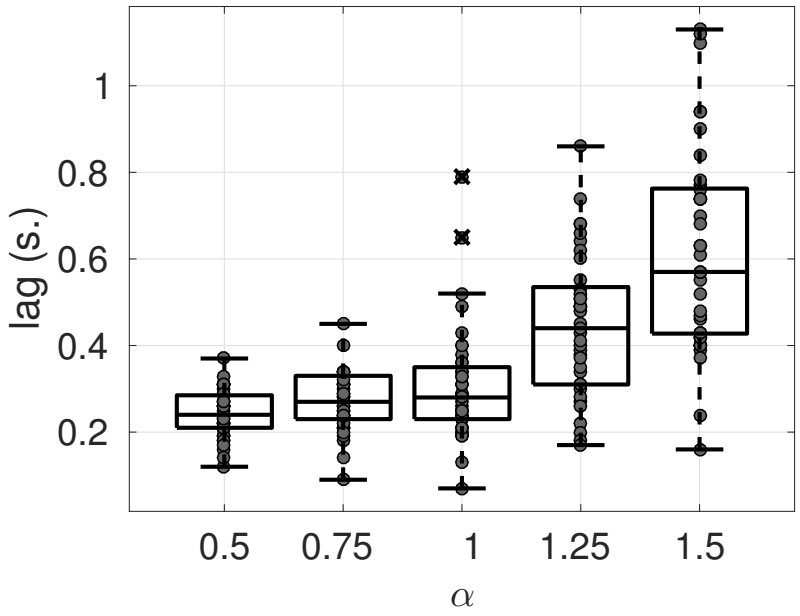

Fig. 3.5 Distribution of the fitted effective time delay values τ for all the studied experimental tests and for each plant type. τ increases along with the order of the plant, especially for $\alpha > 1$.

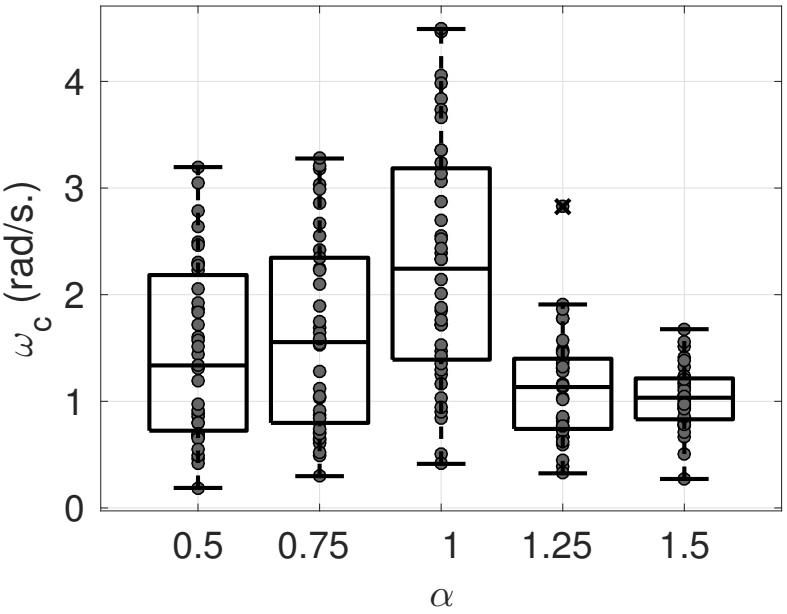

Fig. 3.6 Distribution of the fitted ω_c values for all the studied experimental tests and for each plant. Smaller values of ω_c are generally observed for fractional plants ($\alpha \neq 1$), specially for the higher order ones.

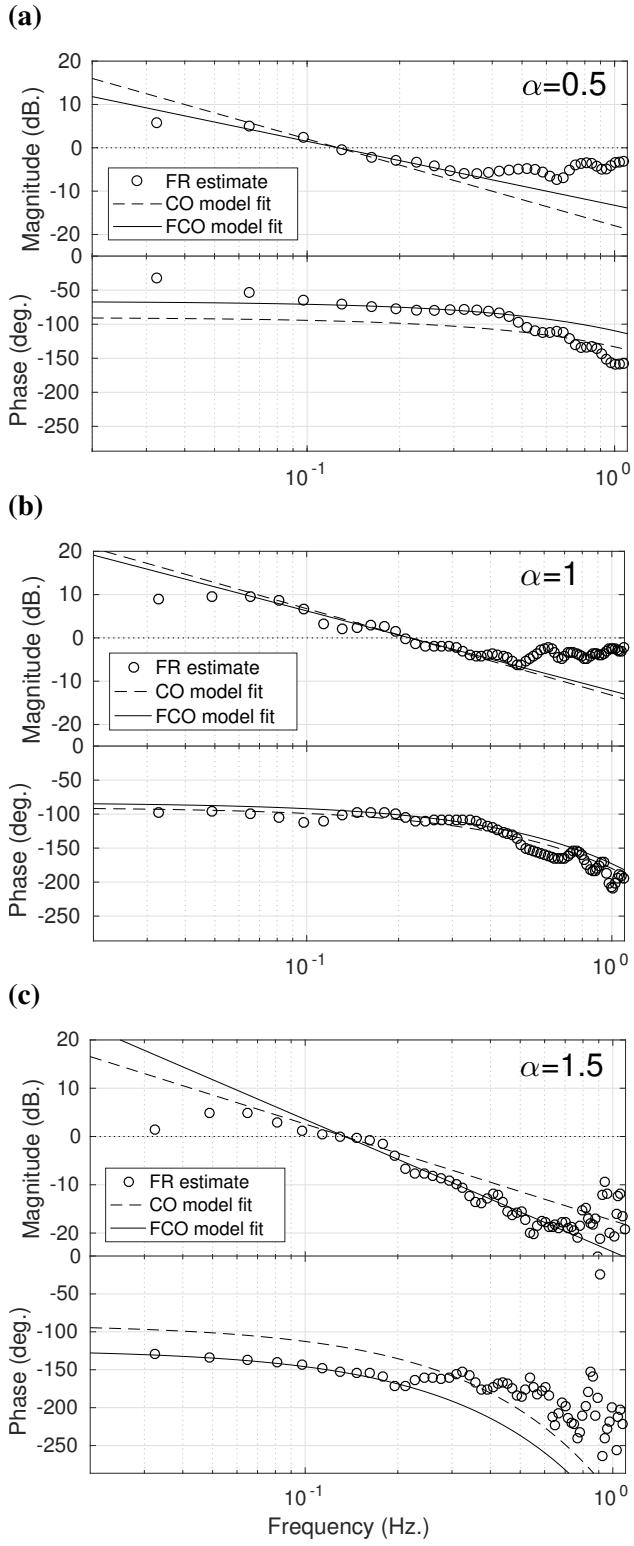

Fig. 3.7 Frequency response fitted to the classical CO model and the FCO model for three experimental tests (using the steering wheel and in pursuit mode). Plant transfer functions: (a) $\alpha = 0.5$, (b) $\alpha = 1$ and (c) $\alpha = 1.5$.

3.4.2 Fractional Crossover (FCO) Model

In light of the above, a generalisation of the CO model is proposed – the *Fractional Crossover* (FCO) model:

$$Y_h(s)\,Y_p^{\alpha}(s) = \frac{(\omega_c)^{\lambda} e^{-\tau s}}{s^{\lambda}}. \tag{3.8}$$

The FCO model includes an additional parameter λ that reproduces the pattern described. $Y_h(s)$ is the human transfer function and $Y_p^{\alpha}(s) = {}^{K}/_{s^{\alpha}(Ts+1)}$ is the plant. When fitting the FCO Model, λ corresponds to the slope of the fitted regression line.

By using the FCO model (3.8), it is clear that the additional parameter λ can correct the slope in the magnitude of the frequency response to match the data (Table 3.2). What is more significant, and justifies the fractional model, is that the correction brought up by the parameter λ also improves significantly the fit in phase response. Hence, the FCO model presents a more effective fit for fractional order plants – a reduction of 38% for the mean squared error (MSE) in magnitude response and of 62% for phase response (Table 3.2).

The amplitude and phase response for the FCO model are:

$$\mathbf{A}_{\lambda}(\omega_f) = 20\lambda(\log\omega_c - \log\omega_f) \quad \text{dB}. \tag{3.9}$$

$$\Phi_{\lambda}(\omega_f) = -\frac{\pi}{2}\lambda - \tau\omega_f \quad \text{rad}. \tag{3.10}$$

3.4.3 Relationship between Plant Order and FCO model parameter

The new parameter λ exhibits an approximate linear relationship with respect to α. In Fig. 3.8 the distributions of λ – for each test subject run – are shown for different α. The relationship is estimated by fitting a linear trend through the median values for each fractional

	Crossover Model		FCO Model	
α	MSE amp.	MSE ph.	MSE amp.	MSE ph.
0.5	0.063	0.162	0.021	0.033
0.75	0.025	0.034	0.018	0.019
1	0.119	0.099	0.090	0.067
1.25	0.010	0.163	0.009	0.045
1.5	0.018	0.252	0.009	0.106
Mean	0.047	0.142	0.029	0.054

Table 3.2 Average of the MSE for the recorded tests between the frequency response in the data and each fitted model.

plant:

$$\lambda = m\alpha + c \approx m\gamma + 1 \tag{3.11}$$

and values $m = 0.31$, $c = 0.72$ are obtained. It is convenient to define $\gamma := \alpha - 1$ as a measure of how far the plant is from a non-fractional model – we may call this the *fractionality* of the plant. Accordingly, the FCO model can be rewritten as:

$$Y_h(s)\,Y_p^{\alpha}(s) = Y_h(s)\,\frac{K}{s^{1+\gamma}(Ts+1)} = \frac{(\omega_c)^{m\gamma+1}e^{-\tau s}}{s^{m\gamma+1}} \tag{3.12}$$

and hence, the response of the human operator is given by

$$Y_h(s) = K^{-1}(\omega_c)^{m\gamma+1}s^{\gamma(1-m)}(Ts+1)e^{-\tau s}. \tag{3.13}$$

The result $m \approx 0.3$ can be interpreted as follows: on average the human operator is able to compensate for about 70% the fractionality of the combined human-machine system. The compensation is represented in the model of the human (3.13) by an additional factor

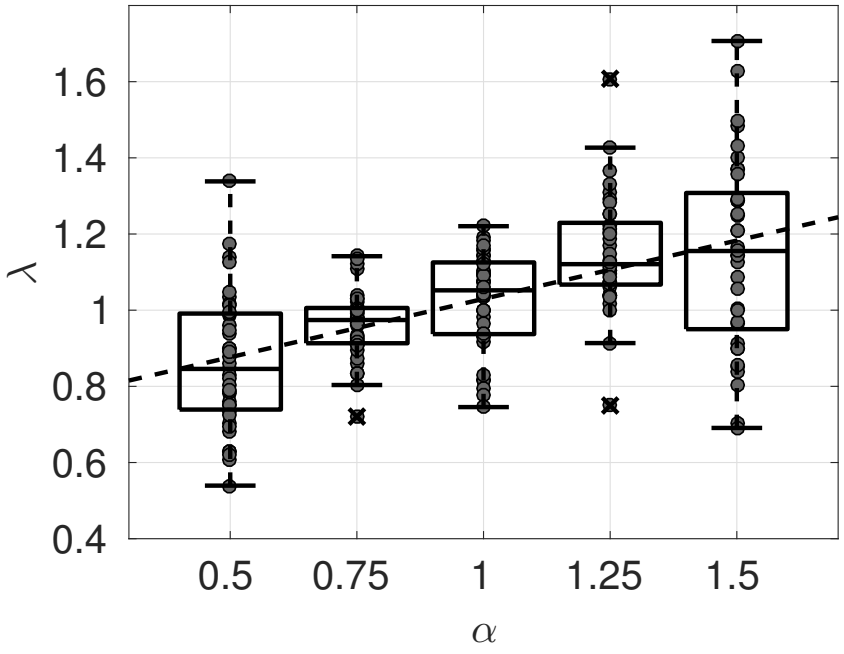

Fig. 3.8 Distribution of the parameter λ, fitted from the experimental data, for all the tests and for each plant with their corresponding box plot. The limits of the boxes denote the 25% (q_1) and 75% (q_3) percentiles. The whiskers have a maximum length of 1.5 the interquartile difference ($q_3 - q_1$). Outside of this range the values are regarded as outliers. The median values are fitted with a dashed line.

$\omega_c^{m\gamma} s^{\gamma(1-m)}$, not present in the CO model. Hence, the FCO model offers a suitable generalisation of the classical CO model, describing human control of a wider category of plants. These may include complex and nonlinear plants or plants with hysteresis effects, and where a fractional order approximation can be determined.

With the given data it is only possible to speculate about what may happen by further increasing the fractionality towards $\alpha = 2$ – or towards $\alpha = 0$. It seems natural that only the difference from α to the nearest integer order is relevant.

An explicit frequency range of validity for the CO model is not reported in the classical literature [MJ67], as it is dependent of the forcing function, the human response characteristics, the control device and the controlled plant. For the presented setup, it is observed that the CO and the FCO models are generally valid on the frequency range of 0.05-0.5 Hz.

It is known that the crossover frequency is larger for more skilled operators [McR80]. Indeed the same result is observed in the HTE dataset (Fig. 3.9). Higher values of ω_c signify that stable tracking occurs across a higher frequency range. For example, lower control gains have been reported for inebriated drivers [AJMD75]. Examining the fitted values of ω_c for every α (Fig. 3.6), smaller values are observed in fractional-order plants. In particular ω_c seems smaller for larger $|\gamma|$, especially for higher order plants. Additionally, for $\alpha > 1$, the variability between the different tests is seen to be smaller. This suggests that fractional-order plants are more difficult to control, and while for some tests subjects were able to achieve relatively larger values of ω_c when $\alpha < 1$, for $\alpha > 1$ the crossover frequency is consistently smaller; the degree of difficulty in a tracking task also increases with the order of the plant. Indeed it has been reported that as the order of the plant increases, time delays increase and performance decreases [Mac03]; control of higher order plants is only adequate when a preview of the states of the plant is available [II75].

Interestingly, while for $\alpha < 1$ the crossover frequency is smaller than that of the non-fractional plant ($\alpha = 1$), the neuromuscular lag is very similar (Fig. 3.5). This indicates that, even when the subjects operate at lower bandwidth when controlling fractional-order plants, for $\alpha < 1$ the values of τ are similar to those in the non-fractional case. It may be that subjects are able to use the memory in the system to predict its behaviour in the lower fractional order cases. This is further supported by the fact that almost identical performance is found for $\alpha < 1$ and for $\alpha = 1$ (Fig. 3.10). On the other hand, the higher order plants ($\alpha > 1$) result in a higher error $e(t) = r(t) - m(t)$. For $\alpha = 1.5$ the variability in the data is significantly higher, which suggests that not all the subjects were able to fully adapt to the plant during the course of the tests.

The simplicity of the CO model relies on the fact that it depends on just two parameters (ω_c and τ), which have an intuitive interpretation. The FCO model adds just one additional

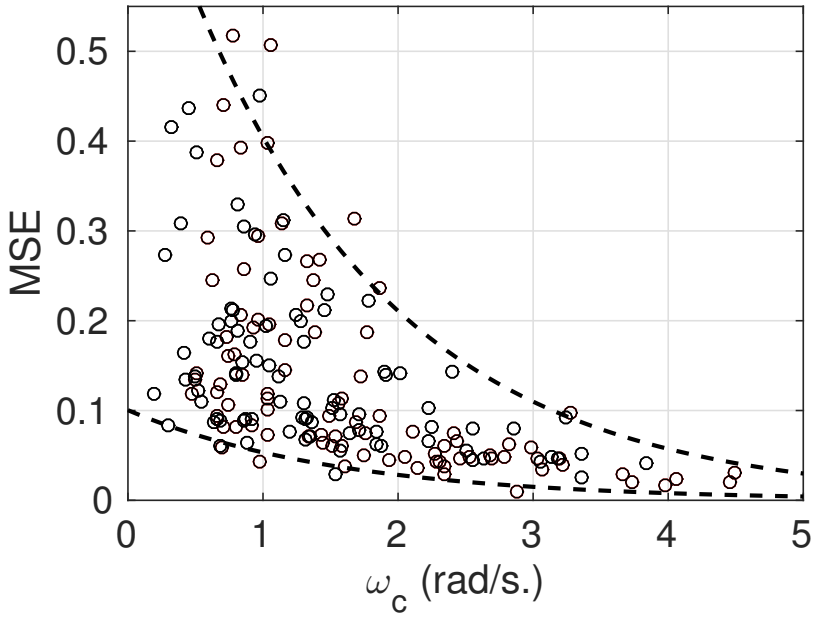

Fig. 3.9 Relationship between the crossover frequency and MSE between $e(t)$ and $m(t)$ in the experimental data. The dotted curves denote the lower and upper envelopes fitted with exponential functions.

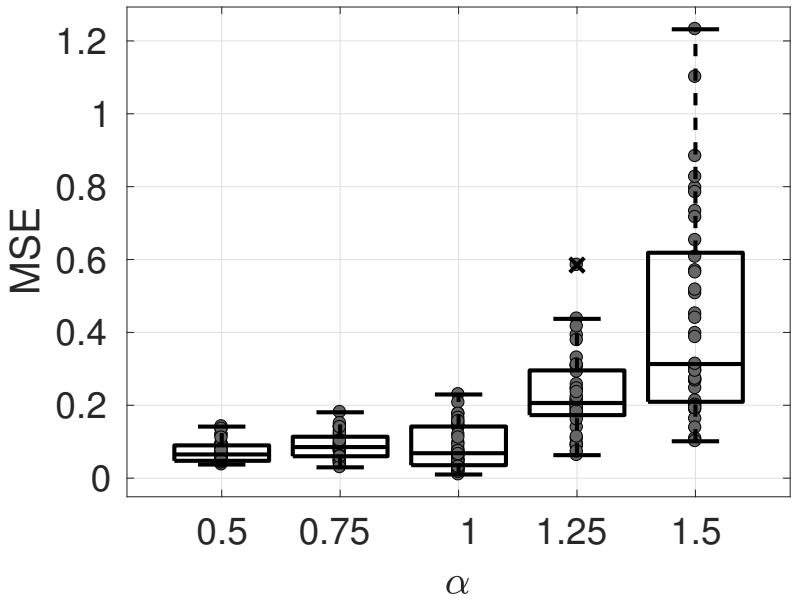

Fig. 3.10 MSE of $e(t)$ for the experimental tests tabulated according to α. The performance is lower for the higher order plants and equivalent for lower order plants.

parameter: the fractional exponent of the combined human-machine system (λ). λ is therefore related to the system memory for the human-machine system. Besides, λ also has an intuitive meaning: it determines the slope of the frequency spectrum (Eq. 3.9) and the added phase offset (Eq. 3.10). Because λ depends on the plant, which in most cases it will be known, the FCO model can still be utilised as a two parameter model.

Since fractional derivatives lie between two integer order derivatives, the results for $\alpha < 1$ suggest that humans can effectively combine information with different levels of differentiation. This is equivalent to combining input variables such as position and velocity or velocity and acceleration, and suggests that it is possible for humans to respond to such composite variables, rather than directly to ordinary *engineering variables*. This motivates the further analysis that will be conducted in Section 3.4.5.

3.4.4 Further Results on the HTE Dataset Related to the CO model

Differences in Control Device

Although neural delays should be equivalent for any control device used, the data shows that muscle activation times differ, producing a different time delay for each device. For the steering wheel the delay is larger than that with the joystick (Fig. 3.11). The obvious explanation is that to achieve the maximum gain with the employed steering wheel requires a rotation of 450°. In the case of the joystick the same gain is achieved with only a few degrees of forearm displacement. Larger time delay bring about larger MSE between tracked and tracking signals. On the other hand, for driving a vehicle this larger gain also tends to amplify the effect of whole-body vibration of the vehicle body, and greater directional precision is offered by a steering wheel with (say) a 16:1 steering ratio. In reference [ARB03] it is reported that the tracking capability is higher with a steering wheel in a regular road, but for crash avoidance manoeuvring, both control devices offer similar performance.

From the experimental Ford FX Atmos (1954) and General Motors Firebird III (1958) to more recent attempts by Nissan and Toyota, the industry has sporadically attempted to implement joysticks in passenger concept vehicles. Probably the high ratio between joystick gain and arm motion limits the feasibility of the concept. While joystick control can yield a faster response, it is too sensitive to allow an intermittently-active driving attendance; it demands constant and quick readjustments. Nevertheless, the median of the MSE for the recorded test subject signals are very similar for the joystick and the steering wheel (Tab. 3.1).

New steering control devices should be developed to achieve good directional precision and low vibration amplification, while at the same time supplying quick response characteris-

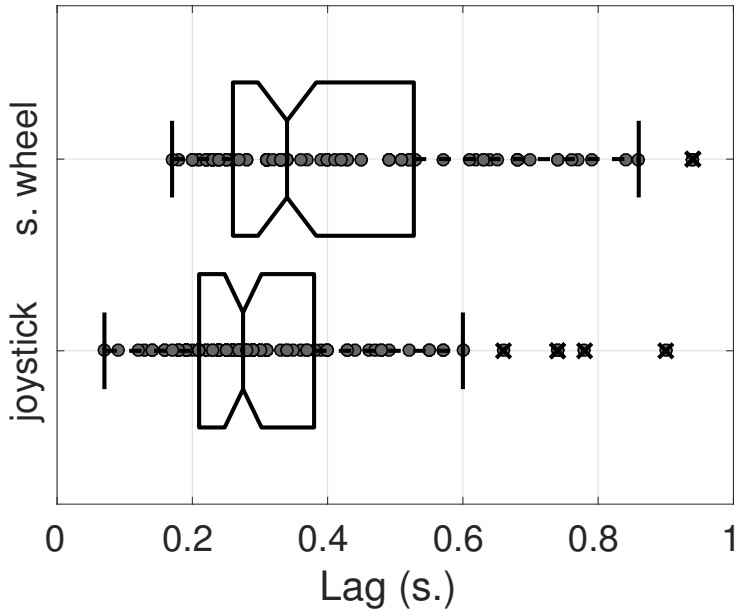

Fig. 3.11 Comparison of the effective time delay in the experimental data for the two tested control devices: joystick and steering wheel. The human operator is able to produce a quicker response with the joystick. The median values are 0.275 s and 0.34 s for the joystick and the steering wheel respectively.

tics in crash avoidance scenarios. This theme will be investigated in Chapter 5 with a unique mechanism for steering control.

Differences in Control Mode

In earlier experiments performed in compensatory and pursuit modes [PDF67], it was observed that after the subjects have gained enough skill there is not significant difference in performance between control modes. In our tests, the subjects were inexperienced in the use of a joystick (Table B.1), and three of them inexperienced with the steering wheel. Thus the data recorded shows differences between display modes. In particular there is significant disparity in the employed gains ω_c (Fig 3.12). In a pursuit tracking task, the subjects applied on average higher gains. We also observed lower MSE in pursuit mode between the tracking and the tracked signals but equivalent average lags.

Prediction Moving Element

Some of the experiments included a *prediction* dot that signalled to the subjects about the future effect of the forcing function on the plant (Appendix B.1). Regarding the difference

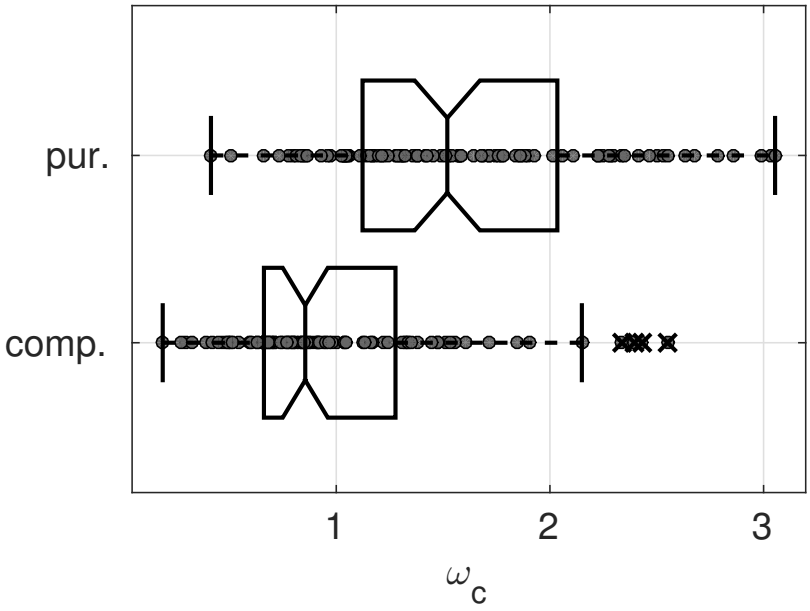

Fig. 3.12 Distribution of the crossover frequency for all the experimental tests and for each display mode (compensatory and pursuit). The triangular indentations in the boxes mark the edges of 95% confidence intervals for the population median location.

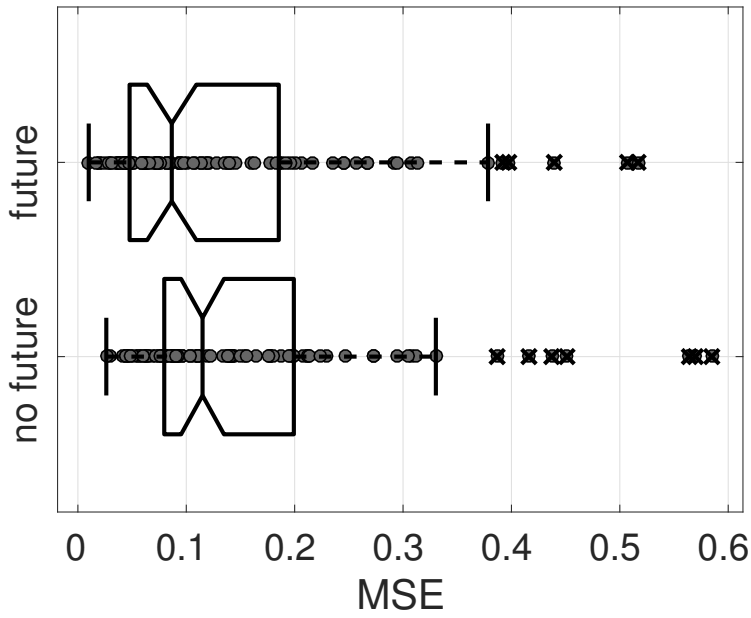

Fig. 3.13 MSE with and without prediction dot in the experiments. The triangular indentations in the boxes mark the edges of 95% confidence intervals for the population median location.

between tracking with or without prediction, some differences are observed among subjects. While some subjects make active use of the future prediction to reduce lag (for one the tests the lag is even negative), to increase the applied gain or to reduce the error, other subjects do not seem to have used the future prediction at all (Fig. 3.13). We believe that more training was needed before all the subjects could use the future prediction to improve their performance.

3.4.5 Sources of Fractionality in Human-machine Systems

While in some cases modelling a system with fractional differential equations represents more accurately its response, real-world plants should be uncomplicated to control, so levels of fractionality are likely to be low for most systems [CPX09]. Nevertheless, the possible sources of fractionality in real-world human-machine systems are analysed in this section by considering the various subsystems. In particular, as the motivation behind this research is its potential application to characterising driver behaviour, the case in which the plant is a ground vehicle is principally considered. Further, the possibility that human operators themselves introduce fractionality in the man-machine control loop is also studied. The following analysis indicates that, although real-world plants can be generally regarded as non-fractional, there is evidence that humans respond to fractionally integrated visual inputs. Furthermore, humans appear able to reduce the fractionality in the visual system to elicit non-fractional responses.

Plant Dynamics

To test the extent to which vehicle response can be considered fractional, the parameters of a fractional linear bicycle model were fitted with data obtained by running a simulation with CarMaker®[IPG15], a high fidelity simulation tool used extensively in the industry. The simulation represented a Toyota Camry 2006 vehicle (Fig. 3.14) with a band limited random steering angle, on a straight road of non-limiting width. The recorded signals were the body slip angle $\beta(t)$ and the yaw rate $\eta(t)$. The data were sampled at 50 Hz[6] and the signal had a duration of 100 min.

The parameters of a linear bicycle model – and of a fractional version of this model – were fitted with the data. The model consisted of two dynamical equations: one equation for the body slip angle and the other for the yaw rate of the vehicle. The considered bicycle model (from [Abe15]) is:

[6]Typically, vehicle dynamics occur within much lower frequencies than 50 Hz. The same is true for human steering response 2.4.2.

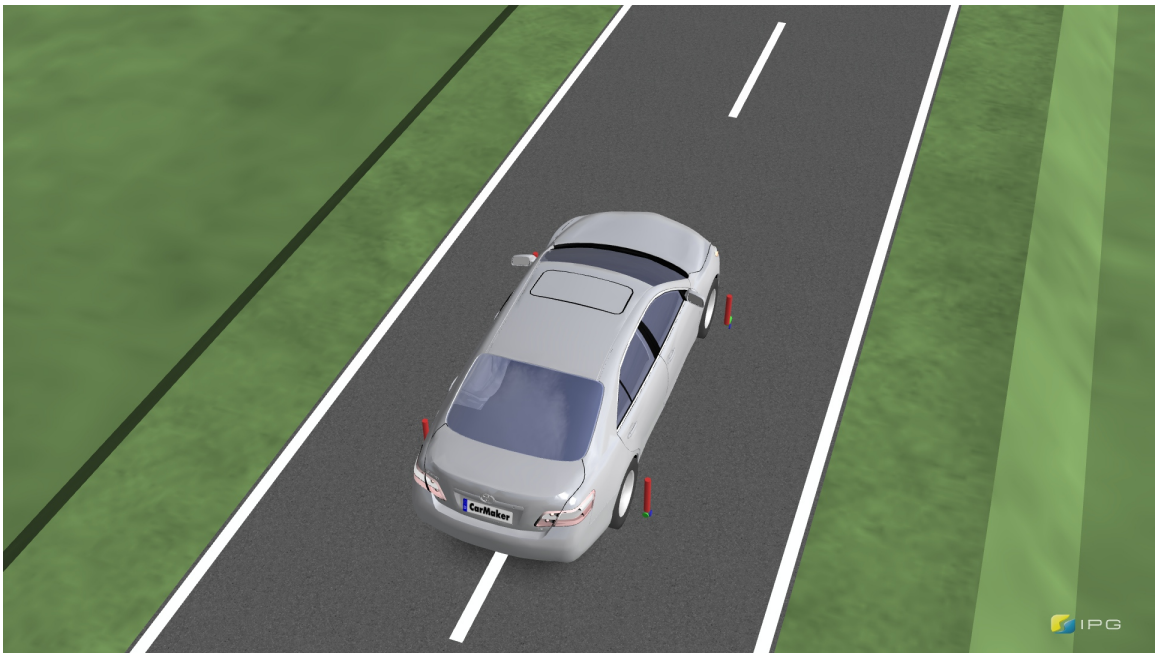

Fig. 3.14 Ground vehicle simulation representing a Toyota Camry 2006 with a band limited random steering angle, on a straight road.

$$\begin{bmatrix} \dot{\beta} \\ \dot{\eta} \end{bmatrix} = -\begin{bmatrix} L_0/MU & 1+L_1/MU^2 \\ L_1/I & L_2/IU \end{bmatrix} \begin{bmatrix} \beta \\ \eta \end{bmatrix} + \begin{bmatrix} C_{\alpha f}/MU \\ l_f C_{\alpha f}/I \end{bmatrix} \delta_f \tag{3.14}$$

with

$$\begin{cases} L_0 = C_{\alpha f} + C_{\alpha r} \\ L_1 = l_f C_{\alpha f} + l_r C_{\alpha r} \\ L_2 = l_f^2 C_{\alpha f} + l_r^2 C_{\alpha r} \end{cases} \tag{3.15}$$

and where $C_{\alpha f}$ and $C_{\alpha r}$ are the *axle cornering stiffness* for the front and rear axle respectively, M is the mass of the vehicle, U the speed – which was chosen to be constant at $100\,^{km}/_{\mathrm{h}}$, l_f and l_r are the distances from the centre of gravity of the vehicle to the front and rear axle respectively, I the yaw moment of inertia and δ_f the front steering angle. A fractional version of the model can be rewritten as a transfer function with an additional parameter μ:

$$\begin{bmatrix} B \\ H \end{bmatrix} = \begin{bmatrix} \dfrac{C_{\alpha f}(IUs^{\mu} - Ml_f U^2 + L_2 - L_1 l_f)}{IMU^2 s^{2\mu} + (IL_0 U + L_2 MU)s^{\mu} + L_0 L_2 - L_1^2 - L_1 MU^2} \\ \dfrac{C_{\alpha f} U(MUl_f s^{\mu} + L_0 l_f - L_1)}{IMU^2 s^{2\mu} + (IL_0 U + L_2 MU)s^{\mu} + L_0 L_2 - L_1^2 - L_1 MU^2} \end{bmatrix} \Delta_f \tag{3.16}$$

where $\mathcal{L}\{\beta(t)\} = B(s)$, $\mathcal{L}\{\eta(t)\} = H(s)$ and $\mathcal{L}\{\delta_f(t)\} = \Delta_f(s)$. For $\mu = 1$ (3.16) is identical to the Laplace transform of (3.14).

A multi-objective optimisation – minimisation – process through a genetic algorithm[7] is used with a grey-box modelling approach: It is pre-assumed some knowledge about the data – it follows approximately (3.16) with known M, U, l_f, l_r and I – but as $C_{\alpha f}$ and $C_{\alpha r}$ are more difficult to approximate experimentally and μ is unknown, the genetic algorithm will fit L_0, L_1, L_2, $C_{\alpha f}$ and μ. Two objective functions, e_B and e_H, represent the relative error between the simulated data and each of the equations of the model:

$$e_B = \sqrt{\frac{1}{N}\sum_{\omega=0.1}^{2\,\mathrm{Hz}} \left| \frac{\hat{B}(j\omega) - B(j\omega)}{B(j\omega)} \right|^2} \tag{3.17a}$$

$$e_H = \sqrt{\frac{1}{N}\sum_{\omega=0.1}^{2\,\mathrm{Hz}} \left| \frac{\hat{H}(j\omega) - H(j\omega)}{H(j\omega)} \right|^2} \tag{3.17b}$$

where $\hat{B}$ and $\hat{H}$ are the estimates of the frequency response of (3.16) and N the number of samples in the range 0.1-2 Hz. Thus the objective function is dimensionless. The step responses for each system are very similar, although the fractional model offers a better fit during the transient phase (Fig. 3.15). Both models present a less precise fit of the steady state response, possibly due to effects introduced by the steering compliance, which the bicycle model does not replicate.

The optimised values of the Pareto frontier are displayed in Fig. 3.16. The fitted parameters show that the fractional bicycle model is very near to the non-fractional case ($\mu = 1$) with $\mu = 0.987$, although the fractional model fits better the transient phase in the step response. The value of μ was selected as a trade-off (Fig. 3.16); increasing or decreasing μ from 0.987 will result in an increase of e_B or e_R respectively (Eq. 3.17). According to this analysis, ground vehicles may introduce a certain degree of fractionality in the human-machine system, but not to the same degree as in the HTE. This fractionality is likely to derive from the viscoelasticity of the tyre, the elasto-kinematics of the steering system or the suspension systems, and may be more significant for heavy vehicles or for vehicles driven off-road.

[7] The initial population of the algorithm was selected through a uniform probability distribution, while the *parents* in each generation were selected by the *stochastic universal sampling technique* [Bak87]. The mutations were produced by adding Gaussian noise to the sample and the *crossover fraction* in each generation was 0.8. The ratio in the Pareto frontier was set to 0.5. The algorithm ran for a fixed number of generations and was executed multiple times with different randomisation.

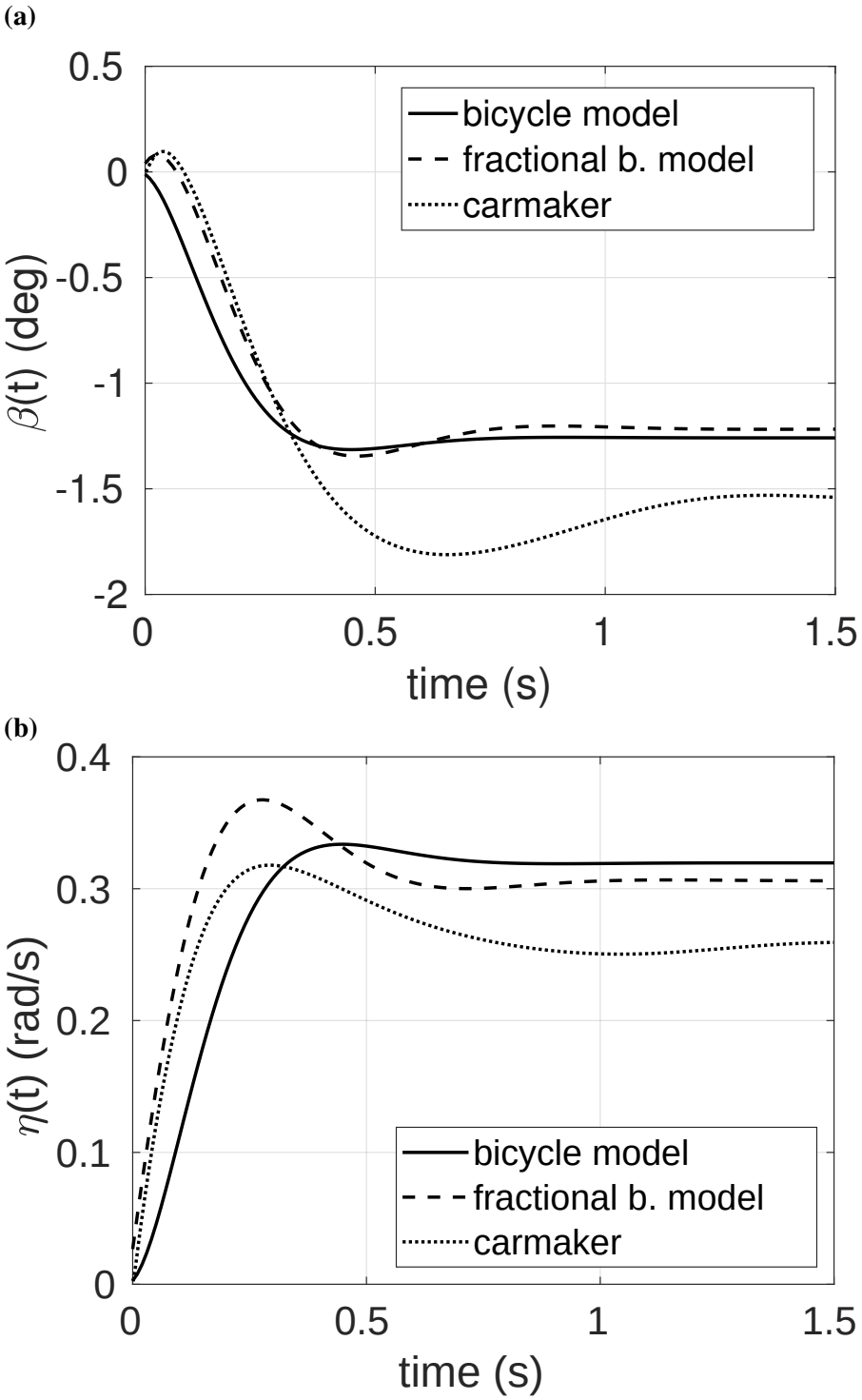

Fig. 3.15 Step response for the optimised solution for (3.16) with $\mu = 1$ (non-fractional), $\mu = 0.987$ and for the CarMaker® simulation setup. While the transient is slightly different for $\mu \neq 1$ – more overshoot is present in fractional case – the steady state response is very similar for both models. The step input is of $\delta_f = 0.05\,\text{rad}$.

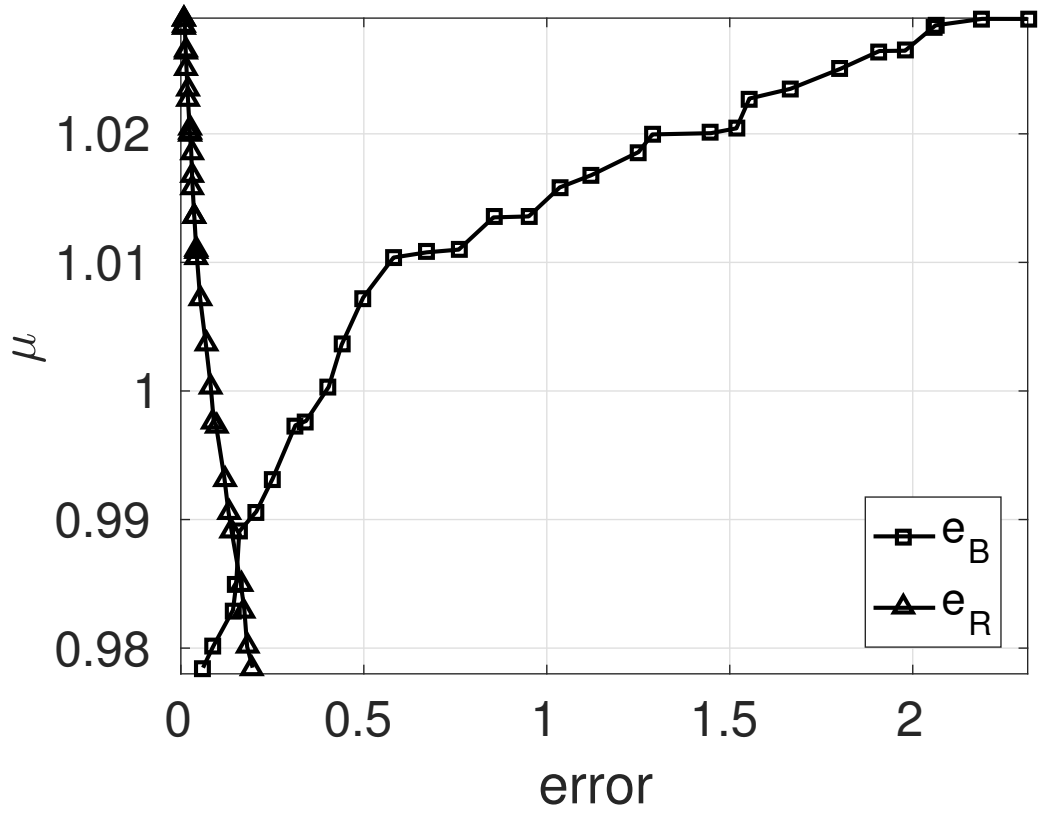

Fig. 3.16 Relative errors e_B and e_R from (3.17a) and (3.17b) vs. the fractional parameter μ. Each point corresponds to a member of the Pareto frontier, which contains the potential optimal solution alternatives yielded by the optimisation algorithm. The two curves intersect at $\mu \approx 0.987$ with $e_B = e_H \approx 0.154$.

Human-operator Dynamics

Section 3.2 suggested two mechanisms involved in visual perception that can imply fractionality within the human operator: trans-saccadic memory and vestibulo-oculomotor neurons.

There is another way in which the visual system may introduce fractionality: perceived visual inputs are processed in different parts of the brain via a complex network of feedforward and feedback connections. The neural visual pathway displays a peak in activation before any motor output is performed [TFM96]; neural processing of a perceived image until identification can take around 150 ms. Thus visual processing has a memory integration time comparable to that of the duration of a saccade.

Here the possibility that visual processing of the tracking error can be modelled with a fractional operator is considered. For the 200 recorded tests, a genetic algorithm was run that maximises the correlation between ${}_0D_t^{\gamma} e(t)$, the fractional derivative or integral of $e(t)$, and

$c(t)$, the human operator manipulative control actions, by varying ν (Fig. 3.17). Through this method, it is inferred that the human operator response displays greater correlation to a delayed fractional error variable, rather than to an integer power of the differential operator. In the analysis, the median correlation was shown to increase from 0.758 to 0.816, when the fractional operator was added.

Further, the fractional error variable relates to the fractionality of the plant through an approximate linear relationship:

$$\nu = n\alpha + d_1 \equiv n\gamma + d_2 \tag{3.18}$$

with $n = 0.56$, $d_1 = -0.40$ and $d_2 = 0.16$.

This result provides *indirect evidence for fractionality in the human controller*. Our interpretation is that the human operator responds to visually interpreted information with

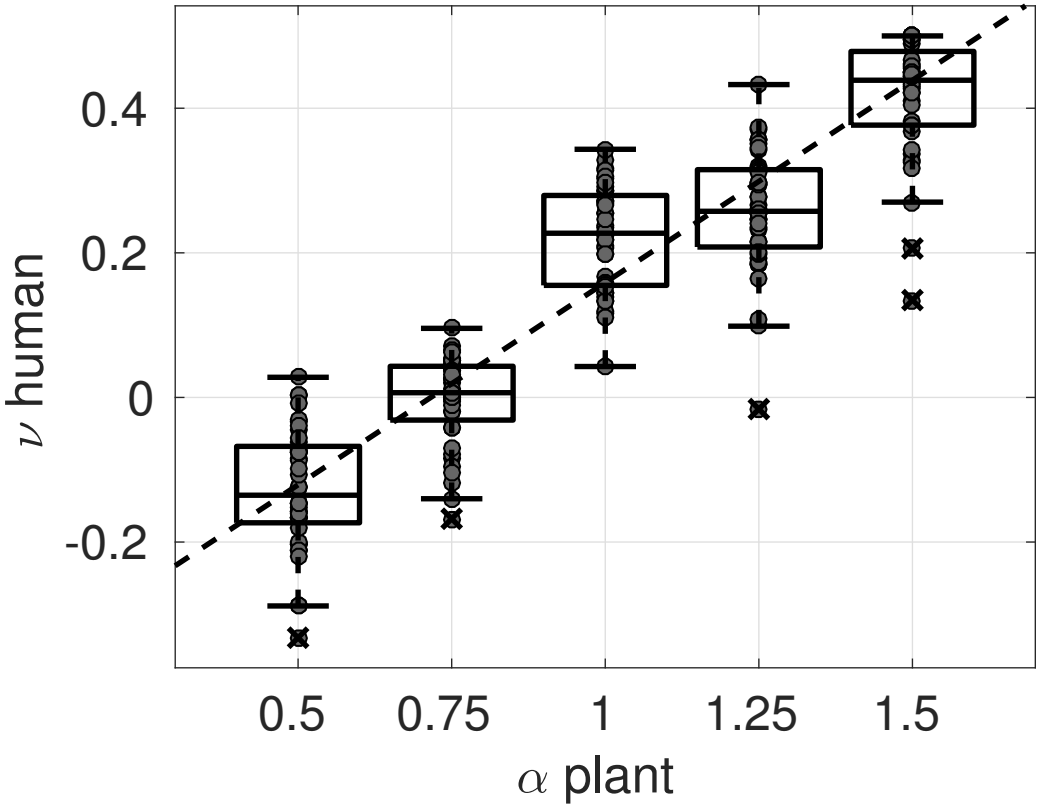

Fig. 3.17 Relationship between the order of the plant (A.12) and the fractional-order ν that brings maximal correlation between ${}_0D_t^{\nu} e(t)$ and $c(t)$ for the experimental recorded tests.

some level of fractionality, and that visual inputs for the tracking task can be modelled as a linear filter that takes into account sampled past observations – Definition $A.3.1$ – (Fig. 3.18).

Discussion

Taking as benchmarks the CO model, the FCO model and the classical literature, it can be concluded that the overall human control response for non-fractional order plants is itself non-fractional. But human responses appear more highly correlated to fractionally integrated visual information. Further, in Section 3.4.3 it was shown that humans are able to reduce the fractionality of the whole human-machine system in about 70%. Considering that most real-world plants are non-fractional, this raises the question of why humans possess some skill to control and compensate fractional order plants. One explanation is that visual perception, muscular dynamics and the CNS contain memory aspects that can be described as a fractional process, and human neuromuscular responses can be characterised as a process that compensates this fractionality, yielding a non-fractional response. In order to interact with a non-fractional plant, the most convenient approach for the operator is to produce a non-fractional manipulative action. A mechanism of fractional compensation has previously been proposed for vestibulo-oculomotor neurons; in [Ana94] it is contemplated that the fractional dynamics of motor neurons compensate the fractional dynamics of the eye. From the analysis presented here, a mechanism of fractional compensation is the most plausible explanation.

The mechanism of fractional compensation can occur in a number of different ways. One possibility is that it occurs in the muscular system. Fractional-order dynamics seem to be general in the muscular system [TVPM13, Mag06]. The musculoskeletal system is composed of viscoelastic polymers, which are known to be well modelled by fractional dynamics. In Section 2.3.3 the plausibility human-control to be characterised by intermittent

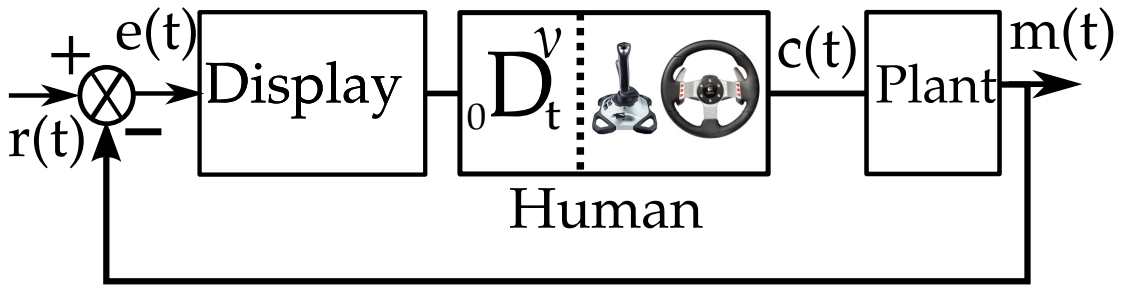

Fig. 3.18 Suggested scheme by the analysis in the recorded data: The human-operator responds to an error variable that can be modelled with a fractional operator. The human operator compensates to produce a non-fractional response $c(t)$ – when interacting with non-fractional plants – according to the FCO model.

pulses was mentioned, and this will be further discussed in Section 4.2. However, human control output recordings appear to be smooth. The fractional aspects of the motor system can explain the transition between discrete pulses and smooth steering response. Regarding the fractional compensation, another possibility is that it occurs during the visual processing stage. However, without a complementary analysis of neural recordings the exact process of compensation cannot be fully characterised.

The FCO has been published already in a conference paper [MGG16] which was later extended to a journal paper [MGGS17].

3.5 Finite Impulse Response Method

Motor response involves a series of self-regulated and coordinated actions, which in many cases are produced unconsciously. Thus there is some type of non-declarative memory involved in a manual control task. The memory encodings of different motor skills have been referred to as *procedural memories* (Sec. 3.2).

In this section, finite impulse response (FIR) filters are employed to identify procedural memory patterns, i.e., unconscious implicit memories that execute motor control actions during manual tasks with visual feedback. For this, the data collected from human subjects in the HTE are utilised (Sec. B.1).

The effect of visual memories in manual control was already investigated through fractional calculus in Sec. 3.4. The fractional calculus approach offers the advantages of adding very few parameters to a model, and integrating relatively well with general differential equations theory. However, because a fractional operator is specified with only one additional parameter – which represents the fractional order of differintegration – this method, although effective for modelling, has a more limited capacity to characterise procedural memory patterns.

On the other hand, the approach presented in this section – FIR modelling – requires a larger parameter set, but it is more appropriate to study the attributes of procedural memories in human control. Thus, the interest is focused more on analysing how VSTMs are integrated by the CNS, by means of long term procedural memories, the latter here represented by a proposed control law, than on obtaining an effective model of human control for automation purposes. Hence the investigated FIR model is used as an analysis tool. FIR modelling applied to human control can be found in the literature [Shi74], but not the study of the resulting memory patterns, under the assumption that *visual memories* at different instants are weighted through an intrinsic procedural memory pattern.

The classical FIR filter approach was selected as an alternative to the more novel fractional calculus method in Sec. 3.4. One of the advantages of this classical control technique is that the fitted gains of the FIR filter (Eq. 3.19) directly yield the impulse response characteristics of the controller – which in this case can be interpreted as the decay through time of the visually acquired memories during a control task. Additionally, as it is also a linear method, it integrates well with the quasi-linear modelling approach (Sec. 2.3.2).

3.5.1 FIR model

The hypothesis tested is that humans employ a history of past observations – visual memories – to control a plant. These past observations are integrated over a specific time pattern (procedural memory pattern), which reflects the use of visual memories during a manual control task. Additionally, signal analysis is performed to study the intrinsic time scale of the procedural memory pattern. Hence, the linearly equivalent system of the human response is modelled by a FIR model, which can be expressed as:

$$h_l(t) = G_H \sum_{i=0}^{N} K_i L^{[\rho+i]}\{e_t\}, \tag{3.19}$$

where $h_l(t)$ is the modelled human response, G_H the control gain, K_i are the normalised visual cue weights (which manifest the relative importance of a visual cue observed at different instants), e_t is the error at time t and L is the back-shift or lag operator. The lag operator delays the error according to a constant term ρ by $\rho\Delta T$ seconds, and a variable term i which delays by $i\Delta T$ seconds, where ΔT is the selected discretisation step specified next. The constant term ρ reflects the effective time delay ($\tau \approx \rho\Delta T$).

The FIR modelling approach assumes that the human operator can be represented as a discrete controller acting with a time step $\Delta T = 50\,\text{ms}$. This assumption is justified by several research studies (see Sec 2.3.3). On the other hand, discrete controllers can better represent interruptions in human perception, such as the ones produced by driver distraction or multitasking [GS14].

The effective time delay (τ) value was already determined in Section 3.4.1. Accordingly, τ averagely is 315 ms for joystick control and 433 ms for steering wheel control (Table. 3.1). From τ the parameter ρ is estimated for the FIR model.

The FIR model is also consistent with the concept that the human brain uses composite variables, which are linear combinations of derivatives of different orders of the observed cues, to predict the states of the tracked system [HBDS97]. By considering that derivatives can be approximated as finite-differences it can be interpreted that, modelling the human

operator with a FIR transfer function is qualitatively equivalent to considering the prediction effects of higher order derivatives; a linear combination of finite-difference operations is a particular case of a FIR filter.

3.5.2 Pattern Analysis

A genetic optimisation algorithm was used to fit the weights K_i with $i = 1, \ldots, 20$ to the HTE dataset. The objective function was the cross-correlation between $h_l(t)$ (Eq. 3.19) and the recorded human response – both controlling a plant acted by the same forcing function input. In the optimisation process, the weights K_i are constrained to be a normalised vector, in order to prevent the generation of spurious patterns by the genetic algorithm[8]. Genetic algorithms are less prone to be captured at local minima, compared to other convex optimisation methods[9]. Thus they have been consistently employed to fit parameters in generic data [WCL15] – or when the objective function has unknown characteristics – such as data recorded from human subjects [KRB$^+$17]. The human gain G_H was fitted by linear least squares. The parameters K_i, with respect to the number of delayed steps, are shown in Fig. 3.19 for the 200 experiments.

Although there is large variability in the data (Fig. 3.19), a clear pattern is exhibited by the median values. Considering all the variants in the experiments – control device, type of plant, display mode and different subjects – and that the human-operator response is in general very noisy, the variability was anticipated. Additionally, with the exception of $K_{3,4}$, the variability seems to increase with the number of delayed units. For $i = 2, 3$ the high variability may be produced by the large slope in the trend. Thus the fact that the variability increases from $i = 5$, while the magnitude of the weights decreases, suggests that humans rely on a more consistent manner on recent information than on older observations.

The observed pattern in the human-operator response results from their adaptation to the plant $Y_p^{\alpha}(s)$. We already saw that the human response characteristics depend on those of the plant, in such a way that the whole human-machine system presents invariant dynamical properties. This is reflected by the evidence that the joint interaction of the human and the machine can be represented by a particular transfer function near the crossover frequency (Sec. 2.3.2).

[8] Similarly to Sec. 3.4.5, the initial population of the genetic algorithm was selected through a uniform probability distribution, while the *parents* in each generation were selected by the *stochastic universal sampling technique*. The *crossover fraction* in each generation was 0.8. The ratio in the Pareto frontier was set to 0.5. The hyperparameters were tuned empirically by running the algorithm multiple times, until the results were consistent through different randomisation.

[9] Such as gradient descent, the Gauss-Newton algorithm or the Levenberg–Marquardt algorithm, which can be considered an interpolation between gradient descent and Gauss-Newton.

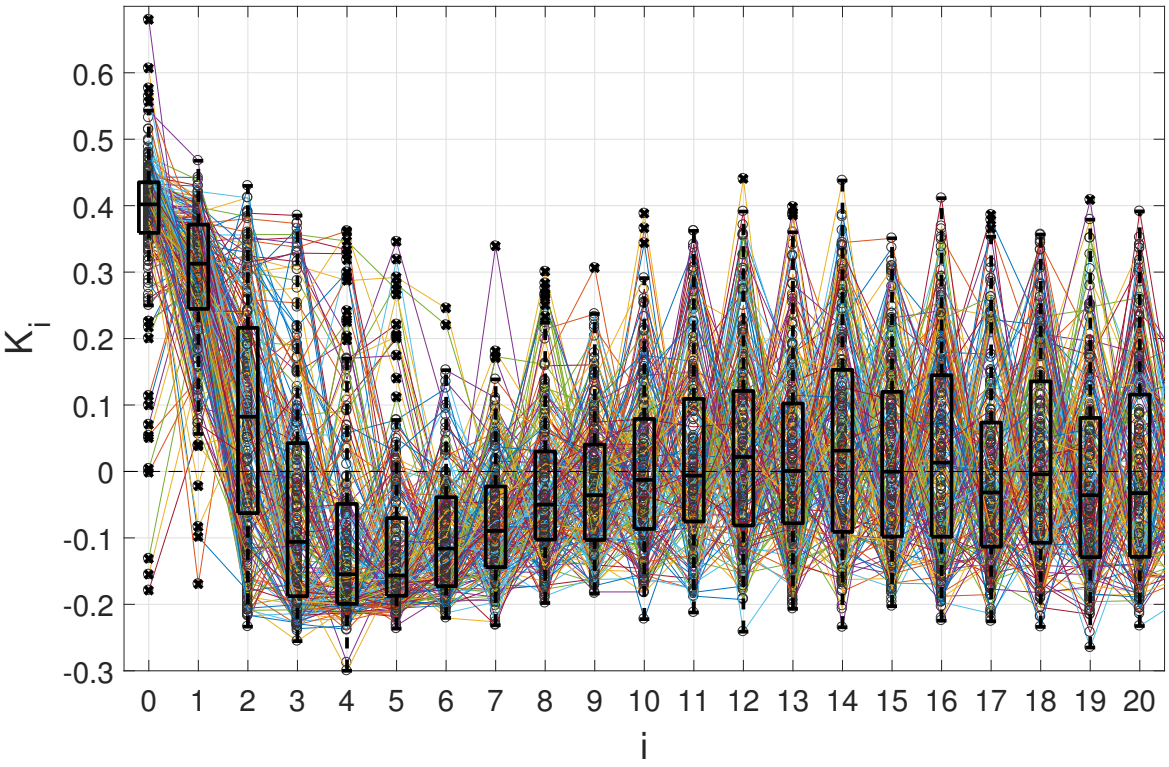

Fig. 3.19 Fitted K_i parameters for all the recorded experiments in the HTE dataset. For each number of delayed steps of duration ΔT, the corresponding box plot is displayed summarising the 200 recorded experiments.

In Fig. 3.19 it is observed that, for the studied plants (3.7), the weights are positive for the first $2-3$ delayed steps (100-150 ms) and remain negative during the continuing 8 delayed steps (≈ 400 ms). Finally, they can be considered essentially zero after approximately 13 delayed steps (650 ms). This value is in agreement with [CMN83], where it is reported that the decay time of a visually perceived image in memory is in the range 90-1000 ms (Sec. 2.4.2). For the chosen plant dynamics, control device and forcing function, it seems that humans use visual memory approximately up to 650 ms. The sign change in the memory pattern between K_2 and K_3 manifests that, visual inputs perceived at different time are weighted in such a way that the rate of change of the error – and higher order rates – can be approximated by the human, allowing the CNS to estimate the future states of the controlled plant.

The same pattern is consistent across different subjects (Fig. 3.20a), qualitatively consistent across different control devices (Fig. 3.20b) and for the different control modes (Fig. 3.21a). Hence, the selected model – for characterising the procedural memory pattern – and the optimisation methodology are adequate, and the data have not been overfitted.

Nevertheless, in relation to the two types of control device tested, the pattern displayed by the weights K_i has quantitative differences between joystick and steering wheel control. In Fig. 3.20b it is shown that for the case of joystick control, there is a higher negative gain and a faster decaying pattern, while for steering wheel control humans tend to use lower cue weights in magnitude but sustain the response longer. This effect is likely to be produced by the fact that controlling a steering wheel involves longer delays resulting from muscle latency (Sec. 3.4.4).

Contrary, the pattern is virtually identical for compensatory and pursuit modes (see Fig. 3.21a). In Section 3.4.4, it was shown that humans display a larger crossover frequency and greater performance in pursuit tasks than in compensatory tasks. Thus not all the aspects of the human response can be represented by the proposed methodology, but the approach is particularly useful to display memory profile patterns.

In Fig. 3.21b the results are compared for the studied plants (3.7). It is observed that as the order of the plant increases, the magnitude of the gains decreases for recent observations, while the decay of the weights over the perceived error is lower. This is possibly caused by the fact that the response of higher order plants is more difficult to predict [II75, Mac03], thus humans rely more on recent observations when the order of the plant is higher.

Further, the gains, G_H in (3.19), are shown in Fig. 3.22 tabulated per subject. The gains are larger for joystick control than for steering wheel control, which is natural since the joystick has a higher output/hand-displacement ratio. Another reason is that untrained humans are not so skilled in joystick control and their output is closer to a bang-bang controller as compared to steering control; in steering wheel control both hands can act in anti-phase, increasing the impedance of the steering action, which is known to reduce the instability [BOF$^+$01].

Furthermore, it is observed that the gains increase with the order of the plant. As already stated, higher order plants are more difficult to control and usually require longer preview time. In [II75] the effects of different preview time intervals were thoroughly examined. For the presented analysis, and in order to simplify the discussion, a preview of the error was not considered.

3.5.3 Reduced Order Infinite Impulse Response Model

With the aim of studying the fitted FIR controller from the perspective of classical control, it is practical to approximate it with the simpler transfer functions of an *Infinite Impulse Response* (IIR) model. Henceforth, the discrete FIR model is fitted to a lower order model with two zeroes and two poles, after discarding the noisy cue weights – only K_0 to K_{13} are considered in (3.19):

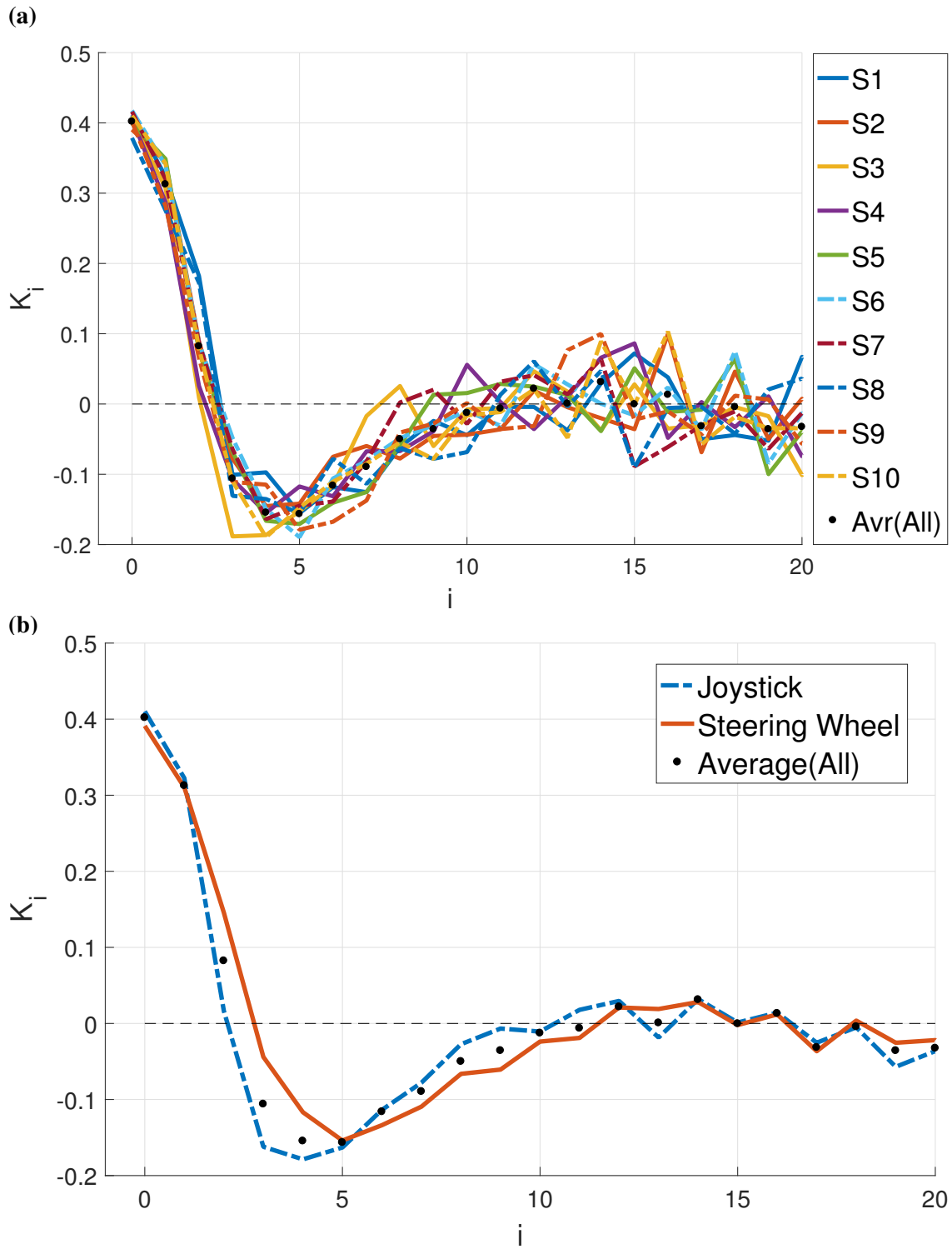

Fig. 3.20 Parameters K_i fitted from the experimental data and averaged (a) for each subject and (b) for different control devices – joystick and steering wheel.

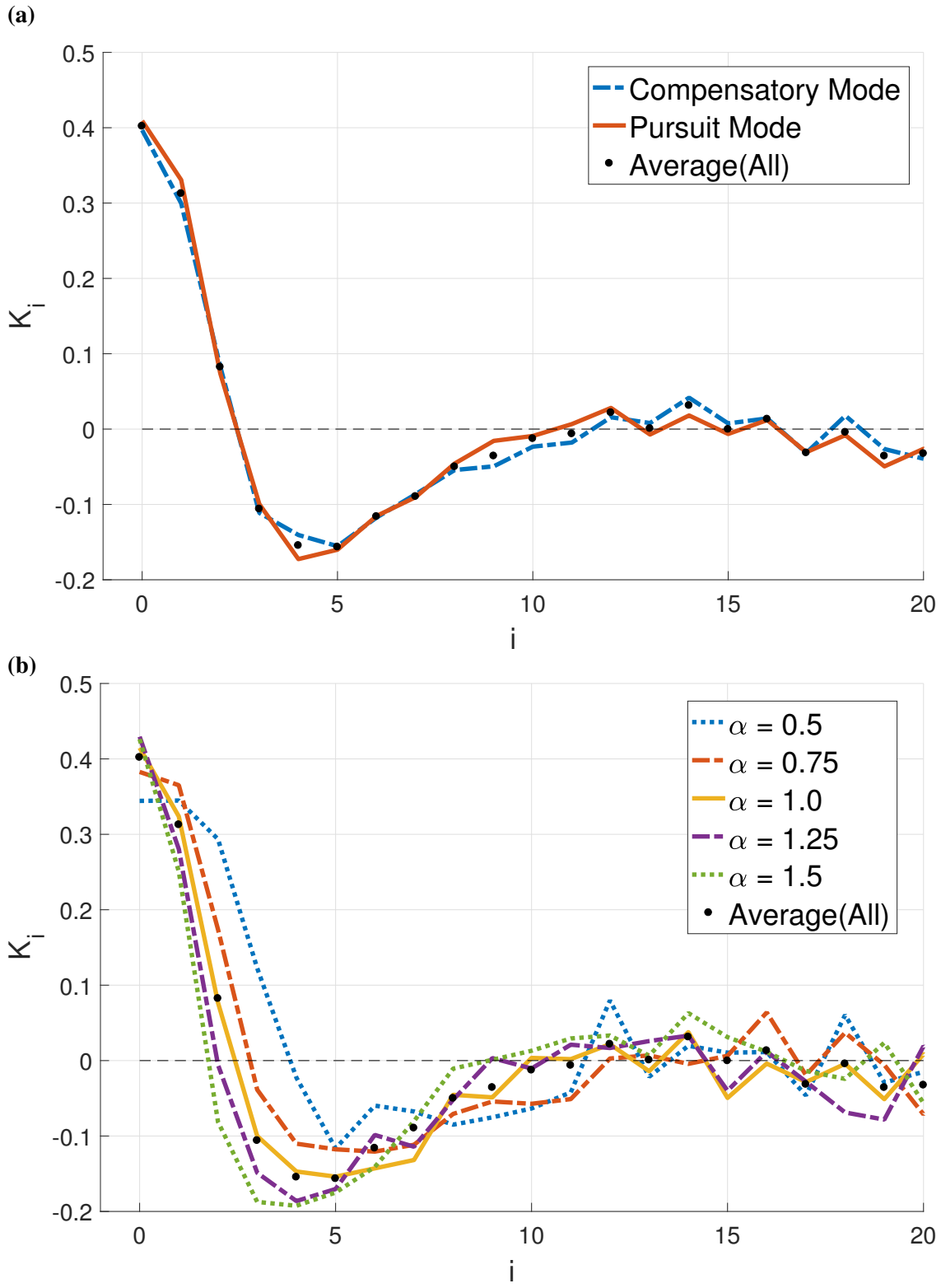

Fig. 3.21 Weights K_i fitted from the experimental data and averaged (a) for different control modes – compensatory and pursuit – and (b) for each controlled plant $Y_p^{\alpha}(s)$.

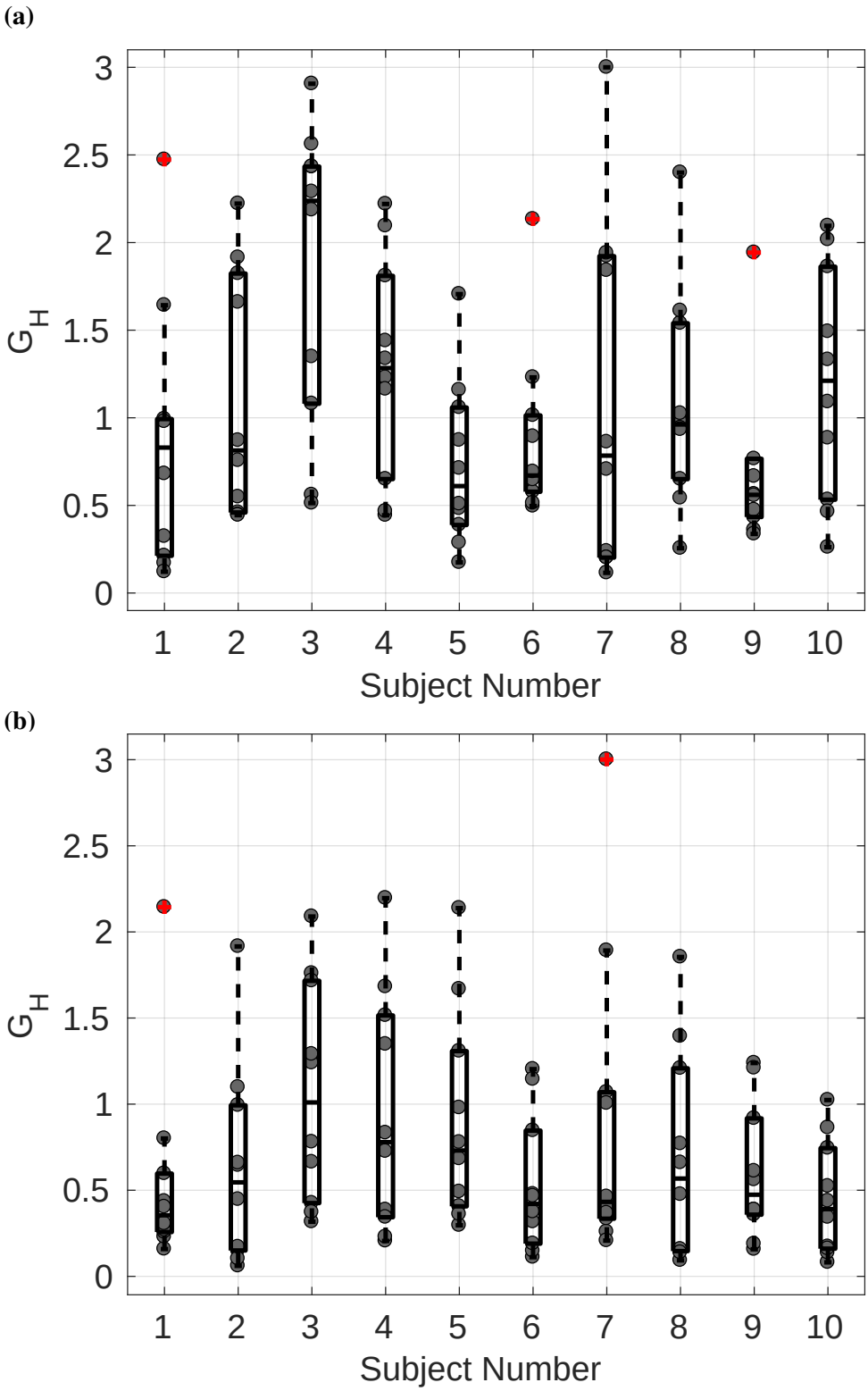

Fig. 3.22 Fitted gain G_H from the experimental data of the different human subjects for (a) joystick control and (b) steering wheel control.

$$\tilde{H}(z) = G_H\{K_0 z^{-\rho} + K_1 z^{-\rho-1} + \cdots + K_{13} z^{-\rho-13}\}. \tag{3.20}$$

The optimal fitted models are shown in Table 3.3 and their corresponding frequency response in Fig. 3.23. The frequency response for the approximated model is accurate within the frequency range where the human-operator can perform a fair level of control; the maximum frequency limit is reported to be in the range 1-5 Hz, depending on the predictive capacity of a given manual control task [Pew07]. Another study [War67] stipulates a limit of 0.7-1.5 Hz for compensatory and pursuit tasks with irregular forcing functions, which do not allow for adequate prediction (Sec. 2.4.2).

For the FIR model (3.20), the pulse and step responses are shown in Fig. 3.24. These can also be compared to the pulse and step response for their approximated lower order counterparts (Fig. 3.25). The lower order model,

$$H^d_\alpha(z) = \frac{a_0(\alpha) + a_1(\alpha)z^{-1} + a_2(\alpha)z^{-2}}{b_0(\alpha) + b_1(\alpha)z^{-1} + b_2(\alpha)z^{-2}} \tag{3.21}$$

is a smoother variant of the FIR model. In both models the step response has a bounded steady state. However, for $\alpha > 1$ the step response stabilises at a negative value. This suggests that the controller may be unstable for those plants.

Plant α	$H^d_\alpha(z)$ (Discr.)	Cont. $H^c_\alpha(s)$ (Cont.)
0.5	$\frac{0.37-0.15z^{-1}-0.11z^{-2}}{1-1.47z^{-1}+0.63z^{-2}}$	$\frac{0.13s^2+12.32s+57.15}{s^2+9.546s+83.86}$
0.75	$\frac{0.39-0.19z^{-1}-0.17z^{-2}}{1-1.4z^{-1}+0.56z^{-2}}$	$\frac{0.13s^2+14.96s+14.51}{s^2+11.72s+68.07}$
1.0	$\frac{0.42-0.25z^{-1}-0.16z^{-2}}{1-1.37z^{-1}+0.53z^{-2}}$	$\frac{0.18s^2+16.09s+8.08}{s^2+12.92s+91.47}$
1.25	$\frac{0.45-0.31z^{-1}-0.14z^{-2}}{1-1.29z^{-1}+0.48z^{-2}}$	$\frac{0.22s^2+17.14s-2.96}{s^2+14.97s+111.2}$
1.5	$\frac{0.42-0.27z^{-1}-0.17z^{-2}}{1-1.25z^{-1}+0.48z^{-2}}$	$\frac{0.19s^2+17.20s-16.27}{s^2+15.31s+132}$

Table 3.3 Lower order discrete transfer functions $H^d_\alpha(z)$ fitted from the FIR model (3.20) for each of the studied controlled plants $Y^\alpha_p(s)$, and their continuous correlate $H^c_\alpha(s)$ obtained through the Tustin's bilinear transform.

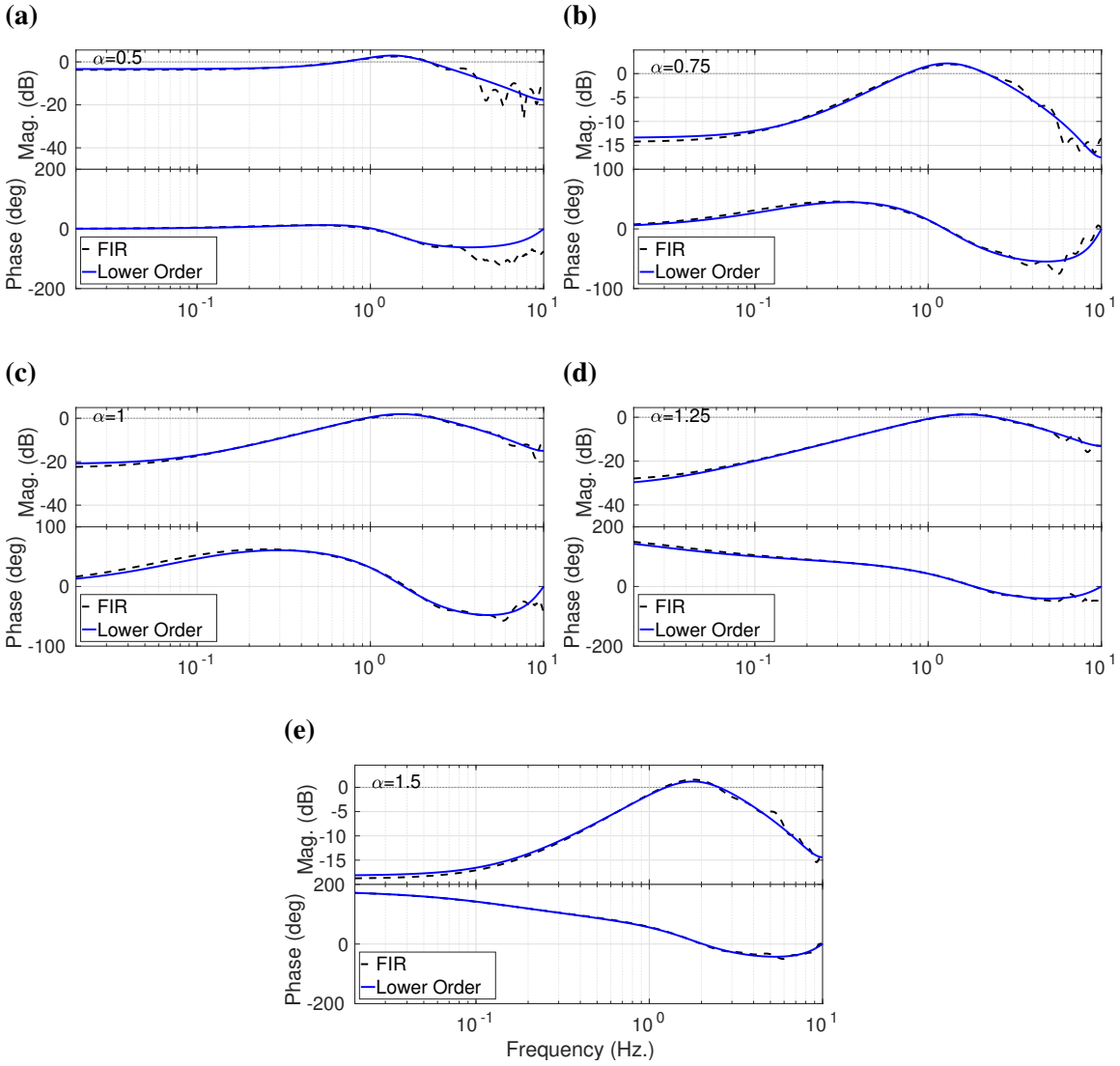

Fig. 3.23 Frequency response for the FIR model and its corresponding lower order approximation for controlling plants with (a) $\alpha = 0.5$, (b) $\alpha = 0.75$, (c) $\alpha = 1.0$, (d) $\alpha = 1.25$ and (e) $\alpha = 1.5$.

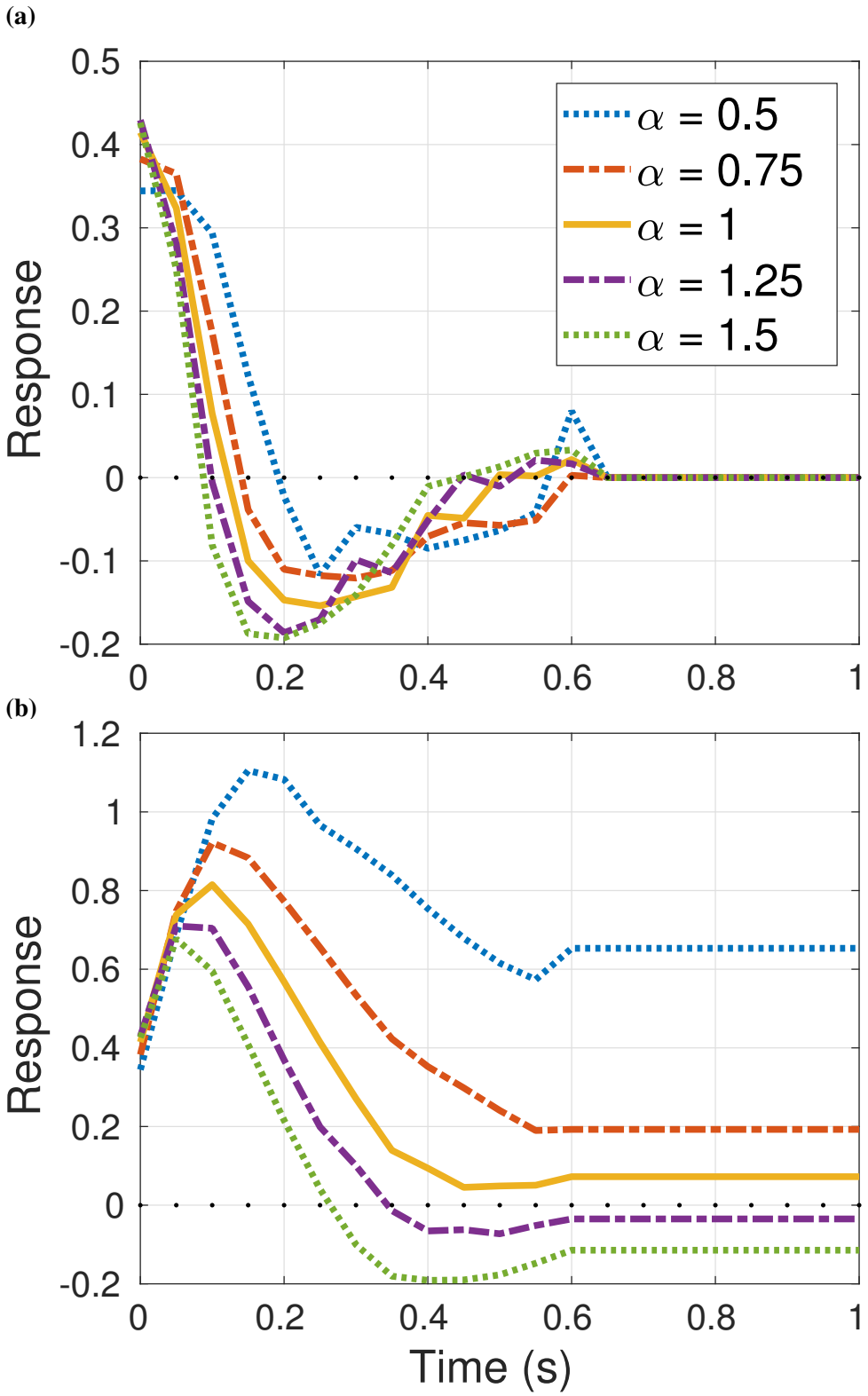

Fig. 3.24 (a) Impulse response and (b) step response for the FIR model with $i = 0, \ldots, 13$ (3.20), for controlling $Y_p^{\alpha}(s)$ for each fractional coefficient α.

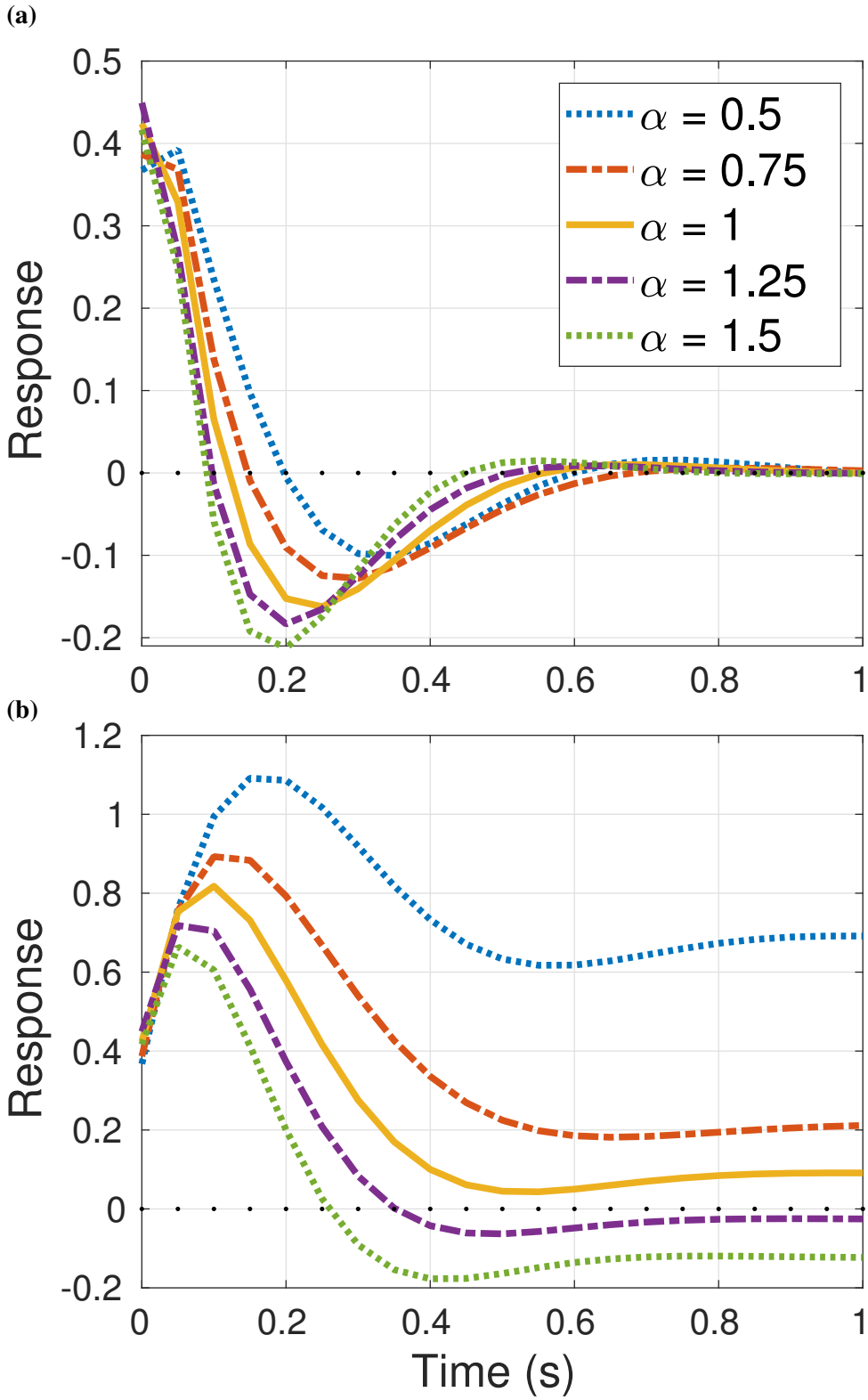

Fig. 3.25 (a) Impulse response and (b) step response for the lower order model $H_\alpha^d(z)$ (Table 3.3), for controlling $Y_p^\alpha(s)$ for each α.

3.5.4 Stability Analysis of Fractional Order Differential Equations

With the purpose of obtaining a clear stability analysis for the virtual human model acting in closed loop, the discrete IIR controller $H_\alpha^d(z)$ is converted to a continuous controller $H_\alpha^c(s)$ (Table 3.3):

$$H_\alpha^c(s) = \frac{c_0(\alpha)s^2 + c_1(\alpha)s + c_2(\alpha)}{d_0(\alpha)s^2 + d_1(\alpha)s + d_2(\alpha)}. \tag{3.22}$$

Although, as mentioned, the human operator can be regarded as a discrete controller, the filtering capabilities of the muscular system make the human motor response resemble a continuous signal [Cra47] (Section 2.3.3).

To perform the stability analysis there is one difficulty: the classical stability theorems do not apply to fractional order transfer functions. The reason is that fractional order systems may present branch points instead of poles. However, in this situation *Matignon's stability theorem* can be applied (Theorem A.3.2 in Appendix A.3.3). This theorem translates the bounded-input, bounded-output (BIBO) stability region of a fractional transfer function to the stability region of a non-fractional one.

By choosing $\zeta = 1/4$ – in Theorem A.3.2 – as a common factor for all the studied plants $Y_p^\alpha(s)$, these are transformed into non-fractional order plants for each α considered:

$$\tilde{Y}_p^\alpha(s) = \frac{1}{s^{4\alpha}(Ts^4 + 1)}. \tag{3.23}$$

And by applying the same transformation ($s \to s^4$) to a Padé approximation of $e^{-\tau s}$, and to the human control model H_α^c (Table 3.3), allows for the computation of the root locus plot of the combined human-machine system (Fig. 3.26). Figs. 3.26a, 3.26b and 3.26c show that the system is stable for $\alpha \leq 1$, as for these plants there exist a gain that keeps all the poles within the stability region (white background region).

On the other hand, Figs. 3.26d and 3.26e show that the system cannot attain stability for any gain when $\alpha > 1$. For $\alpha > 1$ there is always a pole inside the unstable region (grey coloured region).

The evidence that the human subjects could still control the higher order fractional plants, while the linear controller cannot, suggests that a non-linear component or remnant is missing in this type of model. For classical linear transfer functions, the remnant or non-linear characteristics of a human-machine system are commonly regarded as negligible [MJ67]. Thus a possible explanation, for the instability of this model when $\alpha > 1$, is that the remnant may be more significant for higher order fractional plants. Indeed some subjects manifested this opinion during the course of the experiments. Besides, human-control most likely relies on other perceptual cues besides visual memories.

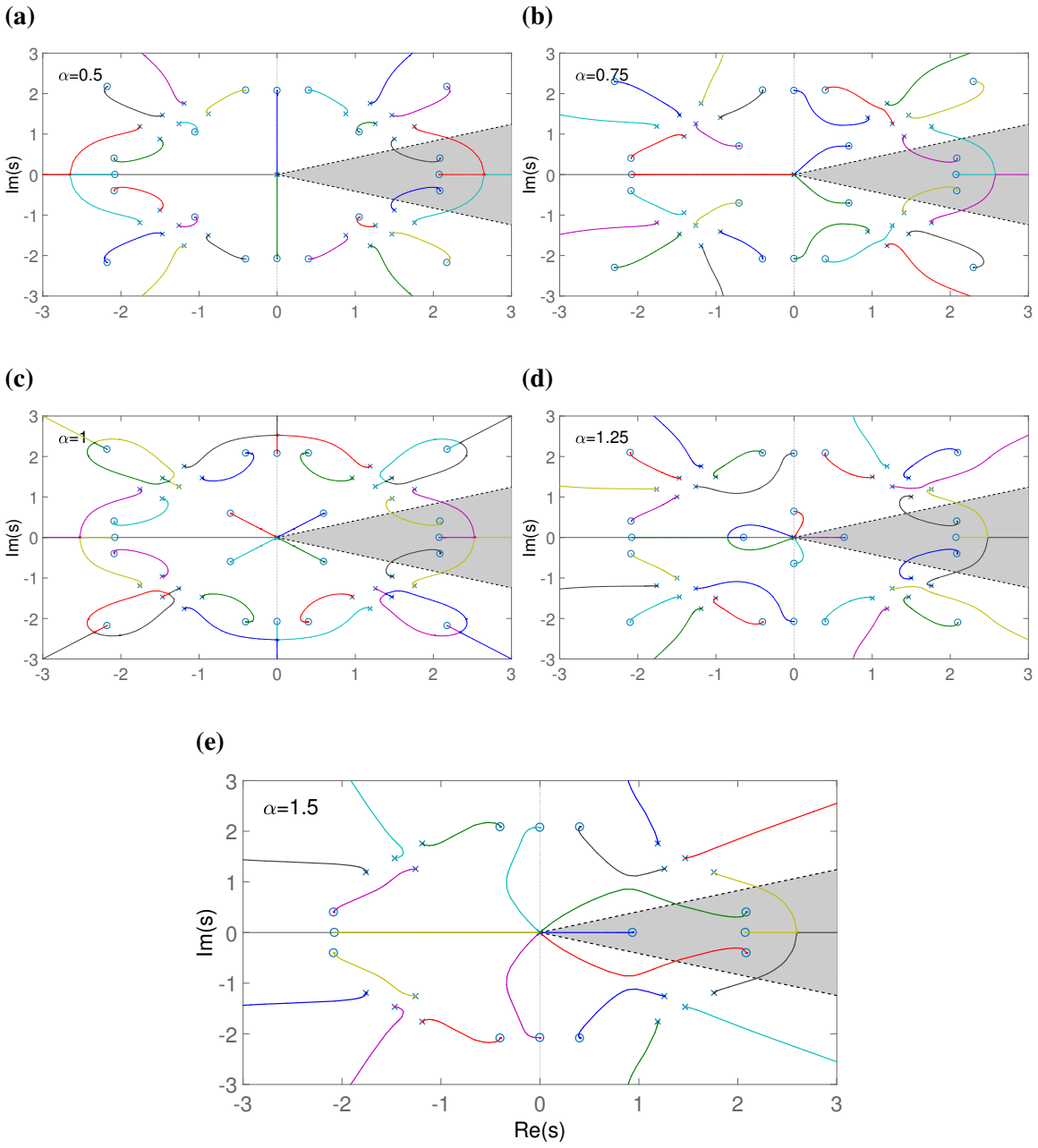

Fig. 3.26 Root locus plots for the continuous analogue of the discrete approximations for controlling plants $H_{\alpha}^{c}(s)$ with (a) $\alpha = 0.5$, (b) $\alpha = 0.75$, (c) $\alpha = 1.0$, (d) $\alpha = 1.25$ and (e) $\alpha = 1.5$. A Padé approximant of the human effective delay was included in the TF. The $\times$ symbol denotes the poles of the open-loop TF while $\circ$ marks the open-loop zeroes.

While adding an additional term to the controller could stabilise the system, this would not tell much about the characteristics of human control, which is the main topic of this research. In general, modelling the remnant has not proven to be useful, due to the variability in human response [Jür07].

Chapter 4

Biofidelic Steering Control Modelling

In this Chapter, signal processing and statistical analysis techniques are utilised over *naturalistic driving data* (NDD) (Appendix. B.2) and data from the HTE (Appendix. B.1). The obtained results lead to the formulation of a new human control model based on multiplicative dynamics. This model reproduces similar statistical properties to those found in the control actions of humans – in compensatory and pursuit tracking tasks. Further, from the proposed human-control model, an original human-centred driver model – for steering control in ground vehicles – is designed. The input variables of this model are justified with NDD, and additional data recorded from specific experiments in a vehicle simulation (Appendix. B.3).

The chapter is organised as follows. Section 4.1 presents background knowledge related to steering control modelling. Signal analysis of the NDD signals is performed in Sec. 4.2; this analysis has been published in a journal paper [MGZG16]. The multiplicative human-control model is in Sec. 4.3, and was first given in a published conference paper [MGG17]. In Sec. 4.4 several aspects of visual acquisition related to driving will be studied, through experiments recorded with test subjects in an OpenGL 3D simulation. The chapter ends with the proposal of a human-centred driver model (Sec. 4.5).

4.1 Background on Steering Control Models

The problem of formulating steering control laws that autonomously steer a car has been studied for more than 60 years. Researchers have often borrowed concepts from the human-machine systems literature (Sec. 2.2) and adapted them to this particular application. In the same way, human-machine system modellers have made use of a number of techniques corresponding to control systems theory. Thus for example, from linear control laws the first steering control models are inspired [Jür07].

Although there has been success in designing models that are able to steer a car in an efficient way from a performance viewpoint, often it is not clear if these models represent driving in a biofidelic manner, or if they merely act as *steering automaton*, lacking many of the human driving characteristics such as anticipation, memory, workload balance, response and perceptual thresholds, switching attention, driver distraction, adaptation and stochastic components.

One of the first linear models which make use of preview is that produced by Kondo in 1953 [PE07]. Kondo's model works by applying proportional control over a prediction of the lateral offset of the vehicle (y_p) with respect to the centre of the road, which is expressed by the following relation:

$$y_p(t) = y(t) + T_p U \psi_c(t), \tag{4.1}$$

where $y(t)$ is the lateral offset at time t, U the vehicle velocity, T_p the preview time and $\psi_c(t)$ the heading-relative bearing with respect to the tangent of the road path – on a straight path it coincides with the heading of the vehicle with respect to a global reference frame ($\psi_c = \psi$). Equation (4.1) can be interpreted as a linearisation of $y_p(t) = y(t) + T_p U \sin\{\psi_c(t)\}$.

Kondo's model is one of the first models introducing the notion of preview of the forward scene. Different modifications of this model exist in the literature [PE07].

Another class of linear steering control models includes those based on the quasi-linear modelling approach (Sec. 2.3.2). For example, in [WM70, MK74] it is proposed the control law

$$\mathcal{H}_L(s) = K \frac{T_L s + 1}{(T_I s + 1)(\tau_N s + 1)} e^{-(\tau_P + \tau_C)s} \approx K \frac{T_L s + 1}{T_I s + 1} e^{-(\tau_P + \tau_C + \tau_N)s}, \tag{4.2}$$

where K is the control gain. T_L and T_I are constants adjusted according to the controlled plant, while τ_P, τ_C and τ_N are described in Section 2.4.1. Thus the term $1/\tau_N s+1$ represents muscle latency lags and $e^{-(\tau_P+\tau_C)s}$ the pure delay of the human driver. The control law in (4.2) has been tested under different types of input error, but only with simple transfer functions – such as K, K/s and K/s^2 – representing the controlled vehicle [WM70]. Likewise, several different variations of (4.2) exist in the literature[1], for example its extension including multi-loop feedback [MWJ+75].

Another variant of quasi-linear models is the CO model itself (Sec. 2.3.2), possessing the advantage that it reproduces human-adaptation to a plant accurately, but with the disadvantage that this is only true near the crossover frequency. The CO model fails specially for frequencies lower than ω_c, where actually most of the human driving occurs [Mac03].

[1] In truth, the model in (4.2) is a simplification of the *precision model*, in which the dynamics of the neuromuscular lag are represented with higher order dynamics [MK74].

A breakthrough in driver modelling was materialised in the seminal paper by Donges [Don78], for this is the first paper which considers that the human driver utilises a combination of feed-forward and feedback while controlling a ground vehicle[2]. It has already been mentioned that human control displays open-loop and closed-loop characteristics (Sec. 3.2), and this concept will be more lengthily discussed in Sec. 4.2.3. In Donges paper, the feed-forward component of the model – which is referred to as *guidance level control* – is a steering angle response resulting from applying difference equations to the curvature of the road. The feedback or compensatory control of the model is a law based on curvature, vehicle heading and lateral offset deviation. Both components of the model – open-loop and closed-loop – act as a linear combination that controls the lateral dynamics of the vehicle. The parameters of Donges model were fitted from data collected in a driving simulator, and were showed to vary according to vehicle speed in the same paper [Don78].

In Section 2.3.5, optimal control models for human-control modelling were discussed. The optimal control approach has also been applied to the particular case of steering control. An example is found in [Mac81], where the human driver is assumed to act as a linear optimal controller after a certain response delay. This model is designed to minimise the integral of the predicted lateral offset:

$$J = \frac{1}{T_p} \int_{t}^{t+T_p} \{[y_d(\eta) - y(t)]\, W(\eta - t)\}^2 \, d\eta, \tag{4.3}$$

according to a desired lateral offset y_d and a weighting function W. More recent approaches of the optimal control method include [Pro01], where a path optimisation problem is proposed, [SBM+16] where attention switching is included to the controller and [KdWA17], where risk assessment of the corresponding manoeuvre is implemented into the optimisation process through a risk parameter.

As stated (Sec. 2.3.5), the main disadvantages of optimal control models are that they require an internal model of the controlled plant, and that a cost function that represents human behaviour may be near impossible to determine; any chosen cost function may not be an invariant of the problem at hand. Additionally, optimal control models result in convoluted mathematical formulations. This viewpoint was raised in [Bes12], where a very simple model was proposed based on modifying the steering angle according to the predicted lateral deviation at a preview point. Nevertheless, some simulation software packages rely on optimal control methods in their incorporated driver models [PE07]. On the other hand, while classical control models – like the CO model – can achieve similar control characteristics to

[2] Although feed-forward paths had already been considered for the case of human-machine systems [MJ67].

those of the human-operator, it is not clear how this is achieved; many control models do not incorporate any *behavioural assumptions* [JF03].

Another approach that has led to a different class of models is that of human cognition modelling. Although there is not a widely accepted framework of how human cognition works, different theories have been proposed. One of them is the ACT-R (Adaptive Control of Thought – Rational) framework, which operates through different specified behavioural rules. The ACT-R model contains a *stack* with goals and sub-goals to be achieved, and it may generate new goals autonomously, whenever these are required to complete the pre-determined goals. ACT-R models have been adapted to driving in [CG07]. In this publication, some of the designed goals are: steering angle update, road scene monitoring and lane changing. One of the advantages of the ACT-R framework is that it can represent attention switching in a natural way. But as stated, it relies on assumptions regarding human cognition that are not globally accepted by all researchers, and it does not produce simple models which can be analysed mathematically. It seems that this methodology can be more useful for integrating different models representing motor control, visual acquisition and adaptation into a unified structure.

From the perspective of modelling driver behaviour, one fundamental question is: which are the road distinctive attributes, or which are the regions of the road ahead, from which the driver extracts the most significant information? Early experiments performed more than fifty years ago on test-tracks [KA68], showed that visual information acquired at a particular sighting distance is of special importance for human lane keeping on straight roads. Later literature [Don78, LH95], advocated that drivers typically use information from *near* and *far* regions of the road relative to the current position of the vehicle, to produce a suitable steering wheel action. These considerations are the basis of the class of driver models which employ multiple preview points as input.

A very well known example of a multiple preview driver model is the Salvucci and Gray (SG) model in [SG04], where a classical controller is proposed based on two preview points – representing the near and far regions of the road respectively. Besides considering multiple road region information, the SG model regards the human-driver as a discrete controller (see Section 2.3.3). This model will be discussed in detail in Section 4.2.1. Another example is the linear control approach presented in [SCS00]. This model employs different preview sample values, which are the predicted lateral offsets according to a desired ideal path.

Another consideration, when modelling the human driver, is that humans present delays and *indifference thresholds* in perception and response, and therefore are not linear actuators (see Section 2.4); for example, human delays are dependent on the magnitude of the stimulus and its duration [Mac03]. Although most driver models in the literature are linear, several

non-linear models exist too. For instance, the linear model considered by Sharp [SCS00] was converted to a non-linear model in the same publication, by adding saturation functions to the perceived visual cues. Other examples are a non-linear version of the CO model [Gor09] and *fuzzy controllers* [SN85, NGGDP08]. Fuzzy control resembles human cognition in some aspects; humans combine information from different sources and use flexible and varying thresholds, instead of classical variables. The main difficulty with fuzzy control systems – when trying to model human behaviour – is the arbitrarity in setting up appropriate fuzzy rules. Further, human behaviour is not necessarily characterised by rules which can be verbally expressed – i.e., declarative knowledge. Human behaviour may obey pre-learned procedural patterns of action (Sec. 3.5.1). Hence, fuzzy control models may be more consistent in applications where decision making is involved, such as lane changing or overtaking vehicles [NGGDP08] than merely in steering control.

Models can also be classified by the type of input variables they employ. These variables can be *engineering variables* which are magnitudes expressed in term of physics variables, and may not be directly accessible to the driver, or *optical variables*, i.e., variables visually accessible to the driver. Some examples of engineering variables are the lateral offset – and its derivatives – and estimated angular measurements, such as non-perceived angles and the yaw rate of the vehicle. Particular cases of engineering variables in vehicle models are y_p in (4.1) and the input variables in the SG model.

Optical variables have been more widely used for aircraft control than for ground vehicle control [GM76]. One example of optical variable is the focus of expansion (FOE) produced by the relative motion of the forward scene [BL96], also referred to as *focus of outflow* [WH$^+$88].

Further approaches in driver modelling have made use of artificial intelligence techniques such as shallow neural networks [MJ96] and deep learning [HWT$^+$15] to achieve human-level performance control. But, as with optimal control methods, such *black box* approaches do not provide much insight or information about the characteristics of human control. And in all the cited cases, the model adopts objective engineering variables as input.

In reality, no driver model can reproduce all the principles of operation of the human-operator. Human behaviour is very variable and therefore difficult to replicate with deterministic models. Nonetheless, from the reviewed literature and the analysis performed in Chapter 3, a list of the characteristics that are desirable in human-control models is here proposed. Human-control – and steering-control – models should satisfy at least several of the following attributes:

1. *Discrete time:* as humans seem to behave as discrete servomechanisms (Sec. 2.3.3).

2. *Hybrid (open-closed loop):* there is evidence that humans use a combination of feed-forward and feedback in control tasks (Sec. 4.2.3).

3. *Threshold based:* as humans present perceptual and indifference thresholds (Sec. 2.3.3).

4. *Non-linear:* human response can not be fully characterised by linear models (Sec. 3.5.1)

5. *Based on optical-variables:* there is no reason to believe that human perception employs engineering variables instead of perceived optical variables – this will be studied in Section 4.4.

6. *Independent of an internal model:* human behaviour is highly adaptive to new controlled dynamics (Sec. 2.1.3 and 3.4.2).

7. *Stochastic:* humans present stochastic properties such as variable delays. A human-operator model should at least reproduce these properties statistically.

8. *Memory characteristics:* The model should represent system memory (Chap. 3).

9. *Simple:* A human steering model should be computationally simple in order to be used as an analysis tool. This is also important because, the effectiveness of the model has to be based on its design, and not on the flexibility given by an unreasonably large number of parameters.

4.2 Data Analysis of NDD

4.2.1 Salvucci and Gray Model

Driver behaviour literature [Don78, LH95], advocates that drivers typically use visual information from the *near* and *far* regions of the road relative to the vehicle, to produce a suitable steering wheel action. The Salvucci and Gray model (SG) [SG04], simplifies the notions of *near* and *far* road regions with a near and a far point at fixed previewed distances – situated at the centre of the road. According to the SG model, the driver makes two types of corrections, one to keep the vehicle within the lane edges, according to the heading-relative bearing of the vehicle to the near point (θ_n), and the other to accommodate the trajectory of the vehicle to the road geometry, by using the same measure with respect to the far point (θ_f).

The SG model is analysed in this Section with NDD, where only roads which are essentially straight are examined[3]. The SG control law is expressed by the relation:

$$\dot{\delta}_f = K_f \dot{\theta}_f + K_n \dot{\theta}_n + K_i \theta_n \tag{4.4}$$

where δ_f is the steering angle at the front wheels.

This approach, while explaining some qualities of human lane-keeping, has some limitations. The control law (4.4) responds to the errors in a continuous manner. Additionally, it reacts simultaneously to information from the near and the far regions of the road. Another important remark is that the controller is linear.

Parameter Fitting of the SG Model with NDD

For parameter fitting, the discrete version of equation (4.4) is considered [SG04]:

$$\Delta\delta_f = K_f \Delta\theta_f + K_n \Delta\theta_n + K_i \theta_n \Delta T \tag{4.5}$$

where $\Delta T = 0.1\,\mathrm{s}$ is chosen to match the sampling rate of the driving data. The discrete version provides a time base for representing discrete control actions (Sec. 2.3.3).

To fit the parameters, all the recorded driving events (Appendix B.2) were sliced in segments 2 s long. For each segment , the parameters K_f, K_n and K_i were fitted using the Moore-Penrose pseudo-inverse matrix, obtaining a distribution of fitted parameters. So for each slice, from

$$\begin{bmatrix} \Delta\delta_{f,1} \\ \Delta\delta_{f,2} \\ \vdots \\ \Delta\delta_{f,20} \end{bmatrix} = \begin{bmatrix} \Delta\theta_{f,1} & \Delta\theta_{n,1} & \Delta T\,\theta_{n,1} \\ \Delta\theta_{f,2} & \Delta\theta_{n,2} & \Delta T\,\theta_{n,2} \\ \vdots & \vdots & \vdots \\ \Delta\theta_{f,20} & \Delta\theta_{n,20} & \Delta T\,\theta_{n,20} \end{bmatrix} \cdot \begin{bmatrix} K_f \\ K_n \\ K_i \end{bmatrix} := M_\Theta \cdot \begin{bmatrix} K_f \\ K_n \\ K_i \end{bmatrix} \tag{4.6}$$

the pseudo-inverse of M_Θ is computed (M_θ^+) and the parameters obtained:

$$\begin{bmatrix} K_f \\ K_n \\ K_i \end{bmatrix} = M_\Theta^+ \cdot \begin{bmatrix} \Delta\delta_{f,1} \\ \Delta\delta_{f,2} \\ \vdots \\ \Delta\delta_{f,20} \end{bmatrix} \tag{4.7}$$

[3]The road segments in the NDD generally had a radius of curvature $> 500\,\mathrm{m}$ (see Appendix B.2).

In the present analysis, the near and far preview point distances are chosen to be $d_n = 6\,\text{m}$, $d_f = 30\,\text{m}$ respectively. These values were found to overall produce a higher clustering density in the parameter distribution (Fig. 4.1). The segment duration of 2 s was chosen according to this same criterion. Considering that we are representing a human control system and that parameter identification in closed-loop is well known to be prone to dispersion – due to actions related to disturbance rejection – the clustering density of the distribution of the fitted parameters appears to be very high – Fig. 4.1 first column.

The distribution of parameters suggests that it can be fitted by a three dimensional Gaussian model which yields mean values $K_f = 1.0826$, $K_n = -0.2228$ and $K_i = 0.0415$ – Fig. 4.1 second column. The distribution shows that the sign of K_i is ill-defined and K_n has clearly a negative sign. Thus, as the parameter fitting seems consistent, it suggests that there is a flaw not in the identification of the parameters but in the model itself.

The most likely reasons for this are: the pulse like nonlinear nature of steering signals, and the evidence that the CNS operates on a combination of feedback and feed-forward control.

The eigenvalues of the SG model, working in closed-loop with the vehicle model in Eq. 3.14, according the the fitted parameters are: $(-0.078 \pm 1.082i,\ -0.357,\ 0.065 \pm 0.225i)$. The eigenvalues correspond to the states: lateral offset y, lateral speed $\dot{y}$, yaw-angle ψ, yaw-rate $\dot{\psi}$ and steering angle δ_f. Thus the system is unstable with the fitted parameters from NDD; one pair of eigenvalues are complex conjugates with positive real part. This suggests that this model does not fully characterise the way in which humans perform steering control.

4.2.2 Identification of Natural Pulses in NDD

Steering signals obtained from NDD do indicate that steering actions consist of a series of relatively short pulse-like corrections rather than smooth, linear and continuous steering motion. It has been verified [Mor81] that hand movement in reaching behaviour follows a bell-shaped pattern over time. As a consequence, it has been hypothesised that motor movements are composed by combining different motor primitives [ABM82]. In [BM14a] it is shown that steering corrections can be fitted by Gaussian functions and that they can be described by superposition of symmetric motor primitives. Thus a possibility in driver modelling is to explicitly include such motor primitives into the controller design. In [GS14], a model of steering control which considers such motor primitives was introduced.

Here it is conjectured that the steering angle signal of a driver can be described as a combination of a *ramp function*, required when taking a curve, a *bump function*, which changes the heading of the vehicle, and a *ripple function*, which brings about a lateral offset shift (Fig 4.2a).

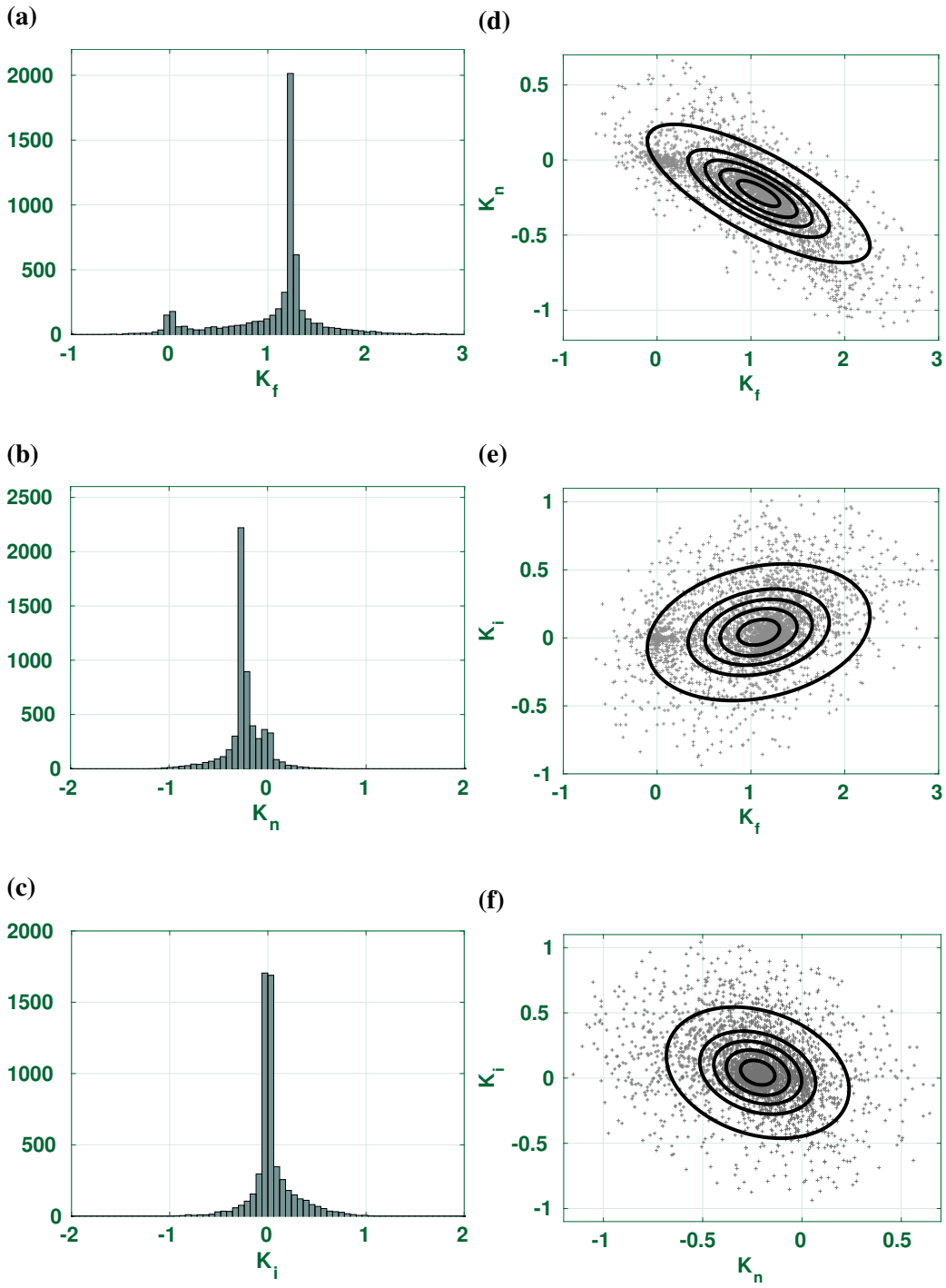

Fig. 4.1 Subfigures (a), (b), (c): Distribution of each of the fitted parameters K_f, K_n, K_i. Subfigures (d), (e), (f): Projections for each parameter pair with the fitted Gaussian model contour lines. The outer ellipses enclose a confidence region of 95%.

The normalised pulses (*ramp* δ_1, *bump* δ_2 and *ripple* δ_3) can be described analytically according to the haversine function:

$$\begin{cases} \delta_1(t,T_a) = 1/2 \cdot \{1-\cos(\frac{\pi}{T_a}t)\} & \text{if } 0 < t < T_a \\ \\ 1 & \text{otherwise} \end{cases} \tag{4.8}$$

$$\begin{cases} \delta_2(t,T_a) = 1/2 \cdot \{1-\cos(\frac{2\pi}{T_a}t)\} & \text{if } 0 < t < T_a \\ \\ 0 & \text{otherwise} \end{cases} \tag{4.9}$$

$$\begin{cases} \delta_3(t,T_a) = 4/(3\sqrt{3}) \cdot \sin(\frac{2\pi}{T_a}t) \cdot \delta_2(t,T_a) & \text{if } 0 < t < T_a \\ \\ 0 & \text{otherwise} \end{cases} \tag{4.10}$$

where T_a is the activation time span of the pulse or pulse duration.

These signals are here referred to as *elementary steering pulses*, and any superposition of them as a *complex steering pulse*. It is shown that steering angle signals, recorded from driver in real road conditions, can be constructed as a sparse representation of *complex steering pulses*, and that the *complex steering pulses* found in real data are linear combinations of the same *elementary steering pulses*. To extract the *elementary steering pulses* from the NDD we will apply an unsupervised feature extraction method: singular value decomposition (SVD) [KL80]. This technique has the advantage of extracting the natural pulses from the data without any prior assumption about the pulse shapes – unsupervised learning. However, it does not provide a suitably sparse representation. The data show that the nature of the steering signal pulses is sparse in human lane keeping control. Once the pulses are identified, a matching pursuit dictionary [MZ93] is built with them. The matching pursuit algorithm will reconstruct the signal as a sparse superposition of the elements in the dictionary.

The adopted approach is to slice each signal into sub-samples of 1 s of duration – since it is verified that for human lane keeping pulses shorter than 1 s are typical. From the slices, a two-dimensional matrix M is built:

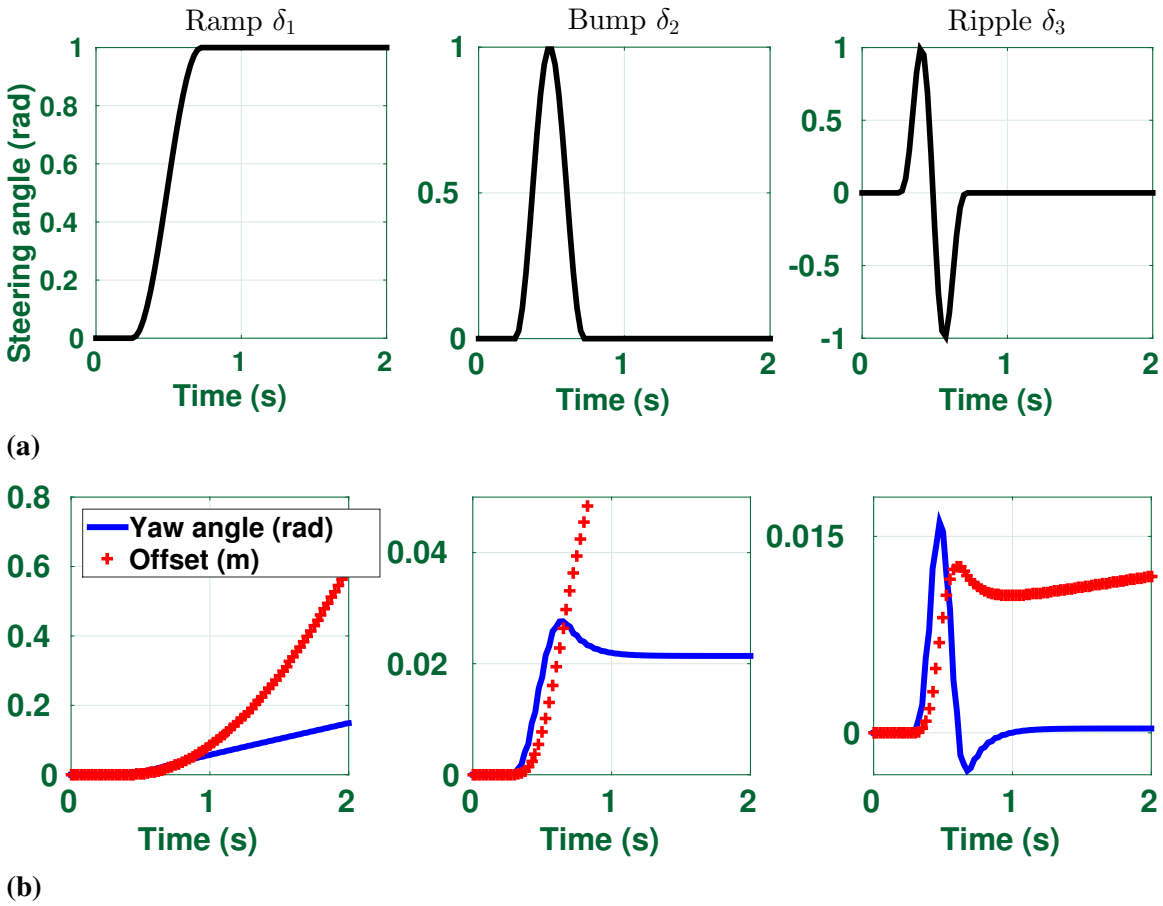

Fig. 4.2 Row (a): Simulated examples of normalised *ramp function*, *bump function* and *ripple function* with $T_a = 0.5\,\mathrm{s}$ of activation each. Row (b): Responses for each of the simulated pulses. The dashed line shows the yaw angle in radians while the sign markers show the offset from the centre of the road in meters.

$$M = \begin{bmatrix} \delta_{f,1} & \delta_{f,11} \dots \delta_{f,591} \\ \delta_{f,2} & \delta_{f,12} \dots \delta_{f,592} \\ \vdots & \\ \delta_{f,10} & \delta_{f,20} \dots \delta_{f,600} \end{bmatrix} \tag{4.11}$$

where the steering angle δ_f was sampled at 0.1 Hz, and principal component analysis SVD [KL80] is employed over M.

The results are found to be very similar for all the driving events, and for a chosen driving event they are displayed in Fig. 4.3. The most dominant mode is a flat curve, containing 84% of the energy of the signal. This flat curve is responsible of dealing with the geometry of the road (compare 4.3a with 4.3c and 4.3d) and is the only pulse that clearly has a constant

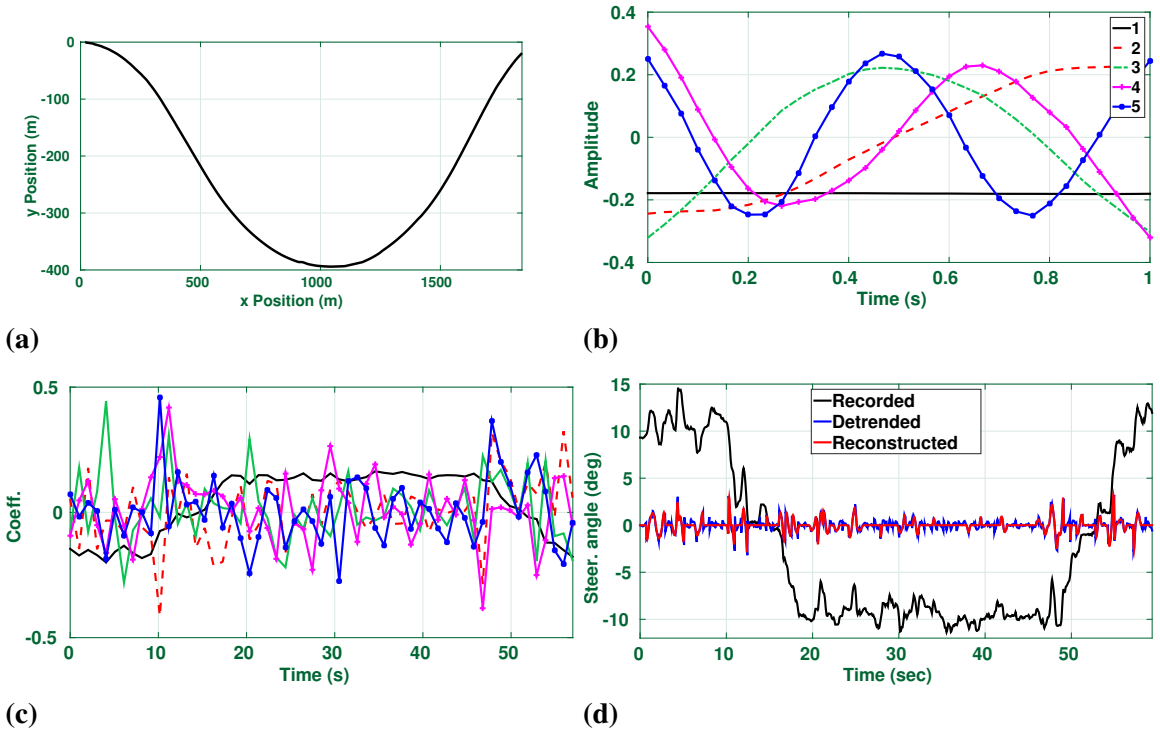

Fig. 4.3 (a): Road geometry for one chosen experimental driving event (event 30 of driver A). (b): The five dominant modes of the steering signal analysed in 1 s slices. (c): Time history of the linear combinations to describe the signals with the modes. (d): Recorded steering signal for the given driving event, along with the detrended version and the reconstruction through matching pursuit – using 60 pulses.

offset in amplitude (4.3b). The flat curve is followed by a *ramp*, a *bump* and a *ripple pulse* of smaller energy content. These three are the steering primitives or *elementary steering pulses* above hypothesised.

The given analyses also suggests a way to detrend the data, as the main interest is to describe human lane keeping, and not how humans follow a particular road geometry. From the SVD output (matrices U, Σ, V such that $U\Sigma V^\top = M$), the rows and columns corresponding to the first mode (flat curve) are eliminated (reduced $\hat{U}, \hat{\Sigma}, \hat{V}$), obtaining a detrended signal with almost no road geometry content ($\hat{M}$ such that $\hat{M} = \hat{U}\hat{\Sigma}\hat{V}^\top$). Thus it is possible to preserve the frequency and amplitude of the pulses for posterior analysis (Fig. 4.3d). After detrending, the relative energies of the *ramp*, *bump* and *ripple* are 48%, 22% and 10% respectively. So the three main modes account for 80% of the energy of the detrended signal.

Pulse Duration

Regarding the question of what is the typical pulse activation span time (T_a) of a human driver, the possibility of these pulses to be asymmetrical is contemplated. In previous literature, symmetrical pulses were already considered [BM14a].

As we are analysing detrended signals, essentially devoid of road geometry content, it is assumed that the *ramp* pulse has no relevance and it may only be used to shape *bumps* by joining a rising and a falling *ramp*. The *ripple* can be constructed in the same way by joining two *bumps*, so the most crucial pulse for lane keeping is the *bump*, as all pulse activity can be reconstructed by a superposition of *bumps*.

Hence, a matching pursuit dictionary of asymmetrical *bumps* is built. These have different rising and falling time – rising and falling duration from 0.05 s to 1.5 s as longer pulses were regarded as spurious and shorter as noise – and running the matching pursuit algorithm over the 200 driving events, the histogram of chosen rising and falling time is obtained (Fig. 4.4a). The matching pursuit algorithm was constrained to utilise one pulse per second on average.

The rising part tends towards a shorter duration than the falling part, the latter also displaying more variability. The distribution of the mean rising and falling time of the pulses for each driving event exhibits differences among drivers. Drivers A and B use shorter pulses, especially driver B, which is the most distinct driver compared to the others (Fig. 4.4c). For all the drivers, the relationship between rising and falling time is inverse – the quicker the driver makes the initial *ramp*, the slower they make the reverse *ramp*. We hypothesise that the rising and falling pulse duration could be used to classify different driving states, although this is not tested here.

4.2.3 Open-loop vs. Closed-loop Control

According to the above, it is proposed that the driver performs an initial response to a potential conflict, by performing a first initial quick adjustment according to an open-loop scheme – the quicker rising part of the *bump* shaped pulse. After this adjustment has been made, that due to its open-loop nature will result in a over- or under-correction, the driver will perform a falling *ramp* in closed-loop. This falling *ramp* will have a different duration depending on how good the initial open-loop guess was. Thus its length has a higher variance than the rising part. In the proposed model, the rising *ramp* will correspond to a learned pattern (pre-cognitive action [GS14]), while the falling *ramp* to a smoother adjustment relative to the current driving scenario and the magnitude of the error produced by the first *ramp*. It is expected that the more imminent the potential conflict, the faster the driver will tend to execute the first *ramp*, and the more error will occur resulting in a longer closed-loop

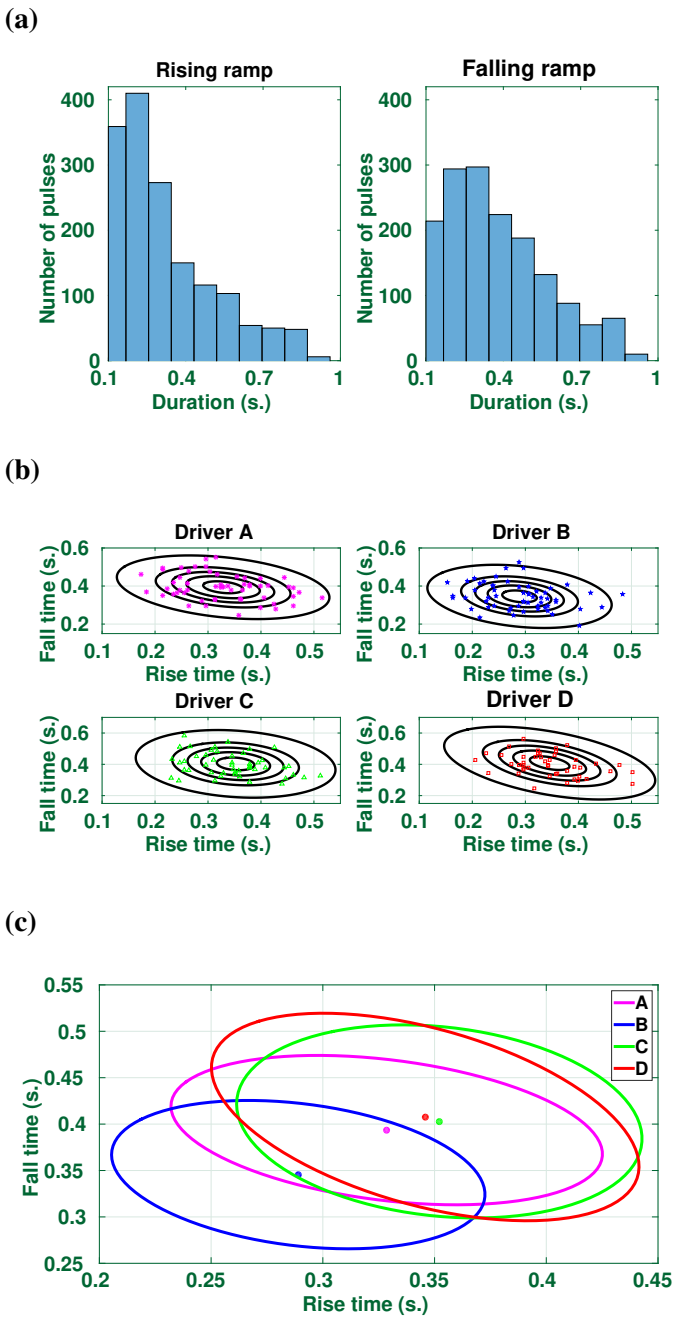

Fig. 4.4 (a) Histogram of rising and falling duration span of the *bumps* chosen by the matching pursuit algorithm over 200 driving events. (b) Distribution of the mean rising and falling duration time over the same driving events tabulated by driver. The mean values after fitting by a Gaussian distribution are: $A : (0.3286, 0.3935)$, $B : (0.2890, 0.3456)$, $C : (0.3521, 0.4029)$, $D : (0.3458, 0.4077)$. The outer ellipse corresponds to a confidence region of 95%. (c) Comparison of the ellipses for each driver that enclose a 50% confidence region and their centres.

correction. The mechanism proposed is consistent with the presented signal analysis, and also is consistent with known mechanisms of the CNS. Specifically, the process is analogous to the way in which the human eye tracks a target. It first produces a quick saccade, to make a first approach to the target, and then smaller saccades that occur $0.15 - 0.3\,\mathrm{s}$ after [JF03, YS63]. Also, experimental research has shown that the CNS uses a combination of open-loop and closed-loop control [HBDS97], and it has been found [BS99] that control only via open-loop cannot reproduce human motor behaviour. Open-loop systems are poor controllers, although they have the advantage of responding quicker.

4.2.4 The Critical Normalised Yaw-rate Metric

Regarding the question of what makes the human driver trigger a pulse, different lane keeping metrics have been defined and considered for human lane keeping, for example, the time to lane crossing (TTLC) [LU96], the yaw-rate error (YRE) [GBB$^+$09] and the near point angle in the two-point model [SG04]. Here, an alternate formulation of the YRE is defined, the *critical normalised yaw-rate* (CNYR). The CNYR is easier to correlate to pulse amplitude than the YRE, although the conceptual meaning of the metric is the same.

To define the CNYR, the *critical yaw rate* must be characterised first; the *critical yaw rate* is the yaw rate ($\dot{\psi}$) that if sustained would cause the vehicle exiting the driving lane at a given distance [GBB$^+$09]. It is expressed independently for each road boundary. For the left boundary it is given by the following relation:

$$\dot{\psi}^{\mathrm{L}}_{\mathrm{crit}} = \frac{2U \sin \phi_{\mathrm{L}}}{d_{\mathrm{L}}}, \tag{4.12}$$

where U is the velocity of the vehicle and d_L the distance from the left front tire to a predefined boundary point in the left boundary. ϕ_L is the left azimuth angle – i.e., the heading-relative bearing to the left boundary point. The right critical yaw rate ($\dot{\psi}^{\mathrm{R}}_{\mathrm{crit}}$) is equivalently defined.

From the critical yaw rate the CNYR (χ) results:

$$\chi = \frac{\dot{\psi} - 1/2\left(\dot{\psi}^{L}_{\mathrm{crit}} + \dot{\psi}^{R}_{\mathrm{crit}}\right)}{1/2\left(\dot{\psi}^{L}_{\mathrm{crit}} - \dot{\psi}^{R}_{\mathrm{crit}}\right)}. \tag{4.13}$$

The CNYR is a non-dimensional variable combining the information of both critical yaw rates – left and right. When $\dot{\psi} = \dot{\psi}^{\mathrm{L}}_{\mathrm{crit}}$ or $\dot{\psi}^{\mathrm{R}}_{\mathrm{crit}}$ then $\chi = 1$ or -1 respectively. Therefore, it suffices to maintain $|\chi| < 1$ in order to keep the vehicle within the lane boundaries at all times.

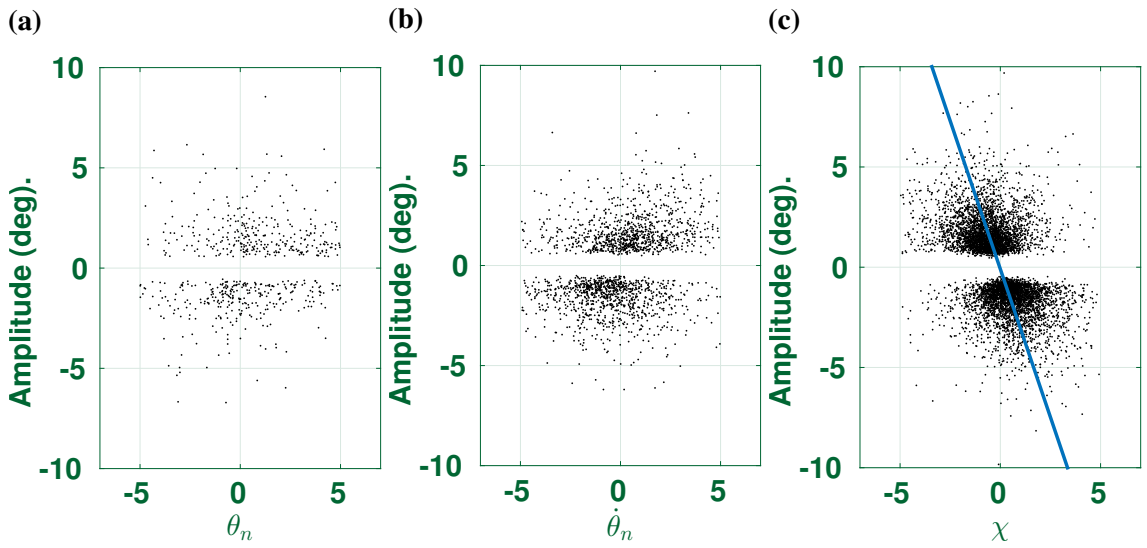

Fig. 4.5 Amplitude of the pulses against different lane keeping error metrics: (a) θ_n (b) $\dot{\theta}_n$ and (c) CNYR (χ).

In Figure 4.5 the amplitude of the pulses obtained by the matching pursuit algorithm is compared to different lane keeping error metrics. The figure is generated by plotting only the amplitude of the pulses that occur in the direction that would neutralise the corresponding error. In this manner, a more populated figure represents a higher correlation between the steering actions and a particular error measure. For the near angle (θ_n), 62% of the pulses occur in the right direction. The derivative of the near angle ($\dot{\theta}_n$) has a slightly higher correlation 65%. On the other hand, for the CNYR the percentage or corrections in the right direction is significantly higher (74%). Additionally, a weak linear correlation can be observed between the error and the response for the CNYR (Fig. 4.5c).

Furthermore, it has been mentioned that the driver may not be persistently responding to errors in a continuous way, as this will involve a high *observational workload* [GZ15] and *steering action workload*. On the other hand, the CNYR does not require constant monitoring because it can be understood as a satisficing metric. In any case, the *elementary steering pulse-*χ relationship seems to be most consistent.

4.2.5 Hybrid Control Law

According to the above considerations, a Hybrid Open-close Loop (HOCL) pulse control scheme is now defined by the relations

$$\begin{cases} \delta(t) = \bar{K} \cdot \bar{C}\left(\bar{E}(t)\right) & \text{if } R\left(\bar{E}(t)\right) \leq T_h \\ \delta(t) = K_{rb} \cdot \delta_{rb}(t - t_0, T_{rb}) \cdot F\left(\bar{E}(t)\right) & \text{otherwise} \end{cases} \tag{4.14}$$

where $\bar{K}$ is a vector of parameters, $\bar{C}$ a vector function controller (working in closed-loop, linear and continuous/discrete) that acts according to another vector function of selected errors $\bar{E}$, when these are below the threshold T_h relative to a function R. When R is above the threshold at a given time t_0, a rising *bump* δ_{rb} is performed (open-loop) of rising duration T_{rb}. For the duration of the rising *bump* $\bar{C}$ is interrupted, then the control is passed back to $\bar{C}$ until the termination of the pulse. The amplitude of δ_{rb} depends on a constant parameter K_{rb} and on the magnitude of the errors according to a function F. The HOCL control scheme also assumes a wait time T_w during which may not trigger further pulses. This is further justified by the sparsity of higher amplitude pulses, as shown in the matching pursuit reconstruction (Fig 4.3d). This control scheme is an adaptation of the model proposed in [GS14].

The HOCL scheme can also be applied with different types of *elementary steering pulse* acting on superposition. Here we consider a HOCL that triggers *elementary steering pulses* according to the right or left boundary margins which are defined as the difference between the critical yaw rate and the actual yaw rate:

$$m_R = \dot{\psi} - \dot{\psi}^R_{crit} \tag{4.15a}$$

$$m_L = \dot{\psi}^L_{crit} - \dot{\psi} \tag{4.15b}$$

and the closed-loop control is the SG model,

$$\begin{cases} \dot{\delta}(t) = K_f \dot{\theta}_f + K_n \dot{\theta}_n + K_i \theta_n & \text{if } \min(m_L, m_R) > 0 \\ \delta(t) = K_{rb} \delta_{rb}(t - t_0, T_{rb}) \cdot (m_R - m_L) & \text{otherwise.} \end{cases} \tag{4.16}$$

K_f, K_i are taken as in the above fitted parameters (Fig 4.1), and $T_{rb} = 0.3$ according to the rising time results (Fig. 4.4).

The parameters K_n – which as fitted through NDD was leading to instability – and K_{rb} are fitted using a genetic algorithm. The objective function evaluates performance based on lane keeping quality and smoothness steering: $\mathcal{P} = \frac{1}{N} \sum_{t=t_1}^{t=t_N} \left(|y_k| + C|\dot{\delta}_k| \right)$, where N is the number of time samples $t_1 \ldots t_N$, y_k is the lateral offset from the centre of the lane and $\dot{\delta}_k$

the steering rate in rad/s at each time sample. C is a constant set empirically to 100 which relates both terms in the objective function. With the given setup the optimised parameters are $K_n = 0.1105$ and $K_{rb} = 0.0119$.

The wait time T_w has been set to 0.5 s. Although this value has not been optimised, it has been observed that much longer or shorter wait times were less effective. With longer wait times the pulse control offers reduced error correction, whereas with shorter wait times the closed-loop part of the model does not have time to counterbalance the effect of the pulses. In this case the trajectory becomes too jerky, which forces the triggering of continuous pulses to rectify this, as the threshold is continuously surpassed.

In simulation, with a linear vehicle model (Eq. 3.14), the above implementation of HOCL model performs better than the SG model with the fitted parameters from NDD. Running the SG model and (4.16) in the road geometry of the same driving event as in Fig. 4.3, it is shown that SG model becomes unstable after about half of the event has been covered (Fig. 4.6a). The hybrid model, although presenting a jerky spot at the same point where SG model becomes unstable, is able to recover the stability and proceed to the end of the event within the lane boundaries (Fig. 4.6b). Testing also the HOCL on a straight track with an initial lane offset of 3 m to the left, the simulations show that the vehicle is able to neutralise the offset and stabilise at the centre of the lane (Fig. 4.6b). The SG model was also tested in a straight track, and even without initial offset the noise in the simulation was enough to destabilise it, and thus not presented in the figure.

Nevertheless, although the HOCL control law is the first steering control model proposed here, this approach involves the introduction of several artificial parameters, which have proven difficult to fit as they tend to produce non-sparse steering angle signals. In the next sections, a new modelling approach with a simple formulation, and that produces pulsing behaviour in a natural way, will be developed.

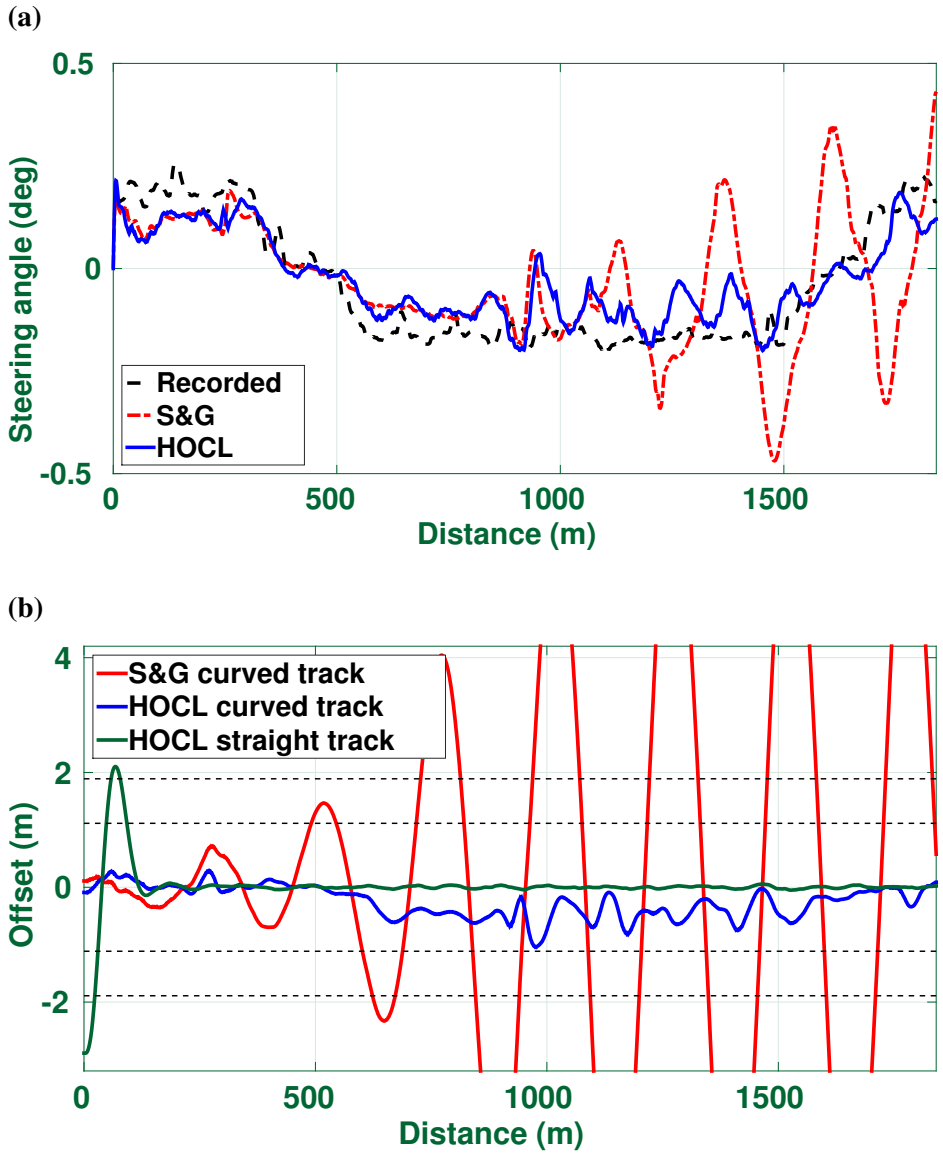

Fig. 4.6 (a) Recorded steering signal for driving event 30 of driver A, along with the steering signals of SG model and the HOCL example (4.16) (b) Lane offset from the centre of the road for the HOCL example in the curved geometry of the same driving event, and on a straight track with an initial offset of 3 m. Negative offsets are to the left and positive offsets to the right. The outer margins are the lane boundaries, while the inner margins mark when the wheels of the vehicle reach to the lane boundaries.

4.3 A Multiplicative Model of Steering Control

Nearly every human-control model incorporates a series of parameters, which not always have physiological interpretation. Usually, with the intention of reproducing the control actions of the human-operator as close as possible, the parameters are adjusted to match the responses of human subjects. This approach, while not incorrect, has one inconvenience: often it is difficult to tell to which extent an accurate model representation is the result of a good model, or of the optimisation procedure to fit its parameters. This is especially true for models with many parameters. The most pre-eminent example is the use of neural networks to model the human [MKS+15]; neural networks can be used to model virtually any dynamical system. Although in many respects these models are very valuable, they do not produce insights on the characteristics of human-control. Furthermore, different subjects may use diverse control strategies that not necessary match the same model. At the same time, for sufficiently complex systems, alternative interpretations can explain the same observed effects.

Hence, when trying to fit the parameters of a deterministic model to data recorded from humans – for example steering signals – multiple caveats make the process difficult, even when the model is representative of human behaviour. With respect to the specific case of modelling the human driver, some of these caveats are:

- Data recorded from humans drivers are very noisy.
- The computation of engineering and optical variables estimates from the recorded driving data may add bias and more noise. In general, variables such as the CNYR or the vehicle lateral offset are not recorded, unless the experiments were conducted with a simulator.
- Human drivers have stochastic components in their response, for example due to variable time delays, which depend on the driver level of attention and intended performance.
- Human drivers may establish varying acceptable error thresholds – according to the desired level of comfort and smoothness of driving, stress or time constraints.
- Usually there is large variability among different human subjects. So even a well-posed biofidelic model may result in overfitting the data, depending on the optimisation process used.
- A model based on a superposition of terms may create local minima in the optimisation process; one parameter may achieve unreasonable values just to compensate

another. This is what may have happened when fitting the parameters of the SG model (Sec. 4.2.1), where a negative parameter was obtained.

In order to avoid some of these obstacles, a statistical approach to biofidelic modelling is here introduced. The approach consists in considering a model to be biofidelic when it reproduces some of the statistical properties of the human-operator in a particular task. The intended goal is to organise the observed results into a model that is as simple as possible. In particular, the log-normal probability distribution is considered, which arises from multiplicative processes.

4.3.1 Log-normal Distributions and Multiplicative Dynamics

A factor of motivational value for this research is that, recent and relevant studies in neuroscience, have shown that several aspects regarding the dynamics of the brain are characterised by long-tailed probability distributions such as the log-normal. One example is the distribution of firing rates in cortical neurons; log-normal distributions yield the best fit for the distribution of neuron firing rates in the cortex [WHM13]. Another example is the activity of neurons in the lower spine of turtles while engaging in rhythmic scratching; this appears to be also distributed according to a log-normal [PB16]. And interestingly, in [GBS99] it is shown that, visual perceptual learning can be described as a process in which the human observer reduces the magnitude of *internal multiplicative noise*. Additionally, in [BM14b], it is suggested that complex interconnected biological systems produce multiplicative and not additive interactions.

So the possibility of steering wheel control in a tracking task to be characterised by a log-normal distribution is considered. Given that the log-normal distribution arises as a result of multiplicative processes, a multiplicative human-control model is proposed.

The derivation of the model starts with a brief outline of log-normal probability distributions. Consider a multiplicative process of the form

$$G_{t_k} = \xi_{t_k} G_{t_{k-1}} = G_{t_0} \prod_{i=t_1}^{t_k} \xi_i, \tag{4.17}$$

where $(t_i, t_{i+1}) \subset \mathbb{R}^+ \cup \{0\}$ are equispaced time intervals and $G_{t_0} > 0$, $\xi_i > 0$. Taking natural logarithms in (4.17) results in

$$\log G_{t_k} = \log G_{t_0} + \sum_{i=t_1}^{t_k} \log \xi_i. \tag{4.18}$$

If ξ_i are identically distributed and independent random variables, the Central Limit Theorem (CLT) applies to the summation term of (4.18) and, for large enough k, $\log G_{t_k}$ will be approximately normally distributed. Therefore, G_{t_k} will follow approximately a log-normal distribution.

As a reminder, a random variable X, whose logarithm has expected value $E[\log(X)] = \mu$ and variance $E[(\log(X) - \mu)^2] = \sigma^2$, is said to be log-normally distributed when its probability density function (PDF) is[4]:

$$f_X(x) = \frac{1}{x\sqrt{2\pi\sigma^2}} e^{-\frac{(\log(x)-\mu)^2}{2\sigma^2}}. \tag{4.19}$$

In general, the discrete observations of a time series (ξ_i) are not independent, unless the series is a Markov process. However, an alternate formulation of the CLT that applies for the analysis of arbitrary time series can be employed [HR+48].

Definition 4.3.1 (m-dependent random variables) *A sequence of random variables X_i for $i = 1 \ldots N$ is said to be m-dependent when $|i - j| > m$ implies that X_i and X_j are independent. If the sequence $\{X_i\}_{i=1\ldots N}$ is understood as a time series, m-dependence means that events occurring at least m time steps away are independent.*

Theorem 4.3.1 (Central Limit Theorem for m-dependent random variables) *If X_i is a sequence of m-dependent random variables with expected value $E[X_i] = 0$ and $E[|X_i|^3] < \infty$, then*

$$Y_\infty = \lim_{N\to\infty} N^{-1/2} \sum_{i=1}^{N} X_i \tag{4.20}$$

is normally distributed with $E[Y_\infty] = 0$ [5]. In particular, for large N, $Y_N = \sum_{i=1}^{N} X_i$ approximates a normal distribution with zero expected value.

This result is more a technical requirement than a limitation. In practice, a given time series – predicted to arise from a multiplicative process – is fitted to a log-normal probability distribution after under-sampling the series with different values of m. If the results are equivalent for $m \geq \hat{m}$, the original time series can be considered $\tilde{m}$-dependent; the under-sampled time series can then be treated as a Markov process.

[4] As the log-normal is a probability distribution of maximum entropy, the presented approach is equivalent to introducing the least possible number of constraints. In this research, the human-operator is modelled based on partial information; only data from recordings of operator's responses in a control task are used. It is considered that almost no knowledge about the features of human-control is known; in reality this turns out to be the case. Thus the methodology is consistent with the Principle of Maximum Entropy [Jay57].

[5] There is also an expression for the variance of Y_∞ in [HR+48].

4.3.2 Statistical Analysis of the HTE Dataset

The uncertainty in the response of a human-operator to an input, is a challenge when trying to identify the operator as a deterministic actuator. The exact input to which the operator responds is itself generally unknown. Hence, the possibility of characterising the responses of the human-operator in a probabilistic manner is examined.

By analysing the magnitude of the human responses ($|c(t)|$) to the displayed error in the HTE dataset[6] (Appendix. B.1), empirically one sees that it has the shape of a skewed distribution (Fig. 4.7a). To visualise the data, the steering responses of all the ten subjects were combined, after being under-sampled to a sampling rate of 1 Hz. This was done in order to confirm that the series is m-dependent (Def. 4.3.1). For $m > 100$ no appreciable differences were observed visually or numerically in the results. Additionally, values such that $|c(t)| < 0.02$ were discarded. This threshold was set because no evident pattern was found in the data for smaller magnitudes, and because the log-normal is defined over a positive support.

The parameters of the log-normal distribution were fitted to the data through maximum likelihood estimation. Subsequently, a goodness-of-fit test was performed – which is described in Appendix C – from which a p value of 0.317 is obtained. Thus the log-normal distribution is accepted to be representative of the data ($p > 0.1$, see Appendix C).

Between the individual subjects the fitted parameters present some variability (Table 4.1), although the values are comparable; since different subjects employ different control strategies and have different skill levels, this was not considered surprising.

Thus the statistical analysis indicates that, the magnitude of the control responses over a threshold, can be explained as a process distributed according to a log-normal. This result induces the possibility of modelling the human-operator responses as a multiplicative process (Eq. 4.17).

4.3.3 Multiplicative Human-control (MHC) Model

A non-linear multiplicative human-control (MHC) model is now proposed. In the MHC model, the control response $C_M(t_k)$, according to a time discretisation $t_1, t_2, \ldots, t_k, \ldots, t_f$ with fixed time-step $\Delta_t = t_k - t_{k-1}$, is defined as

$$C_M(t_k) \equiv K_M S_{t_k} M_{t_k}, \tag{4.21}$$

[6]For this application, only the data recorded with the steering wheel and non-fractional dynamics were considered.

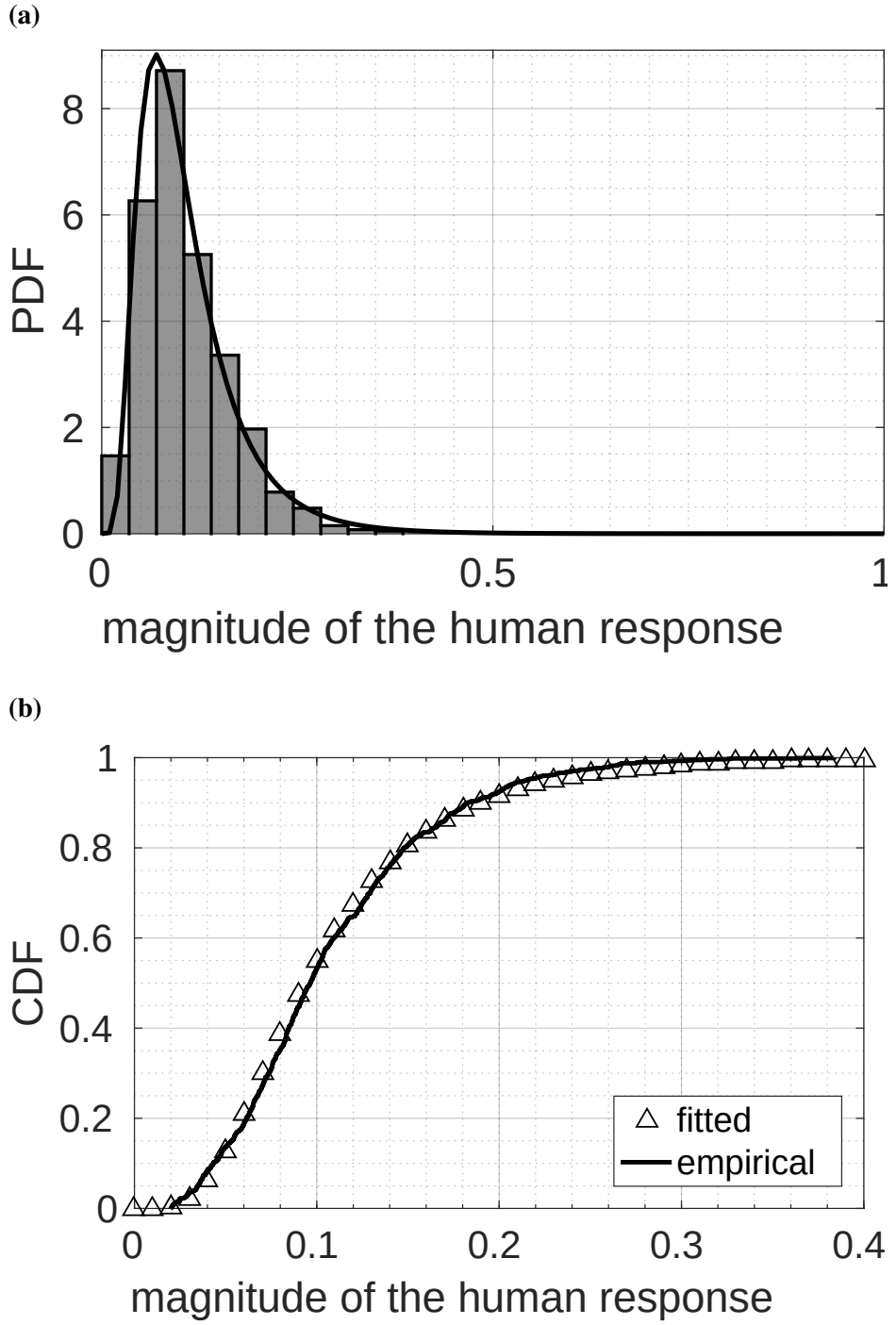

Fig. 4.7 (a) Normalised histogram for the experimental responses of all the subjects combined – recorded from the steering wheel sensor – along with the fitted log-normal PDF. (b) Fitted CDF and empirical values. The fitted parameters for the log-normal are $\mu = -2.368$, with 95% confidence interval $[-2.401, -2.337]$, and $\sigma = 0.550$, with confidence interval $[0.528, 0.573]$.

	human		virtual human		
Subject	μ	σ	gain K_M	μ	σ
S1	−2.641	0.406	10.570	−2.920	0.525
S2	−2.274	0.547	18.940	−2.617	0.627
S3	−2.289	0.603	26.370	−2.602	0.699
S4	−2.036	0.506	15.626	−2.451	0.588
S5	−2.311	0.566	21.650	−2.640	0.587
S6	−2.354	0.401	9.498	−2.862	0.474
S7	−2.602	0.459	11.417	−2.926	0.578
S8	−2.338	0.652	23.759	−2.817	0.617
S9	−2.425	0.458	18.385	−2.827	0.618
S10	−2.406	0.617	15.565	−2.709	0.514

Table 4.1 Fitted parameters for the log-normal distribution (4.19) tabulated per subject. The table shows the results for the data collected from the human subjects, and for the artificial data obtained by running the multiplicative control model – with the same quasi-random forcing function $r(t)$ that was presented to each subject. For the case of the artificial data, the fitted gain of the multiplicative control model K_M is also shown.

where K_M represents the neuromuscular gain, M_{t_k} is the magnitude of the response *intent* of the human-operator, and S_{t_k} is a sign function that determines in which direction the response is applied. M_{t_k} is designed to simulate a multiplicative process dependent on the previous observations of the error signal, with multiplicative factor $\xi_{t_k} : (e_0, \ldots, e_{t_k}) \longrightarrow (0, \infty)$:

$$M_{t_k} \equiv \xi_{t_k} M_{t_{k-1}}. \tag{4.22}$$

With this scheme, different functions S_{t_k} and ξ_{t_k} can be specified. Considering that humans act after a delay τ (Sec. 2.4.1), that can be represented as the number of discretisation steps $n_\tau \approx \tau/\Delta_t$, S_{t_k} and ξ_{t_k} are defined thus:

$$S_{t_k} \equiv \operatorname{sgn}\left(L^{n_\tau}\{e_{t_k}\}\right) \tag{4.23}$$

and

$$\xi_{t_k} \equiv L^{n_\tau}\left\{\left|\frac{e_{t_k}}{e_{t_{k-1}}}\right|^{\rho}\right\}, \tag{4.24}$$

where $\rho > 0$ (here fitted $\rho = 0.914$) and L^{n_τ} is the back-shift operator ($L^{n_\tau}\{e_{t_k}\} = e_{t_{k-n_\tau}}$). For numerical stability, the case where $S_{t_k} = 0$ or $L^{n_\tau}\{e_{t_{k-1}}\} = 0$ can be handled separately by assigning $\xi_{t_k} = \xi_{t_{k-1}}$ or by setting an error threshold. With this particular choice of functions (4.23)-(4.24), the MHC model can be written as

$$C_M(t_k) \equiv K_M \tilde{M}_{t_k} \tag{4.25a}$$

$$\tilde{M}_{t_k} \equiv L^{n\tau}\left\{\frac{e_{t_k}|e_{t_k}|^{\rho}}{|e_{t_{k-1}}|^{\rho+1}}\right\}\tilde{M}_{t_{k-1}} \tag{4.25b}$$

which is a non-linear three parameter model.

Note that the Eq. 4.24 can be interpreted as a multiplicative derivative [BKÖ08]:

$$f^*(t) = \lim_{\Delta_t \to 0}\left\{\frac{f(t+\Delta_t)}{f(t)}\right\}^{\frac{1}{\Delta_t}}. \tag{4.26}$$

4.3.4 MHC Model Validation

Since different subjects present distinct control strategies (Fig. 4.8), the gain K_H was fitted to match the control responses of each subject through a Bayesian optimisation algorithm (Table 4.1). For example, the subject in Fig. 4.8a relies on lower amplitude and higher duration pulses, compared to the subject in Fig. 4.8b. The neuromuscular lag was also fitted from the subjects' data by a cross-correlation method in Section 3.4.1 ($\tau \approx 0.361$ for the studied cases).

Once artificial data were generated by running the model, with the same randomised instances of Equation (B.2) (for $r(t)$) that were presented to each subject during the HTE, the artificial data were fitted to a log-normal distribution. With this purpose, the same method used to fit the subjects' data was applied. For the combined data of all the simulations, the results are summarised in Fig. 4.9. A goodness-of-fit test results in a larger p-value compared to the human's data ($p = 0.752$). This was anticipated since the artificial data originate from a purely multiplicative process. The log-normal parameters for the particular instances of $r(t)$ of the virtual human were also calculated (Table 4.1), showing values comparable to those from the subjects' responses.

MHC and CO Model Compatibility

The MHC model is here contrasted with a standard methodology in human-performance modelling, the CO model (Sec. 2.3.2). The CO model has been widely used as a benchmark to validate other human-control approaches [Mac03, GS14]. For the presented application, the data generated from the virtual human were fitted very well by this model (Fig. 4.10). The CO model only gives an adequate representation of the human-operator frequency response in the vicinity of the crossover frequency ω_c. The MHC model presents CO model behaviour over a wider frequency range.

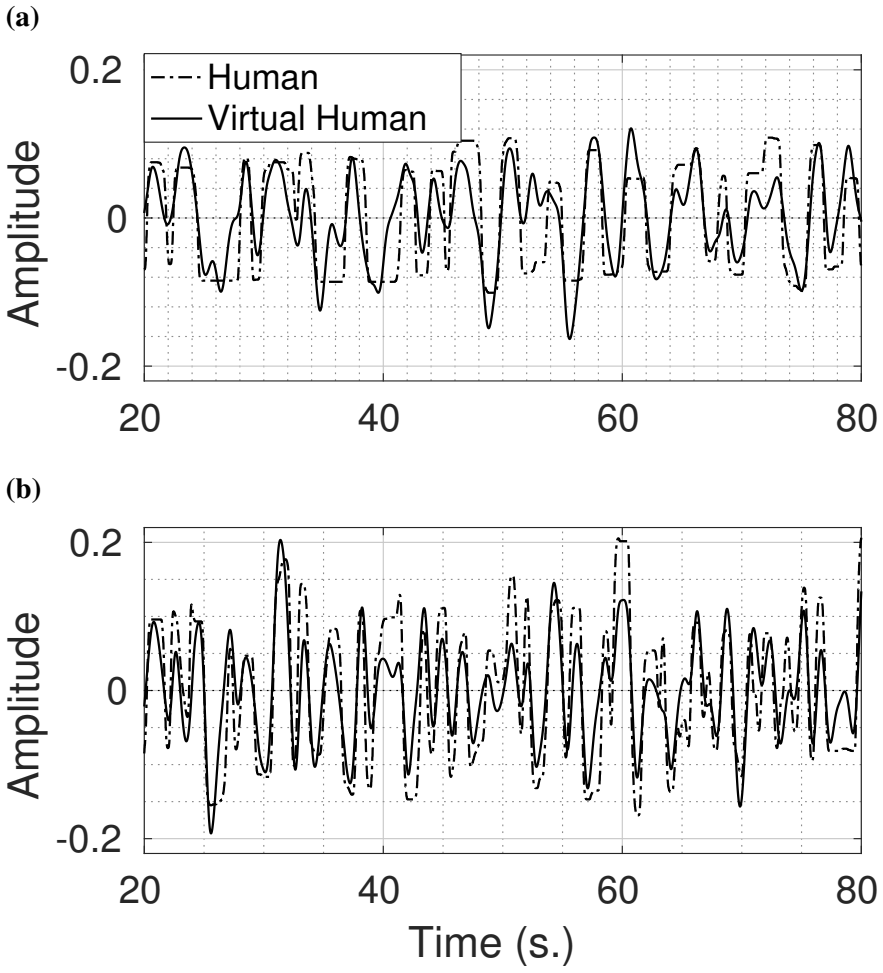

Fig. 4.8 Amplitude of the steering signal for two different randomised forcing functions $r(t)$ in (a) and (b). The two curves in each plot represent the response of a human subject $c(t)$ and the response $C_M(t)$ of the MHC model (4.25) with fitted K_M to match the subjects' response: (a) $K_M = 10.570$ and (b) $K_M = 18.385$.

Relation Between the MHC Model and Fitts' Law

Fitts' law (Sec. 2.2) can be understood as a particular case of MHC. From equation 4.24, and leaving aside the response delay n_τ, we have

$$\xi_{t_k}^{1/\rho} = \frac{|e_k|}{|e_{k-1}|}. \tag{4.27}$$

Now, if the initial error is $D = |e_0|$, we can write

$$|e_k| = \xi_{t_k}^{1/\rho} \xi_{t_{k-1}}^{1/\rho} \ldots \xi_1^{1/\rho} D. \tag{4.28}$$

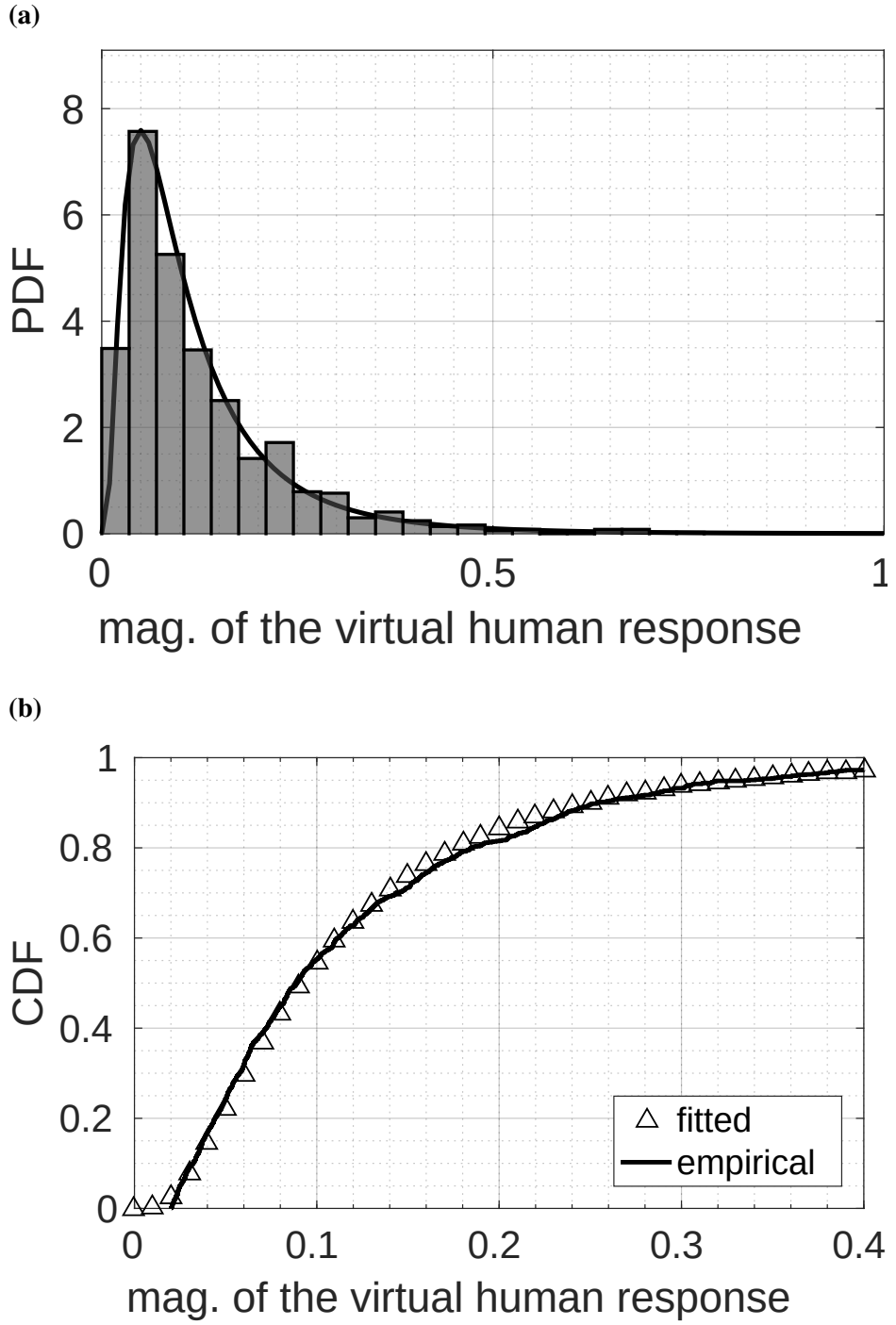

Fig. 4.9 (a) Normalised histogram of the simulated MHC model responses, for all the same instances of $r(t)$ that were presented to the ten subjects, and fitted PDF. (b) Fitted CDF and empirical values. The fitted parameters for the log-normal are $\mu = -2.395$, with 95% confidence interval $[-2.442, -2.347]$, and $\sigma = 0.782$, with confidence interval $[0.751, 0.816]$.

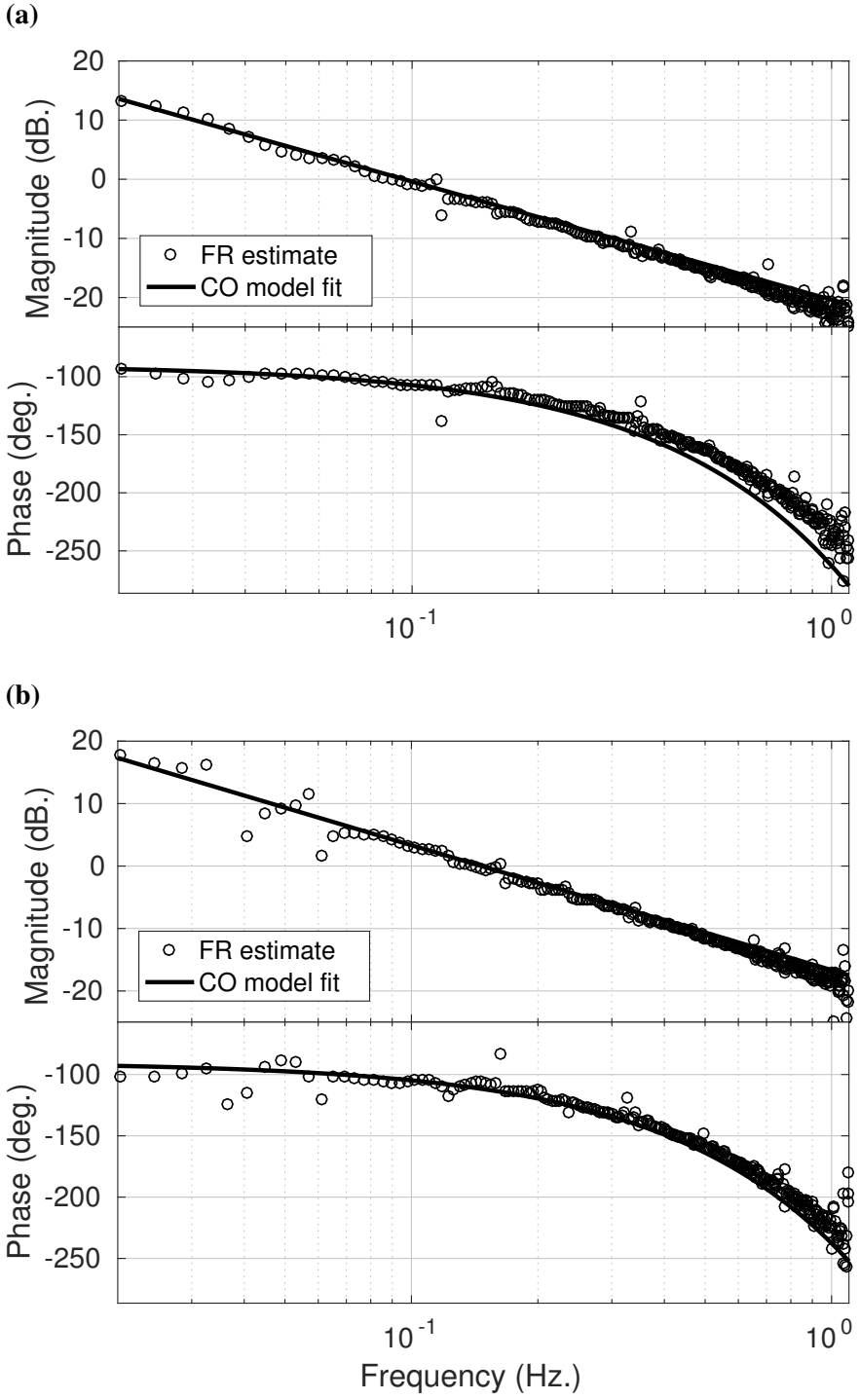

Fig. 4.10 Frequency response estimate from data simulated with the MHC model – for the same simulated responses displayed in Fig. 4.8 (a) and (b) respectively – along with the frequency response of the Crossover Model with parameters ω_c and τ fitted to the data.

	human		virtual human	
Subject	ω_c	RMSE	ω_c	RMSE
S1	0.108	3.506×10^{-3}	0.088	5.271×10^{-3}
S2	0.287	3.055×10^{-3}	0.156	4.914×10^{-3}
S3	0.381	2.340×10^{-3}	0.207	3.311×10^{-3}
S4	0.254	3.915×10^{-3}	0.128	6.510×10^{-3}
S5	0.362	2.812×10^{-3}	0.174	4.233×10^{-3}
S6	0.191	3.833×10^{-3}	0.080	6.111×10^{-3}
S7	0.115	3.440×10^{-3}	0.095	5.170×10^{-3}
S8	0.294	2.044×10^{-3}	0.189	3.119×10^{-3}
S9	0.290	2.367×10^{-3}	0.150	3.583×10^{-3}
S10	0.269	3.037×10^{-3}	0.128	4.691×10^{-3}

Table 4.2 Crossover frequency ω_c (in Hz) and RMSE of the tracking task tabulated for each subject and for the virtual human. In the case of the virtual human, an identical function $r(t)$ (B.2) as in each of the events with human subjects was used.

If the minimum acceptable threshold in the perceived error has magnitude R, the corrections will be performed during n steps until $|e_n| < R$. And, as Fitts' Law applies to static targets, then $\xi_{t_k} < 1$; the error decreases at each step because the target does not move:

$$\xi_{t_n}^{1/\rho} \xi_{t_{n-1}}^{1/\rho} \dots \xi_1^{1/\rho} D < R. \tag{4.29}$$

Now, we make the assumption that ξ_{t_k} is approximately constant $\xi_{t_k} \approx \xi$, then

$$\xi^{n/\rho} D < R, \tag{4.30}$$

and taking logarithms

$$\log_2 \frac{D}{R} < n \left(-\log_2 \xi^{1/\rho} \right). \tag{4.31}$$

Defining the positive constant $\widetilde{IP} = -\log_2 \xi^{1/\rho}$ results in

$$\frac{1}{\widetilde{IP}} \log_2 \frac{D}{R} < n. \tag{4.32}$$

Finally, by adding the number of steps n_τ, corresponding to the human delay, Eq. 4.32 becomes

$$n = n_\tau + \frac{1}{\widetilde{IP}} \log_2 \frac{D}{R}, \tag{4.33}$$

which essentially coincides with Eq. 2.2.

Therefore the MHC law is in accord with Fitts' Law for the case when the target is stationary, and the error is reduced by approximately a constant ratio at each discretisation step. In reality, the index of performance $\widetilde{IP}$ and the human response delay n_τ will experience stochastic variations, hence Fitts' law is only true on average.

Additionally, in the Appendix. D, the stability of this model controlling second order plants is demonstrated.

Although the presented methodology offers satisfactory results, there are a number of discrepancies between the model output and the real data. Humans present a higher crossover frequency than that of the MHC model (Table 4.2). This results in the MHC model having a higher root-mean-squared error (RMSE) in the tracking task for the examined plant. Further, the given approach requires the use of a threshold in the data. Human-control is likely to be explained better below the threshold by another type of model. Moreover, the model assumes that the human manipulative actions are a stationary process, thus learning and adaptation are not considered.

In the following sections, the MHC model will be extended to the control of ground vehicles.

4.4 Visual Input Variables for Steering Control

So far, the MHC model has been formulated as a human tracking control model. Before formulating the MHC model as a driver model for lateral control, the question of which are the variables that drivers employ during a driving task is now addressed.

A good deal of the complexity in driver behaviour is produced at the visual acquisition stage, and a range of concepts regarding eye target acquisition populate the literature, from the stochastic nature of the eye motion [LL94], to variable timing of target recognition [KTIM17] – through Hicks law (Sec. 2.2.2).

With respect to steering control, the driving task can be categorised into two subtasks: *lane keeping* and *guidance level control* (see [Don78] and Sec. 4.1):

Lane Keeping

Lane keeping is a response to perturbations produced by irregularities in the pavement, wind gusts, drift effects in the steering system, vibrations and human induced noise; hence lane keeping resembles a compensatory control task (Sec. 2.3.1). In [KA68] experiments were conducted with test drivers which showed that drivers change their sight point continuously while in a steering task, and that the distance to the sight point increases proportionally to the speed of the vehicle. Also, their response was seen to be more jerky when only the

near region of the road was visible. It has already been discussed that smoother control responses are indicative of feed-forward control ([MWS93] and Sec. 2.3.3). In other reported experiments [LH95], it was verified that drivers rarely fixate their gaze in the near region of the road, but when the near region is not visible vehicle positioning performance decreases. This suggests that drivers use peripheral vision to gather information from the near field. Thus both, the near and the far region of the road, are important for lane keeping (Sec. 4.2.1). Nevertheless, no consistent gaze pattern is found in human subjects while driving on straight roads [LL94].

Guidance Level Control

Guidance level control is performed by anticipating changes in the road geometry, thus it can be considered a feed-forward operation. By tracking drivers eyes in a driving task, it has been established that drivers direct their gaze to the tangent point of the road 1-2 s before the car enters the curve [LL94]. Drivers maintain their gaze near the tangent point during the curve handling manoeuvre, with the exception of sporadic saccades to other parts of the road. In another publication [LLPI13], it was suggested that drivers fixate their gaze in the immediate region after the tangent point. A reasonable explanation for this consistent behaviour is that, from the apparent motion of the tangent point the road curvature can be estimated.

Thus steering a ground vehicle is a combination of feedback and feed-forward components (see also Sec. 4.2.3).

4.4.1 Indirect Visual Acquisition Experiments

Typically, drivers gaze patterns are assessed through eye tracking experiments [Gre97], or by directly constraining driver's head position and gaze direction [KA68]. Here an alternative method is proposed, which consists in introducing perturbations in a computer generated road scene. The two experiments presented next are part of the Driving Simulation Experiments (DSE) described in Appendix. B.3. These experiments with test subjects consisted in a simple 3D simulation representing the forward scene viewed from a car. The aim was to test the possibility of drivers using the position of objects, that are essentially stationary in the visual scene, to obtain course information.

Moon Perturbation Experiment (Exp. # 4 Day 1 in Table B.9)

This experiment consisted in driving during 180 s on a straight path. During the first 20 s, the road had normal visibility (Fig. 4.11a). After that, the road visibility was reduced so that only the near distance – up to 4 m – was visible. At $t = 60$ s, a moon appeared over the

horizon (Fig. 4.11b) which behaved normally – as a stationary celestial body – until $t = 120\,\text{s}$. Between $t = 120 - 180\,\text{s}$ of the experiment, the moon oscillated with gradually increasing amplitude – and at a frequency of 0.1 Hz.

The different phases of the experiment reveal different driver behaviour conditions. As expected, drivers had a larger MSE – measured as the offset from the centre of the road – when the road had limited visibility (Fig. 4.12a). Interestingly, the drivers' performance seems to have less variability when the moon was present at a stationary position; the presence of the moon as a reference point seems to have improved the performance of some subjects. When the moon oscillated, several naïve subjects were deceived by the visual effect, as this increased their MSE and variability considerably. Thus although having a stationary body in the visual field did not increase the performance of all subjects, most subjects seem to have relied on it to sustain course control, because when the moon started oscillating their performance worsened – even compared as when the moon was not present at all. Figure. 4.12b shows the lateral offset through the experiment displayed by Subject 6 (S6); it can be seen that S6 *followed* the celestial body, apparently unaware of the oscillatory effect while neglecting the visible road segment.

After the experiment, the test subjects were asked by the investigator whether they felt anything unusual in the visual display. Only two subjects (S3 and S8) answered affirmatively. While S8 noticed that the moon was oscillating, S3 felt being *followed* by the moon, instead of the other way around.

Moon Perturbation Experiment (Exp. # 1 Day 2 in Table B.9)

A similar experiment was performed on the second day of the tests (Tab B.9). The main difference with respect to the previous experiment is that the subjects drove in a circular path. When the moon first appeared in the display, it behaved normally as a stationary celestial body, with apparent motion from left to right as a result of subjects following the road curvature. The moon appeared a second time during the experiment, but this time it reversed its direction upon reaching the centre of the display. In this case, three subjects noticed the anomaly in the moon's motion (S7, S8 and S9), but it was not observed any consistent change in performance due to the moon perturbation. This suggests that the subjects did not rely on the moon for vehicle positioning during this experiment, although they may have used the moon for curvature estimation. Possibly the surprise effect of the test was lost because of the previous similar experiments.

(a)

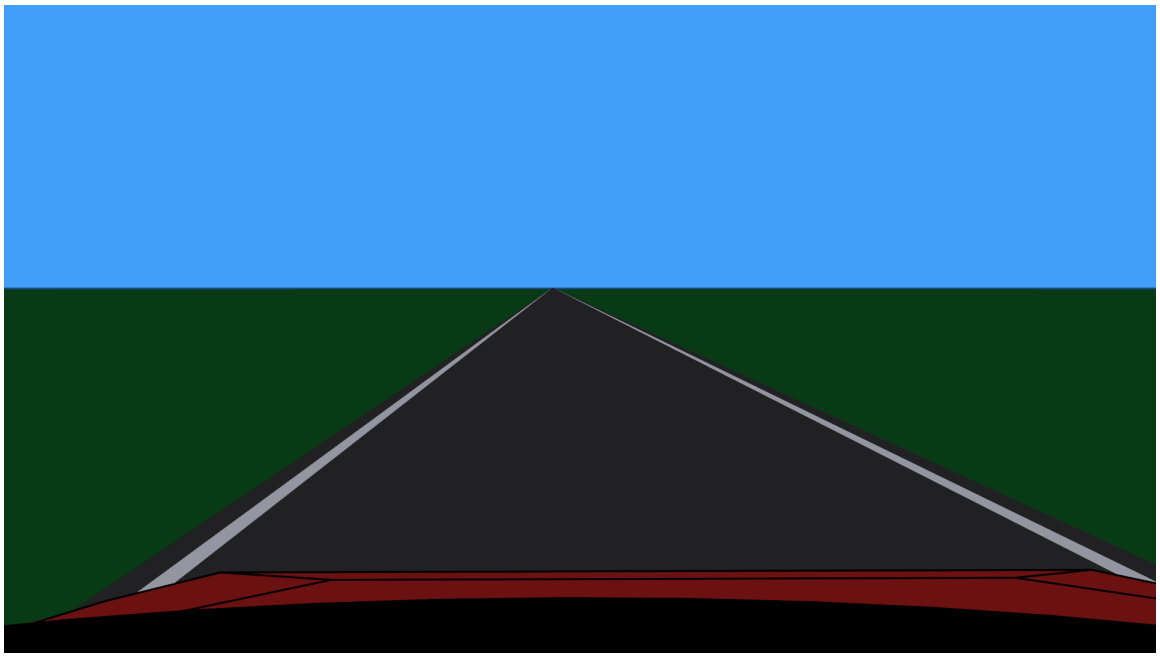

(b)

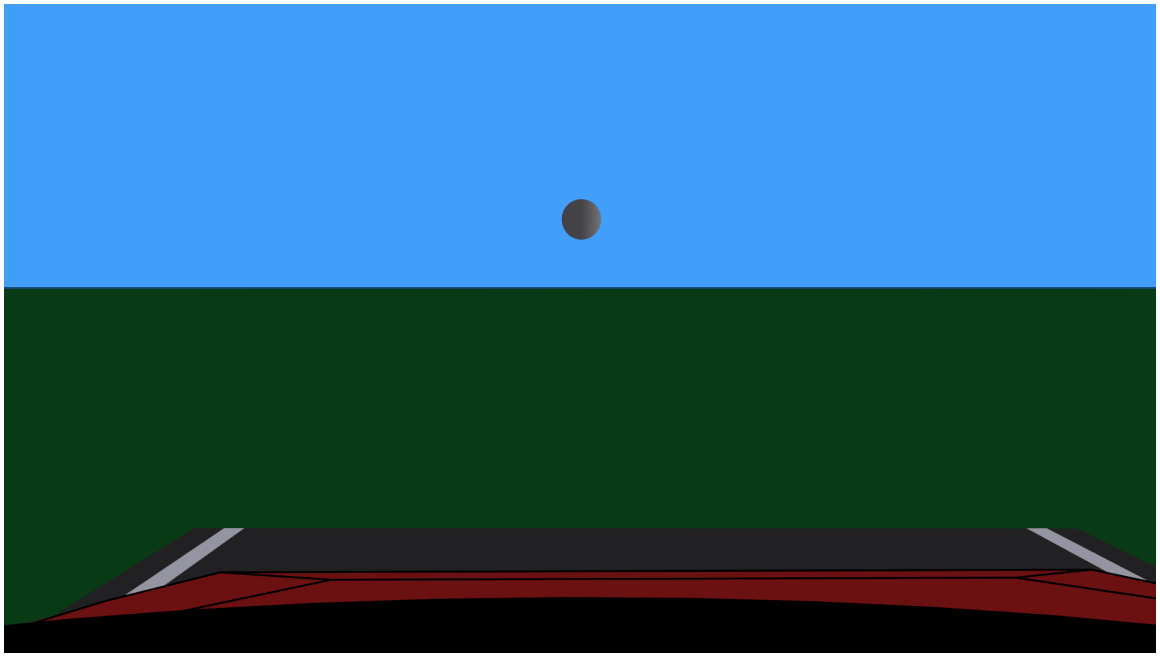

Fig. 4.11 Screenshots from experiment # 4 in Day 1 (Table B.9): (a) During the first phase of the experiment, the road was normally visible. (b) During the second phase, only up to 4 m of road were visible and in the third phase, a celestial object was present over the horizon.

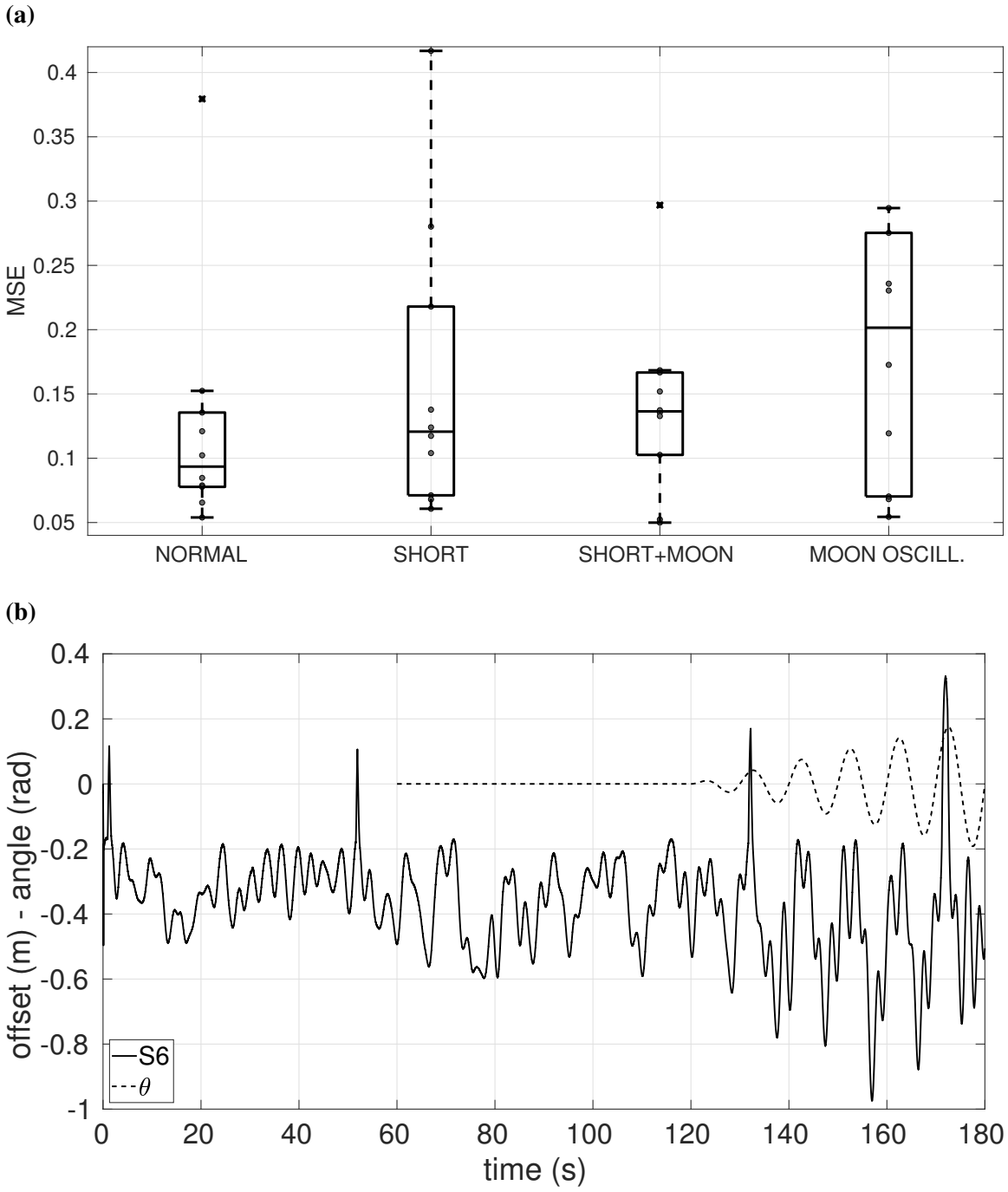

Fig. 4.12 (a) Box plot showing the MSE of the lateral offset during the four phases of experiment # 4 in Day 1 (Table B.9). (b) Lateral offset and moon perturbation (angle θ) displayed by S6 in the same experiment.

4.4.2 Perceived Angles vs. Lateral Offsets

Many human steering control models employ standard engineering variables as a surrogate for visual input. In some models, these variables represent lateral offsets and their respective derivatives. This approach comes with one caveat; the CNS is much better adapted to detect angular misaligments than lateral offsets (Sec. 2.1.2).

The importance of optical flow for sensorimotor control was first suggested in [Gib50], where it was shown that keeping the FOE of the optical flow near the desired target is a plausible course control strategy. More recent literature advocates that the *radial-outflow* is a more relevant cue [WH$^+$88, BL96, WS00]; for example, the case of an animal chasing a prey when the FOE may be occluded by vegetation or the case where a human is driving in the presence of fog can be considered. Indeed humans can perceive motion from outflow patterns with an accuracy approximately 1 deg [WH$^+$88] – and are able to detect angular misalignments of 1 s of arc in laboratory conditions [Cra48]. In more general terms, it can be assessed experimentally that borders and edges are very important in visual perception [Gre97].

Regarding how the radial-outflow lines are actually perceived, in [Gei99] it is proposed that motion streaks caused by pooling the responses of different neurons can be used to identify the direction of flow lines. Although neurons in V1 (Sec. 2.1.2) provide direction information, direction is not necessarily interpreted as motion unless some prefiltering is produced (see [Bur80] and Sec. 3.4.5).

Additionally, the retina in the human eye, which is where the photoreceptors are located, is fundamentally a two dimensional surface. Thus vision can be regarded as a projection from a three-dimensional space to a two-dimensional space. With this in mind, in [BL96] the angles formed by the projection of straight lines in a visual scene – referred to as *splay angles* – were emphasised as potential motion perception cues. With respect to driving, already Donges articulated that lateral offsets may be perceived through the splay angles projected from the road lines [Don78], but this was not included in the modelling strategy.

A summarised list of the advantages in considering angular information, instead of lateral displacements, for modelling visual acquisition in the human-operator follows:

1. From a mathematical standpoint, angles are dimensionless quantities, and therefore not affected by scaling. This means that visual course control based on angle perception is not dependent on the size of the perceived objects.

2. A more practical consideration is that of the case when visual blockage occludes some sections of the perceived scene. While displacement information can be very difficult

to assess in such circumstances, angular information is a more robust measure – we do not need to see the whole lane boundary to understand the road geometry.

3. Angles can be deduced from multiple gaze fixation points. Displacement between objects can only be assessed by gazing at particular locations.

4. The visual cortex seems to be specially tuned to identify angular orientation (Sec. 2.1.2).

4.4.3 The Splay Error as a Lane Keeping Metric

Driving a vehicle is a *boundary avoidance* task, and not necessarily an offset minimisation task. Along these lines, here it is assumed that human drivers respond primarily to angular information for lane keeping. Equivalently, it is easier to design computer vision systems that estimate angles than distances, as angular information can be easily inferred from the projection of images over a two-dimensional subspace. Although there exist driver models in the literature that use angular variables as input – for example the SG model described before (Sec. 4.2.1) – even in this case the angles are assumed to be estimated in inertial coordinates, and not directly perceived from the forward road scene.

Because of these reasons, the projections of the left and right markings of a traffic lane over a flat surface are here considered. From these projections two angles are delineated: θ_L and θ_R (Fig. 4.13a). These angles are referred to as *splay angles*, and are defined as the interior angles of the projections. Here it is considered that human lane keeping at low speeds and for lane positioning at higher speeds is a response to the difference between the splay angles. That is, the human driver is assumed to employ as control variable the *splay error* (Θ):

$$\Theta = \theta_R - \theta_L. \tag{4.34}$$

The splay error has only meaning in the near distance with respect to the position of the vehicle, as in the far distance its projection is altered by the road geometry when the road is not straight. Nevertheless, because in non-curved roads Θ can be inferred by looking far ahead in the road too, it is a variable robust to saccadic motions.

For an observer looking at a straight road path of width W, with a heading angle ψ, a lateral offset l and from an eye level height h – all relative to the path – it can be proved (see Appendix E) that

$$\tan\theta_L = \frac{h}{W/2 - l} \tag{4.35a}$$

$$\tan\theta_R = \frac{h}{W/2 + l}. \tag{4.35b}$$

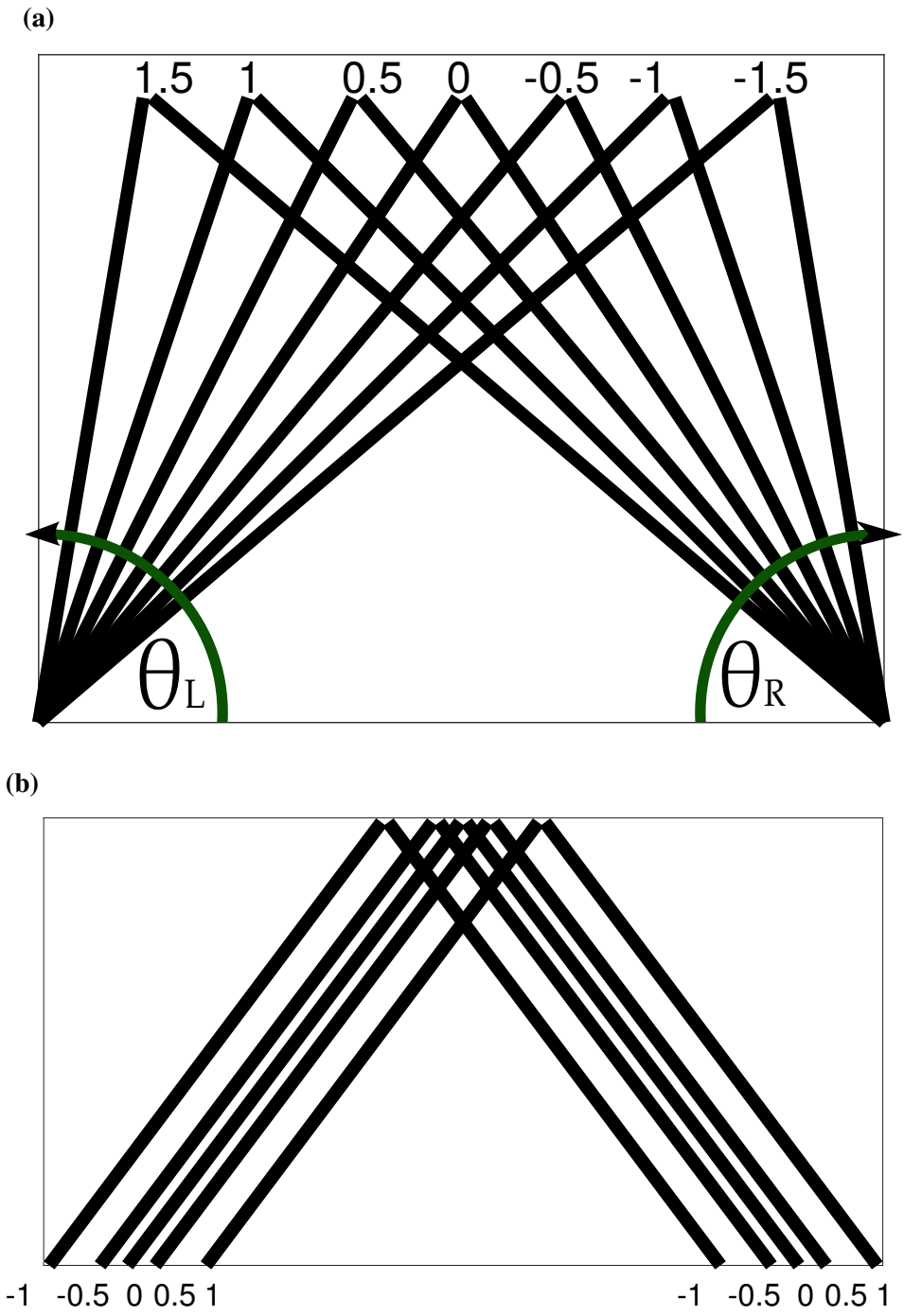

Fig. 4.13 (a) Lateral displacements – presented on top of the figure in meters – translate to changes in the splay angles – i.e., the interior angles resulting from the projections of the road lines over a two-dimensional surface (Appendix E). This is independent of the heading angle ψ. (b) On the other hand, changes in heading ψ – in radians at the bottom of the figure – displace the road lines laterally over the projecting surface.

That is, Θ does not depend on vehicle heading or gazing direction (Fig. 4.13a). This is very relevant because it implies that Θ is not affected by lateral saccadic motions, changes in driver's head rotation or vehicle heading; Θ is *rotation invariant*. Although extra-retinal information allows humans to perceive changes in gaze position [WS00], the splay error does not require of it. On the other hand, it can also be proved that changes in ψ translate in increments in lateral offset proportionally to $\tan\psi$ (Fig. 4.13b and Appendix E).

The splay error can be visually acquired when only a section of the road markings is present. When the road markings are not present, it can be obtained from the edges of the road and, even when the edges are not clear, radial outflow lines could be used instead to replace the markings [Gei99].

The advantage of developing models that consider angular information, instead of lateral displacement, as input can be further evidenced through examining optical illusions and additional indirect visual acquisition experiments:

Optical Illusions

Different visual effects, such as *size constancy*, imply that human's CNS may generate significant errors when estimating objects amplitude or lateral distances [Gre97]. Size constancy effects are corrections generated by the CNS to represent objects in the visual field at approximately constant size, when varying their distance from an observer. These distortions are produced by means of interpreted depth cues. *Size constancy* can be exploited to generate different optical illusions, such as the Ponzo illusion [Gre97]. In Figure 4.14 the Ponzo illusion is reproduced over a road scene. Most people perceive the higher red bar as having a bigger size than the lower bar. The brain interprets that the higher bar is farther away in the distance, and hence its apparent size is increased. It seems unreasonable to believe that humans drive a car by making predictions of lateral offsets in the future.

Another example is what is known as the *leaning tower illusion* [KYG07]. This illusion happens when two identical images are placed side to side – each of the images containing projected parallel lines. Figure 4.15 reproduces the leaning tower illusion for two road scenes, with left and right orientation respectively.

Although the brain preserves the parallelism of the road lines in each contiguous image – as these lines seem to converge at a vanishing point – the vehicles in contiguous each images are further separated by the optical effect – produced by the CNS while trying to analyse both images as one.

Thus optical illusions can reveal mechanisms of perception in driving tasks. Another known illusion, in this case producing wrong interpretations of the road slope, can be found in [Kit15].

Fig. 4.14 Ponzo illusion over a roadway scene. The two red bars are of identical size, but the CNS distorts their magnitude upon depth perception.

Fig. 4.15 The leaning tower illusion for two pairs of images. Most people have difficulty realising that the images on the left are identical to the ones on the right.

Transition in Seating Position Experiment (Exp. # 3 Day 1 in Table B.9)

This experiment consisted of driving for 6 min in a straight lane with a moon on the background. The graphical simulation represented a driver sitting on the left seat of the car – with an offset from the centre of the vehicle of 0.45 m. During the time interval 170-190 s, the simulation modified the apparent driver position by smoothly shifting it from a left seat to a right perspective (offset -0.45 s), producing a change in the projected splay angles (Fig. 4.17a). After the experiment, the subjects were asked if they felt anything unusual during the simulation. Only two subjects noticed that there was a graphical perturbation (S3 and S8). S3 thought that the road was distorted during the simulation but was unsure as to how. S8 thought that the road had become wider during the test.

Figure 4.16 shows the lateral offset from the centre of the road for each subject during the test. Although only two subjects noticed a change in the projected scene, they generally reacted to the change. The data show that the drivers tended to centre their position on the scene, instead of centring the vehicle position. That is, the naïve participants attempted to reduce the perceived splay error (Θ).

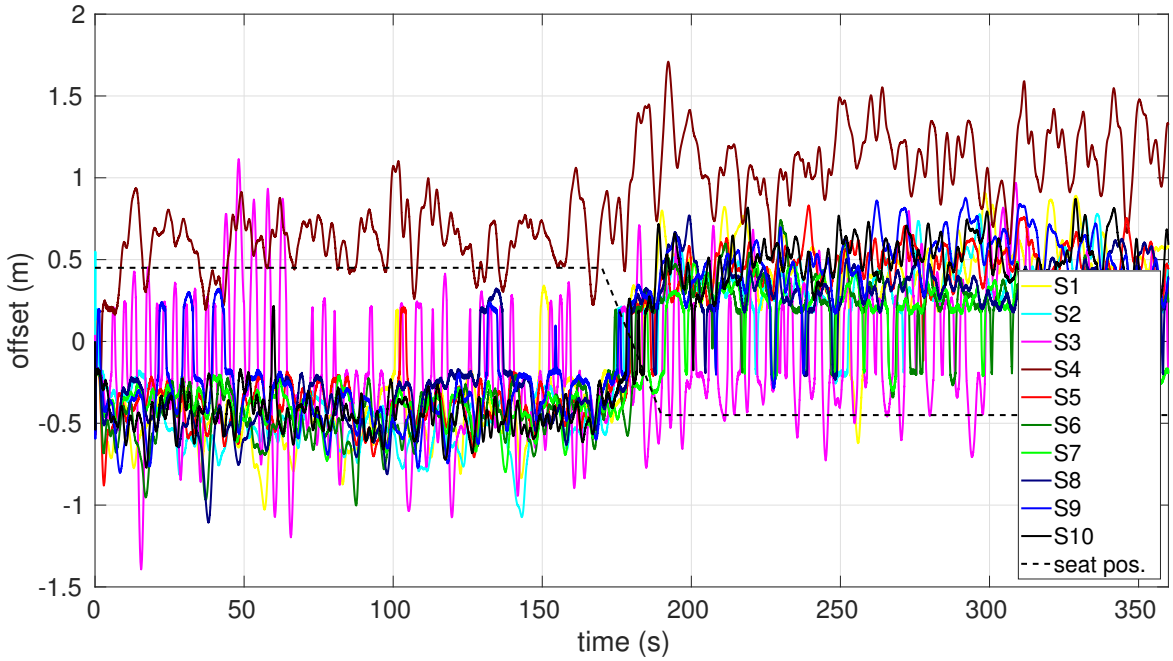

Fig. 4.16 Lateral offset for each of the subjects during experiment #3 in Day 1, along with the seat position during the test.

(a)

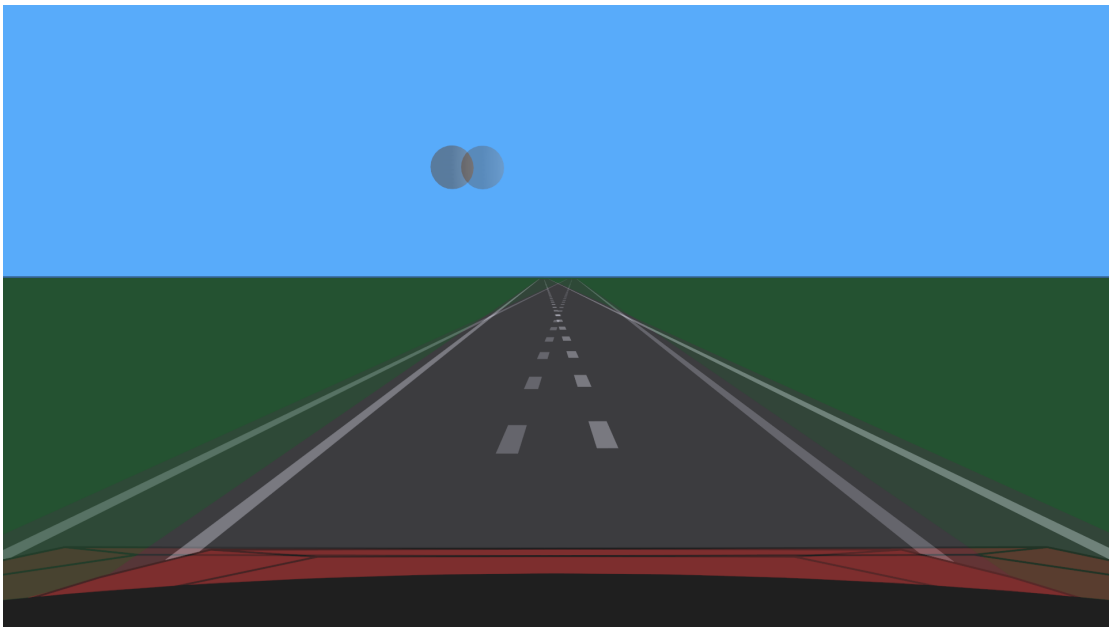

(b)

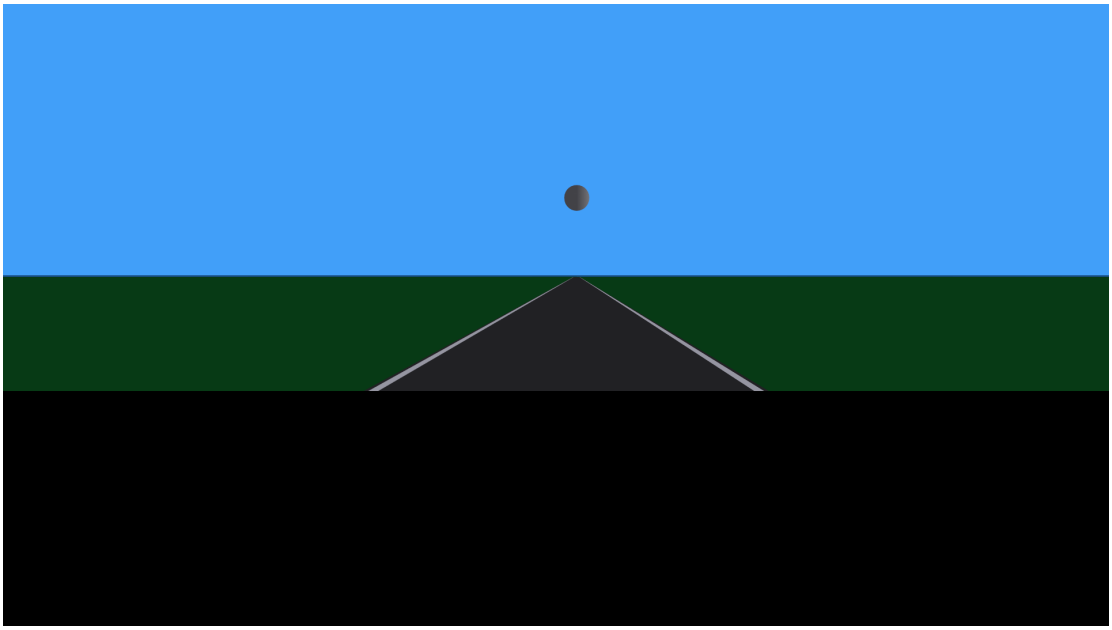

Fig. 4.17 (a) Screenshot for Exp. # 3 Day 1 (Table B.9) – where the visual scenes from the left and from the right seat are overlayed in the same image. (b) Occlusion of the near field up to 14 m in Exp. # 2 Day 2.

Splay Angle Perturbation Experiment (Exp. # 2 Day 2 in Table B.9)

In another experiment – with a duration of 4 min – the subjects were exposed to a direct perturbation in the splay error. This experiment was also performed on a straight road, in this case without centre lane line to make the perturbation less conspicuous. The simulation represented a driver sitting at the centre of the car. During the first 30 s, the subjects steered the car in absence of any display perturbation. At $t = 30$ s, the display was partially occluded with a black screen (Fig. 4.17b), which covered the road up to a distance of 14 m. The subjects had 60 s to adapt to this new display condition – until $t = 90$ s, when the road gradually widened from the right side of the lane by 1 m and returned to its normal width (smoothly during 60 s), followed by 30 s without changes in the display. From $t = 180$ s, the same effect was produced on the left side of the road. The road width was maintained invariant at the vanishing point, thus the widening was perceived as a splay angle perturbation. As the subjects could not see the near end of the road, they were mostly responding to the perceived projected angles.

Upon questioning, three of the subjects claimed that felt some sort of graphical perturbation during the test (S7, S8 and S9). Subjects 7 and 8 were unsure about what had happened, while S9 thought that the vehicle had been pushed and pulled by a lateral force. Nevertheless, again most of the subjects responded to the visual perturbation (Fig. 4.18a); initially the subjects positioned the vehicle around the centre of the lane – as the simulation represented driving from the centre of the car. When the road widened, the drivers adjusted the vehicle to the new centre of the lane, although they could not see it. Anyhow, the subjects were less consistently tricked during the second perturbation – road widening to the left.

Thus the subjects manoeuvred the vehicle based only on splay angle information. Additionally, their performance was lower when the occlusion was presented (Fig. 4.18b).

4.5 Human-centred Driver Model

4.5.1 MHC model for Low Speed Driving

For low-speed driving, local compensatory feedback is expected to dominate the steering angle signal. Hence MHC is here implemented for low-speed driving. The input error to the MHC model is taken to be the splay error – $e_{t_k} = \Theta(t_k)$, and the output the *steering wheel angle* (SWA) – $C_M(t_k) = \delta(t_k)$.

Typically, the human operator is assumed to be a discrete actuator with a cycle time of ≈ 50 ms (Sec. 2.3.3), and with response delays that are in the range $133 - 528$ ms [War67]. Thus the Δ_t and τ are set to be 50 ms and 250 ms ($n_\tau = 5$) respectively.

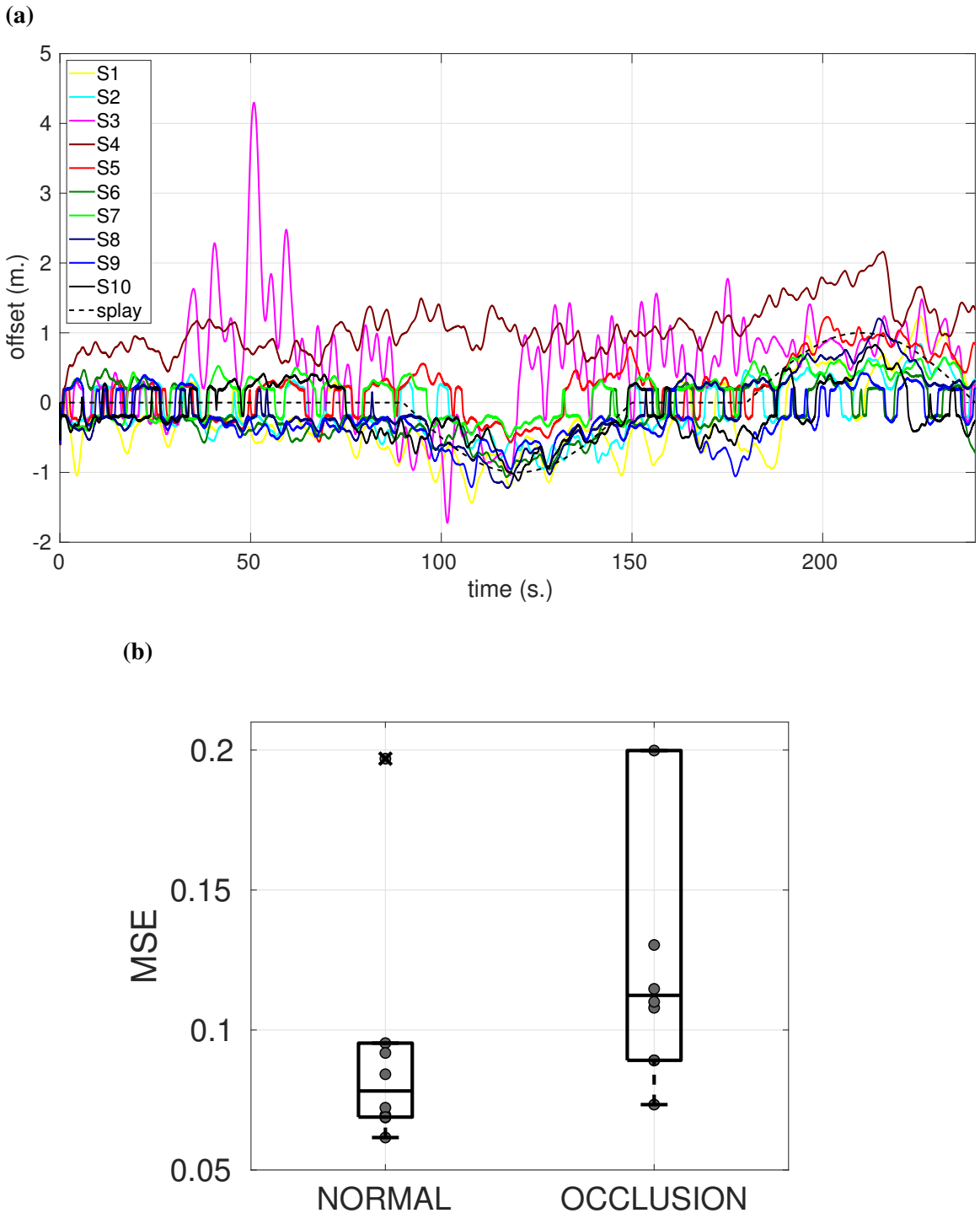

Fig. 4.18 (a) Lateral offset for each subject during experiment #2 Day 2, along with the road widening effect – to the right and to the left – during the test. (b) Box plots of the MSE in the lateral offset for each subject during the normal and occlusion phases for the same experiment.

Additionally, humans present thresholds in visual perception. These are established by the CNS to filter potential residual firing occurring within the photoreceptors [Gre97]. In consequence, a threshold is set in the MHC model so that it updates its response only when $|\Theta(t_k)| > 1\,\text{deg} = \text{TH}_\Theta$ (Sec. 4.4.2 and Tab. 2.2).

With these settings, the parameters in the MHC (Eq. 4.22-4.24) scheme were fitted using multiobjective optimisation through a genetic algorithm. The algorithm run a simulation in the IPG Carmaker environment [IPG15] at $6\,\text{ms}^{-1}$ on a straight roadway. A random torque perturbation over the heading of the vehicle was added every 0.1 s. The two dimensional cost function for the optimisation process consisted of the *total splay error* (T_Θ) and the *steering workload* (W_s) [Pau12]:

$$T_\Theta = \int_0^T \Theta^2(t)\,dt \tag{4.36a}$$

$$W_s = \int_0^T \dot{\delta}^2(t)\,dt. \tag{4.36b}$$

The genetic algorithm yielded optima near $K_M \approx 1.11$ and $\rho \approx 0.13$. Figure 4.19 displays the steering response $\delta(t_k)$ of the MHC model with the fitted parameters, along with the splay error $\Theta(t_k)$. The MHC model produces *ballistic movements* in the response. This is supportive of the MHC model to behave in a biofidelic manner – i.e., to approximately reproduce the principles of human control – as the hypothesis of human control consisting of ballistic movements or pulses has long been recognised (Sec. 4.2.2).

Although we already proposed a steering control law that mimics the ballistic behaviour exhibited by humans, it is relevant that the MHC model generates ballistic behaviour without it being *a priori* considered during the design of the controller.

4.5.2 Far-point Error for Steering Control

At higher speeds, the steering response of the model Eq. 4.39 becomes excessively jerky when only the splay error is available. The same effect is observed in humans when only the near region of the road is accessible [LH95]. This is caused by the lack of preview information to compensate for the response delay τ. Thus far-point preview control needs to be incorporated into the model. Here, integral control results in a steering-rate proportional to the CNYR and with the same response delay τ:

$$\frac{dC_\chi(t)}{dt} = -K_\chi L^{n_\tau}\{\chi(t)\}. \tag{4.37}$$

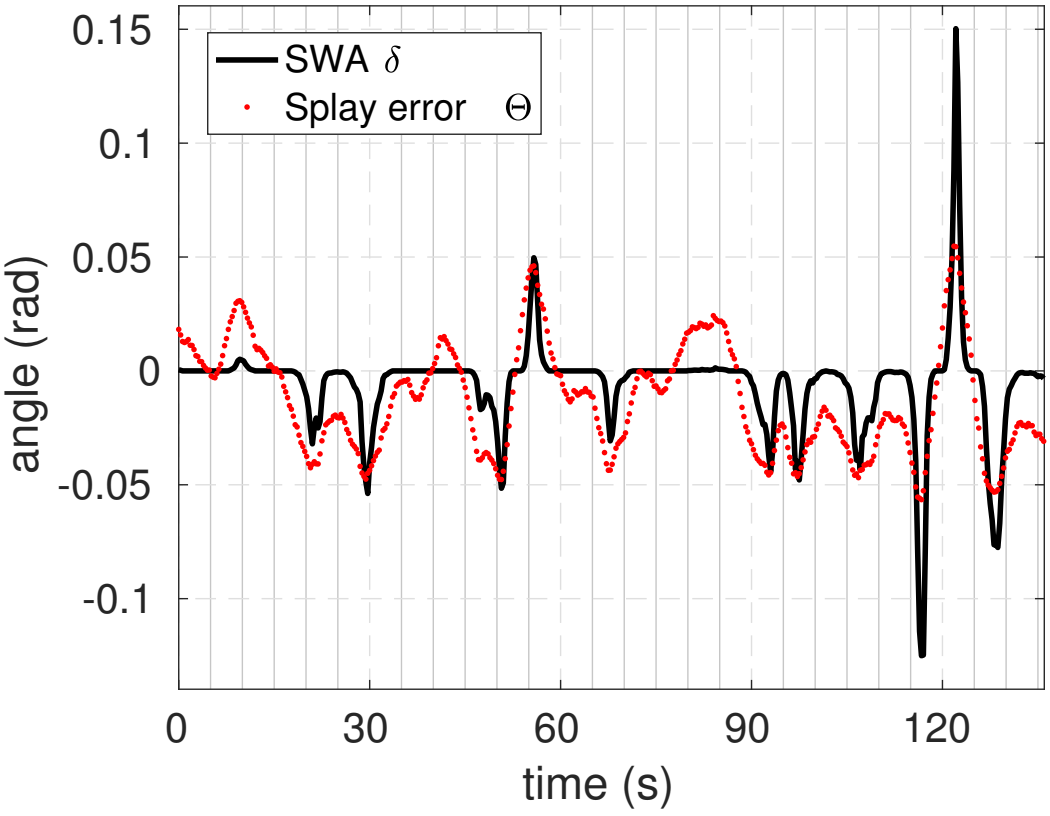

Fig. 4.19 Splay error (Θ) and SWA (δ) for a simulated event representing a Toyota Camry 2006 running with the control parameters $K_M = 1.11$ and $\rho = 0.13$, and in a straight lane at $6\,\mathrm{ms}^{-1}$.

The preview distance to the left and right boundary points ($d_{L,R}$) is set at a preview time of $T_p = 1.5\,\mathrm{s}$ according to the current speed of the vehicle ($d_{L,R} = UT_p$).

Besides error corrective control, human drivers use *guidance level control* to anticipate changes in the road geometry [Don78]; driving is a combination of feed-forward and feedback actions. According to the relation for the Ackermann angle, the feed-forward component of driving is reflected in the model by the relation:

$$C_\kappa(t_k) = r_s \kappa(t_k) L \tag{4.38}$$

where r_s is the steering ratio, κ the road curvature and L the wheelbase of the vehicle. Because drivers do anticipate changes in road curvature, there is no response delay in this term. The curvature of the road can be estimated by looking at the *tangent point* of the road [LH95].

Hence, from the superposition of the three control terms in (4.25), (4.37) and (4.38), the proposed model results (Fig. 4.20):

$$\delta(t_k) = C_M(t_k) + C_\chi(t_k) + C_\kappa(t_k). \tag{4.39}$$

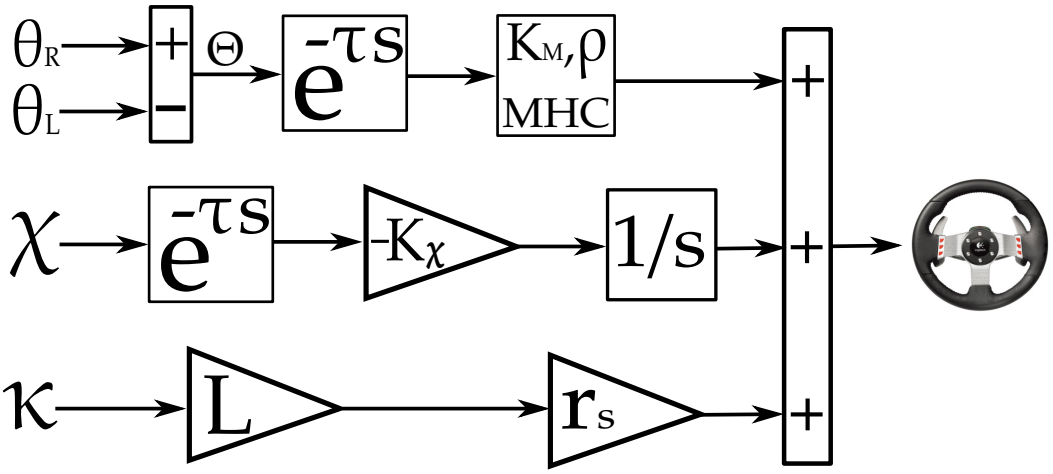

Fig. 4.20 Schematic of the proposed steering control model. The first two terms (C_M and C_χ) act as error compensators after a delay time τ, while the last term is a feed-forward controller. Only the last two terms (C_χ and C_κ) include road preview.

Model Parameters Optimisation at High Speed

The parameters of model (4.39) were fitted with the same setup as in Section 4.5.1, with the exceptions that the ground vehicle simulation run over an oval circuit with curves of 200 m radius and at a speed of $30\,\mathrm{ms}^{-1}$. The resulting optima in the Pareto front were found to be clustered around the values $K_M \in [1.3, 2.3]$, $\rho \in [0.018, 0.027]$ and $K_\chi \in [0.24, 0.31]$ (Fig. 4.21). With the chosen cost function (Eq. 4.36), the effect of the multiplicative controller becomes negligible ($\rho \approx 0$) at high speeds. However, there is no reason to believe that human steering control corresponds to minimising the total splay error (4.36a) and the steering workload 4.36b, but rather to act as a *satisficing controller*. Therefore, steering workload analysis and parameter estimation through NDD is performed to make the response of the model correlate more closely to that of human drivers.

4.5.3 Driver Workload Analysis and Model Validation with NDD

To compare the behaviour of the model with that of human drivers, analysis of the steering signal through the *steering entropy* metric (described in Appendix F) is conducted. Different

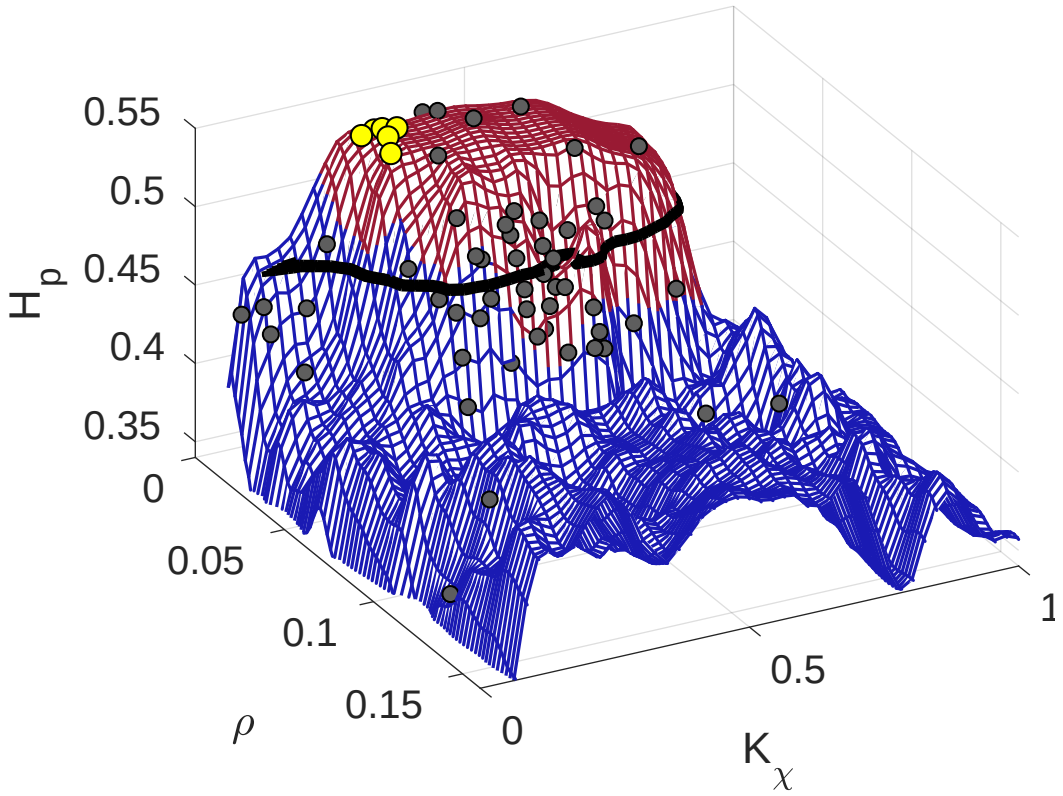

Fig. 4.21 Steering entropy H_p for fixed $K_M = 1.6$ and for varying ρ and K_χ. The surface corresponds to simulated data where the model was stable – in red – or unstable – in blue. The optima for low workload driving are displayed as yellow dots. In black, the contour line for $H_p \approx 0.47$ is shown. The grey dots are fitted values from NDD.

values of steering entropy (H_p) reflect different levels of driver attention directed to the steering task. For example, $H_p = 0.47$ approximately matches the steering entropy of attentive drivers – not performing additional tasks such as attending a conversation or typing into a cell phone [NFNB99].

In Figure 4.21 the steering entropy is plotted for different control parameters. The magnitude of H_p was obtained by running the vehicle simulation with $K_M = 1.6$ – which approximately corresponds to the mean value found in the Pareto front – and with different values for ρ and K_χ. In the same figure, the contour line corresponding to $H_p = 0.47$ is displayed. The optimised values obtained in above are also visible.

The optimised parameters produce higher values of H_p than those found in typical human drivers ($Hp \approx 0.54$). In particular, the optimal points present a steering entropy analogous to that of a partially distracted driver checking a navigation display – but certainly not due to the same mechanism.

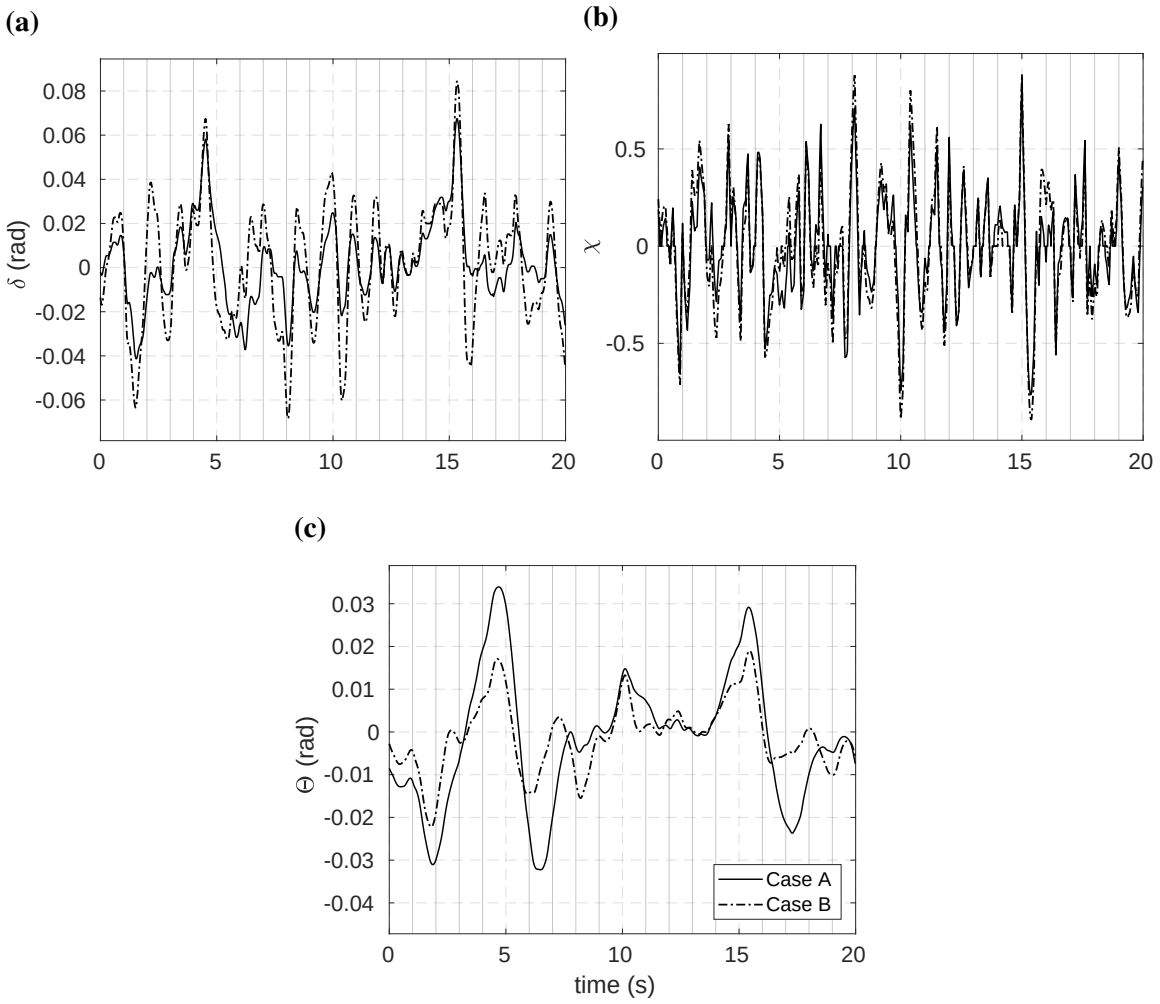

Fig. 4.22 (a) Response of the model (4.39), (b) CNYR (χ) and (c) splay error (Θ) for simulated data with two different sets of parameters: $\{K_M = 1.6, \rho = 0.02, K_\chi = 0.3\}$ (Case *A*) and $\{K_M = 1.6, \rho = 0.05, K_\chi = 0.48\}$ (Case *B*).

Commonly, driver parameters vary during the course of the driving task [Pau12]. With this in mind, sliced segments – lasting for 5 s – of the steering signal from the NDD were utilised to fit the parameters of the model (4.39). This was done by keeping K_M fixed – again to 1.6 – and fitting ρ and K_χ to minimise the MSE between the SWA of the human drivers and the model. The fitted parameters are shown in Fig. 4.21. Because human control is partially stochastic – as a result of variable response delays due to varying levels of attention – the fitted parameters appear scattered, but with higher density in the stable region near $H_p \approx 0.47$.

Taking this into account two different sets of parameters are now compared. In Case *A*, an *optimising driver* – according to (4.36) – with parameters in the Pareto front $K_M =$

1.6, $\rho = 0.02$ and $K_\chi = 0.3$ is considered. Case *B*, represents a driver with parameters fitted from NDD: $K_M = 1.6$, $\rho = 0.05$ and $K_\chi = 0.48$. The simulation was run for Case *A* and Case *B* with the same pseudo-random perturbation, so the model was responding to the same input in both cases. As expected, for Case *B* the steering response has a higher gain and in some instants occurs earlier than in Case *A* (Fig. 4.22a). In both cases, the far-point error control is relatively similar, although with slightly higher amplitude peaks in Case *B*; this is due to the effect of the steering pulses of the MHC model (Fig. 4.22b). Further, Case *B* exhibits a significantly lower splay error Θ (Fig. 4.22c). And lastly, Case *B* yields a higher steering workload ($W_s = 0.39$) as compared to Case *A* ($W_s = 0.11$). Thus Case *B* reflects a *satisficing driver* according to W_s. The optimisation process (Section 4.5.2) seems to have placed excessive emphasis on W_s minimisation, due to the fact that small increments in ρ can place the model near instability.

4.5.4 Discussion

At the beginning of this chapter, a list of potentially necessary characteristics that a steering control model should possess was proposed (Sec. 4.1). Here, some retrospective thoughts on how much of it has been achieved are included as concluding remarks.

First we presented a MHC model, for the simplified case of compensatory and pursuit tracking tasks, and single loop closures. This model has non-linear characteristics and works in discrete time. Additionally, the MHC model includes an *indifference threshold* – over the perceived error variable – and replicates statistically the stochastic effects of the human-operator. The model is further validated by contrasting it with the CO model – showing that MHC is consistent with CO behaviour in the frequency domain – and by proving that Fitts' law can be understood as a particular case of MHC, when the error is reduced at a constant ratio. Both analyses are significant; the CO is an accepted standard benchmark for compensatory tracking behaviour while Fitts' law is a classically accepted human performance result. Further, the MHC model has a reduced number of easily interpretable parameters and is able to control second order dynamics, or any system that can be approximated by second order dynamics – such as ground vehicles – without the presence of an internal model in the control scheme.

A major part of the motivation for the design of the MHC scheme is towards shared control systems [GG05]. In [ACMvP12] it was determined that for achieving good performance in a shared control task, the steering movements produced by the AI must be in agreement with those of the driver. With a deterministic methodology this is very difficult to accomplish.

The driver behaviour literature has commonly applied human control techniques and adapted them for the steering control of ground vehicles. In here, the same approach is

applied; the MHC model is extended for the case of the human-operator being a driver controlling the lateral dynamics of a car. The most relevant differences between steering control of ground vehicles and a simplified compensatory task are: the type and number of optical cues employed as error variables, the inclusion of a preview condition and the evidence that driver behaviour presents feed-forward actions in a higher magnitude. Thus these aspects are considered.

Through signal processing of NDD, a relationship was found between the steering movements of test drivers and the CNYR. From a deep analysis, which included novel experiments regarding visual acquisition, the splay error was identified as a very likely candidate of visual cue for lane keeping at low speeds. And, as it has been long regarded that humans act as hybrid controllers, this was also included in the proposed scheme. All this resulted in a Human-centred driver model. This model, reflects pulse characteristics – as those found in human drivers – and displays similar steering entropy features; the model is able to produce stable control of vehicles within the same steering entropy values found in test drivers.

The Human-centred driver model is extended from MHC, hence one valid question is how it relates to the CO model. As already explained, in the human-machine systems literature typically two control modes are employed: compensatory and pursuit (Sec. 2.3.1). For simple dot following tasks such as in the HTE – and in the classical experiments performed by Tustin and McRuer – compensatory and pursuit modes are very similar to each other. In a roadway environment and while controlling a car, there are larger differences between the two control modes; while controlling a car, the driver can use preview of the forward scene, thus pursuit control is more related to feed-forward control than compensatory control. Nevertheless, in the literature there are attempts to interpret driving as compensatory and pursuit cursor tracking behaviour [WM70]. For example, the Human-centred driver model can be understood as the compensatory loop depicted in Figure. 4.23.

However, this approach yields several complications. In particular, the inner loop closure – corresponding to χ in Figure. 4.23 – modifies the relationship between the forcing function and the response of the virtual human. The effect of the inner loop is difficult to characterise as it further depends on the road geometry, because in this case we are not dealing with a simple human-machine – or driver-vehicle – system, but with a *driver-vehicle-roadway* system. Even on straight roads, when the system can be reduced to a driver-vehicle system, the effect of the inner loop on the whole control loop (Fig. 4.23) will depend on the control parameters and the speed of the vehicle. That is, although for low speeds, small K_χ and on straight roadways the model will present similar frequency behaviour as that of the CO model, when varying these conditions the frequency response will change in different ways.

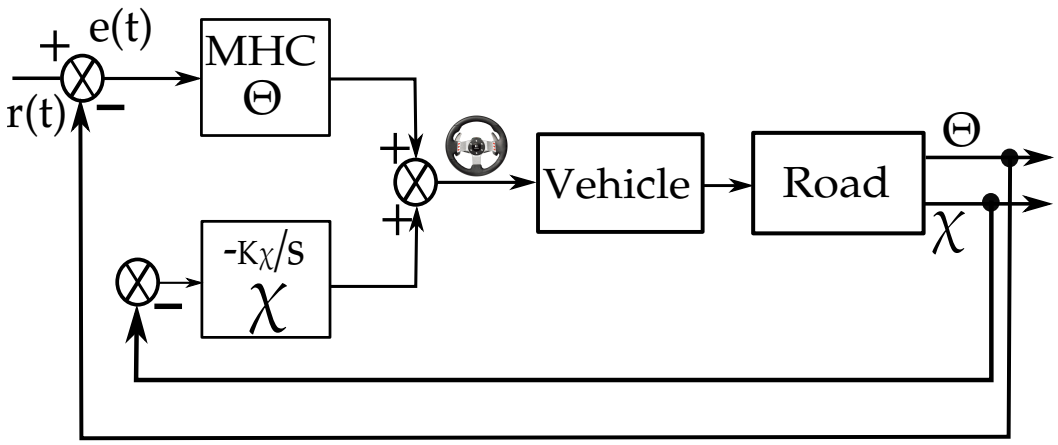

Fig. 4.23 Driver-vehicle-roadway system in which the Human-centred driver model can be interpreted as a compensatory loop closure.

Because of these difficulties, the multi-loop approach was developed to extend the applicability of the CO model to the more general case of multiple control variables [WM70]. However, this alternative approach has the inconvenience that it requires uncorrelated input variables. For real cases such as driving a vehicle, the control manoeuvres over one variable will also affect the other control variables; in our model, integral control over χ will also affect Θ and vice-versa.

Lastly, as a result of the analyses in Chapter 3, it was also suggested that a human control model should represent system memory. With respect to this, although the MHC model acts as multiplicative accumulator, it does not include the explicit memory characteristics of fractional calculus. This was done purposely to preserve the simplicity of the MHC. Nonetheless, the proposed scheme to add memory effects to the control model can be seen in Fig. 3.18. Hence, we offer a modular methodology in which the two control approaches can be combined in blocks.

Chapter 5

Driving by Torque

Despite the fact that fully autonomous cars may still be far away in the future, ground vehicles will gradually become more automated – for example through conditional automation systems, advanced driver-assistance systems (ADAS), vehicle-to-vehicle (V2V) communication, vehicle-to-infrastructure (V2X) connectivity, brain-to-vehicle (B2V) technology and infrastructure adaptation[1]. In front of the possibility that these technologies become common for private and public transportation, one valid research inquiry is to explore the role of the conventional steering wheel (SW) within this approaching scenario; is it functional to have a SW rotating in front of the passenger when the car is driving autonomously? This may be unnecessarily distracting for passengers performing side tasks – such as watching a movie or using a cell phone – while the intelligent system drives the vehicle, and it may be confusing in cases where the human must regain vehicle control – the human driver may need more time to regain control when the SW is already performing movements under the command of an AI system.

In this chapter, the novel concept of a fixed steering wheel, or *Isometric Steering Wheel* (ISW) is explored conceptually and experimentally.

5.1 Background on Isometric Control Devices

The isometric control devices that have been tested in the literature until now, are control sticks (or joysticks) and pointing sticks (or trackpoints). One of the earliest appearances of an isometric control stick in the literature is found in [Gib54], where isometric control was applied through a lever in a tracking task and compared with that of a moving lever. The plants controlled by the lever represented proportional, rate and acceleration control.

[1] Semi-autonomous vehicles do already exist, although these are only reliable under certain conditions and produce accidents under relatively low probability situations (see Sec. 1.1).

Interestingly, isometric control was shown to be consistently more efficient for the control of those plants. In the same publication it is also reported that subjects learned to manipulate the isometric device more rapidly. With a similar experimental apparatus, and some years later, McRuer communicated comparable results [MM66]. For the experiments reported in both publications, the test subjects were skilled at tracking tasks – naval officers and pilots.

Later, in [CEB78] a rate isometric joystick – thumb controlled – was compared to a computer mouse and to the arrow keys found on computer keyboards. In this case it was concluded that the quickest performance and the lowest error were produced by the computer mouse. Nevertheless, in this case the task at hand did not consist in a tracking exercise; it was a pointing task in which test subjects had to select text in a display by moving the cursor.

In a later paper [RS90], the comparison between an isometric control device and a computer mouse – here also for pointing tasks – was further studied. In this case the research was aimed at identifying optimal transfer functions between the forces applied to the device and the pointer speed. The tested transfer functions were of linear, parabolic and sigmoid shapes. It was concluded that the sigmoid transfer function yielded the best results, and that a dead-band was needed for better results for when the hands are not steady. In this case, the isometric controller was a pointing stick very similar to what today is still incorporated into ThinkPad® laptops, for the research in the mentioned publication is related to the development of these particular devices by IBM Corporation®. In [RS90] it is also shown that for pointing tasks a computer mouse is more efficient than a pointing stick, but for the case when pointing is combined with typing, the pointing stick was reported to be slightly superior.

A further advancement was incorporated into the design of the ThinkPad trackpoints, which is perhaps the most well known application of an isometric control device to date; in a following publication, by incorporating a transfer function with a *negative inertia* effect, the pointing performance was significantly increased [BSRO95]. Negative inertia can be accomplished for example through transfer functions of the form:

$$G(s) = \frac{0.4s+1}{0.1s+1}. \tag{5.1}$$

The response of Eq. 5.1 is displayed in Fig. 5.1. Negative inertia yields an overreaction at the initial stage of the control pulse and an under-reaction at the end of it. This effect assists in reducing the latency between control transitions. Although this is useful for pointing tasks, it is not a desirable feature for controlling a vehicle, where an overreaction could be fatal. A similar concept to negative inertia was explored previously by Tustin [Tus47], but in this case a spring-centred lever was used instead of an isometric controller (Sec. 2.3.2). Anyhow,

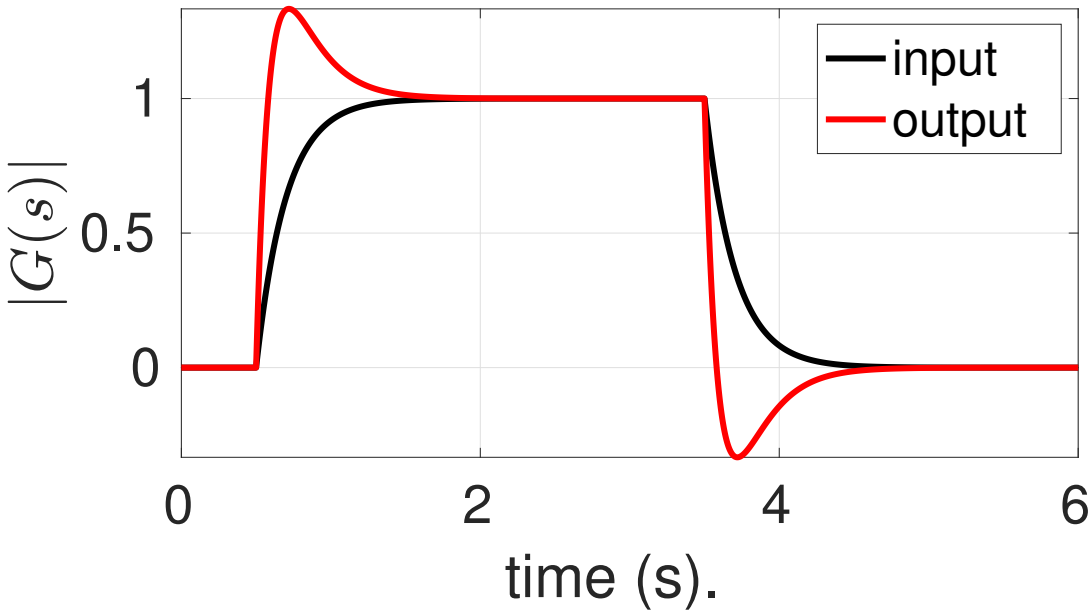

Fig. 5.1 In red, response of a transfer function with negative inertia effect (Eq. 5.1) under an input pulse (black line).

the conclusion was the same, the negative inertia effect improved the aiming performance in tank turrets among the test subjects.

With respect to what causes isometric control to improve performance – for the reported cases – different explanations can be recognised. In Section 3.4.4 it was seen that response delays are smaller with a joystick than with a SW (Fig. 3.11). A joystick involves a lower ratio between hand movement and control gain than a SW. In the same manner, an isometric control device reduces the motion required to generate a control pulse to its lowest point. We also saw that control with a joystick was less precise [ARB03], due to more uncomfortable arm positioning – as compared to the SW – and muscle and tendon vibration. Hence, for the case of steering a ground vehicle, could it be that by implementing an ISW the advantages of both control devices are combined? That is, a quicker response than that of a SW which is smooth and precise – with reduced hand vibration amplification.

Additionally, there is the possibility that with an ISW the hands may use the control device to stabilise the arms, thus reducing even more hand vibrations and instabilities . In [GO98], it is shown that the viscoelastic properties of muscles are adjusted to produce smooth and stable hand movements – *viscoelastic regulation*. The same idea is claimed by Kawato [Kaw99]. And in [BOF+01] it is studied how the CNS increases impedance in unstable directions of arm motion, also with the intent of generating smoother control movements. Thus a part of any control strategy involves stabilising the arm itself. With an isometric controller, arm stabilisation is achieved by just holding the device, and all the effort can be

directed towards the control action itself. The reduction of arm vibration has another potential benefit; it is known that externally induced tendon vibration can alter human's perception on applied force [JH85], thus a fixed arm position could improve control precision.

Another potential advantage is that an operator, controlling an isometric device, does not need to look at the hand to assess visually the control input, thus unloading the visual channel of control device supervision. Further, it is known that when the hand is not visible visual drift occurs [BC98]. Hence, in low visibility conditions, isometric control devices may reduce ambiguity in the control responses.

An ISW was already utilised in [NGD07] to assess the effects of steering feel, but not as a steering control device for vehicle driving. And, besides IBM's pointing sticks, there have been other examples of technology products containing some sort of isometric controller, like the C-Stick included in some Nintendo® video-game systems, which is used to pan the camera and adjust the field of view.

5.2 Training Experiments with an ISW

Part of the Driving Simulation Experiments (DSE) – Appendix B.3 – were designed to study the characteristics of human control when using an ISW. The setup for the experiments, in which ten subjects participated, consisted in a fixed steering wheel of 32 cm diameter mounted on a torque sensor (Fig. B.4). During the DSE, the subjects had to control a vehicle simulation with this device (ISW). The experiments were separated in two consecutive days, with the intent of adapting the naïve subjects gradually to the task. Specific details regarding the experimental setup can be found in Appendix B.3. The DSE also included visual acquisition experiments, which are reported in Sec. 4.5. In this chapter, only the DSE relevant to isometric control are discussed.

The first two experiments with the ISW were intended to adapt the subjects to the use of the ISW, and were performed in the same day (Day 1):

5.2.1 First ISW Training Experiment (Exp. # 5 Day 1 in Table B.9)

In the first training experiment, a red target circle was presented in the display, which varied position along an arc between two alternate locations – corresponding to a torque of $\pm 10.5\,\mathrm{N}\cdot\mathrm{m}$ (Fig. 5.2). The target changed its position every 20 s, and the total duration of the experiment was 180 s. A blue cursor dot represented the applied torque to the ISW in the display. The subjects were requested to apply force on the ISW to place the cursor (blue dot)

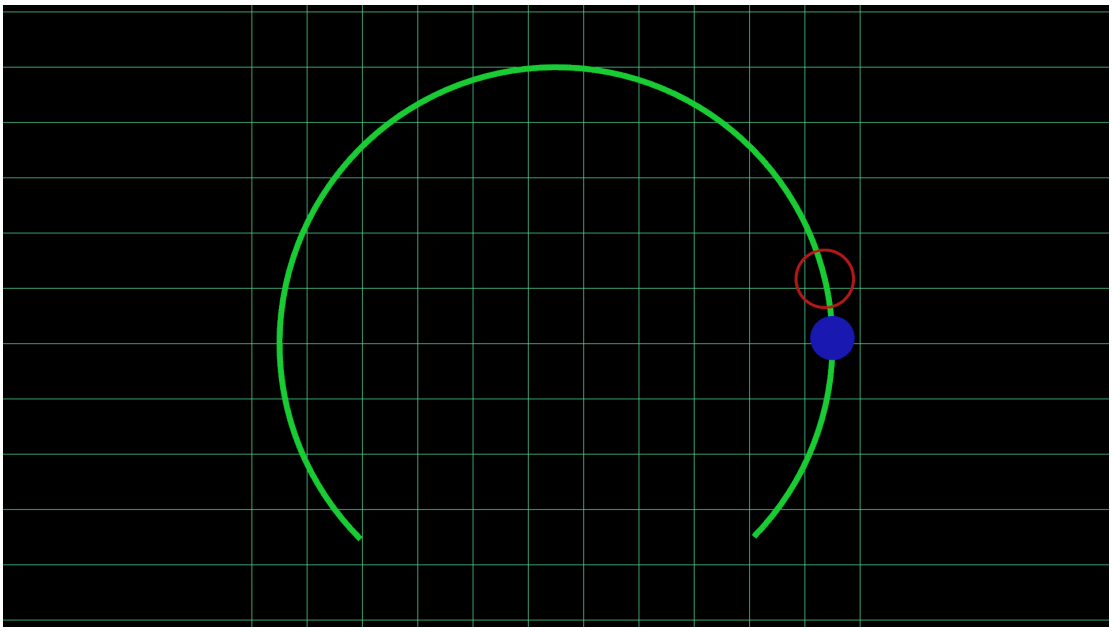

Fig. 5.2 Visual display as in experiments #5 and #6 during Day 1 of the DSE. The subjects had to apply torque to the ISW to position the cursor (blue dot) inside the target (red circle) – which varied its position at each time interval. The cursor and target moved only over the circular arc (green dial), with rest state at its topmost position.

in the centre of target (red circle). For this experiment, there was no filtering between the sensor and the position of the follower cursor in the display.

Generally the subjects adapted promptly to the test (Fig. 5.3a), although two of them, Subject 3 and Subject 4 (S3 and S4), found that it was difficult to maintain that degree of torque ($\pm 10.5\,\mathrm{N}\cdot\mathrm{m}$) for 20 s. Nevertheless, once they improved their hand positioning strategy, they eventually became adapted to the ISW.

Besides accustoming the subjects to the ISW, one of the motivating factors for this test was to determine if humans exhibit arm tremors when holding the ISW – due to isometric muscle contraction – at particular frequencies. Peaks in the power spectrum at specific frequencies during isometric contraction are reported in the literature, and this has been suggested as evidence of coordinated neural firing acting in a rhythmic manner [MRM97]. This idea is also consistent with human operators being discrete controllers (Sec. 2.3.3). In our data, we did not find any characteristic peak in high frequencies (Fig. 5.3b). It is likely that, because subjects used both hands to control the ISW, any frequency peak was filtered out by both hands acting in anti-phase and muscle co-contraction.

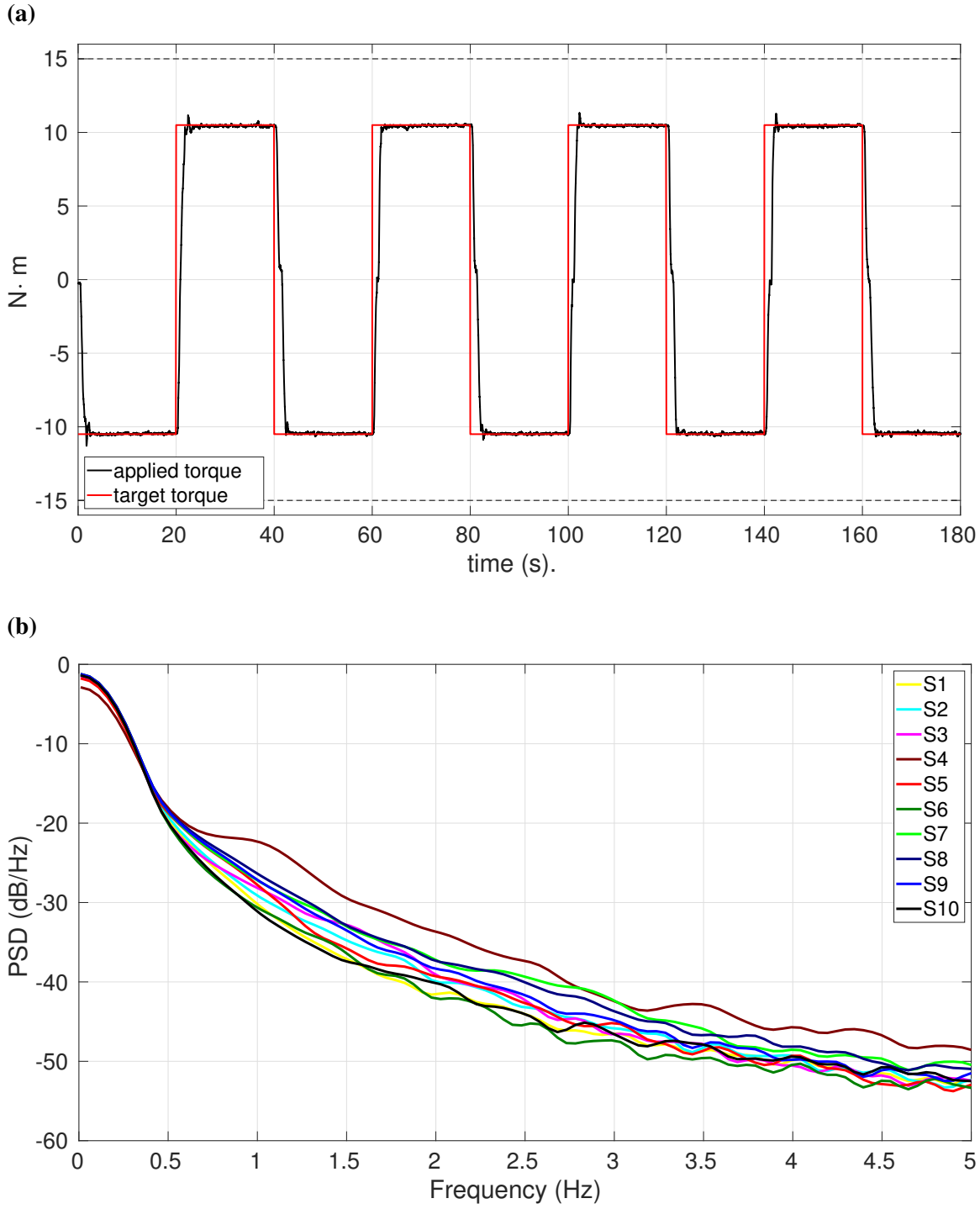

Fig. 5.3 Data collected in the first ISW training experiment. (a) Target position and torque applied by subject 5. (b) PSD during the same test and for all the test subjects.

5.2.2 Second ISW Training Experiment (Exp. # 6 Day 1 in Table B.9)

The second ISW training experiment was very similar to the first, and lasted also for 180 s. The difference was that the target changed position more frequently – every 6 s – and at randomised locations over the dial (Fig. 5.4). The test subjects seemed to be able to track comfortably the target during this exercise.

The data collected from this experiment were analysed through Fitts' Law (Sec. 2.2.1): The parameters of

$$T = N_t + \frac{1}{IP}\log_2\left(\frac{D}{R}\right) \tag{5.2}$$

were fitted to the data recorded in this experiment (Fig. 5.5). Here D was considered to be the initial distance to target position while R the distance at time T. The data yielded $N_t = 0.3228\,\text{s}$ and $IP = 4.1789\,{}^{bits}/_{\text{s}}$. It is shown that the linear relationship of Fitts' law applies for the ISW up to feasible values of the ratio ${}^{D}/_{R}$.

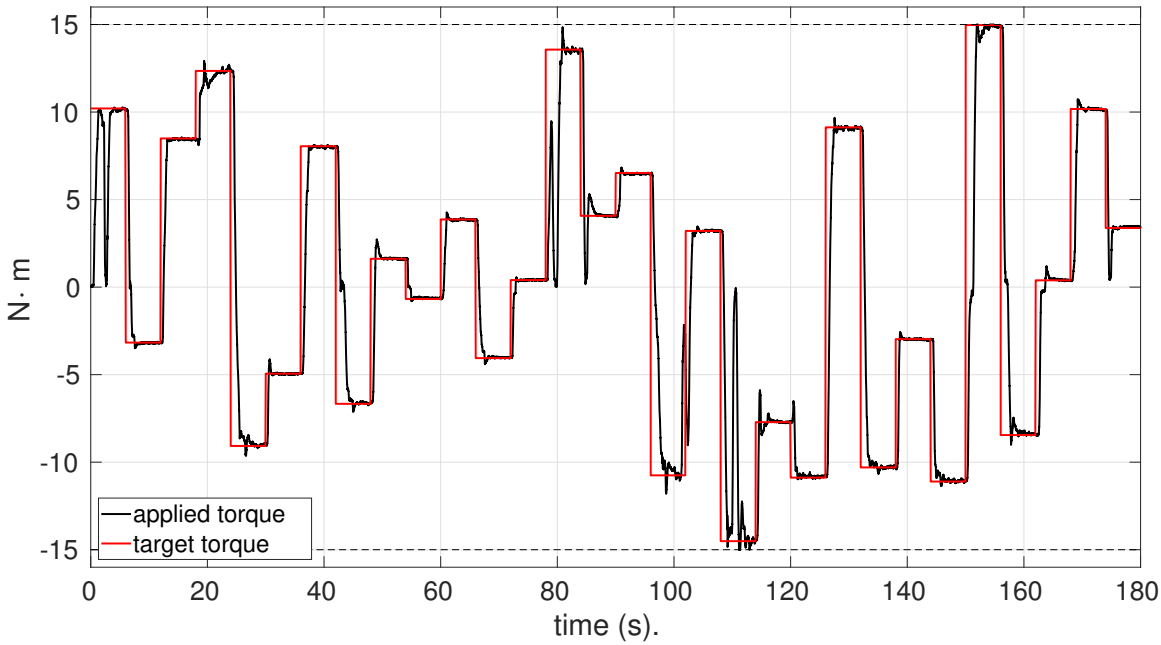

Fig. 5.4 Target position and torque applied during Exp. # 6 Day 1 by S5.

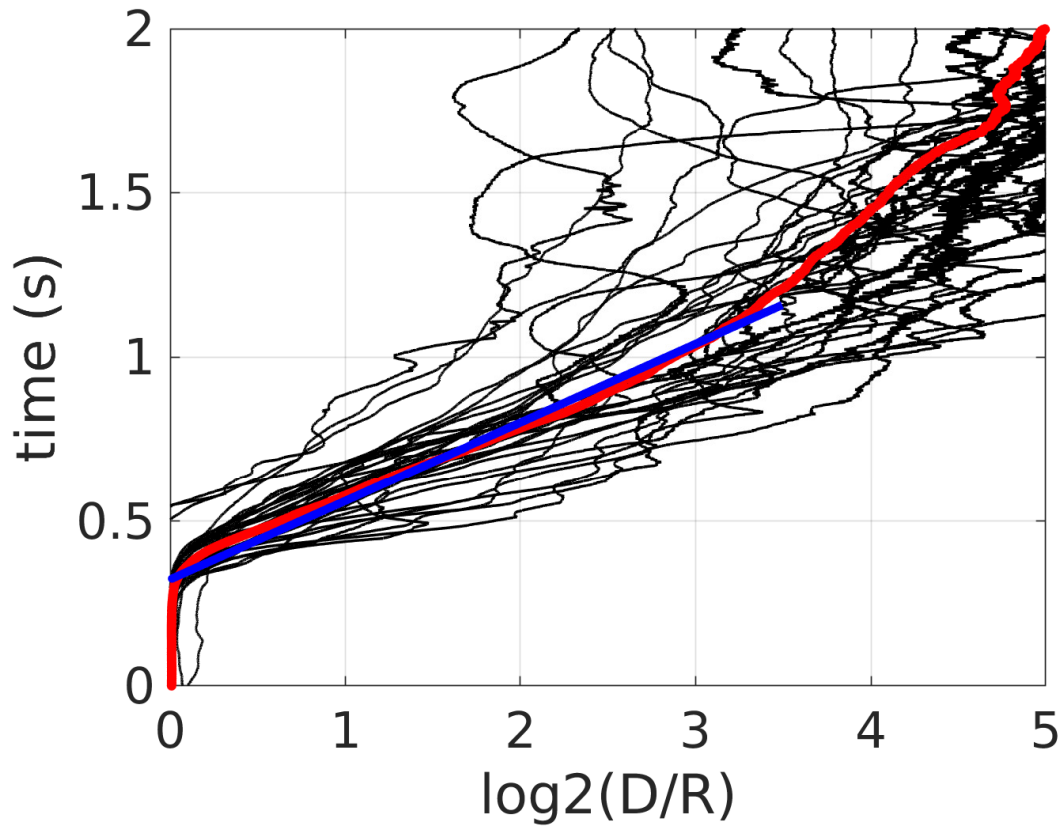

Fig. 5.5 In black, each line is the average time vs. $\log_2 \frac{D}{R}$ relationship for the ten subjects and for each of the randomised target positions they encountered – which were the same for all the subjects. The average for each target position – black curves – is displayed in red, and a line is fitted to this curve (in blue) for $0.1 < \log_2 \frac{D}{R} < 3.5$.

5.3 Driving Experiments with the ISW

All the other experiments with the ISW involved driving a vehicle simulation, which consisted of a linear vehicle model on a pseudo-randomly generated roadway – represented in OpenGL 3D graphics (see Fig. 5.6 and Appendix. B.3). Mostly, all the driving experiments with the ISW were executed during Day 2. The only exception was Exp. #7 in Day 1, which was performed in both days.

The emphasis was placed in investigating potential transfer functions between the torque sensor and the vehicle model – translating torque to SW angle. And with this aim in mind, different transfer functions were tested, which are summarised in Table. 5.1 and discussed in more detail in the following.

As a baseline filter, a simple gain was first considered. The value of this gain, and those of the parameters in the other transfer functions, were tuned empirically before the experiments

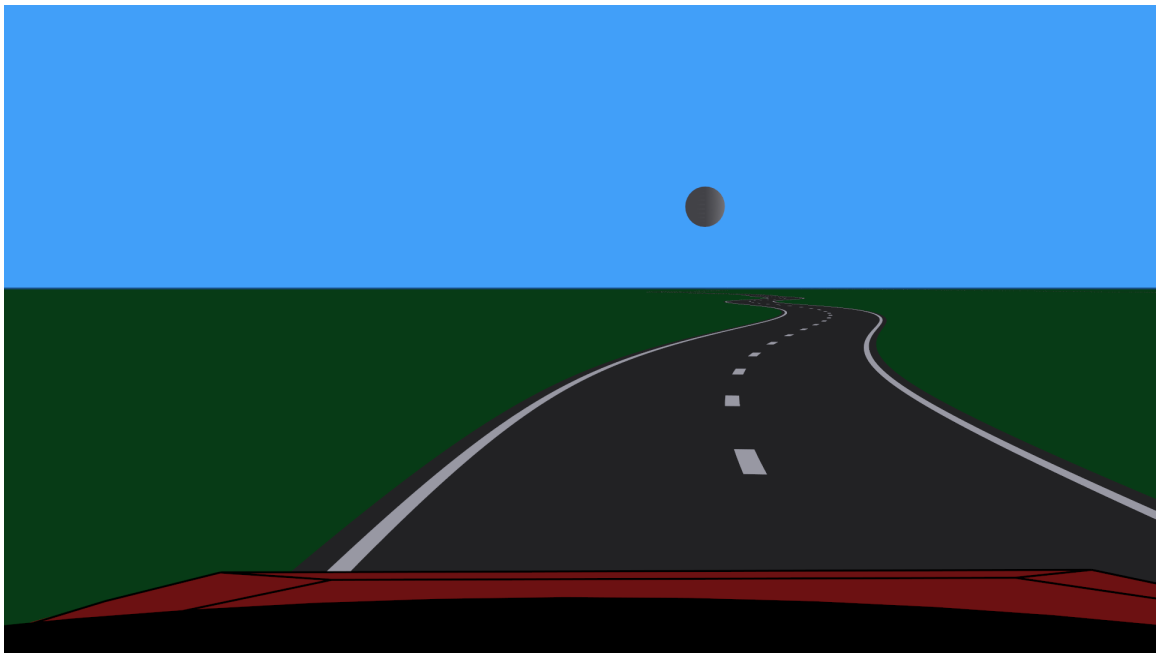

Fig. 5.6 Forward view of the simulated road in the OpenGL simulation as it was presented to the subjects in the ISW driving experiments

by informal testing. This was done to keep the experimental variants presented to the subjects at an acceptable level. Next, a fractional order filter D^{ν} was also considered as a candidate (see Appendix A for an introduction to fractional calculus). As the experiments involved driving the simulation at different speeds $(30, 50, 70\,^{km}/_{\mathrm{h}})$, the index of fractional integration was tuned empirically for each speed value. In the informal tests it was observed that higher order of fractional integration was better for higher speeds. In addition, to contrast the effects of the memory added by the fractional operator with a standard approach, a proportional integral (PI) filter was also examined. In this case, as the PI filter involves a pure integral with a very extreme memory effect – as compared to low level fractional integration – it was observed that lowering the effect of the integrator was seemingly better at higher speeds (Tab. 5.1).

TF↓ **speed**→	$30\,^{km}/_{\mathrm{h}}$	$50\,^{km}/_{\mathrm{h}}$	$70\,^{km}/_{\mathrm{h}}$
Gain K_p	$K_p = 0.75$	$K_p = 0.75$	$K_p = 0.75$
Fractional Integrator D^{ν}	$\nu = 0.05$	$\nu = 0.25$	$\nu = 0.35$
PI TF $K_p + (1 - K_p)\frac{1}{s}$	$K_p = 0.5$	$K_p = 0.6$	$K_p = 0.7$
Steven's Law $K_S S^{\sigma}$	$K_S = 0.15, \sigma = 1.7$	$K_S = 0.15, \sigma = 1.7$	$K_S = 0.15, \sigma = 1.7$

Table 5.1 Different filters employed during the DSE with the ISW.

Furthermore, because the intensity of perceptual cues does not necessarily map in a proportional manner to human perception, Stevens' Law (Eq. 2.10) was introduced in the tests. The gain of Stevens' law was also tuned empirically, while the exponent was taken from previous research in laboratory experiments (Tab. 2.2).

5.3.1 Driving with an ISW at 30 km/h (Exp. # 3 Day 2 in Table B.9)

This experiment involved 7 min of driving with an ISW on a simulated roadway – which was the same for all the subjects. The simulation represented a vehicle with a constant speed of $30\,^{km}/_{\mathrm{h}}$ and the driver sitting at the left seat of the car. Every 60 s, an acoustic signal and an intermittent change in colour in the background sky, indicated to the driver that a change in the dynamics of the vehicle had occurred[2]. The change in the dynamics reflected a different transfer function between the torque sensor and the vehicle model.

The order in which the transfer functions were presented is specified in Table 5.2. Thus the experiment consisted in seven phases. In each phase, after the subject had driven for approximately 30 s, the investigator asked them if the current vehicle response was easier, more difficult or equivalent to the one just before. The answers of the subjects were recorded and numerically coded as *better* $(+1)$, *worse* (-1) and *same* (0). After, these answers were compared to their actual performance, measured as the MSE of the offset of the vehicle with respect to the centre of the lane.

In Figure. 5.7a the MSE for each subject and at each phase of the experiment is shown. In Figure 5.7b, the answers regarding steering feel are presented with a different coloured marker for each subject. In the same figure, the cumulative sum of the mean – for the numerically coded answers – through the different phases is displayed in black colour.

[2]The subjects had been informed about the procedure before the experiment was conducted. Additionally, the subjects had performed the same experiment in Day 1, to achieve acceptable adaptation to the ISW.

Phase #	Transfer Function	Duration
1	Gain	60 s
2	Fractional	60 s
3	PI	60 s
4	Fractional	60 s
5	Stevens's Law + Fractional	60 s
6	PI	60 s
7	Stevens's Law + PI	60 s

Table 5.2 Filter used at each of the phases of the driving experiments with the ISW. The filters were defined in Tab. 5.1

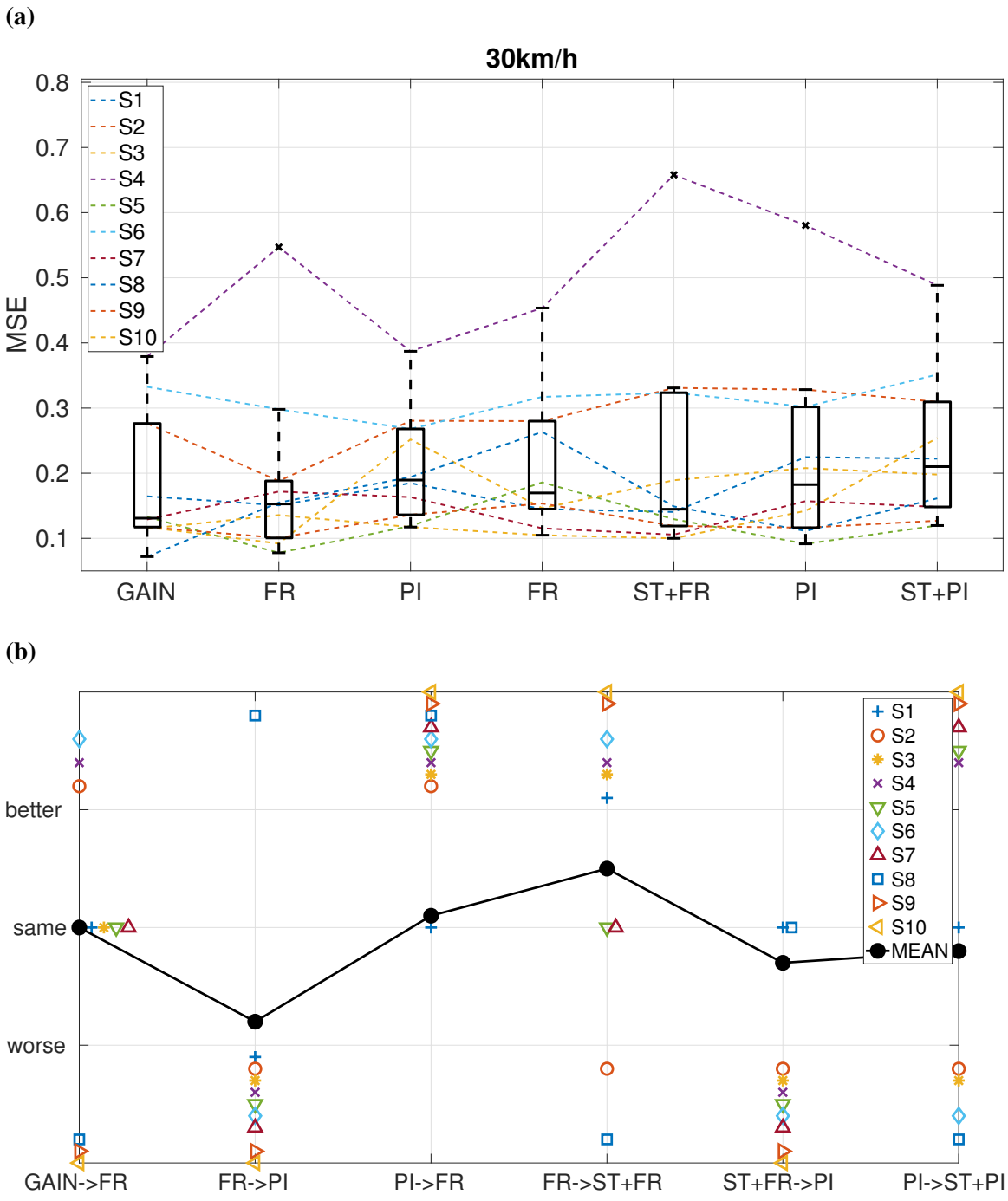

Fig. 5.7 Results for Exp. # 3 Day 2. (a) MSE for each subject and for each phase of the experiment. Boxplots of these values are also included in the figure. (b) The answers of the subjects regarding steering feel with each filter are displayed with coloured markers. In black, the cumulative sum of the mean for the numerically coded answers – through the phases of the experiment – is presented.

At $30\,^{km}/_{\mathrm{h}}$, the subjects did not find on average that the fractional filter improved their control. On the other hand, Stevens' law seemed to improve their steering feel – when combined with the fractional filter – while the PI filter appeared to make it worse. The same can be observed from the MSE of the lateral offset from the centre of the lane (Fig. 5.7a). The subjects produced a larger MSE with the PI transfer function and a lower MSE with a simple gain and with the fractional controller with Stevens' law[3].

5.3.2 Driving with an ISW at 50 km/h (Exp. # 4 Day 2 in Table B.9)

This experiment is analogous to the one before with the exception of the vehicle speed, which in this case was $50\,^{km}/_{\mathrm{h}}$. An identical experiment to this one had been performed already in Day 1, as part of the adaptation process to the ISW. Additionally, during the first day of the experiments, the subjects drove the simulation with a SW on the same road and at the same speed (Exp. #1 Day 1)[4].

Figure 5.8a shows the evolution of the MSE through the different phases of the experiment. The solid dots are the median of the MSE among all the subjects in Day 1. The boxplots summarise the results for the same experiment in Day 2; there was a consistent improvement in performance. The blue line indicates the median performance with a SW. It is noticeable that the subjects showed a lower MSE with the ISW, but this may be related to the characteristics of the employed Logitech SW and the vehicle simulation, which may not necessarily mimic realistic driving. Anyhow this was unanticipated, and several subjects were surprised by their own skill while using the ISW as they spontaneously manifested.

At $50\,^{km}/_{\mathrm{h}}$ the differences between the tested transfer functions (Tab. 5.1) were more significant than those at $30\,^{km}/_{\mathrm{h}}$; the fractional transfer function yielded the lowest median MSE – although adding Stevens' law made it the worse performer, followed by the PI controller as the second worse performer together with the proportional transfer function. The answers of the subjects with respect to steering feel agree with these results (Fig. 5.8b). Several subjects also claimed that the PI controller was *too slow*.

In Figure. 5.9 the steering movements produced by S7 in this experiment with the ISW and with the SW – Exp. #1 Day 1 – are compared. For the ISW, the signal is shown before and after the fractional filter was applied. The steering signal in the ISW incorporates some of the features of joystick control; it is composed of shorter pulses but of higher amplitude than those of the SW. Thus somewhat the ISW combines the comfort of the SW with the rapid control actions of a joystick (Sec. 3.4.4).

[3]Note that S4 control responses were in the outlier range for this and for most of the conducted experiments.

[4]For the case of the SW, the transfer function between the control device and the vehicle simulation was simply the steering ratio gain (r_s). A force-feedback effect was also implemented (Appendix B.3).

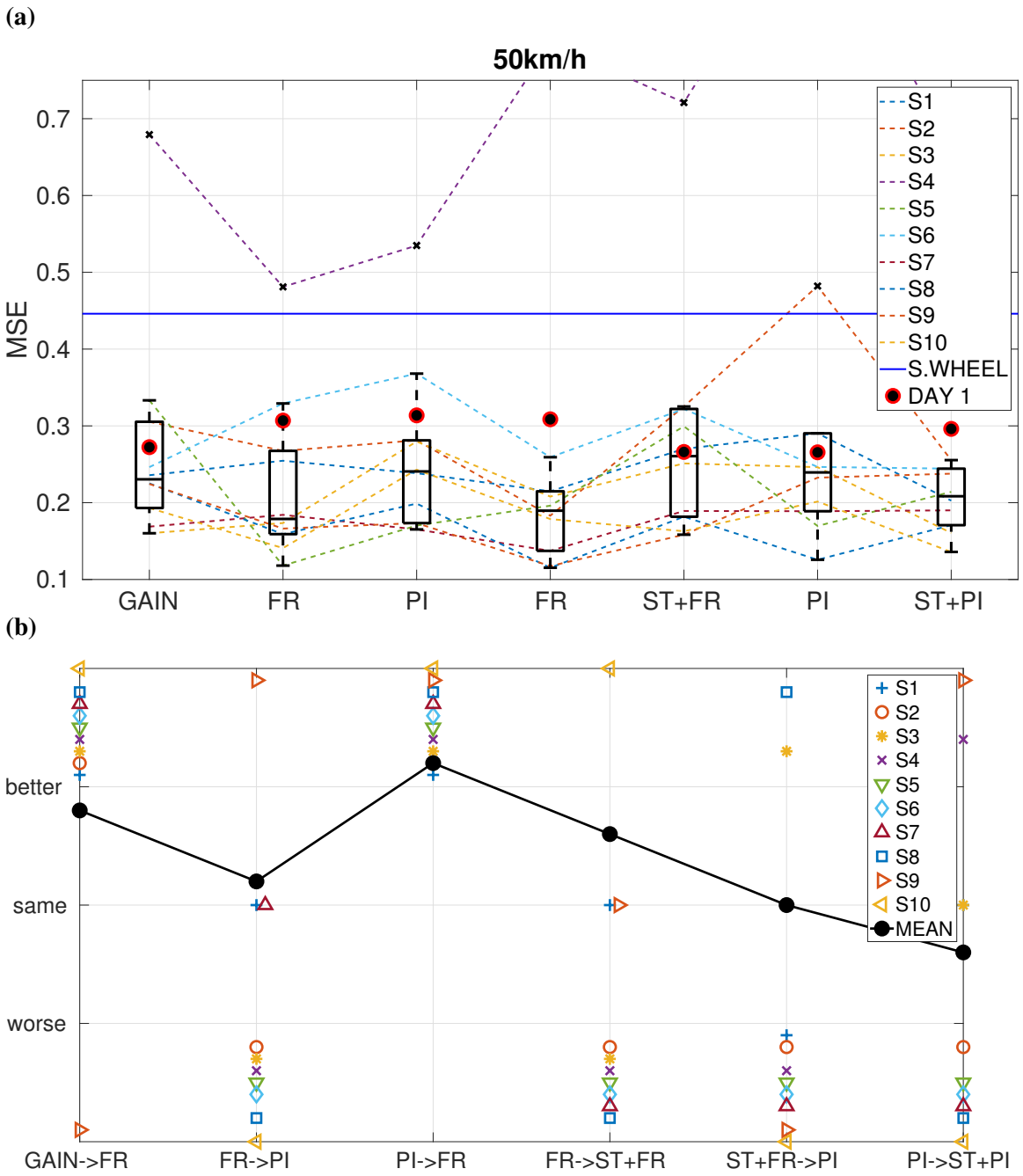

Fig. 5.8 Results for Exp. # 4 Day 2. (a) MSE for each subject and for each phase of the experiment. Boxplots of these values are also included in the figure along with the median values (solid dots) of the lane keeping error in Day 1 (ISW). In blue, the performance with the SW is shown. (b) The answers of the subjects regarding steering feel with each filter are displayed with coloured markers. In black, the cumulative sum of the mean for the numerically coded answers – through the phases of the experiment – is presented.

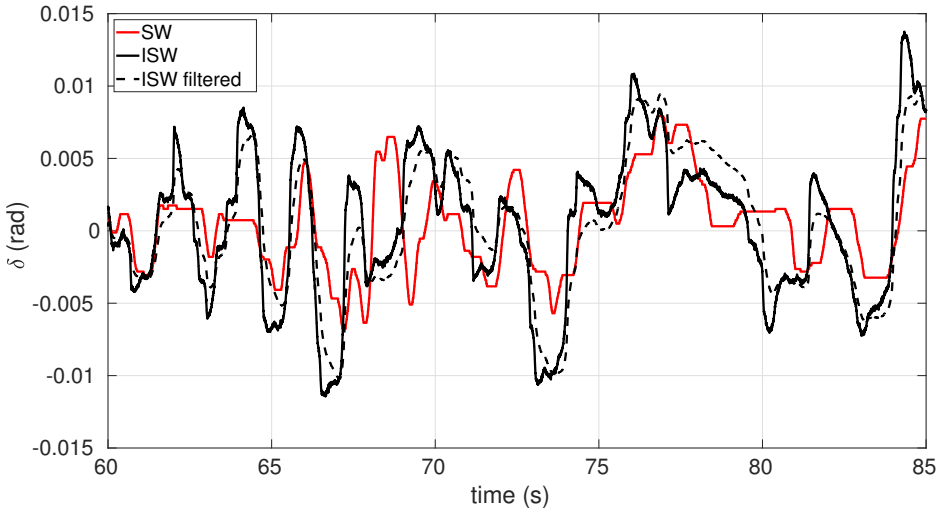

Fig. 5.9 Comparison of the steering signals from Exp. #1 Day 1 (SW) with Exp. # 4 Day 2 (ISW) at $50\,{}^{km}/_{\mathrm{h}}$ on a pseudo-random road for S7 with the fractional filter.

5.3.3 Driving with an ISW at 70 km/h (Exp. # 5 Day 2 in Table B.9)

The same experiment was repeated at $70\,{}^{km}/_{\mathrm{h}}$. At this speed, the differences between transfer functions were even more pronounced but the results were very similar; the proportional and the PI transfer functions were the worse performers (Fig. 5.10a). The lowest MSE was obtained again with the fractional filter. Looking at the difference in performance between the fractional and the proportional transfer functions, it is concluded that filtering becomes more necessary as the speed increases. Even so, the extreme memory effect of a classical integral – in the PI transfer function – makes the vehicle very difficult to control at higher speeds. Nevertheless, the subjects were less sensitive while assessing their own performance in this experiment (Fig 5.10b).

Albeit other transfer functions remain to be tested – for instance second order filters – the results are suggestive of fractional order filtering to be effective and easily tuned. One conceivable explanation is the evidence that the neuromuscular system presents fractionality [Mag06]. As an ISW involves static control, some of the viscoelastic properties of the muscles may be diminished, and a fractional filter could act as a surrogate of them. This is compatible with the fact that at higher speeds larger fractional integration is needed; humans will hold more tightly a SW for higher workload driving, increasing their arms mechanical impedance to achieve greater limb stabilisation.

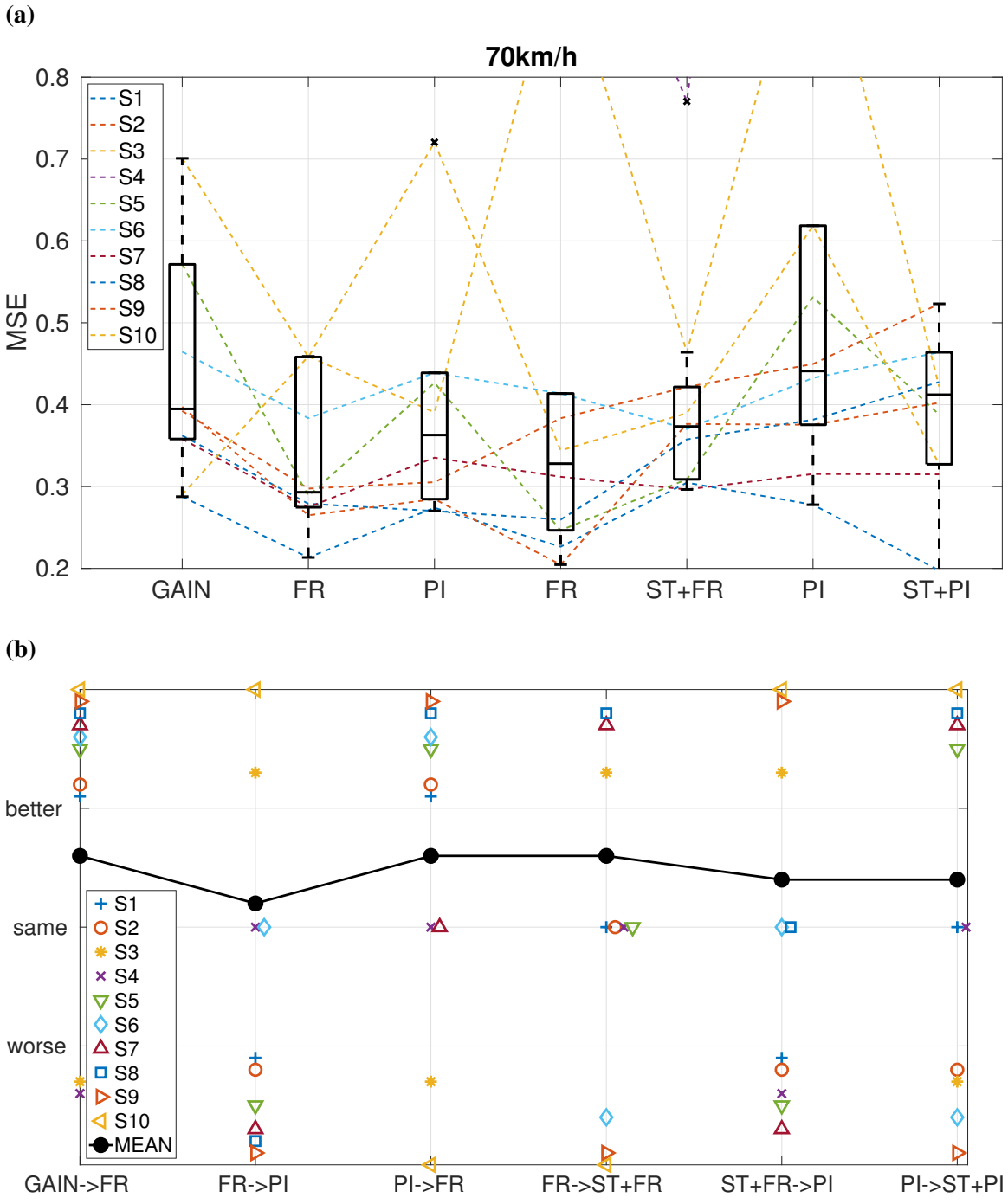

Fig. 5.10 Results for Exp. # 5 Day 2. (a) MSE for each subject and for each phase of the experiment. Boxplots of these values are also included in the figure. (b) The answers of the subjects regarding steering feel with each filter are displayed with coloured markers. In black, the cumulative sum of the mean for the numerically coded answers – through the phases of the experiment – is presented.

Regain of Control Experiments

One concerning condition, in autonomous driving systems research, is the transition of control between the machine and the human. In [MJ09], experiments with subjects performing simulated regain of control situations were reported; the subjects were requested to regain control of a vehicle in a near collision scenario. It was shown that driver's reaction time to a potential hazard is larger when regaining control from an autonomous driving system.

A part of the DSE (Sec. B.3) was designed to test if the reaction time, when regaining control, can be reduced with an ISW. In experiments 7a and 7b the subjects were asked to look at the OpenGL simulation while the vehicle drove autonomously through a curved road geometry – this was done with an implementation of the SG model (Sec. 4.2.1). The subjects were requested to keep the hands off the SW (or ISW). At times, the display was temporarily occluded with a black screen. This was done in order to represent switching attention to secondary tasks, such as checking a cell phone. During the simulation, the subjects could see the vehicle autonomously dodging an obstacle in the middle of the road, by slightly going outside of the lane and returning to its centre. After a second full display occlusion was cleared, and the subjects could see the road again, an acoustic signal and an intermittent flash in the background signalled the drivers to take hold of the SW (or ISW) and regain control of the vehicle[5] to avoid a collision with a new obstacle (Fig. 5.11).

Experiments 7a and 7b were identical, with the exception that experiment 7a was executed with the SW and 7b with the ISW. Nevertheless, the subjects were told that both experiments were different, in order to minimise adaptation effects. Additionally, half of the subjects performed experiment 7a before 7b, while for the other half the order was reversed. In experiment 7a the SW rotated according to the steering angle applied by the autonomous system. For the case of the ISW, steering control was implemented with the fractional transfer function (Table. 5.1).

In Fig. 5.12a, the path of the vehicle for each subject in experiments 7a and 7b is shown, from the time they were requested to regain control by the system. The subjects managed to obtain higher distance margins from the obstacle and return to the centre of the lane quicker with the ISW. All of the subjects decided to steer tangentially to the road, with the exception of S9 when using the ISW.

Fig. 5.12b shows the steering movements of S6 with both control devices, and during the obstacle avoidance manoeuvre; generally all subjects produced a higher amplitude response in a shorter time with the ISW. This was expected, as the ISW does not involve arm

[5] The subjects had already performed a very similar, but much easier test (Exp.# 6 Day 2) before this one, so they were familiar with all the elements in Exp. #7 in advance: autonomous driving, temporary occlusion, and regain of control to avoid an object in the centre of the road.

Fig. 5.11 Screenshot of the regain of control experiment at the moment the screen flashed – different sky colour – and an acoustic signal was produced, requesting the driver to take control of the vehicle in a potential collision scenario.

displacement. The notable result is that after the initial control pulse, the subjects with the ISW managed to stabilise the vehicle in a shorter time.

5.4 Applications of an ISW

The presented study of vehicle control through an ISW is not specifically directed to propose ground vehicles being driven with an ISW. In semi-static manoeuvres such as parking a vehicle, it can be difficult to assess the wheels turning angle based only on steering feel. This is even more true considering that the relationship between torque and steering feel is non-linear (Sec. 2.2). Thus semi-static manoeuvres have not been considered here, and are left for future work. Nonetheless, there are a number of schemes in which the ISW is a feasible technology for vehicle driving. Perhaps the most relevant application is the design of *shared control* systems.

It has been long recognised that, although vehicle technologies must be aimed to *unburden* the human-operator, full automation is impractical in many situations [BT54]. Thus, as humans are better controllers of plants with low order simple dynamics – specifically, proportional control – SBW technology could be employed to reduce driving to a more simple task, in which steering control is shared between the human and an intelligent system.

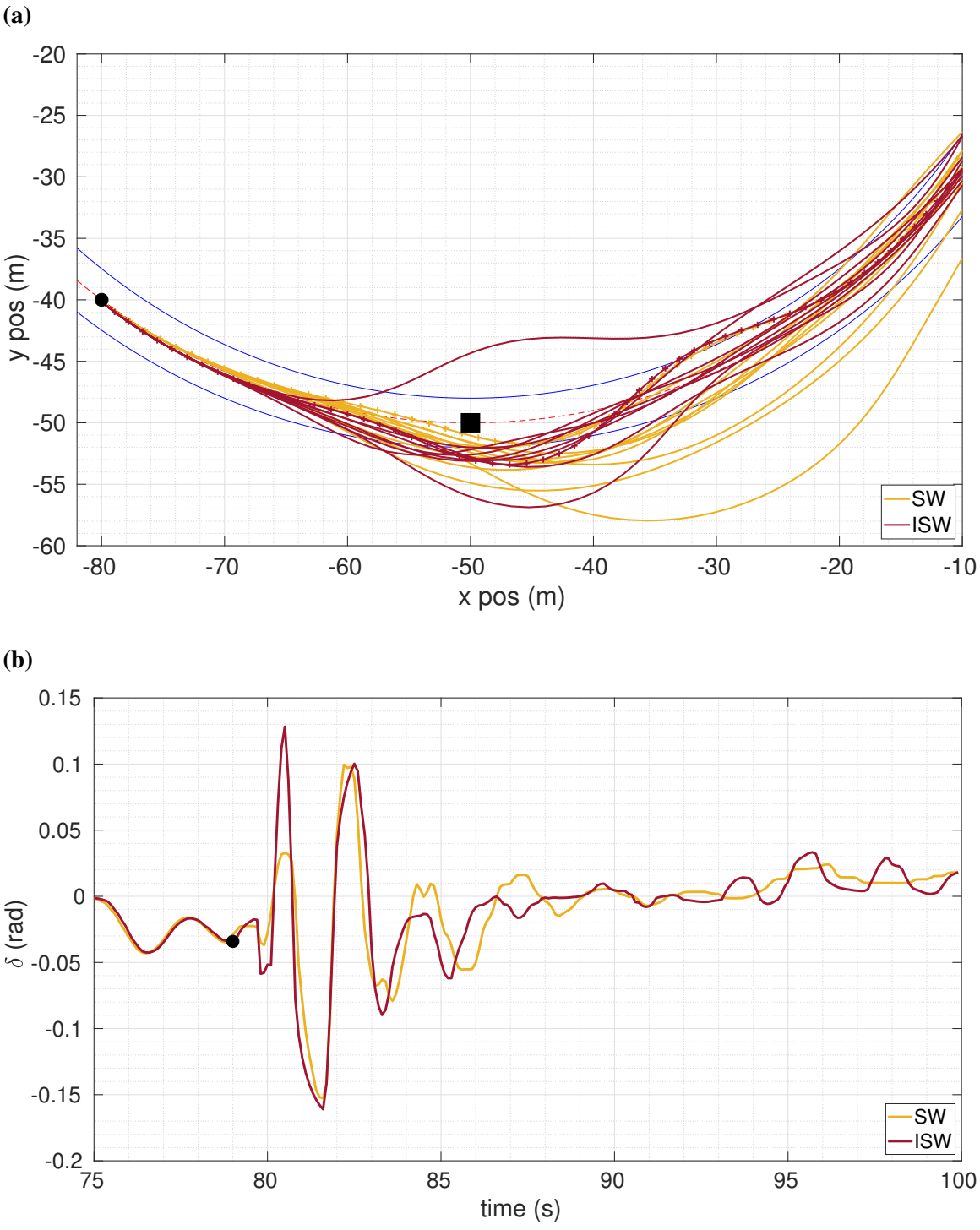

Fig. 5.12 (a) Path of the cg of the vehicle for all the subjects in experiments 7a and 7b. The blue lines display the position of the left and right lane lines, while the red dashed line represents the middle lane line. (b) Steering signal in experiments 7a and 7b for S6. The black dot marks the time at which the control was transferred back to the driver.

One of the difficulties in designing shared control systems, is in determining the degree of control that the intelligent system shares with the human. In [AMB12] this concept is referred to as the *Level of Haptic Authority* (LoHA), and it specifies the resisting force of the control device to the applied force by the human. Thus the LoHA is set to establish how much of the control task is taken from the human-operator by the intelligent system. An analogous but more illustrative concept is that of the H-mode [FCA+17], which compares shared control to holding the reins of a horse more tightly – manual control from the human-operator – to loosely – fully automated system. This is usually known as the H(Horse)-metaphor.

However, the control task at hand and the H-mode cannot be considered independent of each other; the impedance of the SW may change the control response of the human, in the same manner as muscle impedance changes the stability of motor control. The ISW though, *orthogonalises* the control signal from the H-mode; thus it is a control device specially well suited for the implementation of shared control systems.

To conclude the chapter, some of the schemes in which the ISW is applicable are summarised. A more detailed study of these possibilities is also intended as future work.

1. **Non automated control:**

    - **Speed adaptive ISW:** One possibility is a system that transitions from a SW – at very low speed – to an ISW for highway driving at higher speeds. Although this has not been tested, the ISW does not seem *a priori* appropriate for semi-static manoeuvres.

2. **Automated control:**

    - **Strategic and manoeuvring levels of control:** According to Minchon's model, driving is composed of three levels: control, manoeuvring and strategic level [GS14]. The ISW could be used to control only some of these levels. For example, a driver model could easily handle the control level by keeping the vehicle within the lanes at all times, and adjusting the speed to avoid collisions. The driver would communicate to the intelligent system – using the ISW – with the intention of switching lanes (manoeuvring level) or exiting a highway to reach a destination (strategic level) as examples.
    - **Low probability situation handling with full control:** In view of the possibility of an intelligent system capable of autonomous driving, it seems more reasonable to consider an ISW instead of a moving wheel in front of the driver. In case of a hazard which the automated system cannot handle, the human driver could bring forth a swifter control regain with an ISW – in the same manner as in the regain

of control experiments above (Fig. 5.11). Typically, AI or other sort of intelligent systems are not efficient in handling low probability situations [Lic60].

3. **Shared control:**

   - **Low probability situation handling with shared control:** Similar to the case above, the driver could use the ISW to modify or over-ride the AI control manoeuvres or decisions. Input pulses on the ISW would be superposed to the control response intended by the intelligent system. For instance, if the intelligent system is handling the road curvature but there is an unexpected obstacle on the road, the human driver could add a correction to the undergoing control action. This steering pulse would be relative to the steering angle at the wheels applied by the AI, and hence independent of any visual interpretation of the current steering angle.
   - **Shared control through H-mode:** With this scheme, the human driver controls the car at all times, but with the help of the intelligent system. The intelligent system utilises a driver model to maintain the vehicle within the lanes, but the driver can over-ride the control decisions of the model according to a preset (or adaptive) H-mode. ISWs are more analogous to the reins of a horse than a conventional SW, as the position of the ISW is independent of the yaw rate. Hence transitions in H-mode may be more natural to the driver with an ISW.

Lastly, the shape configuration of the controls in ground vehicles may also be reconsidered. One immense and obvious advantage in using a circular configuration, for conventional SW design, is its invariance with respect to the applied steering angle; hence it is uncomplicated to perform suitable steering movements even when $\delta(t) > \frac{pi}{2}$ rad. With an ISW this is inconsequential, and one can think on the design of new configurations. For instance a handle bar or other options found only in concept cars until now, such as the Wrist-Twist Instant Steering system – included in some Ford prototypes in the past – or the twin-levers in the Honda EV-STER model. In this last example, the driver controls the car with two control sticks – one at each hand. The sticks are coupled to each other, hence the anti-phase filtering properties of the SW are preserved. This system makes use of SBW technology to modify the torque in the sticks to neutralise the perturbations produced by lateral acceleration on the driver.

Chapter 6

Conclusions and Future Work

The study of driver behaviour covers a broad spectrum of scientific domains, from neuroscience and psychology to control systems engineering and artificial intelligence. At the same time, and within any of these domains, driver behaviour can mean several different things, such as gaze fixation patterns on the forward roadway scene, speed control, crash avoidance manoeuvring, anxiety level measurements and drowsiness monitoring, just to name a few. In this dissertation, the effort has been directed towards the study of steering control.

This research has been conducted with the purpose of designing modelling strategies that mimic the responses of the steering movements produced by humans – while controlling a car on a public roadway. Even within this purpose, multiple research frameworks can be adopted. For example, there is a vast literature on steering control models aimed at creating software packages to test vehicles in computer simulations, removing the human driver from the control loop or implementing conditional automation systems. Here, the modelling strategies were designed with the idea of being deployed in shared control systems, i.e., systems in which the control of the car – or of another type of machine – is shared between a human and an intelligent system simultaneously. Shared control systems have gained relevance in recent times – partly due to the availability of *steer-by-wire* technology in conventional cars, artificial intelligence developments and an increase in the computational capacity of low-power devices, such as FPGAs.

As it has been mentioned in this dissertation, and established in previous literature, shared control systems in which the model for the virtual human is not representative of the human steering movements may decrease control performance. On the other hand, when the assisting virtual human model can imitate to an extent human control behaviour – and hence referred to as *biofidelic* – shared control may increase performance. Thus the objective is, as the dissertation title suggests, to construct a biofidelic model for steering control.

Starting from before, and progressing in parallel to steering control modelling research, a rich literature in human-machine systems has come to existence. This research seems to have been initiated within the defence research realm in the 1940s. Hence the present study was commenced by reviewing pertinent results on the human-machine literature, some of which have been expanded and generalised; one of them being the well known Crossover model. In particular, this classical research was initially more concerned with aeroplanes and tanks than with cars, so not all of its results generalise to the case of steering control on roadways.

Commonly, the human-machine systems literature has borrowed numerous concepts belonging to control systems theory, for instance classical linear control approaches through transfer functions and optimal controllers. As these methods have analogous correlates in the more general domain of ordinary differential equations, they elicit control responses only according to a single vector of initial conditions – or at most weak memory effects such as those produced by statistical measures and additive accumulators. Contrarily, biological systems – and more generally any complex system – show responses based on a history of past events, i.e., they are systems with memory effects or *fractionality*. Thus one of the first contributions in this dissertation, was to extend the Crossover model for the control of systems with memory. And for that, data collection experiments where naïve test subjects had to control plants with fractionality were executed for the first time. From these data, and by using the mathematical theory of *fractional calculus*, the Crossover model was generalised to include the control of such plants. These analyses led to additional results, such as assessing fractionality in the visual system while the human is engaged in dot following tasks, representing a vehicle with a grey-box modelling approach that compensates the uncertainty in some parameters through fractional operators, and representing human control patterns with finite impulse response filters. All these results add now to the already ample literature on the topic of human-machine systems, offering new modelling possibilities.

More specific to the task at hand, which as indicated was modelling steering control, the investigation was continued by analysing the steering movements found in naturalistic driving data. From this inquiry two main conclusions were drawn. On the one hand, the steering movements displayed by drivers, during lane keeping manoeuvres, can be explained as a superposition of characteristic steering pulses. These pulses are asymmetrical, which further endorses the hypothesis of humans using a combination of feed-forward and feedback control in manual control tasks. On the other hand it is declared that, it is impractical attempting to fit the parameters of deterministic steering control models in the time domain from naturalistic driving data – for models with only a few parameters it is virtually impossible, while for models with a large number of parameters it results in overfitting the data. This notion challenges the traditional view and is justified with multiple

arguments: the human driver switches their attention to different things at different times, humans present stochastically varying effective time delay, driving data are essentially noisy – with additional neuromuscular noise introduced by the human, and the human driver may attempt to optimise different things at different times, to name but a few. All these were supplementarily corroborated, with the case example of the well known linear model by Salvucci and Gray. Putting it in layman's terms, a human driver will produce different steering movements by driving through the same roadway segment at different times. These differences may be even larger between different drivers. Hence, when fitting a steering control model from data to represent the human driver, which human driver and at what particular time are we thinking about? Does there exist a *generic human driver* – or a *generic human-operator* in the more general case?

If a generic human-operator is there to exist, one possible way to characterise them is in the frequency domain. Even if the control responses of humans are very variable, they may present characteristic frequency response. This has been done extensively in the classical literature, with the Crossover model as its foremost example. Here an alternative approach has been developed, which consists in characterising the human-operator from a statistical perspective. And this approach led us to the novel concept of multiplicative human control. Summarising, the magnitude of human control responses in compensatory tasks is shown to be well described by log-normal probability distributions. As log-normal probability distributions arise from multiplicative dynamics, a multiplicative controller to act as surrogate of the human operator is proposed here. The multiplicative model is validated by comparing it with the manipulative control actions of human subjects, shown to be consistent with the Crossover model and proved to be a generalisation of Fitts' law – for the case when the errors are reduced at a constant ratio.

To generalise compensatory *dot following* tasks – such as the ones explained by multiplicative control – to automobile driving, the greatest obstacle is on determining which visual cue(s) drivers employ. Although there is literature with consistent results on the gaze patterns of humans while driving on curved tracks, no conclusive results on which optical cues are employed for lane keeping on straight paths were produced to date. Thus an extensive study regarding this was conducted here. The study included new data collection experiments with test subjects; these involved designing a simple driver simulator software application specifically for this research. The results suggest that drivers employ the optical information produced by the projection of the so-called *splay angles* over the retina as principal optical variables, for lane-keeping and at low speeds. This is further justified from the viewpoint of neuroscience, optical illusions and mathematical consistency. For lane-keeping at higher speeds, further analysis of naturalistic driving data suggested that steering pulses have a

stronger correlation with the Critical Normalised Yaw-rate than with other lane keeping metrics.

Thus from all these conclusions a new model, reflecting multiplicative dynamics and far-point error control – which it is termed the Human-centred Driver model – was designed and first proposed here. Besides all the described human-like – or biofidelic – features exhibited by multiplicative control and perception based on optical information, the model displays pulse-like behaviour for lane keeping and is able to produce stable control, within the same steering entropy value range as that of human drivers. Further, the model uses feed-forward control for roadway guidance. Besides its potential application to shared control systems design, the Human-centred Driver model can be applied for vehicle testing, developing semi-autonomous control systems or as an analysis tool for driver behaviour. In a broader context, the multiplicative human control model is an additional tool for human-machine systems research.

As mentioned, this research has gained renewed interest, in correspondence with an increasing interest in ground vehicle automation and the availability of steer-by-wire controls. On that account, the dissertation concludes with an extension towards vehicle controls; experiments were conducted in which naïve test subjects had to control a vehicle simulation *driving by torque*. These experiments additionally expanded classical literature in which isometric control sticks were tested, and where it was shown that subjects perform more efficient control with these devices as compared to conventional control sticks. Here, analogous results were obtained with an *isometric steering wheel*, specially for the case in which the driver has to take back the control from an autonomous system to avoid a collision with an obstacle. Moreover, various transfer functions – acting as transducers between applied torque and the steering angle at the wheels of the car – were evaluated. It was found that fractional transfer functions are suitable options. We believe that this may have some relation to the fact that muscular dynamics are well modelled through fractional differential equations; hence a fractional filter yields filtering properties similar to those exhibited by the human neuromuscular system.

6.1 Future Work

Commonly, when trying to bring out some answers, we find ourselves discovering new questions. This is even more true for an interdisciplinary scientific project such as this one. So there are a number of related topics that have been identified for forthcoming examination.

First of all, there is the question of online parameter adaptation of the Human-centred Driver model. Different sets of parameters represent different operational regimes of the

human driver and variability among drivers. If the model has to offer relatively good predictions of what the human driver would do, so that there is good understanding between the intelligent system and the human, the parameters need to change along a subspace representing their biofidelic regime. One possibility is using adaptive *self-tuning* systems, with some added constraints to maintain the parameters within the required subspace. Hence for example, for different speeds, driver workload and driver's level of intended performance, the assisting model will employ different parameter sets. The Human-centred Driver model would provide a sketch of the necessary steering movements a particular parameter set, while the human driver could add high frequency information or further corrections.

A second prospect, related to the one above, is the possibility of the Human-centred Driver model being used to monitor the driver, instead of assisting in the control of the automobile. Thus similarly as already described, the control parameters will move along a *biofidelic subspace*, and upon the parameters exiting it, distinct driver's operational regimes can be characterised: drowsiness, driver distraction, inebriation, or high anxiety levels to name a few. In both of the pointed cases, the technical challenge resides more on the data acquisition part than on the analysis, as similar techniques have been extensively applied for monitoring industrial systems.

With respect to the here called *biofidelic-subspaces*, one parameter of special interest is the effective time delay (τ). A first investigation regarding this is currently being put forward [ZMGG18], by considering the restricted one-dimensional case of the τ biofidelic-subspace; the parameter τ is shown to fluctuate according to a Gamma distribution with parameters representative of *normal driving*.

Furthermore, regarding the driving by torque concept introduced at the end of the dissertation, a variety of fronts have been left open. Although preliminary testing through experiments has been conducted for this research, additional combinations of *torque-steering angle* transducer parameters may be tested, or different classes of transfer function can be employed. Additionally, other configurations of the control device could be assessed – like twin levers for instance. Most importantly, the integration of the *isometric steering wheel* with the multiplicative human controller – in a shared control scheme – remains to be tested.

References

[Abe15] Masato Abe. *Vehicle handling dynamics: theory and application*. Butterworth-Heinemann, 2015.

[ABM82] W Abend, Ea Bizzi, and P Morasso. Human arm trajectory formation. *Brain: a journal of neurology*, 105(Pt 2):331–348, 1982.

[AC61] Emanuel Averbach and Abner S Coriell. Short-term memory in vision. *Bell Labs Technical Journal*, 40(1):309–328, 1961.

[ACMvP12] David A Abbink, Diane Cleij, Mark Mulder, and Marinus M van Paassen. The importance of including knowledge of neuromuscular behaviour in haptic shared control. In *Systems, Man, and Cybernetics (SMC), 2012 IEEE International Conference on*, pages 3350–3355. IEEE, 2012.

[AJMD75] R Wade Allen, Henry R Jex, Duane T McRuer, and Richard J DiMarco. Alcohol effects on driving behavior and performance in a car simulator. *IEEE transactions on systems, man, and cybernetics*, 5(5):498–505, 1975.

[AMB12] David A Abbink, Mark Mulder, and Erwin R Boer. Haptic shared control: smoothly shifting control authority? *Cognition, Technology & Work*, 14(1):19–28, 2012.

[AMK89] Richard A Abrams, David E Meyer, and Sylvan Kornblum. Speed and accuracy of saccadic eye movements: characteristics of impulse variability in the oculomotor system. *Journal of Experimental Psychology: Human Perception and Performance*, 15(3):529, 1989.

[Ana94] Thomas J Anastasio. The fractional-order dynamics of brainstem vestibulo-oculomotor neurons. *Biological cybernetics*, 72(1):69–79, 1994.

[ARB03] Brian Andonian, William Rauch, and Vivek Bhise. Driver steering performance using joystick vs. steering wheel controls. *SAE transactions*, 112(6):1–12, 2003.

[Bak87] James E Baker. Reducing bias and inefficiency in the selection algorithm. In *Proceedings of the second international conference on genetic algorithms*, volume 206, pages 14–21, 1987.

[BC98] Matthew Botvinick and Jonathan Cohen. Rubber hands 'feel'touch that eyes see. *Nature*, 391(6669):756, 1998.

[Bes12] Matt C Best. A simple realistic driver model. In *Proceedings of the 11th International Symposium on Advanced Vehicle Control*. © Korean Society of Automotive Engineers and the Society of Automotive Engineers of Japan, Inc., 2012.

[BK69] Sheldon Baron and David L Kleinman. The human as an optimal controller and information processor. *IEEE Transactions on Man-Machine Systems*, 10(1):9–17, 1969.

[BKÖ08] Agamirza E Bashirov, Emine Mısırlı Kurpınar, and Ali Özyapıcı. Multiplicative calculus and its applications. *Journal of Mathematical Analysis and Applications*, 337(1):36–48, 2008.

[BL96] Andrew C Beall and Jack M Loomis. Visual control of steering without course information. *Perception*, 25(4):481–494, 1996.

[BM14a] Ola Benderius and Gustav Markkula. Evidence for a fundamental property of steering. In *Proceedings of the Human Factors and Ergonomics Society Annual Meeting*, volume 58, pages 884–888. SAGE Publications, 2014.

[BM14b] György Buzsáki and Kenji Mizuseki. The log-dynamic brain: how skewed distributions affect network operations. *Nature Reviews Neuroscience*, 15(4):264–278, 2014.

[BOF+01] Etienne Burdet, Rieko Osu, David W Franklin, Theodore E Milner, and Mitsuo Kawato. The central nervous system stabilizes unstable dynamics by learning optimal impedance. *Nature*, 414(6862):446–449, 2001.

[BS99] Nikhil Bhushan and Reza Shadmehr. Computational nature of human adaptive control during learning of reaching movements in force fields. *Biological cybernetics*, 81(1):39–60, 1999.

[BSRO95] Robert C Barrett, EJ Selker, JD Rutledge, and RS Olyha. Negative inertia: a dynamic pointing function. In *Conference companion on Human factors in computing systems*, pages 316–317. ACM, 1995.

[BT54] HP Birmingham and FV Taylor. A design philosophy for man-machine control systems. *Proceedings of the IRE*, 42(12):1748–1758, 1954.

[Bur80] David Burr. Motion smear. *Nature*, 284(5752):164, 1980.

[CEB78] Stuart K Card, William K English, and Betty J Burr. Evaluation of mouse, rate-controlled isometric joystick, step keys, and text keys for text selection on a crt. *Ergonomics*, 21(8):601–613, 1978.

[CG07] Delphine Cody and Timothy Gordon. Trb workshop on driver models: A step towards a comprehensive model of driving? In *Modelling Driver Behaviour in Automotive Environments*, pages 26–42. Springer, 2007.

[CI02] Colin WG Clifford and MR Ibbotson. Fundamental mechanisms of visual motion detection: models, cells and functions. *Progress in neurobiology*, 68(6):409–437, 2002.

[CMN83] Stuart K Card, Thomas P Moran, and Allen Newell. *The psychology of human-computer interaction*. L. Erlbaum Associates Inc., 1983.

[CPL78] Martha Constantine-Paton and Margaret I Law. Eye-specific termination bands in tecta of three-eyed frogs. *Science*, 202(4368):639–641, 1978.

[CPX09] YangQuan Chen, Ivo Petráš, and Dingyü Xue. Fractional order control-a tutorial. In *American Control Conference, 2009. ACC'09.*, pages 1397–1411. IEEE, 2009.

[Cra47] Kenneth JW Craik. Theory of the human operator in control systems (i). *British Journal of Psychology. General Section*, 38(2):56–61, 1947.

[Cra48] Kenneth JW Craik. Theory of the human operator in control systems (ii). *British Journal of Psychology. General Section*, 38(3):142–148, 1948.

[Cro59] ERFW Crossman. A theory of the acquisition of speed-skill. *Ergonomics*, 2(2):153–166, 1959.

[CT07] Jessie YC Chen and Jennifer E Thropp. Review of low frame rate effects on human performance. *IEEE Transactions on Systems, Man, and Cybernetics-Part A: Systems and Humans*, 37(6):1063–1076, 2007.

[DCS12] Thomas L Dean, Greg Corrado, and Jonathon Shlens. Three controversial hypotheses concerning computation in the primate cortex. In *AAAI*, 2012.

[DFF04] Kai Diethelm, Neville J Ford, and Alan D Freed. Detailed error analysis for a fractional adams method. *Numerical algorithms*, 36(1):31–52, 2004.

[Die10] Kai Diethelm. *The analysis of fractional differential equations: An application-oriented exposition using differential operators of Caputo type*. Springer, 2010.

[Don78] Edmund Donges. A two-level model of driver steering behavior. *Human Factors*, 20(6):691–707, 1978.

[FCA+17] Frank Flemisch, Yigiterkut Canpolat, Eugen Altendorf, Gina Weßel, Marcel Baltzer, David Abbink, Makoto Itoh, Marie-Pierre Pacaux-Lemoine, and Paul Schutte. Shared and cooperative control of ground and air vehicles: Introduction and general overview. In *Systems, Man, and Cybernetics (SMC), 2016 IEEE International Conference on*, pages 858–863. IEEE, 2017.

[Fel86] Anatol G Feldman. Once more on the equilibrium-point hypothesis (λ model) for motor control. *Journal of motor behavior*, 18(1):17–54, 1986.

[Fit54] Paul M Fitts. The information capacity of the human motor system in controlling the amplitude of movement. *Journal of experimental psychology*, 47(6):381, 1954.

[Fre14] Frank Nugent Freeman. *The teaching of handwriting*. Houghton, Mifflin Company, 1914.

[GBB+09] Tim Gordon, Adam Blankespoor, Michelle Barnes, Dan Blower, Paul Green, and Lidia Kostyniuk. Yaw rate error–a dynamic measure of lane keeping control performance for the retrospective analysis of naturalistic driving data. In *21st International Technical Conference on the Enhanced Safety of Vehicles, Stuttgart, Germany*, pages 09–0326, 2009.

[GBS99] J Gold, PJ Bennett, and AB Sekuler. Signal but not noise changes with perceptual learning. *Nature*, 402(6758):176–178, 1999.

[Gei99] Wilson S Geisler. Motion streaks provide a spatial code for motion direction. *Nature*, 400(6739):65–69, 1999.

[GG05] Paul G Griffiths and R Brent Gillespie. Sharing control between humans and automation using haptic interface: primary and secondary task performance benefits. *Human factors*, 47(3):574–590, 2005.

[Gib50] James J Gibson. The perception of the visual world. 1950.

[Gib54] CB Gibbs. The continuous regulation of skilled response by kinaesthetic feed back. *British Journal of Psychology. General Section*, 45(1):24–39, 1954.

[GL15] TJ Gordon and Mathias Lidberg. Automated driving and autonomous functions on road vehicles. *Vehicle System Dynamics*, 53(7):958–994, 2015.

[GM76] Arthur J Grunwald and SJ Merhav. Vehicular control by visual field cues-analytical model and experimental validation. *IEEE Transactions on Systems, Man, and Cybernetics*, 6(12):835–845, 1976.

[GO98] Hiroaki Gomi and Rieko Osu. Task-dependent viscoelasticity of human multijoint arm and its spatial characteristics for interaction with environments. *Journal of Neuroscience*, 18(21):8965–8978, 1998.

[Gor09] Timothy J Gordon. Nonlinear crossover model of vehicle directional control. In *American Control Conference, 2009. ACC'09.*, pages 451–456. IEEE, 2009.

[Gre97] Richard Langton Gregory. *Eye and brain: The psychology of seeing*. Princeton University Press, 1997.

[GS14] Timothy Gordon and Krithika Srinivasan. Modeling human lane keeping control in highway driving with validation by naturalistic data. In *Systems, Man and Cybernetics (SMC), 2014 IEEE International Conference on*, pages 2507–2512. IEEE, 2014.

[GZ15] Timothy Gordon and Yu Zhang. Steering pulse model for vehicle lane keeping. In *Computational Intelligence and Virtual Environments for Measurement Systems and Applications (CIVEMSA), 2015 IEEE International Conference on*, pages 1–5. IEEE, 2015.

[HA05] Jonathan C Horton and Daniel L Adams. The cortical column: a structure without a function. *Philosophical Transactions of the Royal Society B: Biological Sciences*, 360(1456):837–862, 2005.

[Haw07] Jeff Hawkins. Learn like a human. *IEEE Spectrum*, 4, 2007.

[HBDS97] S Hanneton, Alain Berthoz, Jacques Droulez, and Jean-Jacques E Slotine. Does the brain use sliding variables for the control of movements? *Biological cybernetics*, 77(6):381–393, 1997.

[Hol82] John M Hollerbach. Computers, brains and the control of movement. *Trends in Neurosciences*, 5:189–192, 1982.

[HR+48] Wassily Hoeffding, Herbert Robbins, et al. The central limit theorem for dependent random variables. *Duke math. J*, 15(3):773–780, 1948.

[HRL08] Andrew Hollingworth, Ashleigh M Richard, and Steven J Luck. Understanding the function of visual short-term memory: transsaccadic memory, object correspondence, and gaze correction. *Journal of Experimental Psychology: General*, 137(1):163, 2008.

[HW68] David H Hubel and Torsten N Wiesel. Receptive fields and functional architecture of monkey striate cortex. *The Journal of physiology*, 195(1):215–243, 1968.

[HW77] David H Hubel and Torsten N Wiesel. Ferrier lecture: Functional architecture of macaque monkey visual cortex. *Proceedings of the Royal Society of London. Series B. Biological Sciences*, 198(1130):1–59, 1977.

[HWT+15] Brody Huval, Tao Wang, Sameep Tandon, Jeff Kiske, Will Song, Joel Pazhayampallil, Mykhaylo Andriluka, Pranav Rajpurkar, Toki Migimatsu, Royce Cheng-Yue, et al. An empirical evaluation of deep learning on highway driving. *arXiv preprint arXiv:1504.01716*, 2015.

[II75] K Ito and M Ito. Tracking behavior of human operators in preview control systems. *Electrical Engineering in Japan*, 95(1):120–127, 1975.

[IPG15] IPG. Carmaker®(5.0.1), 2015. http://ipg.de/.

[Jay57] Edwin T Jaynes. Information theory and statistical mechanics. *Physical review*, 106(4):620, 1957.

[JF03] Richard J Jagacinski and John M Flach. *Control theory for humans: Quantitative approaches to modeling performance*. CRC Press, 2003.

[JH85] LA Jones and IW Hunter. Effect of muscle tendon vibration on the perception of force. *Experimental neurology*, 87(1):35–45, 1985.

[Jür07] Thomas Jürgensohn. Control theory models of the driver. In *Modelling driver behaviour in automotive environments*, pages 277–292. Springer, 2007.

[KA68] Masaichi Kondo and Akio Ajimine. Driver's sight point and dynamics of the driver-vehicle-system related to it. Technical report, SAE Technical Paper, 1968.

[Kaw99] Mitsuo Kawato. Internal models for motor control and trajectory planning. *Current opinion in neurobiology*, 9(6):718–727, 1999.

[KBL71] D Kleinman, Sheldon Baron, and W Levison. A control theoretic approach to manned-vehicle systems analysis. *IEEE Transactions on Automatic Control*, 16(6):824–832, 1971.

[KdWA17] Sarvesh Kolekar, Joost de Winter, and David Abbink. A human-like steering model: Sensitive to uncertainty in the environment. In *Systems, Man, and Cybernetics (SMC), 2017 IEEE International Conference on*, pages 1487–1492. IEEE, 2017.

[KGZ+14] Jinseop S Kim, Matthew J Greene, Aleksandar Zlateski, Kisuk Lee, Mark Richardson, Srinivas C Turaga, Michael Purcaro, Matthew Balkam, Amy Robinson, Bardia F Behabadi, et al. Space–time wiring specificity supports direction selectivity in the retina. *Nature*, 509(7500):331, 2014.

[Kit15] Akiyoshi Kitaoka. Slope illusion (magnetic hills) in radan. *ART AND ITS ROLE IN THE HISTORY: BETWEEN DURABILITY AND TRANSIENT-ISMS*, pages 751–760, 2015.

[KL80] Virginia C Klema and Alan J Laub. The singular value decomposition: Its computation and some applications. *Automatic Control, IEEE Transactions on*, 25(2):164–176, 1980.

[KRB+17] Sue E Kase, Frank E Ritter, Jeanette M Bennett, Laura Cousino Klein, and Michael Schoelles. Fitting a model to behavior reveals what changes cognitively when under stress and with caffeine. *Biologically Inspired Cognitive Architectures*, 22:1–9, 2017.

[KTIM17] Ryunosuke Kodera, Shigehito Tanahashi, Atsuhiko Iijima, and Yoshinobu Maeda. Measurement of eye movement in visual search for a target symbol and simulation to construct a small-world network. *Advanced Biomedical Engineering*, 6:129–133, 2017.

[KYG07] Frederick AA Kingdom, Ali Yoonessi, and Elena Gheorghiu. The leaning tower illusion: a new illusion of perspective. *Perception*, 36(3):475–477, 2007.

[Lam91] John Denholm Lambert. *Numerical methods for ordinary differential systems: the initial value problem*. John Wiley & Sons, Inc., 1991.

[Lap14] Otto Lappi. Future path and tangent point models in the visual control of locomotion in curve driving. *Journal of vision*, 14(12):21–21, 2014.

[LeB06] David LeBlanc. Road departure crash warning system field operational test: methodology and results. volume 1: technical report. Technical report, University of Michigan, Ann Arbor, Transportation Research Institute, 2006.

[LH95] Michael Land and Julia Horwood. Which parts of the road guide steering? *Nature*, 377(6547):339–340, 1995.

[Lic60] Joseph CR Licklider. Man-computer symbiosis. *IRE transactions on human factors in electronics*, 1(1):4–11, 1960.

[LL94] Michael F Land and David N Lee. Where we look when we steer. *Nature*, 369(6483):742–744, 1994.

[LLPI13] Otto Lappi, Esko Lehtonen, Jami Pekkanen, and Teemu Itkonen. Beyond the tangent point: gaze targets in naturalistic driving. *Journal of Vision*, 13(13):11–11, 2013.

[LU96] Chiu-Feng Lin and A Galip Ulsoy. Time to lane crossing calculation and characterization of its associated uncertainty. *Journal of Intelligent Transportation Systems*, 3(2):85–98, 1996.

[Lub86] Ch Lubich. Discretized fractional calculus. *SIAM Journal on Mathematical Analysis*, 17(3):704–719, 1986.

[Lue79] David G Luenberger. *Introduction to dynamic systems: theory, models, and applications*, volume 1. Wiley New York, 1979.

[Mac81] Charles C MacAdam. Application of an optimal preview control for simulation of closed-loop automobile driving. *IEEE TRANSACTIONS ON SYSTEMS, MAN, AND CYBERNETICS*, 1981.

[Mac89] I Scott MacKenzie. A note on the information-theoretic basis for fitts' law. *Journal of motor behavior*, 21(3):323–330, 1989.

[Mac03] Charles C Macadam. Understanding and modeling the human driver. *Vehicle System Dynamics*, 40(1-3):101–134, 2003.

[Mag06] Richard L Magin. *Fractional calculus in bioengineering*. Begell House Redding, 2006.

[Mat74] Ethel Matin. Saccadic suppression: a review and an analysis. *Psychological bulletin*, 81(12):899, 1974.

[Mat98] Denis Matignon. Generalized fractional differential and difference equations: stability properties and modelling issues. In *Mathematical Theory of Networks and Systems symposium*, pages 503–506, 1998.

[MAT18] MATLAB. *version 9.4.0 (R2018a)*. The MathWorks Inc., Natick, Massachusetts, 2018.

[McR80] Duane McRuer. Human dynamics in man-machine systems. *Automatica*, 16(3):237–253, 1980.

[MF89] Christine Métin and Douglas O Frost. Visual responses of neurons in somatosensory cortex of hamsters with experimentally induced retinal projections to somatosensory thalamus. *Proceedings of the National Academy of Sciences*, 86(1):357–361, 1989.

[MGG16] Miguel Martínez-García and Timothy Gordon. Human control of systems with fractional order dynamics. In *Systems, Man, and Cybernetics (SMC), 2016 IEEE International Conference on*, pages 2866–2871. IEEE, 2016.

[MGG17] Miguel Martínez-García and Timothy Gordon. A multiplicative human steering control model. In *2017 IEEE International Conference on Systems, Man, and Cybernetics (SMC)*, pages 1–6, Oct 2017.

[MGG18] Miguel Martínez-García and Timothy Gordon. A new model of human steering using far-point error perception and multiplicative control. In *2018 IEEE International Conference on Systems, Man, and Cybernetics (SMC)*, pages x–x, Oct 2018.

[MGGS17] Miguel Martínez-García, Timothy Gordon, and Lei Shu. Extended crossover model for human-control of fractional order plants. *IEEE Access*, 5:27622–27635, 2017.

[MGZG16] Miguel Martínez-García, Yu Zhang, and Timothy Gordon. Modeling lane keeping by a hybrid open-closed-loop pulse control scheme. *IEEE Transactions on Industrial Informatics*, 12(6):2256–2265, 2016.

[MJ67] Duane T McRuer and Henry R Jex. A review of quasi-linear pilot models. *Human Factors in Electronics, IEEE Transactions on*, 8(3):231–249, 1967.

[MJ96] Charles C MacAdam and Gregory E Johnson. Application of elementary neural networks and preview sensors for representing driver steering control behaviour. *Vehicle System Dynamics*, 25(1):3–30, 1996.

[MJ09] Natasha Merat and A Hamish Jamson. How do drivers behave in a highly automated car. In *Proceedings of the 5th international driving symposium on human factors in driver assessment, Training and Vehicle Design*, pages 514–521, 2009.

[MK74] Duane T McRuer and Ezra S Krendel. Mathematical models of human pilot behavior. Technical report, DTIC Document, 1974.

[MKS+15] Volodymyr Mnih, Koray Kavukcuoglu, David Silver, Andrei A Rusu, Joel Veness, Marc G Bellemare, Alex Graves, Martin Riedmiller, Andreas K Fidjeland, Georg Ostrovski, et al. Human-level control through deep reinforcement learning. *Nature*, 518(7540):529–533, 2015.

[MM66] Duane T McRuer and RE Magdaleno. Human pilot dynamics with various manipulators. Technical report, SYSTEMS TECHNOLOGY INC HAWTHORNE CALIF, 1966.

[Mor81] Pietro Morasso. Spatial control of arm movements. *Experimental brain research*, 42(2):223–227, 1981.

[Mou57] Vernon Mountcastle. Modality and topographic properties of single neurons of cat9s somatic sensory cortex. *Journal of neurophysiology*, 20(4):408–434, 1957.

[Mou78] Vernon Mountcastle. An organizing principle for cerebral function: the unit module and the distributed system. *The mindful brain*, 1978.

[Mou97] Vernon Mountcastle. The columnar organization of the neocortex. *Brain*, 120(4):701–722, 1997.

[MR93] Kenneth S Miller and Bertram Ross. *An introduction to the fractional calculus and fractional differential equations*. Wiley-Interscience, 1993.

[MRM97] JH McAuley, JC Rothwell, and CD Marsden. Frequency peaks of tremor, muscle vibration and electromyographic activity at 10 hz, 20 hz and 40 hz during human finger muscle contraction may reflect rhythmicities of central neural firing. *Experimental Brain Research*, 114(3):525–541, 1997.

[MWJ+75] Duane T McRuer, David H Weir, Henry R Jex, Raymond E Magdaleno, and R Wade Allen. Measurement of driver-vehicle multiloop response properties with a single disturbance input. *Systems, Man and Cybernetics, IEEE Transactions on*, 5(5):490–497, 1975.

[MWS93] R Christopher Miall, DJ Weir, and JF Stein. Intermittency in human manual tracking tasks. *Journal of motor behavior*, 25(1):53–63, 1993.

[MZ93] Stéphane G Mallat and Zhifeng Zhang. Matching pursuits with time-frequency dictionaries. *Signal Processing, IEEE Transactions on*, 41(12):3397–3415, 1993.

[New91] KM Newell. Motor skill acquisition. *Annual review of psychology*, 42(1):213–237, 1991.

[NFNB99] Okihiko Nakayama, Tohru Futami, Tomokazu Nakamura, and Erwin R Boer. Development of a steering entropy method for evaluating driver workload. Technical report, SAE Technical Paper, 1999.

[NGD07] AC Newberry, MJ Griffin, and M Dowson. Driver perception of steering feel. *Proceedings of the Institution of Mechanical Engineers, Part D: Journal of Automobile Engineering*, 221(4):405–415, 2007.

[NGGDP08] Jose E Naranjo, Carlos Gonzalez, Ricardo Garcia, and Teresa De Pedro. Lane-change fuzzy control in autonomous vehicles for the overtaking maneuver. *IEEE Transactions on Intelligent Transportation Systems*, 9(3):438–450, 2008.

[OF03] David J Ostry and Anatol G Feldman. A critical evaluation of the force control hypothesis in motor control. *Experimental brain research*, 153(3):275–288, 2003.

[Pau12] Joop Pauwelussen. Dependencies of driver steering control parameters. *Vehicle system dynamics*, 50(6):939–959, 2012.

[PB16] Peter C Petersen and Rune W Berg. Lognormal firing rate distribution reveals prominent fluctuation–driven regime in spinal motor networks. *eLife*, 5:e18805, 2016.

[PDF67] Richard W Pew, John C Duffendack, and Linda K Fensch. Sine-wave tracking revisited. *Human Factors in Electronics, IEEE Transactions on*, 8(2):130–134, 1967.

[PDSM07] Igor Podlubny, Vladimir Despotovic, Tomas Skovranek, and Brandon H McNaughton. Shadows on the walls: Geometric interpretation of fractional integration. *Journal of Online Mathematics and its Applications*, 7, 2007.

[PE07] Manfred Plöchl and Johannes Edelmann. Driver models in automobile dynamics application. *Vehicle System Dynamics*, 45(7-8):699–741, 2007.

[Pew07] Richard W Pew. Some history of human performance modeling. *Integrated models of cognitive systems*, pages 29–44, 2007.

[Pod98] Igor Podlubny. *Fractional differential equations: an introduction to fractional derivatives, fractional differential equations, to methods of their solution and some of their applications*, volume 198. Academic press, 1998.

[Pro01] Günther Prokop. Modeling human vehicle driving by model predictive online optimization. *Vehicle System Dynamics*, 35(1):19–53, 2001.

[Roi62] Robert W Roig. A comparison between human operator and optimum linear controller rms-error performance. *IRE Transactions on Human Factors in Electronics*, 3(1):18–21, 1962.

[RS90] Joseph D Rutledge and Ted Selker. Force-to-motion functions for pointing. In *Proceedings of the IFIP TC13 Third Interational Conference on Human-Computer Interaction*, pages 701–706. North-Holland Publishing Co., 1990.

[SBM+16] Felix Schmitt, Hans-Joachim Bieg, Dietrich Manstetten, Michael Herman, and Rainer Stiefelhagen. Exact maximum entropy inverse optimal control for modeling human attention switching and control. In *Systems, Man, and Cybernetics (SMC), 2016 IEEE International Conference on*, pages 002807–002813. IEEE, 2016.

[SC70] Joseph C Stevens and William S Cain. Effort in isometric muscular contractions related to force level and duration. *Perception & Psychophysics*, 8(4):240–244, 1970.

[SCS00] RS Sharp, DANIELE Casanova, and P Symonds. A mathematical model for driver steering control, with design, tuning and performance results. *Vehicle System Dynamics*, 33(5):289–326, 2000.

[SG04] Dario D Salvucci and Rob Gray. A two-point visual control model of steering. *Perception-London*, 33(10):1233–1248, 2004.

[SG+09] Dave Shreiner, Bill The Khronos OpenGL ARB Working Group, et al. *OpenGL programming guide: the official guide to learning OpenGL, versions 3.0 and 3.1*. Pearson Education, 2009.

[Shi74] Stanley M Shinners. Modeling of human operator performance utilizing time series analysis. *IEEE Transactions on Systems, Man, and Cybernetics*, 4(5):446–458, 1974.

[SMQ93] Winfried Stute, Wenceslao Gonzáles Manteiga, and Manuel Presedo Quindimil. Bootstrap based goodness-of-fit-tests. *Metrika*, 40(1):243–256, 1993.

[SN85] M Sugeno and M Nishida. Fuzzy control of model car. *Fuzzy sets and systems*, 16(2):103–113, 1985.

[Sno26] George S Snoddy. Learning and stability: a psychophysiological analysis of a case of motor learning with clinical applications. *Journal of Applied Psychology*, 10(1):1, 1926.

[Squ04] Larry R Squire. Memory systems of the brain: a brief history and current perspective. *Neurobiology of learning and memory*, 82(3):171–177, 2004.

[SVS01] P Szendro, Gy Vincze, and A Szasz. Bio-response to white noise excitation. *Electro-and Magnetobiology*, 20(2):215–229, 2001.

[Teg17] Max Tegmark. *Life 3.0: Being human in the age of artificial intelligence*. Knopf, 2017.

[TFM96] Simon Thorpe, Denise Fize, and Catherine Marlot. Speed of processing in the human visual system. *nature*, 381(6582):520, 1996.

[Tod04] Emanuel Todorov. Optimality principles in sensorimotor control. *Nature neuroscience*, 7(9):907, 2004.

[Tus47] Arnold Tustin. The nature of the operator's response in manual control, and its implications for controller design. *Electrical Engineers-Part IIA: Automatic Regulators and Servo Mechanisms, Journal of the Institution of*, 94(2):190–206, 1947.

[TVPM13] Inés Tejado, Duarte Valério, Pedro Pires, and Jorge Martins. Fractional order human arm dynamics with variability analyses. *Mechatronics*, 23(7):805–812, 2013.

[TWM+09] Antonella Toffetti, Ellen Wilschut, Marieke Martens, Anna Schieben, Amon Rambaldini, Natasha Merat, and Frank Flemisch. Citymobil: Human factor issues regarding highly automated vehicles on elane. *Transportation Research Record: Journal of the Transportation Research Board*, (2110):1–8, 2009.

[VMPS00] Laurie Von Melchner, Sarah L Pallas, and Mriganka Sur. Visual behaviour mediated by retinal projections directed to the auditory pathway. *Nature*, 404(6780):871–876, 2000.

[W+48] Norbert Wiener et al. *Cybernetics*. JSTOR, 1948.

[War67] Michael J Wargo. Human operator response speed, frequency, and flexibility: A review and analysis. *Human factors*, 9(3):221–238, 1967.

[WCL15] Michal Weiszer, Jun Chen, and Giorgio Locatelli. An integrated optimisation approach to airport ground operations to foster sustainability in the aviation sector. *Applied Energy*, 157:567–582, 2015.

[WH+88] William H Warren, Daniel J Hannon, et al. Direction of self-motion is perceived from optical flow. *Nature*, 336(6195):162–163, 1988.

[WHM13] Adrien Wohrer, Mark D Humphries, and Christian K Machens. Population-wide distributions of neural activity during perceptual decision-making. *Progress in neurobiology*, 103:156–193, 2013.

[Wil15] Clare Wilson. What does a memory in my brain look like? *New Scientist, November*, 3049:34–39, 2015.

[WM70] David H Weir and Duane T McRuer. Dynamics of driver vehicle steering control. *Automatica*, 6(1):87–98, 1970.

[WS00] John P Wann and David K Swapp. Why you should look where you are going. *Nature neuroscience*, 3(7):647, 2000.

[YHU08] Essa Yacoub, Noam Harel, and Kâmil Uğurbil. High-field fmri unveils orientation columns in humans. *Proceedings of the National Academy of Sciences*, 105(30):10607–10612, 2008.

[YS63] LR Young and L Stark. Variable feedback experiments testing a sampled data model for eye tracking movements. *Human Factors in Electronics, IEEE Transactions on*, 1:38–51, 1963.

[ZMGG18] Yu Zhang, Miguel Martínez-García, and Timothy Gordon. Human response delay estimation and monitoring using gamma distribution analysis. In *Systems, Man, and Cybernetics (SMC), 2018 IEEE International Conference on*, pages x–x. IEEE, 2018.

Appendix A

Fractional Order Systems

In this appendix a more formal presentation of the theory of fractional calculus is given. The brief notes in Section 3.3 deal primarily with fractional operations in the frequency domain, aligned with some intuitive remarks. Here, mainly fractional computation in the time domain – which is the standard way to present the concept – is derived. The summary starts with the gamma function, an essential part in the definition of fractional derivatives and integrals. Then, after introducing some of the properties of fractional calculus, the general aspects of fractional differential equations are explained, including the methods used to integrate the equations in real time in the experiments presented in this dissertation (Appendix B).

A.1 The Gamma Function

In order to compute non-integer powers of the differential operator $D^n\{\cdot\} := {}^{d^n\{\cdot\}}/_{dt^n}$, by replacing $n \in \mathbb{N}$ with an arbitrary positive real number $\nu \in \mathbb{R}^+$, it is convenient to start with some motivational examples of what to expect. It seems natural to conjecture that, a fractional differential operator inherits the patterns exhibited by the classical derivative which it generalises. Thus for example, as $D^n e^{at} = a^n e^{at}$ ($a \in \mathbb{R}$), it may be conjectured that

$$D^\nu e^{at} = a^\nu e^{at} \text{ for } \nu \in \mathbb{R}^+. \tag{A.1}$$

Further, for $f(t) = t^p$ with $p \in \mathbb{N}$, as $D^n f(t) = {}^{p!}/_{(p-n)!} t^{p-n}$, in order to mirror this behaviour into the fractional operator, we see that an equivalent of the factorial operation that works with non-integer numbers is needed. This operator exists and it is known as the *gamma function*.

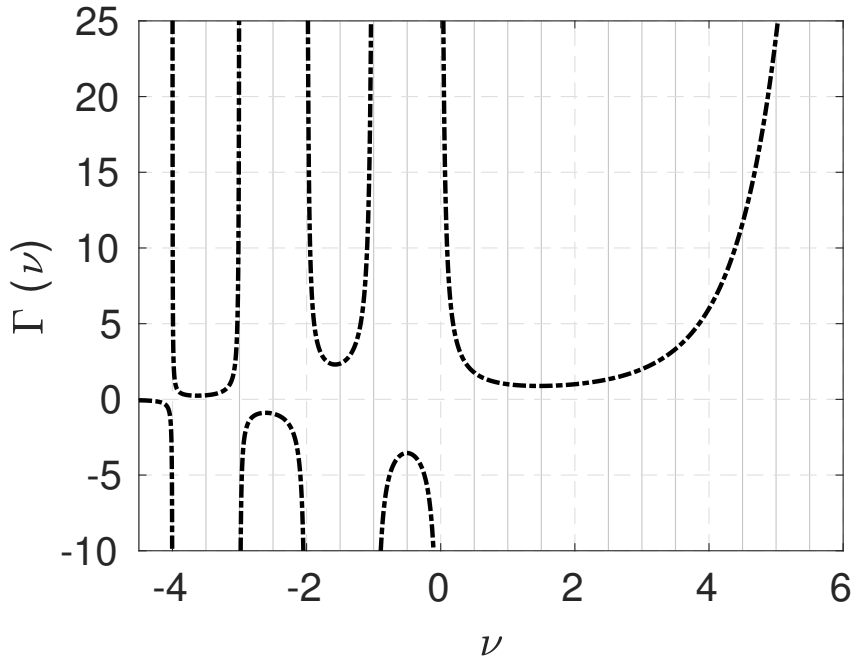

Fig. A.1 Gamma Function evaluation over the real numbers.

Definition A.1.1 (Gamma Function) *For $\nu \in \mathbb{R} \setminus \{\mathbb{Z}^- \cup \{0\}\}$, the gamma function is defined as:*

$$\Gamma(\nu) = \int_0^\infty x^{\nu-1} e^{-x} dx.$$

One thing to notice is that Γ is not defined for $\nu = 0$ neither for negative integers – it has poles for such values alternating between $\pm\infty$ (Figure A.1). On the other hand Γ is defined for complex values $z \in \mathbb{C} \setminus \{\mathbb{Z}^- \cup \{0\}\}$ ($z = x + iy$). This implies that a potential definition of fractional operator could be extended to include complex powers of the differential operator; and that is generally done in the mathematical literature [MR93]. For the sake of simplicity here we will only consider real powers of the fractional differential and integral operator.

From Definition A.1.1 it can be proven that the gamma function satisfies the following properties:

1. $\Gamma(n) = (n-1)! \quad \forall n \in \mathbb{N}$
2. $\Gamma(z) = (z-1)\Gamma(z-1) \quad \forall z \in \mathbb{C}$ except when $(z-1) \in \mathbb{Z}^- \cup \{0\}$
3. $\Gamma(z) = \pm\infty \quad \forall z \in \mathbb{Z}^- \cup \{0\}$.

The first property shows that Γ is a shifted version of the extended factorial. Accordingly, going back to the case of the monomial, from a fractional differential operator we would expect that

$$D^{\nu}t^{p} = \frac{\Gamma(p+1)}{\Gamma(p-\nu+1)}t^{p-\nu}. \tag{A.2}$$

For if this is the case, then the operator will work in a consistent manner across all the analytic functions – i.e., functions $f(t)$ which coincide with their Taylor series expansion.

A.2 The Differintegral Operator

So far only the possibility of fractional derivatives has been discussed in a non-formal manner. However, commonly fractional integrals are defined first. For the case of integration the limits must be specified in the integral operator – we will write ${}_hD_t^{-1}f(t) = \int_h^t f(t)\,dt$. The intuitive motivation behind the definition of the fractional operator is rather transparent. In [MR93] it is shown that the nested integral

$${}_hD_t^{-n}f(t) \coloneqq \int_h^t dt_1 \int_h^{t_1} dt_2 \int_h^{t_2} dt_3 \ldots \int_h^{t_{n-1}} f(\xi)\,d\xi, \tag{A.3}$$

is equivalent to the expression

$${}_hD_t^{-n}f(t) = \frac{1}{(n-1)!}\int_h^t (t-\xi)^{n-1} f(\xi)\,d\xi. \tag{A.4}$$

So in order to define fractional integrals, it is only required to substitute n by a non-integer value, and replace the factorial term by the gamma function. Thus for $\nu < 0$,

$${}_hD_t^{\nu}f(t) \coloneqq \frac{1}{\Gamma(-\nu)}\int_h^t (t-\xi)^{-\nu-1} f(\xi)\,d\xi. \tag{A.5}$$

As Equation (A.5) depends on the chosen limit of integration h, there are infinite potential definitions of fractional integral. Going back to the case of a monomial ($f(t) = t^p$), it can be shown that Equation (A.2) is only true for fractional integration ($\nu < 0$) if $h = 0$ [MR93]. Hence this is the value typically chosen in the literature, although other values have been considered; in fact Equation (A.1) is only true for integration if $h = -\infty$[1]. In this dissertation, only $h = 0$ is considered.

[1] Choosing $h = -\infty$ leads to the Liouville definition of the fractional operator

Once fractional integration is defined, fractional differentiation results as a combination of fractional integration and classical differentiation in a trivial manner:

$$ {}_0D_t^{\nu} f(t) = D^{\lceil \nu \rceil} \{ {}_0D_t^{\nu - \lceil \nu \rceil} f(t) \}, \tag{A.6} $$

where $\lceil \cdot \rceil$ represents the ceiling function. Hence the complete definition of differintegral operator follows:

Definition A.2.1 (Riemann-Liouville Fractional Differintegral Operator) *Given $\nu \in \mathbb{R}$, then*

$$ \begin{cases} {}_0D_t^{\nu} f(t) = \frac{1}{\Gamma(-\nu)} \int_0^t (t-\xi)^{-\nu-1} f(\xi)\, d\xi & \text{for } \nu < 0 \\ {}_0D_t^{\nu} f(t) = \mathcal{I}\{f(t)\} & \text{for } \nu = 0 \\ {}_0D_t^{\nu} f(t) = D^{\lceil \nu \rceil} \{ {}_0D_t^{\nu - \lceil \nu \rceil} f(t) \} & \text{for } \nu > 0 \end{cases} $$

where $\mathcal{I}$ is the identity operator. Regarding the conditions on f for ${}_0D_t^{\nu} f(t)$ to exist, if $\nu < 0$ a sufficient condition is that f is piecewise continuous function over the interval $(0,t]$, and integrable in the classical sense on $[0,t]$. For fractional differentiation ($\nu > 0$), it suffices that f is differentiable up to order $\lceil \nu \rceil$ according to the classical differential operator.

What is interesting about ${}_0D_t^{\nu}\{\cdot\}$, is that it is an operator with *memory*. This is true also for differentiation, as fractional derivatives are defined through an integral. Thus fractional calculus is useful for modelling dynamics where memory aspects can be consequential, such as viscoelastic materials or electrical circuits with memory effects [Die10]. Additionally, for the case of integration, fractional calculus allows to modulate the *temporal footprint* of the system – from no memory at all ($\nu = 0$) to an integer order integral ($\nu = -1$), where every past event has equal importance (Figure A.2).

The fractional operator is still a linear operator and satisfies a series of properties; some of them are what we expect from a derivative or integral, while others greatly differ from the behaviour of classical calculus. For example, fractional differentiation does not obey the chain rule in general. On the other hand, for a constant $k \in \mathbb{R}$ it is true that ${}_0D_t^{\nu} f(kt) = k^{\nu} \left[{}_0D_t^{\nu} f(t) \right]$. Also, the following theorem correspondent to the fundamental theorem of calculus is established:

Theorem A.2.1 (Fundamental Theorem of Fractional Calculus) *Let f be an analytic function in a vicinity of the origin then, $\forall \nu \in \mathbb{R}$ and $\forall \rho \in \mathbb{R}^-$*

$$ {}_0D_t^{\nu} \left[{}_0D_t^{\rho} f(t) \right] = {}_0D_t^{\nu+\rho} f(t). $$

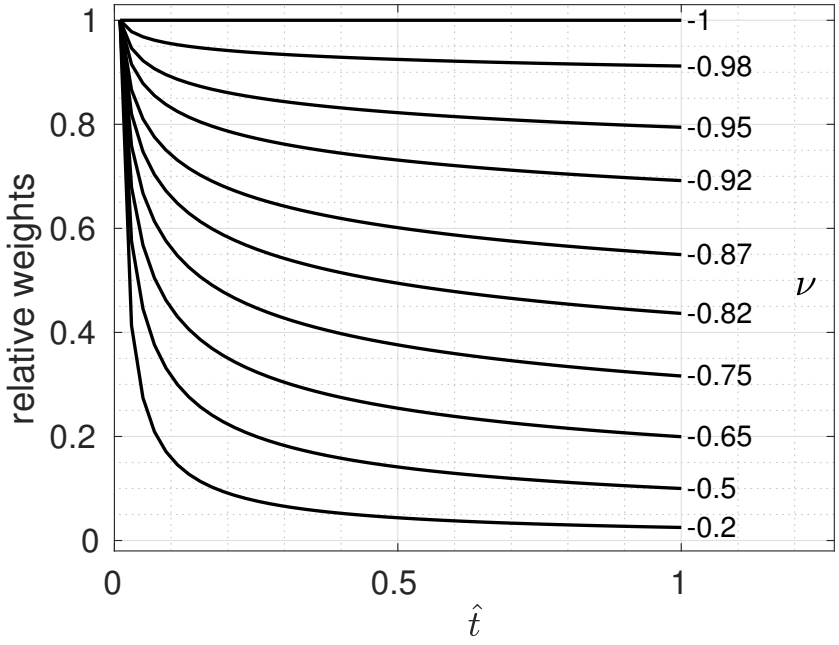

Fig. A.2 Temporal footprint of the differintegral operator; the relative importance of $f(t-\hat{t})$ in the magnitude of the operator ${}_0D_t^{\nu}\{f(t)\}$ for different values of ν is displayed. For $\nu=-1$, at time t every *past event* $f(t-\hat{t})$ has equal effect on the differintegral operator. Different values of ν – displayed on the right side of the plot – weight the past events differently.

The above property only holds in general when fractional integration is performed first. Other properties of the fractional differintegral operator can be found in [Pod98, Die10].

An example of special interest is the fractional differintegral of the exponential function. It can be shown, that for $a,\nu\in\mathbb{R}$

$$ {}_0D_t^{\nu}e^{at} = a^{\nu}\sum_{k=0}^{\infty}\frac{(at)^{k-\nu}}{\Gamma(k+1-\nu)}. \tag{A.7}$$

This could have been deduced simply by integrating the Taylor series of e^{at} $n\in\mathbb{N}$ times, then substituting n by $-\nu$, and replacing the factorial by the gamma function – because we chose $h=0$ in Definition (A.2.1) to ensure that analytical functions are well behaved under the differintegral operator. Nevertheless, we see that ${}_0D_t^{\nu}e^{at}$ is not an exponential function, but something similar. Moreover as linear differential equations have solutions which can be expressed in terms of exponentials, this anticipates that solving fractional differential equations may not be trivial. In fact, if $\nu>0$ Equation (A.7) *blows up* for $t=0$. Further,

stability analysis of such fractional differential equations cannot be performed by direct analysis of the eigenvalues of the system – or the poles of the corresponding transfer function.

Now as $\cos(z) = \left(e^{iz}+e^{-iz}\right)/2$ and $\sin(z) = \left(e^{iz}-e^{-iz}\right)/2i$, and by linearity, Equation (A.7) lets us compute fractional integrals and derivatives of sines and cosines. As $\int \cos(t)$ involves a translation to the right of the cosine function by $\pi/2$ units, it seems reasonable to speculate that ${}_0D_t^{\nu}\cos(t) \approx \cos(t - \pi/2\nu)$. Indeed this is true if we disregard the transient (Figure A.3).

A.3 Fractional Differential Equations

A.3.1 Analytical Results

For a *fractional order differential equation* (FODE), the existence and uniqueness results are not as general as for an ODE. Still some partial results hold, specially for the case of linear FODEs [Pod98]:

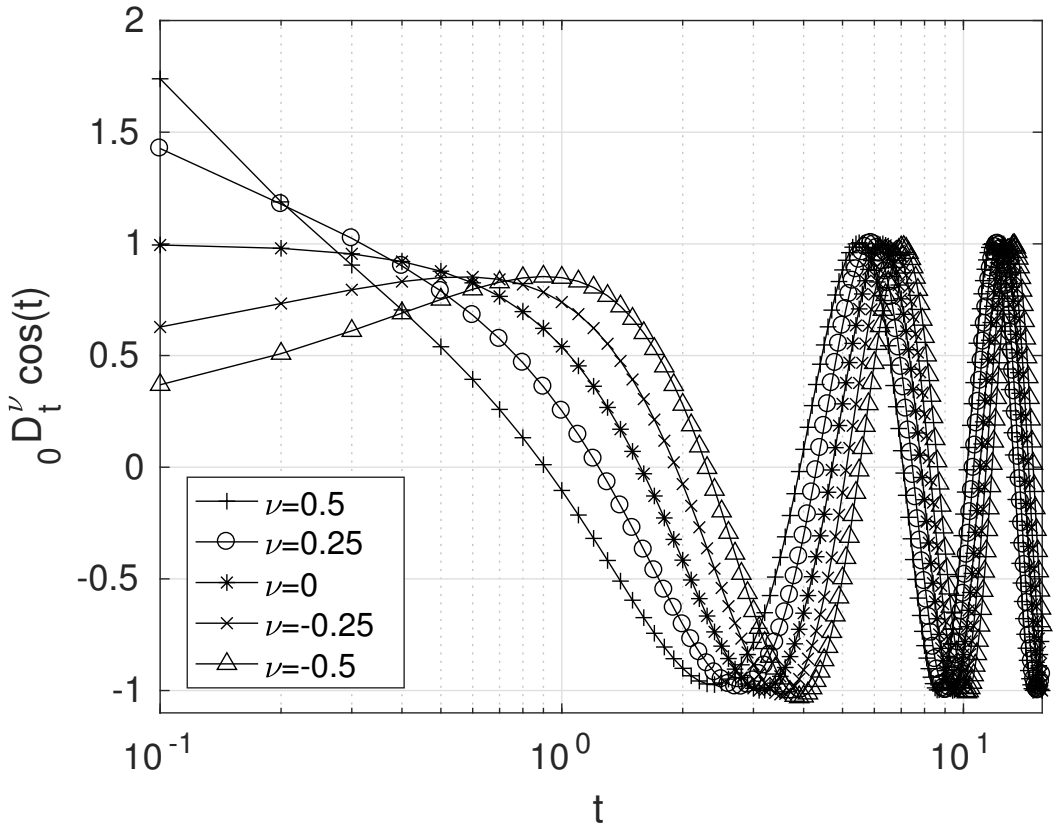

Fig. A.3 Differintegral of a cosine function for different values of ν. The plot is displayed in logarithmic scale to better visualise the transient.

Theorem A.3.1 (Existence and Uniqueness Theorem for linear FODE) *Given a FODE of the form*

$$ {}_0D_t^{\nu_n} y(t) + \sum_{j=1}^{n-1} \{ r_j(t) \left[{}_0D_t^{\nu_j} y(t) \right] \} + r_0(t) y(t) = f(t) $$

where $r_j(t)$ (for $j = 0, \ldots, n-1$) are continuous functions in $[0,T]$ and $\nu_j > 0$ (for $j = 1, \ldots, n$) and $\nu_n \in [m-1, m)$ ($m \in \mathbb{N}$), then the initial value problem corresponding to $D^k y(0)$ for $k = 0, 1, \ldots, m-1$ has a unique continuous solution over $[0,T]$.

Finding $y(t)$ as an analytical solution can be complicated, although it is possible for simple cases through the method of the Laplace transform – and when $f(t)$ is a known function and not a varying input. One of the caveats of this approach is that, when applying the inverse Laplace transform to non-integer powers of s, usually initial conditions of fractional order appear (${}_0D_t^{\nu_n} y(0)$). If zero initial conditions can't be assumed in a particular type of problem, it is not clear how initial conditions of fractional order could be measured from a system[2]. Nevertheless, in most situations numerical integration methods are used, as in the simulations presented in this dissertation.

A.3.2 Numerical Integration of FODE

Definition (A.2.1) is the most common for mathematical analysis, but there is an alternative definition for fractional differentiation which is helpful in deriving methods for integrating FODE numerically – the Grüwald-Letnikov fractional operator. In this other definition, fractional differintegration is expressed as the sum of a time series, and it follows from the expression to define classical derivatives from backward differences,

$$ D^n f(t) = \lim_{h \to 0} \frac{1}{h^n} \sum_{m=0}^{n} (-1)^m \binom{n}{m} f(t - mh), \, n \in \mathbb{N} \tag{A.8} $$

that can be extended to non-integer order differentiation and integration, again by using the gamma function[3]:

Definition A.3.1 (Grünwald-Letnikov fractional operator) *Given a function f which is differentiable up to order $m \in \mathbb{N}$, then for $\nu \in (m-1, m)$ the Grünwald-Letnikov fractional*

[2] In this case there is another definition of the fractional operator that can be used. Caputo's fractional differintegral operator is defined by inverting the order of integration and differentiation in A.6 [Die10]. This method is not used here and thus not presented.

[3] And by applying the property of the Gamma function: $\Gamma(n-z)\Gamma(z-n+1) = (-1)^n \Gamma(-z)\Gamma(1+z)$ for $z \in \mathbb{C}$ and $n \in \mathbb{N}$.

operator is defined as

$$ {}_0D_t^{\nu} f(t) = \lim_{h\to 0} \frac{1}{h^{\nu}} \sum_{j=0}^{t/h} \frac{\Gamma(j-\nu)}{\Gamma(-\nu)\, j!} f(t-jh). $$

Both given definitions for ${}_0D_t^{\nu}\{\cdot\}$ are equivalent for smooth functions. Therefore it is justified to use the Grünwald-Letnikov to solve FODE without changing the context of the system. The relation in Def. (A.3.1) can be approximated with its discretised counterpart:

$$ {}_0\widetilde{D}_t^{\nu} f(t) = \frac{1}{h^{\nu}} \sum_{j=0}^{t/h} \frac{\Gamma(j-\nu)}{\Gamma(-\nu)\, j!} f(t-jh). \tag{A.9} $$

The last expression, essentially a linear filter, displays more clearly that the fractional operator is a weighted sum of past observations, and therefore it is an operator with memory. It can be proved (see [Pod98]) that the discretisation error when computing ${}_0\widetilde{D}_t^{\nu} f(t)$ satisfies[4]

$$ {}_0D_t^{\nu} f(t) - {}_0\widetilde{D}_t^{\nu} f(t) = \mathcal{O}(h). \tag{A.10} $$

The truncation error, by considering only a finite memory window of width L can be bounded as follows:

$$ \left| {}_0D_t^{\nu} f(t) - {}_{t-L}D_t^{\nu} f(t) \right| \leq \frac{ML^{-\nu}}{|\Gamma(1-\nu)|} \tag{A.11} $$

where M is a bound for $|f|$. Equation (A.11) is referred to as the *short-memory principle*, and encapsulates the idea that recent events are more relevant than distant ones. Thus by choosing L such that $ML^{-\nu}/|\Gamma(1-\nu)| \approx h$ the total approximation error is $\mathcal{O}(h)$.

In what follows, it is described how to integrate linear FODE using Equation (A.9). In the tracking experiments described in Section B.1, the following type of transfer functions is considered:

$$ \frac{Y(s)}{U(s)} = \frac{K}{s^{\alpha}(Ts+1)} \text{ for } \alpha > 0 $$

which is equivalent to the FODE

$$ T\, {}_0D_t^{\alpha+1} y(t) + {}_0D_t^{\alpha} y(t) = Ku(t). \tag{A.12} $$

[4]For analytic functions.

Substituting (A.9) into (A.12) and reorganising terms yields:

$$y(t) = \frac{1}{T+h}\Big[h^{\alpha+1}Ku(t) - T\sum_{j=1}^{t/h}\frac{\Gamma(j-\alpha-1)}{\Gamma(-\alpha-1)j!}y(t-jh) \\ -h\sum_{j=1}^{t/h}\frac{\Gamma(j-\alpha)}{\Gamma(-\alpha)j!}y(t-jh)\Big] + \mathcal{O}(h). \tag{A.13}$$

By using (A.13) in a step-wise manner, equation (A.12) can be numerically integrated with a local discretisation error $\mathcal{O}(h)$. While there exist higher order algorithms to approximate fractional derivatives and for numerical integration of fractional differential equations [Lub86, Die10], for use in human-in-the-loop interactions and real time application the method in Equation (A.13) seems to be appropriate. Also, there is little risk of drift arising from any approximation error, since the human operator is constantly cancelling errors when performing closed-loop control.

If higher accuracy is required, an additional property of fractional operators is needed in order to develop higher order methods [Die10]:

$${}_0D_t^{-\nu}\left[{}_0D_t^{\nu}y(t)\right] = y(t) - \sum_{j=0}^{m-1}\frac{D^j y(0)}{j!}t^j \text{ with } \nu > 0 \text{ and } m = \lceil \nu \rceil. \tag{A.14}$$

As stated, the fundamental theorem (A.2.1) only works when fractional integration is applied first. Now, for the initial value problem ${}_0D_t^{\nu}y(t) = f(t)$ with $D^j y(0) = y_0^j$ we have

$$y(t) = \sum_{j=0}^{m-1}\frac{y_0^j}{j!}t^j + {}_0D_t^{-\nu}\left[f(t)\right], \tag{A.15}$$

and by integrating the last term in the expression above – from Definition (A.2.1) – the FODE can be solved. According to the order of the quadratures chosen to approximate the integral, different methods are obtained. If the integral is computed by means of the rectangle rule, a second order Adams-Moulton-Bashford method results. These methods are expensive computationally speaking. The Adams-Moulton-Bashford method to solve ODEs has a numerical complexity of $\mathcal{O}(h^{-1})$, while its fractional counterpart exhibits $\mathcal{O}(h^{-2})$ [DFF04], due to the non-locality of fractional derivatives.

A.3.3 Stability Analysis

Stability analysis of linear FODEs is a little more intricate than for ODE case. This is reflected – in the time domain – because fractional derivatives of exponential functions are

not exactly exponential functions (Equation A.7). In the frequency domain, the transfer function of an ODE exhibits non-integer powers of s. Thus instead of poles, the denominator presents branch points. So the general strategy of using the eigenvalues of a linear system – or their corresponding poles – to assess its stability does not work. Still, the following theorem – which applies to the Laplace domain – extends the classical method to the fractional case [Mat98]:

Theorem A.3.2 (Stability of Fractional Order Systems) *Given a fractional order transfer function $G(s)$ and a non-fractional transfer function $\tilde{G}(s)$ such that, for a particular value $0 < \zeta < 1$, it satisfies $\tilde{G}(s^{\zeta}) = G(s)$ then,*

$$G(s) \text{ is BIBO stable} \iff |\arg(p)| > \zeta \frac{\pi}{2}$$

for every pole p of $\tilde{G}(s)$.

The theorem has a simple visual interpretation as it can be seen in Section 3.5.4, where it is applied to assess the stability of a FIR filter controlling a fractional order plant. In particular, for $\zeta = 1$ the theorem coincides with the classical stability criteria for non-fractional transfer functions based on pole location in the complex plane.

Appendix B

Data Collection And Data Sources

B.1 Human-in-the-loop Tracking Experiments (HTE)

A number of human tracking experiments were recorded from ten naïve test subjects of mixed gender, whose ages spanned from 22 to 33 years. In this dissertation, we refer to the data collected in these experiments as the Human-in-the-loop Tracking Experiments (HTE) dataset.

SUBJECT:	S1	S2	S3	S4	S5	S6	S7	S8	S9	S10
GENDER:	M	F	M	M	M	F	M	M	M	M
AGE:	32	24	22	28	22	28	24	28	33	32
EXP. VID. GAMES:	NO	YES	YES	YES	YES	NO	YES	YES	YES	YES
EXP. JOYSTICK:	NO	NO	NO	NO	NO	NO	NO	NO	NO	NO
DRIV. LICENSE:	YES	YES	YES	YES	NO	NO	NO	YES	YES	YES
EXP. DRIVER:	NO	YES	NO	YES	NO	NO	NO	YES	YES	YES

Table B.1 Gender and age of the 10 participants in the HTE. In the table it is also detailed for each subject their previous experience playing video games, using a joystick and driving experience status.

The experimental setup consisted of two different control devices – a joystick and a steering wheel – and a real time software application that run on a desktop computer (Fig. 2.1). At each time step, the application read the output of a control device and integrated a FODE according to the method described in Section A.3.2. The display was updated during the real time simulation at 15 Hz, as with this frame rate the motion of the presented moving cursors in the display seemed continuous (see also Sec. 2.4.2).

In each of the experiments, four signals were recorded: the forcing function $r(t)$, the plant output $m(t)$, the error signal $e(t)$ and the human response $c(t)$ (Fig. 2.2). The controlled

moving cursor was presented on a computer monitor as a circular solid dot, which varied in colour for each plant considered, so that the test subjects were aware of a change in the dynamics and thus the adaptation time was shortened. The reference target point was displayed as a circle of slightly larger size and different colour (Fig. B.1).

The experiments were performed in compensatory and pursuit modes (Section 2.3.1). Besides the two control modes, the HTE were presented other variants: two different control devices, five different plants, and with or without a future prediction indicator. Whenever the future prediction was active, an additional dot was presented in the screen. This dot gave prediction information to the subjects about the speed and direction of the plant response, by displaying its predicted position 0.5 s after the present instant[1].

A training round of tests, which were not recorded, was performed prior to the actual tests in order to habituate the participants to the experimental setup. Each participant performed 20 experiments grouped in rounds of five. Each experiment lasted for 90 s. After each round of five experiments the subjects were requested to rest by the investigator for some minutes. The five considered transfer functions of the controlled plants are

$$\frac{Y(s)}{U(s)} = \frac{K}{s^{\alpha}(Ts+1)} \tag{B.1}$$

with parameters $\alpha = 0.5, 0.75, 1, 1.25, 1.5$ (and $T = 0.1$). K was adjusted empirically for the joystick ($K = 2$) and the steering wheel ($K = 5$). The steering wheel was calibrated to allow a total of 900 degrees of rotation lock to lock.

The order of the different plants was randomised for each subject (Table B.2 and B.3). For each participant, half of the experiments were executed with the joystick and half with the steering wheel. Half of the subjects performed the joystick experiments in compensatory mode and the steering wheel experiments in pursuit mode.

The forcing function $r(t)$ was composed of a sum of sinusoids with a range of frequencies $f_k = 0.01 - 20\,\text{Hz}$:

$$r(t) = \sum_{f_k \in \{0.01, 0.02, \ldots, 20\}} e^{-4 f_k} \sin(f_k \cdot 2\pi t - \varphi_k) \tag{B.2}$$

where $\varphi_k \in [-\pi, \pi]$ is a randomised phase for each summation term. With this choice, the amplitude is negligible for frequencies outside of the range where a human-operator can perform adequate control (Sec 2.4.2).

[1] It was observed that, while some subjects made active use of the future prediction dot to reduce the response delay, other subjects do not seem to have used it at all. We believe that more training was needed before all the subjects could use the future prediction dot to improve their performance. As the results were found to be inconclusive, they are not reported here.

The experimental data were sampled at 100 Hz. For each of the 90 s events, the initial 20 s were excluded, in case the subjects were adapting to the new plant dynamics. Another reason to exclude these initial data is to allow the fractional operators to populate their internal memory. Similarly the final 10 s were excluded, as during that time the forcing function was gradually returned to zero, to minimise discontinuity during a change in plant dynamics. Thus from each event, only 60 s of data were analysed.

In Table B.4 the experimental setup parameters are summarised. In Tables B.2 and B.3, the order in which the rounds of experiments were performed is detailed.

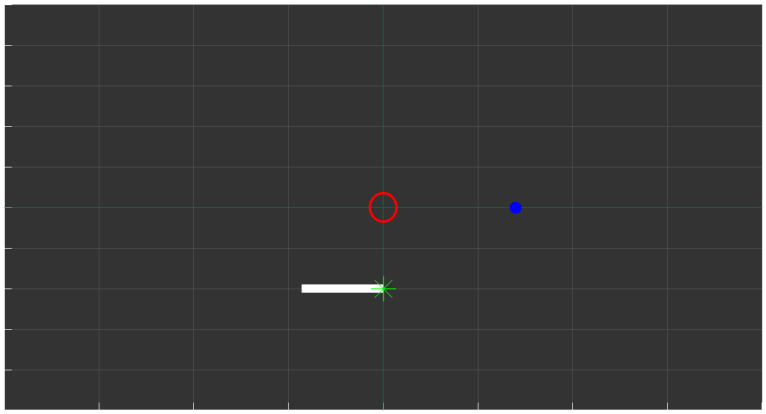

(a) Compensatory mode

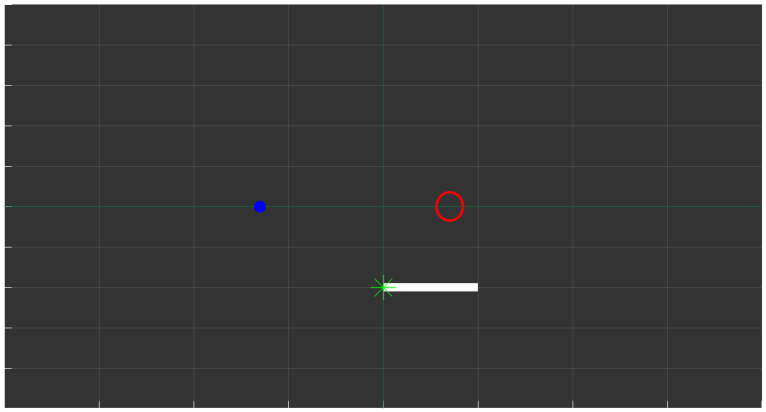

(b) Pursuit mode

Fig. B.1 Display presented to the subjects during the HTE. The blue dot, controlled by the subject, follows the target – red circle. A white bar indicates the applied control gain.

	SUBJECT										
EXPERIMENT #:	S1	S2	S3	S4	S5	S6	S7	S8	S9	S10	
1	1	1	1	1	1	1	1	1	1	1	NO PRED.
2	0.5	0.5	0.75	0.75	1.25	0.5	0.5	0.75	0.75	1.25	
3	1.5	0.75	1.25	0.5	0.5	1.5	0.75	1.25	0.5	0.5	
4	0.75	1.25	0.5	1.5	1.5	0.75	1.25	0.5	1.5	1.5	
5	1.25	1.5	1.5	1.25	0.75	1.25	1.5	1.5	1.25	0.75	
6	1	1	1	1	1	1	1	1	1	1	PRED.
7	0.5	0.5	0.75	0.75	1.25	0.5	0.5	0.75	0.75	1.25	
8	1.5	0.75	1.25	0.5	0.5	1.5	0.75	1.25	0.5	0.5	
9	0.75	1.25	0.5	1.5	1.5	0.75	1.25	0.5	1.5	1.5	
10	1.25	1.5	1.5	1.25	0.75	1.25	1.5	1.5	1.25	0.75	
MODE:	C	P	C	P	C	P	C	P	C	P	

Table B.2 HTE performed with a joystick as control device. The table shows the fractional order α of the plant (B.1) for each subject and for each experiment in the order they were performed – in compensatory and pursuit modes and with or without prediction dot. For each subject the experiments were presented in a different order.

	SUBJECT										
EXPERIMENT #:	S1	S2	S3	S4	S5	S6	S7	S8	S9	S10	
1	1	1	1	1	1	1	1	1	1	1	NO PRED.
2	1.25	1.5	1.5	1.25	0.75	1.25	1.5	1.5	1.25	0.75	
3	0.75	1.25	0.5	1.5	1.5	0.75	1.25	0.5	1.5	1.5	
4	1.5	0.75	1.25	0.5	0.5	1.5	0.75	1.25	0.5	0.5	
5	0.5	0.5	0.75	0.75	1.25	0.5	0.5	0.75	0.75	1.25	
6	1	1	1	1	1	1	1	1	1	1	PRED.
7	1.25	1.5	1.5	1.25	0.75	1.25	1.5	1.5	1.25	0.75	
8	0.75	1.25	0.5	1.5	1.5	0.75	1.25	0.5	1.5	1.5	
9	1.5	0.75	1.25	0.5	0.5	1.5	0.75	1.25	0.5	0.5	
10	0.5	0.5	0.75	0.75	1.25	0.5	0.5	0.75	0.75	1.25	
MODE:	P	C	P	C	P	C	P	C	P	C	

Table B.3 HTE performed with a steering wheel as control device. The table shows the fractional order α of the plant (B.1) for each subject and for each experiment in the order they were performed – in compensatory and pursuit modes and with or without prediction dot. For each subject the experiments were presented in a different order.

Experimental Parameters	
Number of subjects	10
Age of subjects	22-33 years
Duration of each event	90 s (60 analysed)
Number of recorded events	200
Forcing function freq. range	0.01-20 Hz*
Sampling frequency	100 Hz
Steering wheel range	-450 to 450 degrees

Table B.4 Summarised experimental parameters. $(\star)$ The frequencies of the forcing function are spaced every 0.01 Hz. Note that the frequencies are weighted so that they are only effective up to 0.5 Hz (B.2). The remaining frequency values are added to simulate noise in the system.

The HTE were approved by the College of Science Research Ethics Committee of the University of Lincoln with UID COSREC491.

B.2 Naturalistic Driving Data (NDD)

It is only recently that rich databases of *naturalistic driving data* (NDD) have become available for research. Here, the source of the data is the Road Departure Crash Warning (RDCW) Field Operational Test [LeB06]. The NDD dataset corresponds to 200 driving events with 4 different drivers – 50 driving events per driver. This database was collected on Nissan Altima 3.5SE vehicles (Tab. B.5) at 0.1 Hz.

For a part of the presented analysis and parameter estimation these 200 driving events were used. The data are considered *naturalistic*, that is, the data are recorded in real road conditions where subjects don't have to interact with the logging equipment, and eventually become unaware of it. Thus the data represent *normal driving*. Each of the driving events has a duration of 60 s. The four drivers – here called (A,B,C,D) – are all within the age range from 40 to 50 years old. Drivers (A,B) are female while drivers (C,D) are male. The initial speed of the events is $28-32\,\mathrm{ms}^{-1}$ with an overall variation less than $\pm 5\,\mathrm{ms}^{-1}$. The driving events were recorded on roads relatively straight, with a radius of curvature of at least 500 m.

B.3 Driving Simulation Experiments (DSE)

NDD (Appendix B.2 and Section 4.2) are inherently noisy and complicated to analyse. On the other hand, data collected from subjects in laboratory tasks, although may be less representative of realistic driving, are more interpretable; this is partly due to the fact in laboratory experiments the sensory inputs presented to the human-operator can be restricted

Nissan Altima 3.5SE (2003) Parameters	
Steering ratio (r_s)	16 : 1
Curb weight (M)	1471 kg
Dist. from cg to front axle (l_f)	1.064 m
Dist. from cg to rear axle (l_f)	1.736 m
Wheelbase (l)	2.8 m
Track	1.552 m
Yaw moment of inertia (I)	1981 kg $\cdot$ m^2

Table B.5 Summarised parameters of a Nissan Altima 3.5SE (2003) vehicle.

to relevant variables. The data collected in Appendix B.1 consisted of a simple laboratory task, designed to assess the basic features of human control and establish a methodology. Here a semi-realistic setup was designed to collect steering data under varying conditions. We will refer to this dataset as Driving Simulation Experiments (DSE) dataset.

B.3.1 Experimental Setup

Software

An application in C code was created for the purpose of performing the experiments. The graphics were generated in 3D with the Open Graphics Library (OpenGL) API [SG+09] and the OpenGL Utility Toolkit (GLUT), through the GPU of a high performance desktop computer[2] with a Linux operating system. The graphics in the display were refreshed at a variable frame rate (40 Hz minimum) by the GPU.

The graphical simulation consisted of a forward road scene (Fig. B.2), with additional elements in some of the experiments, such as a moon near the horizon or an obstacle on the road. The geometry of the road path was first generated with Matlab® [MAT18] and saved into a comma-separated values (CSV) file.

The software application loaded the road geometry CSV file into memory and initialised the graphical window presented to the subject, then the simulation run in real time at 1000 Hz. At each time step the variables of the vehicle simulation were updated through a Runge-Kutta method of order $\mathcal{O}(h^4)$ [Lam91]. The vehicle states were simulated with the linear vehicle model in [Abe15] (Eq. 3.14 and Table B.6). Additionally, a random perturbation was added to the yaw rate of the vehicle in order to mimic the effect produced by road pavement irregularities and wind gusts. The perturbation was composed by a sum of sinusoids of different frequencies and was tuned empirically.

[2]With an Intel 7th Gen Quad Core I7 7700K 4.2GHz CPU, a NVIDIA GeForce GTX 1070 8GB GDDR5 GPU and a low latency SSD drive.

Mass of the vehicle M	1500 kg
Distance from vehicle c.g. to front axle l_f	1.1 m
Distance from vehicle c.g. to rear axle l_r	1.6 m
Wheelbase $l = l_f + l_r$	2.7 m
Front cornering stiffness (both wheels) $C_{\alpha f}$	55000 N/rad
Rear cornering stiffness (both wheels) $C_{\alpha r}$	60000 N/rad
Yaw moment of inertia I	2500 kg·m^2
Steering Ratio r_s	16:1

Table B.6 Linear vehicle model parameters in the DSE.

Data were saved to another CSV file for each time step at the end of each test. The recorded variables were the simulation time, vehicle position, vehicle heading, yaw rate, lateral offset, body slip angle, steering angle (or torque, depending on the control device) and associated variables according to the presented perturbations (moon position or splay angle modifications).

Hardware

Attached to the computer, there were two displays and two control devices – one display for each control device (Fig. B.4). Also, a pair of speakers were used to signal the driver of varying conditions during the experiments. The two control devices were a Logitech G27 steering wheel, and an Isometric Steering Wheel (ISW). During the simulation the motor of the gaming wheel was controlled from the C code routine to produce a self-aligning torque effect.

The ISW was built for this particular experiment and consisted of a torque sensor (Tab. B.7 and Fig. B.3) attached to a support frame, made of wood and other materials. The signal

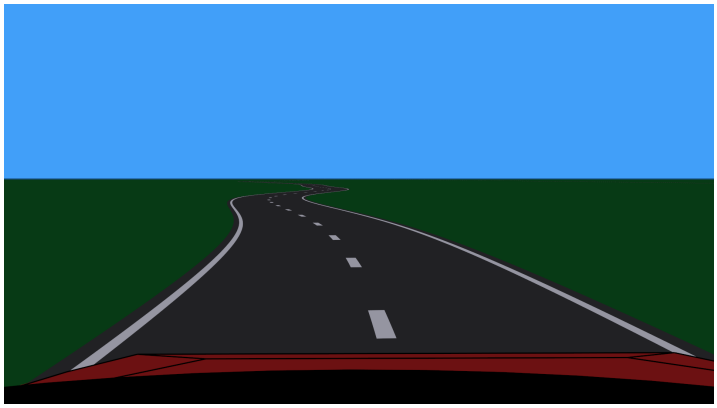

Fig. B.2 Forward view of the simulated road in the OpenGL simulation as it was presented to the subjects.

Model	Omega TQ301-45N
Range Sensor	$0-45\,\mathrm{N\cdot m}$
Range in the set up – limited	$0-15\,\mathrm{N\cdot m}$
Accuracy	$\pm 0.2\,\%$FSO
Wheel Diameter	0.32 m

Table B.7 Specifications of the torque sensor and the ISW.

from the torque sensor was read by a single-board micro-controller[3] acting as a transducer. The simulation application requested the state of the sensor to the micro-controller at each simulation step. When requested, the micro-controller broadcasted the torque sensor back to the application. The communication between the devices was set at 921600 baud.

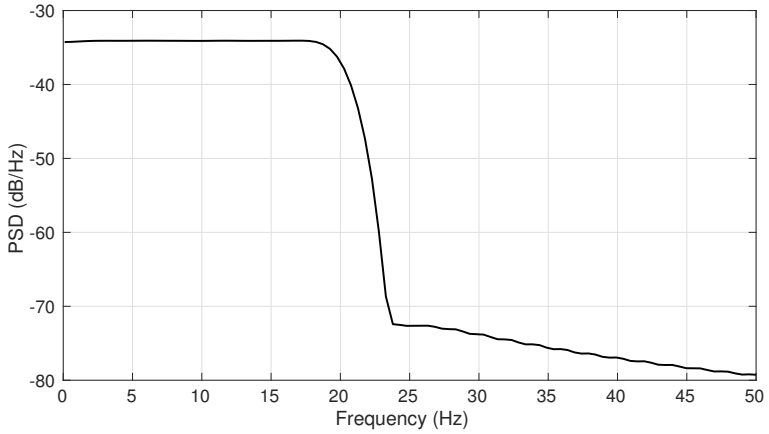

Fig. B.3 PSD of the torque sensor noise. The sensor, when in rest state, produces band limited white noise. The PSD was computed with the Welch method with a window of $\approx 0.5\,\mathrm{s}$ and 50% overlap.

B.3.2 Driving Experiments with Test Subjects

Ten subjects of varying age, gender and level of driving experience participated in the experiments (Table B.8). The experiments are summarised in Table B.9 and were performed in the same order as in the table with one exception: odd subjects performed experiment 7a before 7b while even subjects performed 7b first. The experiments were executed over two different days – each day involving approximately 30 m of driving with some rest periods – to monitor human adaptation to isometric control. In all the experiments – with the exception of Exp. #3 Day 1, Exp. #2 Day 2 and the ISW training experiments – the visual projection represented a driver view from the left seat of the car – offset 0.45 m.

[3] An Arduino Due.

SUBJECT:	S1	S2	S3	S4	S5	S6	S7	S8	S9	S10
GENDER:	M	M	F	M	F	M	M	M	M	F
AGE:	32	33	34	41	25	28	22	20	30	28
EXP. VID. GAMES:	NO	YES	NO	NO	NO	NO	YES	YES	NO	NO
DRIV. LICENSE:	YES	YES	NO	YES	YES	YES	YES	YES	YES	YES
EXP. DRIVER:	YES	YES	NO	YES	YES	YES	YES	YES	YES	YES

Table B.8 Gender and age of the 10 participants in the DSE. In the table it is also detailed for each subject their previous experience in playing video games, whether the subjects hold driving license or not and their driving experience.

The experiments with the Logitech G27 wheel were designed to assess different aspects of visual acquisition during driving, and are discussed in Chapter 4. The experiments with the ISW were executed to measure the capacity of humans to perform vehicle control based on torque input (Chapter 5).

The DSE were approved by the College of Science Research Ethics Committee of the University of Lincoln with UID COSREC491.

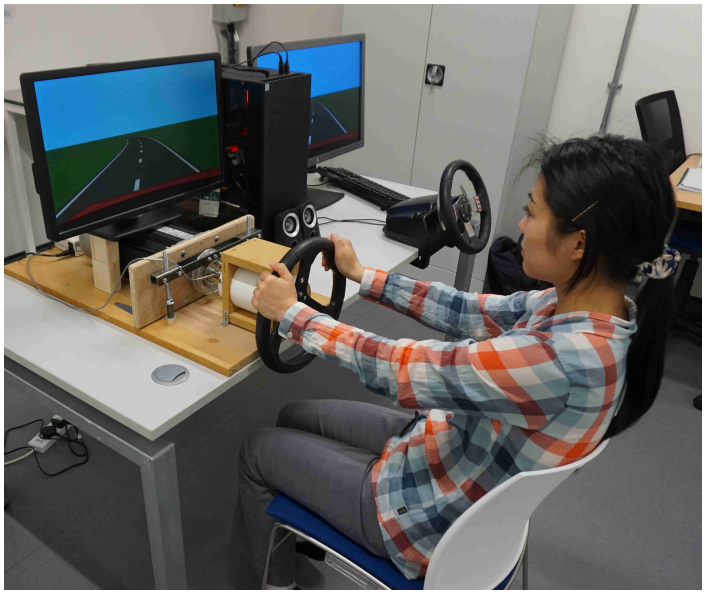

Fig. B.4 Human subject testing the experimental setup. The ISW is on the left side – controlled by the subject. The gaming steering wheel is on the right side.

DAY 1			
Exp.#	**Wheel**	**Duration**	**Description**
1	Logitech	180 s	Pseudorandom road path. Basic steering control to adapt the subjects to the used setup (50 km/h).
2	Logitech	220 s	A more challenging road than that in Exp.#1 – with sharper turns to further adapt subjects to the setup (50 km/h).
3	Logitech	360 s	Driving on a straight road. During $t = 170 - 180$ s the graphical simulation changes the seat position of the driver smoothly – from the left to the right seat (50 km/h).
4	Logitech	180 s	Driving on a straight road (50 km/h). From $t = 20$ s the drivers can only see the near 4 m of the road. At $t = 60$ s a moon appears over the horizon. From $t = 120$ s the moon oscillates with increasing amplitude.
5	ISW	180 s	A circle alternates between two positions in the display every 20 s. The drivers adjust the position of the follower by applying torque to the ISW. This test is to adapt subjects to the ISW.
6	ISW	180 s	A circle alternates between random positions in the display every 6 s. The drivers adjust the position of the follower by applying torque to the ISW. This test is to further adapt subjects to the ISW.
7	ISW	420 s	The subjects control a simulated vehicle on a pseudo-random curved road with the ISW. Every 60 s a flash in the screen and a sound in the speakers signal of a change in the transfer function between the ISW and the vehicle (50 km/h).
DAY 2			
1	Logitech	180 s	Subjects drive on a circular road (800 m radius). At $t = 20$ s, the road visibility is shortened to 4 m. At $t = 60$ s the road visibility normalises. During the test a moon appears on the background – the moon moves normally according to the road curvature and disappears on the left. At $t = 120$ s the road visibility shortens again, and another moon appears from the right, which 30 s later reverses its direction (50 km/h).
2	Logitech	240 s	This test consists in driving on a straight road at 50 km/h. At $t = 30$ s a black screen occludes a part of the display, allowing the drivers to see only in the far distance (from 14 m ahead). During the test the lane lines perturbate their relative angles; the road becomes progressively broader towards the right side by one meter, and then gradually returns to its initial width (90-150 s). This is followed by the same effect with in the left lane line (180-240 s).
3	ISW	420 s	Same as test 7 in Day 1 but at 30 km/h.
4	ISW	420 s	Identical to test 7 in Day 1 (50 km/h).
5	ISW	420 s	Same as test 7 in Day 1 but at 70 km/h.
6	Logitech	70 s	The vehicle self drives and the subject keeps hands off the wheel for 50 s. At times the display becomes fully occluded. At $t = 50$ s the vehicle requests the driver to take control (with a coloured flash and a sound). The subject must dodge an object in the middle of the road (straight driving at 50 km/h). This is an easy adaptation test for 7a and 7b.
7a	Logitech	100 s	The vehicle self drives and dodges an object on the road. The display occludes at $t = 75$ s. At $t = 78$ s the display visibility normalises and the driver is requested to intervene and dodge an obstacle on a curved road – within a short reaction time – (50 km/h).
7b	ISW	100 s	Identical to test 7a but with the ISW.

Table B.9 Summary of the DSE in the order they were performed.

Appendix C

Bootstrap Test of Goodness-of-fit

Once a probability distribution is selected to be representative of a data set $\mathbb{X}$, and its parameters are fitted to the data giving a probability density function (PDF) $f_{\mathbb{X}}$ and a cumulative distribution function (CDF) $F_{\mathbb{X}}$, in order to quantify the goodness-of-fit the following bootstrap method can be used [SMQ93]:

1. Determine the distance between the fitted probability distribution and the empirical data by using some statistical measure, for example the Kolmogorov-Smirnov distance can be used:
$$D = \max_{x \in \mathbb{X}} |F_{\mathbb{X}}(x) - \tilde{F}_{\mathbb{X}}(x)| \tag{C.1}$$
where $\tilde{F}_{\mathbb{X}}$ is the empirical CDF.

2. Generate a set of pseudo-random numbers $\mathbb{Y}$ distributed according to $F_{\mathbb{X}}$.

3. The parameters of the chosen probability distribution are fitted again to the new artificial data $\mathbb{Y}$, obtaining a new CDF $F_{\mathbb{Y}}$.

4. The Kolmogorov-Smirnov distance is calculated for the artificial data set $\mathbb{Y}$,
$$d = \max_{y \in \mathbb{Y}} |F_{\mathbb{Y}}(y) - \tilde{F}_{\mathbb{Y}}(y)|.$$

5. Steps 2 to 4 are iteratively repeated many times (say $10000 - 100000$ times) generating a set of distances $\mathbb{D} = \{d_1, d_2, \ldots, d_N\}$.

6. The p-value of the goodness-of-fit test is estimated according to
$$p = \frac{\#\{d \in \mathbb{D} | \, d > D\}}{N} \tag{C.2}$$

where # denotes the cardinality of the specified set, that is, p is the proportion of distances in $\mathbb{D}$ greater than D. If $p > 0.1$ the goodness-of-fit test rejects the null hypothesis of the data not belonging to the specified distribution; the data can be explained by the distribution considered.

Appendix D

Stability of the MHC model

In this appendix, the stability of the MHC model (Sec. 4.3), acting in closed-loop with a second order system, is demonstrated.

System Equation

Considering a second order system with state x, input u and assuming that its relaxed state is at $x-u=0$, the system can be written as

$$mx''(t) = -b\left(x'(t) - u'(t)\right) - k\left(x(t) - u(t)\right) \tag{D.1}$$

or

$$mx''(t) + bx'(t) + kx(t) = ku(t) + bu'(t). \tag{D.2}$$

Also, considering a forcing function $r(t)$, the error of the system in closed-loop is $e(t) = r(t) - x(t)$. Equation D.2 can now be rewritten as a first order system introducing an additional variable $w(t) = e'(t)$:

$$e'(t) = w(t) \tag{D.3a}$$

$$mw'(t) + bw(t) + ke(t) = -ku(t) - bu'(t) + \left(mr''(t) + br'(t) + kr(t)\right). \tag{D.3b}$$

MHC Model Equations in Continuous Time

For convenience, the equations of the MHC model in discrete time can be written as:

$$\xi_{t_k} = \left(\frac{|e_{t_k}|}{|e_{t_{k-1}}|}\right)^{\rho} \text{ with } \rho > 0 \tag{D.4a}$$

$$h_{t_k} = \xi_{t_k} h_{t_{k-1}} \tag{D.4b}$$

$$u_{t_k} = K h_{t_k} \frac{e_{t_k}}{|e_{t_k}|}. \tag{D.4c}$$

Now, given a small time step Δt, we have

$$\frac{h_{t_k} - h_{t_{k-1}}}{\Delta t} = \frac{(\xi_{t_k} - 1) h_{t_{k-1}}}{\Delta t}, \tag{D.5}$$

and taking limits

$$h'(t) = \lim_{\Delta t \to 0} \frac{|\frac{e(t)}{e(t-\Delta t)}|^\rho - 1}{\Delta t} h(t - \Delta t) = \frac{(|e(t)|^\rho)'}{|e(t)|^\rho} h(t). \tag{D.6}$$

Then

$$\frac{h'(t)}{h(t)} = \rho \frac{(|e(t)|)'}{|e(t)|} \text{ when } h(t) > 0 \text{ and } e(t) \neq 0, \tag{D.7}$$

which can be written as

$$(\log h(t))' = \rho (\log |e(t)|)'. \tag{D.8}$$

Taking initial conditions such that $h(0)/|e(0)|^\rho = 1$, the equation above solves to

$$h(t) = |e(t)|^\rho. \tag{D.9}$$

Thus from Eq. D.4c and D.9 results

$$u(t) = K \frac{e(t)}{|e(t)|} h(t) = K e(t) |e(t)|^{\rho - 1} \tag{D.10a}$$

$$u'(t) = K \rho |e(t)|^{\rho - 1} w(t). \tag{D.10b}$$

System in Closed Loop

Putting together the system (Eq. D.3) with the MHC response (Eq. D.10) acting in feedback results in

$$e'(t) = w(t) \tag{D.11a}$$

$$w'(t) = \frac{1}{m} \{ -bw(t) - ke(t) - K(ke(t) + b\rho w(t)) |e(t)|^{\rho - 1} + mr''(t) + br'(t) + kr(t) \}. \tag{D.11b}$$

Or when $r(t) = 0$,

$$e'(t) = w(t) \tag{D.12a}$$

$$w'(t) = \frac{1}{m}\{-bw(t) - ke(t) - K(ke(t) + b\rho w(t))|e(t)|^{\rho-1}\}. \tag{D.12b}$$

Stability of the System

The stability of the system D.12 can be established by finding a Liapunov function [Lue79], that is, a continuous function V that is positive within all the trajectories and its derivative is negative for every trajectory. In this case we can choose the function:

$$V(e,w) = \frac{1}{2}ke^2 + \frac{m}{2}w^2 + \frac{K \cdot k}{\rho+1}|e|^{\rho+1} \tag{D.13}$$

which satisfies $V(e,w) > 0$ except at $(e,w) = (0,0)$, and

$$\frac{dV}{dt}(e,w) = \frac{\partial V}{\partial e}e' + \frac{\partial V}{\partial w}w' = -bw^2 - K\rho bw^2|e|^{\rho-1} \tag{D.14}$$

which satisfies $\frac{dV}{dt}(e,w) < 0$ except at $(e,w) = (0,0)$. Therefore the orbits of D.11 converge to the fixed point $r(t)$ (Fig. D.1).

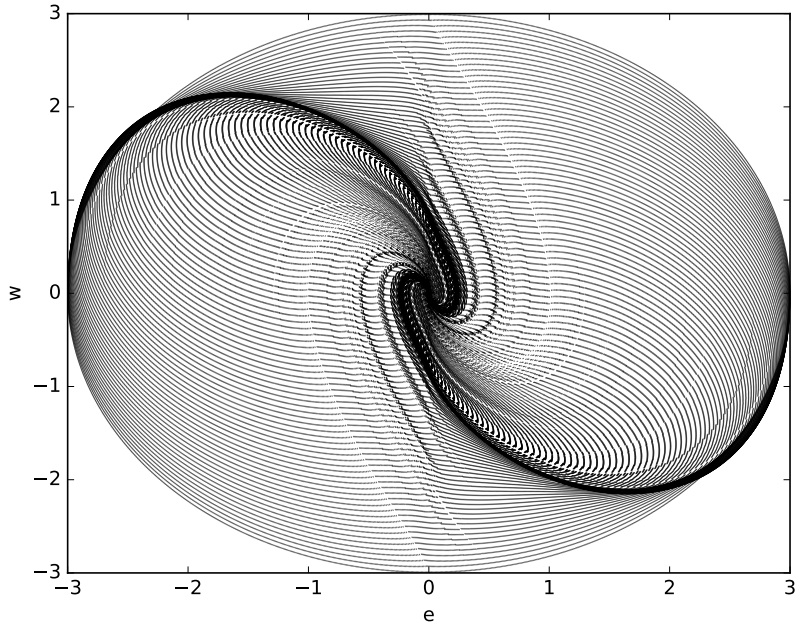

Fig. D.1 Orbits of the system in Eq. D.12 for $m = 1$, $b = 0.9$, $k = 1$, $\rho = 0.4$ and $K = 1$.

Appendix E

Splay Angles Computation

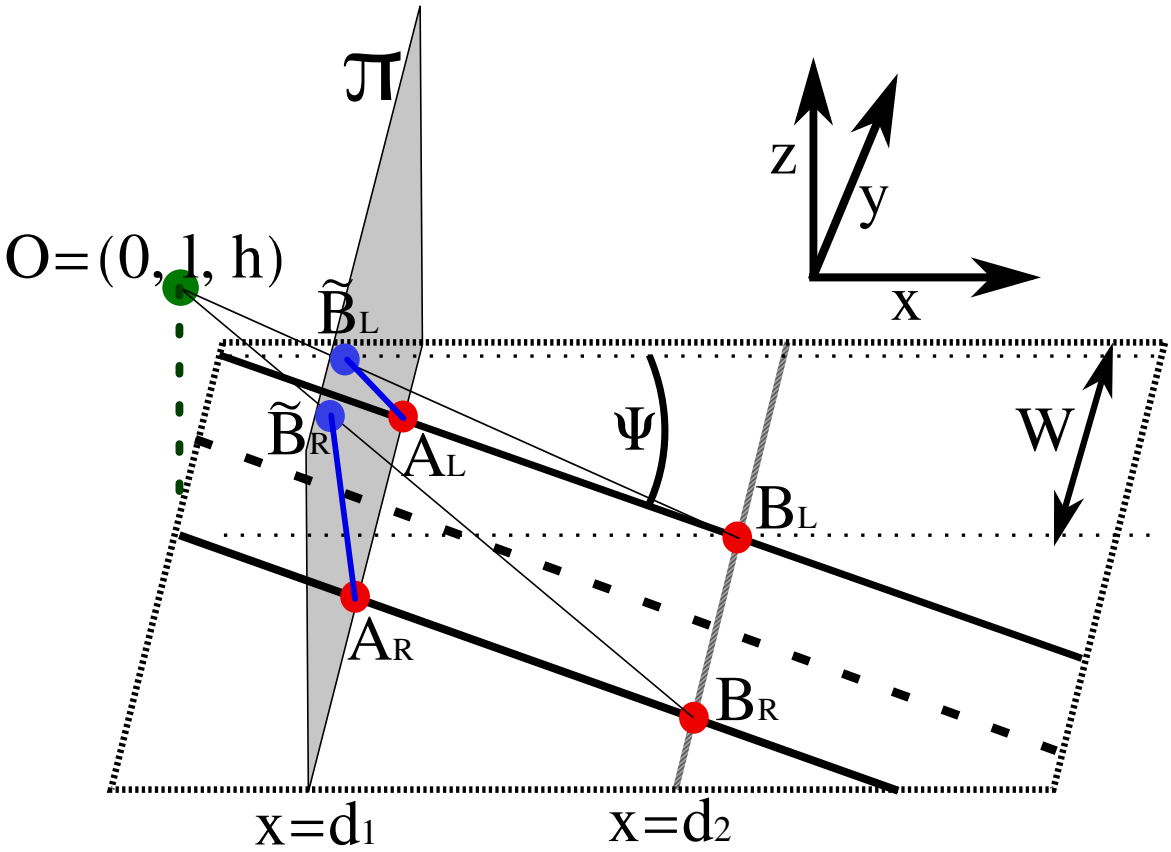

Fig. E.1 Diagram of the projection of the splay lines – in blue – on a plane π. The observer is situated at O. Here a road of width W is considered.

The *splay angles* are defined as the interior angles of the projection of the road lines over a plane π, situated at a distance d_1 from an observer O. The observer has its oculus at height

h with coordinates $O = (0, l, h)$ – with respect to the reference frame in Fig. E.1 – where l is the lateral offset, which is positive to the left.

Two points from each road line are considered: A_L and B_L on the left road marking, and A_R and B_R on the right. The road is at an angle ψ with respect to the line of sight of the observer. Thus,

$$\begin{cases} A_L = (d_1, {}^{W}/_{2} + d_1 \tan\psi, 0) \\ B_L = (d_2, {}^{W}/_{2} + d_2 \tan\psi, 0). \end{cases} \tag{E.1}$$

The projection of these points over π are,

$$\begin{cases} \tilde{A}_L = A_L \\ \tilde{B}_L = \left(d_1, l + {}^{d_1}/_{d_2}\left({}^{W}/_{2} + d_2 \tan\psi - l\right), h - h{}^{d_1}/_{d_2}\right). \end{cases} \tag{E.2}$$

Thus changes in heading (ψ) result in lateral displacement of the left splay line (Fig. E.1 in blue and Fig. 4.13b) by $d_1 \tan\psi$. The left splay angle θ_L (Fig. 4.13a) results from the relation

$$\tan\theta_L = -\frac{h - h{}^{d_1}/_{d_2}}{l + {}^{d_1}/_{d_2}\left({}^{W}/_{2} + d_2 \tan\psi - l\right) - {}^{W}/_{2} - d_1 \tan\psi} = \frac{h}{{}^{W}/_{2} - l}. \tag{E.3}$$

Equivalently, it can be proven that

$$\tan\theta_R = \frac{h}{{}^{W}/_{2} + l}. \tag{E.4}$$

Appendix F

Computation of the Steering Entropy

The steering entropy (H_p) is obtained by first computing the difference between a steering signal $\delta(t_k)$ and its prediction $\tilde{\delta}(t_k)$. The prediction $\tilde{\delta}(t_k)$ results from the second order Taylor series approximation of $\delta(t)$ at every time step. From the prediction errors $e(t_k) = \delta(t_k) - \tilde{\delta}(t_k)$, the 90% percentile α is then calculated and the values $e(t)$ separated into the nine groups determined by the following bin edges: $\{-\infty, -5\alpha, -2.5\alpha, -\alpha, -1/2\alpha, 1/2\alpha, \alpha, 2.5\alpha, 5\alpha, \infty\}$. Lastly, the entropy of the percentage of values p_i ($i = 1, \ldots, 9$) inside each of the bins is obtained [NFNB99]:

$$H_p = -\sum_{i=1}^{9} p_i \log_9\{p_i\}. \tag{F.1}$$